

Surface-assisted formation and development of model protocells

Dissertation for the Degree of Philosophiae Doctor

Elif Senem Köksal



Department of Chemistry

Faculty of Mathematics and Natural Sciences

University of Oslo

June 2021

© **Elif Senem Köksal, 2021**

*Series of dissertations submitted to the
Faculty of Mathematics and Natural Sciences, University of Oslo
No. 2401*

ISSN 1501-7710

All rights reserved. No part of this publication may be
reproduced or transmitted, in any form or by any means, without permission.

Cover: Hanne Baadsgaard Utigard.
Print production: Representralen, University of Oslo.

Preface

This thesis finalizes the research carried out during the candidacy for Philosophiae Doctor at the Department of Chemistry, Faculty of Mathematics and Natural Sciences, University of Oslo, in the time period August 2017 to May 2021 (including parental leave from 08/2019-06/2020) under the supervision of Dr. Irep Gözen (principal supervisor), and co-supervision of Dr. Reidar Lund and Dr. Andreas Carlson.

First and foremost, I express my gratitude to my supervisor Dr. Irep Gözen for accepting me as a PhD student and for her patience, endless support and motivation. Thank you for acknowledging the hard work and being generous.

I thank my co-supervisors Dr. Reidar Lund and Dr. Andreas Carlson for their support and for all the advice and discussions.

I express my gratitude to all former and current members of Softlab Norway; Karolina, Aysu, Inga, Lin, Ingrid, Maivizhi, Ilayda and Gizem for your good spirit, help and pleasant times in lab and outside the work.

I thank Aldo for helpful discussions and for fixing all the broken stuff so that I can keep working.

I acknowledge all my co-authors for enabling my work through valuable contributions.

I am grateful to the people in NCMM and Minalab for providing a nice working environment and the members of the Bio3 section in Department of Chemistry for all the helpful discussions during section meetings.

Last but not least, I dedicate a special thanks to my family for their unconditional love and support. I couldn't have done this without my husband Hakan and our daughter Helen.

Elif Senem Köksal

Oslo, March 2021

Table of Contents

Preface	iii
Table of Contents	v
List of Publications	vii
Author's Contributions	ix
Abstract	xi
1. Introduction	1
2. Origins of life	3
2.1. Building blocks and constituents of protocells.....	3
2.1.1. RNA world	5
2.1.2. Lipid world	6
2.1.3. Membranous prebiotic compartments	7
2.2. Protocell formation on mineral interfaces.....	10
2.3. Suitable geological environments for the origin of life.....	12
2.3.1. Warm little pond hypothesis	12
2.3.2. Deep-sea hydrothermal vents	14
2.3.3. Comparison of conditions associated with primitive cell constituents	15
2.4. Other theories and recent developments	16
3. Surface energy and natural surfaces	19
3.1. Surface free energy and wetting phenomena	19
3.1.1. Surface defects and grain boundaries.....	21
3.2. Natural surfaces	22
4. Lipid membranes and membrane mechanics	25
4.1. Amphiphiles	25
4.1.1. Fatty acid vesicles	26
4.1.2. Phospholipid vesicles.....	28
4.2. Membrane mechanics.....	30
4.3. Formation of vesicles	30

4.4.	Supported membranes	32
4.5.	Double bilayer spreading	33
4.6.	Membrane rupturing	34
4.7.	Tube formation	35
4.8.	Diffusion and tension-driven transport through nanotubes	37
4.9.	Protocell nucleation, growth and division	38
4.10.	Membrane permeability and transient pores.....	41
5.	Methods	43
5.1.	Preparation of lipid vesicles.....	43
5.2.	Surface fabrication and characterization	44
5.2.1.	Surface fabrication.....	44
5.2.2.	Preparation of thin sections of natural surfaces.....	46
5.3.	Microscopy	47
5.3.1.	Fluorescence and confocal laser scanning microscopy	47
5.3.1.	Variable pressure scanning electron microscopy (VP SEM)	50
5.4.	The microfluidic pipette.....	50
5.5.	Near infrared (NIR) laser heating system	51
5.6.	Genetic materials.....	52
5.7.	Mathematical model and simulations	53
6.	Summary of the Main Findings in the Papers.....	55
7.	Conclusions and Future Outlook	59
	References.....	61
	Appendix.....	75

List of Publications

- Paper I. E. S. Köksal, S. Liese, I. Kantarci, R. Olsson, A. Carlson, I. Gözen.
Nanotube-mediated path to protocell formation
ACS Nano, 2019, 13, 6867-6878.
- Paper II. M. O. Rydmark, M. K. Christensen, E. S. Köksal, I. Kantarci, K. Kusatinovich, V. Yantchev, A. Jesorka, I. Gözen.
Styrene maleic acid copolymer induces pores in biomembranes
Soft Matter, 2019, 15, 7934-7944.
- Paper III. E. S. Köksal, S. Liese, L. Xue, R. Ryskulov, L. Viitala, A. Carlson, I. Gözen.
Rapid growth and fusion of protocells in surface-adhered membrane networks
Small, 2020, 16, 2002529.
- Paper IV. K. Spustova, E. S. Köksal, A. Ainla, I. Gözen.
Subcompartmentalization and pseudo-division of model protocells
Small, 2021, 17, 2005320.
- Paper V. I. Põldsalu, E. S. Köksal, I. Gözen.
Mixed fatty acid-phospholipid protocell networks
Submitted manuscript
- Paper VI. E. S. Köksal, I. Põldsalu, Henrik Friis, Stephen Mojzsis, Martin Bizzarro, I. Gözen.
Spontaneous formation of prebiotic compartment colonies on Hadean Earth and pre-Noachian Mars
Submitted manuscript

List of related peer-reviewed publications by the author that are not included in the thesis

Paper VII. E. S. Köksal, P. Belletati, G. Reint, R. Olsson, K. Leitl, I. Kantarci, I. Gözen.

Spontaneous formation and rearrangement of artificial lipid nanotube networks as a bottom-up model for endoplasmic reticulum

J. Vis Exp., 2019, 143, e58923.

Author's Contributions

- Paper I. Performed all confocal microscopy experiments, showed the step-by-step transformation of the phospholipid reservoirs to giant unilamellar vesicles proceeding via lipid nanotube networks. Performed the membrane lamellarity and fluorescence intensity analyses, and determined the vesicle counts. Contributed to the writing of the manuscript.
- Paper II. Developed the surface-adhered vesicle system, performed the confocal microscopy experiments showing the superfusion of the different concentrations of the SMA polymer with the surface-adhered compartments and performed the associated fluorescence intensity analyses on leakage of fluorescence contents from the compartments. Contributed to the writing of the manuscript.
- Paper III. Designed and performed the microscopy experiments for heat-induced formation, growth and fusion of cell-like compartments, analyzed the time-dependent changes in vesicles in terms of number, size and area. Performed the encapsulation of fluorescein and fluorescently labeled RNA into vesicles and the associated fluorescence intensity-based fusion analysis. Contributed to the writing of the manuscript.
- Paper IV. Made the initial experimental setup, determined the surface type and lipid composition leading to the subcompartmentalization behavior. Contributed to the writing of the manuscript.
- Paper V. Performed the initial experiments to make fatty acid reservoirs and show autonomous vesicle growth from fatty acids. Performed first encapsulation and leakage experiments on fatty acid compartments with fluorescein and RNA oligonucleotides and the associated analysis on roundness. Proposed the measurements of free fatty acid concentrations and performed the analyses together with Põldsalu. Contributed to the writing of the manuscript.
- Paper VI. Performed all confocal microscopy experiments except the initial experiments on quartz and granite. Performed RNA and DNA encapsulation experiments and non-enzymatic DNA reactions as well as the fluorescence intensity analysis of lamellarity, RNA uptake and DNA reactions. Assisted Dr. Friis during SEM-EDX experiments on mineral surfaces and the meteorite. Contributed to the writing of the manuscript.

Abstract

The main focus of this thesis is the surface-assisted formation and development of model protocells. In the publications that emanated from my research, I present experimental evidence for the possibility of protocell formation from various amphiphiles on numerous high energy solid surfaces and under conditions reasonably related to prebiotic environmental conditions. I describe a self-transformation pathway of multilamellar lipid reservoirs to unilamellar compartments on solid substrates, which remain connected via lipid nanotubes. At elevated temperatures, nucleation and growth of model protocells are accelerated, and fusion is promoted between adjacent compartments. The compartments can take up small molecules such as fluorescein as well as RNA and DNA. I show that the surfaces assist subcompartmentalization in giant, dome-shaped model protocells. The subcompartments can later rupture and lead to the formation of surface-adhered daughter protocells. Finally I report that natural surfaces *e.g.* glasses, minerals, rocks and a Martian meteorite fragment promote the self-formation of nanotube-protocell networks and dense robust protocell colonies, which encapsulate genetic fragments and accommodate a non-enzymatic DNA reaction. The observed processes are governed by surface-membrane interactions and point to an over-looked feasible pathway for the formation and development of protocells at the origin of life.

1. Introduction

The physico-chemical mechanisms behind the formation, growth and division of protocells, the hypothetical precursors of the first living cells, are among the key questions concerning the origin of life. Establishing simple and consistent pathways for the assembly of protocell structures from the primordial soup, and for their self-replication and division, is a particular challenge. In this thesis, I investigate the governing function of solid surfaces in self-formation and development of model protocells, characterize the driving mechanisms at the mesoscale, and investigate the unique features of the observed structures.

The key transformations investigated in this study require a minimal amount of components, and are entirely driven by surface interactions and free energy minimization, without the requirement of hydrolysis of organic molecules, or external stimuli. Various hypotheses that are proposed in the context of the emergence of life involve the presence of liquid water, and amphiphilic organic compounds that can self-assemble¹. Natural surfaces in the form of mineral interfaces with adsorbed small organic molecules were abundant on the early Earth, but their involvement in compartmentalization is mostly overlooked. This work focuses on the impact of the innate energy provided by solid interfaces on the self-organization of amphiphilic molecules, and the properties of the resulting model protocells.

There is a strong link between the formation of protocells and the origin of life. Despite the well-established bulk hypothesis, in which the protocellular compartments assemble and freely suspend in water, our understanding of early evolution from the formation of self-organized structures displaying certain characteristics of living cells, to self-sustaining and reproducing systems², is quite limited. Phylogenomic analysis indicate that the Last Universal Common Ancestor (LUCA), *i.e.* the urancestor, must already have a complex molecular and cellular structure and advanced bioenergetics³. In this context, Tibor Ganti's chemoton model² is commonly referred to define a minimal cell. According to Ganti's model, a protocell contains three autocatalytic subsystems: a membrane subsystem which keeps the components together and intact, an information subsystem that processes and transfers heritable information to progeny and a metabolic subsystem that captures energy and material resources. To be considered alive, these subsystems must be unified and function co-operatively for the survival and evolution of the supersystem. This well aligns with NASA's definition for life: "a self-sustaining chemical system capable of Darwinian evolution". This thesis aims to identify the surface-assisted protocell formation and development pathways, through which the transition from non-living to living can be re-thought. The formation of protocellular compartments is considered to be a small but an essential step towards formation of first living cells.

In Paper I⁴, I describe the step-by-step transformation of lipid reservoirs upon their contact with solid substrates to unilamellar compartments, proceeding *via* intermediate nanotubular structures. In Paper III⁵, I show rapid nucleation and growth of the protocells described in Paper I at elevated temperatures, which is one of the possible energy sources on the early Earth. Robust surface-adhered compartments, being the experimental outcome of the mechanisms reported in Paper I&III, were applied in a method to study the interaction of polymers with free-standing bilayers in Paper II⁶. In Paper IV,⁷ surface-governed spontaneous subcompartmentalization and the transformation of initial model protocells to daughter cells via a unique pseudo-division pathway was reported. Paper V reports on the transformations of membranes consisting of fatty acids with phospholipids at various concentrations into protocell-nanotube networks via a formation pathway similar to the one characterized in Papers I&III. Finally, the self-formation of protocells on natural surfaces: glasses, minerals, rocks and a Martian meteorite fragment was investigated and reported in Paper VI.

In Part 2 of the thesis, I provide a background of the most widely accepted theories on the origins of life, recent findings on the impact of mineral microparticles on protocell formation, and selected relevant information on the search for life outside our planet.

In Part 3, I introduce fundamental concepts of surface and interfacial energy, and surface tension.

In Part 4, I describe amphiphiles and biomembrane assembly, as well as membrane mechanics and energetic aspects concerning the topological changes reported in the papers.

In Part 5, I describe the key methods used in the articles presented in this thesis, including various light microscopy techniques, surface fabrication, and technical features of the microfluidic device and the infrared laser-based heating system.

In Part 6, I summarize the main findings of the published papers, and submitted and prepared manuscripts.

In Part 7, I conclude my thesis and discuss future perspectives.

2. Origins of life

The idea that life arose from a primordial soup, an aqueous suspension of organic molecules which gradually underwent chemical changes and gave rise to prebiotic reactions and eventually to life, was originally proposed by Haldane⁸ and Oparin⁹. Haldane wrote in 1929 that “The cell consists of numerous half living chemical molecules suspended in water and enclosed in an oily film. When the whole sea was a vast chemical laboratory, the conditions for the formation of such films must have been relatively favorable”. The later experiments by Urey-Miller, where an electrical discharge was applied through a mixture of CH₄, H₂ and NH₃ gases resulting in formation of numerous amino acids¹⁰ such as glycine, alanine, aspartic acid and α-aminobutyric acid, provided direct experimental support for the prebiotic soup theory. However, the mere presence of organic molecules in a hot, dilute soup is not equivalent to efficient interactions and polymerization. Possibilities of concentrating organic molecules with the help of dry-wet cycling in small ponds, tidal pools and by adsorption on minerals were therefore put forward for consideration¹¹.

2.1. Building blocks and constituents of protocells

Early Earth mainly had three major sources¹² of organic molecules. Firstly, the endogenous organic synthesis enabled by natural energy sources such as UV light, heat, and electrical discharges. Secondly, organic synthesis could have been driven by shock waves of impacts of meteors, airburst of objects and post-impact vapor plumes¹². Lastly, direct delivery from extraterrestrial sources has been considered¹¹⁻¹².

In order to understand how the endogenous sources of organic materials led to the assembly of more complex molecules relevant for the emergence of life, researchers have performed various experiments by simulating prebiotically plausible conditions. Simple compounds present in the early Earth atmosphere such as N₂, CO₂, HCN, SO₂ and H₂S were used as ingredients to form compounds with more complex structure and function^{11, 13}.

One well-known example is the Miller-Urey experiment, which led to the formation of numerous amino acids¹⁰ by applying electrical discharge through a mixture of reducing gases. The knowledge on composition of the early atmosphere was reassessed over time, and it is now generally agreed upon that the early Earth's atmosphere contained redox-neutral gases. New experiments performed accordingly in 2008 showed that amino acids can still be generated with redox neutral gases CO₂, N₂ and H₂O¹⁴. Hydrocarbons were synthesized from CO and H₂ in a series of Fischer–Tropsch type chemical reactions¹⁵.

Formation of both single chain fatty acids and more complex phospholipids has been shown under potentially prebiotic conditions. For example, hydrocarbon chains of 2-33 atoms in length were detected in solutions of oxalic acid, acting both as carbon and hydrogen source¹⁶. Phospholipids such as phosphatidylethanolamine (PE), phosphatidylcholine (PC), phosphatidic acid (PA) and phosphatidylglycerol (PG) were also synthesized under early Earth conditions¹⁷⁻²⁰, the detailed conditions of which will be discussed in detail in 2.3.1. Suitable geological environments for the origins of life. Recently, a cyanosulfidic protometabolism was identified in which precursors of RNA, protein and lipids could all be derived from hydrogen cyanide and some of its derivatives²⁰. This means that constituent forming the compartments and metabolic systems, could have been simultaneously produced from one pot.

Origin of biomolecular homochirality during formation of constituents of protocells is one of the unanswered questions²¹⁻²². Laboratory synthesis of molecules results in racemic mixtures, containing equal amounts of left-handed and right-handed enantiomers of a chiral molecule. Biological molecules in nature however, almost exclusively exist in only one of the two forms of the enantiomers. For example, amino acids are exclusively left handed where sugars and nucleic acids are right handed molecules. Homochirality of these molecular species is critical for recognition and replication processes in biology. When and why the production of single enantiomers was favored and how this has been sustained during evolution, is not exactly known. One plausible theory suggests 'symmetry breaking', where a random imbalance between two enantiomers, is followed by the asymmetric amplification of the excess enantiomer²¹. The other enantiomer then can be eliminated by cross-inhibition²³. Experimental evidence leading to the enrichment of single enantiomer has been shown for the first time with the Soai reaction, an alkylation of pyrimidyl aldehydes²⁴. Other experimental efforts leading to the enrichment of one form of a chiral molecule over the other have been ongoing since and have been extensively discussed in a recent review by Blackmond²¹.

High UV radiation, vacuum-like pressure and extreme cold temperatures might have enabled the synthesis of organic compounds in space. The compounds originate in the extraterrestrial space could then be delivered to Earth from space by cosmic dust particles, comets and meteorites. Examples of meteorite analyses indeed show a large repertoire of organic compounds. Hydrocarbons, alcohols, aldehydes, carboxylic acids, ethers and N-bearing compounds and more than 14,000 organic compounds including 70 amino acids have been detected on interstellar material or meteorites^{13, 25}. Extensive analysis on the Murchison meteorite, a carbonaceous chondrite discovered in Australia in 1969, revealed a rich content of amino acids, purines, pyrimidines, monocarboxylic acids and compounds

derived from ribose and deoxyribose²⁶. A variety of single chain amphiphilic molecules were extracted from the Murchison and other carbonaceous meteorites and shown to self-assemble into vesicular structures in aqueous media²⁷.

2.1.1. RNA world

RNA world represents the hypothetical stage in evolution where the RNA molecules were synthesized from a nucleotide soup and replicated themselves before the formation of DNA and proteins²⁸⁻²⁹. RNA can act both as a genetic information carrier, and as a ribozyme catalyzing biochemical reactions and its own replication³⁰.

It was later proposed that a physical membranous compartment was required which would encapsulate and keep together the two RNA molecules, one acting as a template and other as a replication enzyme. This membrane must have self-formed and spontaneously encapsulated RNA during self-assembly³¹. Over time, advantageous mutations led to the development of RNA adapter molecules, which could bind to activated amino acids and synthesize proteins. The proteins initially acquired similar catalytic functions to RNA, but became more efficient later on, and eventually took over the ribozyme functions.

At the final stage, DNA appeared and acquired the information from RNA. Due to its double stranded structure, it ensured a stable storage of information, and the ability to correct errors, while still allowing mutations and recombination^{29, 31}. RNA enzymes have vital roles in contemporary DNA-based life, such as enabling protein synthesis. They are considered as fossils from the RNA world.

The RNA world hypothesis enjoys wide support, as it describes a reasonable route of evolution. However, there are critical views, too. For example Orgel argued that the RNA world hypothesis would be validated only if RNA synthesis under prebiotic conditions could be shown³². Steps have been taken towards that goal. Recently, a reaction network starting with plausible prebiotic molecules such as cyanoacetylene, NH₃, NH₂OH, HCN, urea, formic acid, and isocyanate was driven by fluctuations in temperature, pH and dry-wet cycles to produce purine and pyrimidine nucleotides³³.

Synthetic routes to carbohydrates such as glycerol are needed for the backbone of RNA. The synthesis of glycerol from methanol-based, model interstellar ices exposed to ionizing radiation has been shown recently³⁴. Ribose sugar is difficult to form selectively³⁵, but Powner *et al.* showed a pathway for synthesis of pyrimidine nucleotides in which ribose sugar and nucleobase are produced from common precursors³⁶. These studies show that the prebiotic synthesis of building blocks of RNA is possible.

2.1.2. Lipid world

Segre and Lancet *et al.* suggested the lipid world hypothesis and coined the term lipozymes, which are catalytic lipid molecules, similar to ribozymes in the RNA world hypothesis³⁷. Segre suggested a similar catalytic role of lipids for prebiotic vesicles which can transfer the information to daughter vesicles by fission or fusion³⁷⁻³⁸.

One of the primary roles of lipids in modern cells is **compartmentalization**. They enable concentration of reactive molecules and reactions in confined volumes. For example, it has been shown that activated amino acid derivatives inside a lipid compartment are protected against potential hydrolysis in the external environment and can form dipeptides by reacting with each other³⁹.

Lipid membranes were suggested to have **hereditary potential** since most membranes are generated from other membranes instead of assembling *de novo*³⁷. Membranes can therefore potentially store compositional information and propagate to daughter membranes.

Lipid assemblies can be **autopoietic**⁴⁰ and can **self-replicate**. Autopoietic systems are defined by a boundary and can build the same boundary and components by a series of interdependent reactions, which then assemble into the structure itself⁴⁰. This behavior has been observed in reverse octanoic acid micelles⁴¹. Catalysts present inside the aqueous core of the reverse micelles enable the hydrolysis of octanoic acid octyl ester, which results in the formation of octanoic acid. The increase in micelle concentration has been detected with Fourier-transform infrared spectroscopy. Highly dynamic reverse micelles exchange the aqueous content through collisions, leading to micelles with homogenous content. A similar reaction was repeated, this time starting from the generation of amphiphiles leading to the formation of micelles, followed by self-replication⁴².

Certain combinations of lipid species can provide a **selective advantage** to the protocellular structures. For example, it has been shown that the fatty acid vesicles containing a small amount of phospholipids grow by consuming those containing less phospholipids or pure fatty acids⁴³. This competitive process was considered a selective advantage towards Darwinian evolution⁴³. A similar compositional transition from fatty acids to phospholipids in vesicular membranes was observed when Mg²⁺ in the ambient environment preferentially removed fatty acids from the mixed membranes⁴⁴. Considering that micelles can catalyze the formation of double chained amphiphiles from two single chained amphiphiles which can form liposomes⁴⁵, it is plausible that lipids are able to transform themselves into more complex entities in order to gain a selective advantage.

Lipid vesicles also have the ability to **grow** by incorporation of new amphiphiles without the need of enzymes or proteins,⁴⁶ and **self-reproduce** via the so called 'matrix effect'⁴⁷. The matrix effect is observed when fatty acid monomers initially bind to the external monolayer of pre-existing phospholipid bilayer, followed by flip-flop to the internal monolayer. The free fatty acids in the environment later interact preferentially with fatty acids in the bilayer. This leads to the growth of elongated unilamellar structures. The elongated vesicles can split upon sonication into similarly sized vesicles, keeping the size distribution strongly biased towards the original vesicles⁴⁸⁻⁴⁹. Lipid vesicles containing different lipid phases can perform fission, and vesicles with different charges, fusion⁵⁰.

The work contained in this thesis shows a wide spectrum of the capabilities of lipid assemblies at the solid-liquid interfaces. The solid-supported lipid membranes are able to self-form compartments which are connected with nanotubular channels (Paper I-III, V-VI), form subcompartments (Paper IV, VI), encapsulate water soluble molecules (Paper I-V), RNA (Paper III, V-VI) and DNA (Paper VI), and perform division in ways which were previously not considered. Overall, the results show that lipid membranes are capable of doing considerably more than just being a confining protective barrier. This introduces a fresh approach to the lipid world hypothesis.

In several examples, the combination of RNA and lipid membrane has been shown to provide a mutual benefit for each other. For example, RNA encapsulated inside fatty acid vesicles causes the build-up of osmotic pressure, thus creates tension on the membrane which drives the incorporation of more fatty acids from the solution into the membrane⁵¹. Confinement of RNA aptamers inside fatty acid and phospholipid vesicles has been shown to increase the binding affinity of the RNA aptamer for its ligand and locally stabilizes the conformation of bound RNA⁵². The presence of RNA inside a protocell could have therefore provided an advantage for Darwinian evolution⁵¹. In light of the findings mentioned above, and work contained in this thesis, it is conceivable that the RNA and lipid worlds co-existed.

2.1.3. Membranous prebiotic compartments

All modern cellular membranes are composed of phospholipids. In the context of protocellular membranes, a variety of amphiphiles and molecular assemblies have been considered as possible materials⁵³⁻⁵⁵. The limitations and strengths of the phospholipids, the key compounds of which biological cells of today are made, will be discussed in detail in chapter 4.1 in the context of protocell materials. In this section I will focus on prebiotic compartmentalization from fatty acids. Fatty acids have a single chain molecular structure,

and are thought to have been present before the emergence of phospholipids on the early Earth. I will also discuss the transition from purely fatty acid protocellular membranes to the ones containing both fatty acids and phospholipid in mixtures, and describe the advantages of the mixed systems.

Prebiotic compartments must have had a variety of roles, such as promoting catalytic reactions, stabilizing reaction intermediates by providing compartment boundaries, regulating the molecule exchange with the environment by tuning the permeability, support energy uptake and conversion, trigger self-reproduction and pass on evolutionary advantages due to composition^{54, 56}. Among those, the most frequently studied tasks are spontaneous growth, spontaneous division, nucleotide uptake, physical stability especially under the conditions required for RNA replication, and compatibility with ribozyme activity^{31, 57}.

Vesicle self-assembly and spontaneous growth by incorporation of monomers from the aqueous environment were shown in fatty acid membranes^{43, 58} (**Figure 2.1**). Growth of the vesicular bilayer due to the insertion of monomers leads to an imbalance between inner and outer monolayer leaflets. With their small head groups, fatty acids can rapidly flip between the leaflets^{43, 58}. Also, at physiological pH, the fatty acids are efficiently protonated and can flip-flop in their unionized form⁵⁹. In modern cells with phospholipid membranes, the flip-flop of lipid molecules within a bilayer has a high energy cost, and thus does not occur at reasonable rates spontaneously, requiring the activity of flippase enzymes⁵⁷.

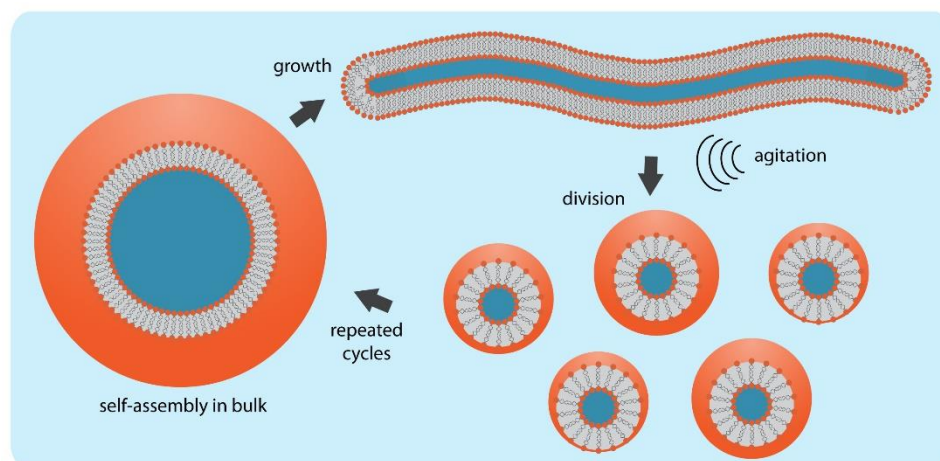


Figure 2.1. Schematic representation of a spontaneous growth and division cycle of fatty acid vesicles⁵⁸.

Growth proceeds with extrusion of thin tubular tails from the vesicle, followed by the complete transformation of original spherical vesicle to a long, narrow filamentous vesicle. This results from the lag between the growth of the membrane surface area and growth of vesicle volume; the volume cannot expand as fast as the membrane due to the slow permeation of the water through the lipid membrane. When shear force is applied, for example by applying sonication in the laboratory, the filamentous vesicular structures split into small spherical vesicles. Multiple cycles of growth and division can occur in this manner (**Figure 2.1**). The vesicles are able to spontaneously encapsulate RNA from the ambient environment during this process, and re-distribute them into daughter vesicles upon division^{43, 58}. The mechanistic details of the division remain unclear. One possibility is pearling, where small vesicles connected with very thin nano-sized tethers resembling a string of beads form from a lipid assembly. Later, a shear force would disrupt the membrane connections between the vesicles, leading to separation and formation of daughter cells⁶⁰.

The transition from fatty acids to phospholipids is thought to be gradual through evolution. Fatty acid membranes are highly permeable and dynamic, as compared to phospholipid membranes. Fatty acids allow the entry of essential solutes into the protocells⁶¹. Protocell membranes containing phospholipids have relatively low permeability and would need a transport machinery to overcome this problem. Compartments made from fatty acid membranes compete with each other to incorporate the fatty acid monomers in their surrounding⁴⁶. A low amount of phospholipids (10 mol % phospholipid and 90 mol % fatty acid) has been shown to enhance the growth of protocell membranes, by consuming vesicles containing less phospholipids or pure fatty acids, providing a selective advantage towards Darwinian evolution⁴³ (**Figure 2.2**). Hybrid fatty acid-phospholipid membranes have also been shown to provide stability in the presence of divalent cations such as Mg^{2+} ⁴³. Mg^{2+} is essential for prebiotic RNA chemistry⁶², but Mg^{2+} and other divalent cations also bind to the carboxylate head groups and precipitate fatty acids⁶³. Similar findings, showing the transition from fatty acid to mixed membranes, and eventually to pure phospholipid membranes in the presence of Mg^{2+} have been presented⁴⁴. It has been further hypothesized that increased phospholipid content decreased the negative charge density of fatty acid membranes, and increased the concentration of Mg^{2+} ions required for disruption. Additionally, Mg^{2+} appears to still preferentially bind to fatty acids in mixed membranes, and removes them from the membrane, leading to an increase in the fraction of phospholipids. Eventually, the mixed membranes have made the transition to purely phospholipid-containing structures (**Figure 2.2**).

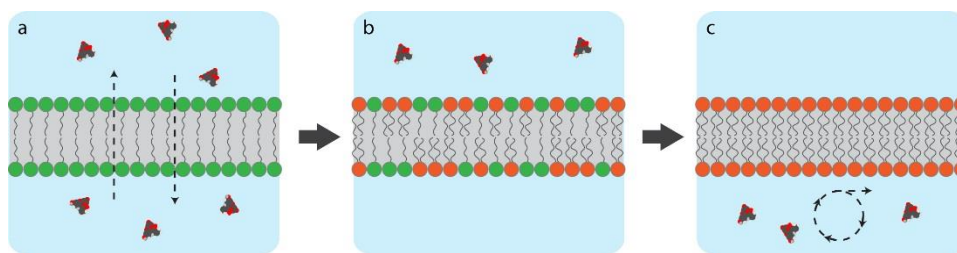


Figure 2.2. Gradual transition from fatty acid to phospholipid membranes. (a) Highly permeable fatty acid membranes, (b) semi-permeable membranes from mixed species of fatty acids and phospholipids, and (c) nearly impermeable phospholipid membranes.

2.2. Protocell formation on mineral interfaces

The abundance of mineral surfaces on the early- and current Earth, which are composed of various inorganic compounds, and their natural interface to water: seas, oceans, lakes and ponds, as well as their often catalytic properties, makes it conceivable that mineral- water interfaces would accommodate and promote protocell formation and development^{13, 64}.

Clay and quartz were first proposed by Bernal *et al*⁶⁵ as templates or containers for concentrating and assembling organic compounds. Adsorption of molecules on minerals, especially on phyllosilicates containing parallel sheets of silica, has been shown to catalyze numerous polymerization reactions. Upon completion of polymerization, the polymers can be released from the surface binding sites of the minerals. This is, on one hand, not true compartmentalization, and minerals cannot increase the concentration of the polymers in a confined space. On the other hand, it is still highly probable that minerals played a role in prebiotic synthesis of organics at the origins of life by adsorption and catalysis. However, the idea that minerals intrinsically possess a compartmentalization ability like amphiphilic vesicles has been abandoned⁵³.

Clay surfaces, specifically of montmorillonite, has been shown to facilitate adsorption of nucleotides and polymerization of RNA⁶⁶⁻⁶⁸, as well as peptides,⁶⁹⁻⁷¹ and enhance bilayer formation from fatty acids^{50, 72}. The addition of small quantities of montmorillonite particles to a mixture of myristoleate (C₁₄) increases the vesicle assembly rate by a factor of up to 100⁵⁰. A similar effect was observed for longer chain fatty acids such as palmitoleic (C₁₆) and oleic (C₁₈) acids⁵⁰. In addition to the montmorillonite, particles of other negatively charged minerals, specifically silicate, aluminasilicate and borosilicate, were incubated with fatty acids, and strong acceleration of vesicle assembly was observed⁵⁰. A follow up study, where a larger spectrum of materials of microparticles were mixed with amphiphiles, revealed that particles such as hydroxyapatite and the highly hydrophobic poly(tetrafluoro ethylene) did not lead to rapid vesicle assembly⁷². Surface charge density has been

identified to be one critical parameter in vesicle assembly rate, and to beneficially affect vesicle formation⁵⁰.

Another influential parameter was determined to be the isoelectric point (IEP), the pH at which the surface of the particle is electrically neutral⁷³. The IEP depends on the crystal structure, chemical composition and surface hydration. The particles made from minerals such as amorphous silica, quartz and montmorillonite that have a low IEP of ~2 showed relatively low decanoic acid vesicle amplification, compared to particles with higher IEP (~9), *e.g.* zincite, γ -alumina and goethite at pH 7⁷³. The reason for enhanced vesicle amplification on surfaces with high IEP is their positive charge at the pH that experiments are performed. Oxide surfaces are positively charged at pH smaller than their isoelectric potential. Negatively charged amphiphiles (decanoic acid and decanoic acid/decanol) used in the study can absorb more on positively-charged surfaces with van der Waals, H-bonding and electrostatic forces, compared to negatively charged surfaces⁷³. These studies showed that the enhancement of vesicle assembly was not solely due to the introduction of soluble agents, *e.g.* metal ions, to the environment, a change in pH or change in critical concentration was needed for vesicles to form from fatty acids. The particle surface itself was the most prominent cause⁷². It was hypothesized that the presence of a layer of positively charged cations close to the mineral surface attracts negatively charged amphiphiles, and facilitates their adsorption onto the mineral surface. The adsorbed sheets then can fold into vesicles, can detach from the surface and be released into the bulk solution⁷³. The experimental setup is similar to our experiments; we use negatively charged surfaces at pH 7.4 and the divalent cation Ca^{2+} in order to provide the electrostatic interaction between the negatively charged surface and negatively charged phospholipid head groups.

The incubation of surface-treated minerals with excess amount of fatty acids also shows that vesicles form even though the surface of the mineral is covered with a bilayer. In other words, the vesicle formation is amplified regardless of direct contact with the mineral surface⁷². Although a lipid layer coats the particle surface, lipid molecules in solution are still attracted onto the particle surface and can transform into vesicles. Extended Deraguin-Landau-Verwey-Overbeek (DLVO) theory explains that electrostatic charge of the surface is effective up to 12 nm distance from the surface for quartz (α - SiO_2) and 18 nm for corundum (γ - Al_2O_3)⁷⁴. These distances are sufficient to attract 2 or 3 stacked lipid bilayers (5 nm each) on quartz and corundum, respectively⁷⁵. This is in agreement with our findings in Paper I, III, V and VI, where a bilayer resides between the surface and the nanotubular network of vesicles.

2.3. Suitable geological environments for the origin of life

The Earth is optimally distant from its star, the Sun. The surface temperature is mainly above the freezing point, but it is so hot that water is boiling. Liquid water is a pre-requisite for the life we know, and the oxygen isotopes in the oldest known zircons suggest that liquid water may have been present on the Earth's surface as early as 4.3 to 4.4 Ga⁷⁶. This corresponds to the Hadean era, the period from ~4.54 Ga to ~3.8 Ga. In this eon, the surface temperature of the Earth was believed to be much higher than the boiling point of water. The Greenstone Belt in Isua, Greenland, indicates that at ~3.7 Ga, permanent oceans existed⁷⁷. Recently, the earliest fossil stromatolites were located in the layered sedimentary microbial mats in a fresh water hydrothermal field in the 3.5 Ga old Dresser formation in Pilbara Craton, Western Australia⁷⁸. Even though the exact time is still debated, life might have originated as early as water existed on the planet, approximately 4.4-3.5 Ga ago, originating from self-organization of available organic compounds. Various geochemical environments for this process have been proposed^{1, 79-80}. The presence of water, and minerals that enable adsorption and synthesis of organic compounds, and high concentration of organic compounds are considered essential in these environments^{1, 11, 13, 81}.

2.3.1. Warm little pond hypothesis

Hydrothermal fields (HFs) are considered as a suitable geological environment for life to originate. Similar hot pond environment was originally proposed by Darwin in 1871, when he mentioned warm little ponds as potential sites for assembly of protocells from concentrated organic molecules. The above mentioned 3.5 Ga old stromatolite fossils⁷⁸ were also located in the fresh water of a hydrothermal field. HFs are hot spring environments with water pools of different sizes at elevated temperatures ranging from 60-100 °C. The pH is acidic and around 2-3. HFs constantly undergo hydration-dehydration cycles. During continuous cycles, membranous compartments can encapsulate polymers e.g. oligonucleotides, peptides. The environmental selection of these polymer-encapsulating vesicles may have led to the emergence of functional systems capable of growth, reproduction and evolution⁸⁰. The HFs comprise intertidal pools, inland evaporitic playas, flanks of volcanic crater lakes, sedimentary pores in the unsaturated zone of groundwater, and altiplano desert soils. Similar sites are present today on the Kamchatka Peninsula in the Mutnovskii geothermal area, Russia, which contains multiple hot pools and lakes, boiling springs and geysers. Hydrocarbons and lipid precursors detected in this area supports the hypothesis that life is compatible with HF environments, despite the seemingly extreme conditions⁸².

Several studies mimicking the dry-wet and freeze-thaw cycles, which facilitate the condensation and concentration of organic compounds²⁵, have resulted in syntheses of various organic molecules. Some examples are: the condensation of glycine to oligopeptides in fluctuating clay environments⁸³, the formation of lipids (up to C₃₃) from oxalic acid at temperatures ranging from 100-400 °C¹⁶, the formation of PE and PC phospholipids under evaporating pond conditions when the mixture of organics was heated to temperatures from 25 to 100 °C¹⁸⁻¹⁹, and the synthesis of PA and PG in dry-hot pond conditions in the presence of silicate minerals as condensing agents¹⁷.

Dry-wet cycles of surface-adsorbed activated nucleotides may have resulted in polymerization of RNA. The presence of mononucleotides within dried multilamellar lipid structures was detected with X-ray diffraction measurements, and it has been hypothesized that anhydrous conditions could drive the synthesis of phosphodiester bonds between nucleoside monophosphates polymerizing RNA⁸⁴. In the presence of phospholipids, 5'-mononucleotides could form RNA-like polymers after several dehydration/rehydration cycles⁸⁵. When a phospholipid film was dehydrated, mononucleotides were trapped in between the lamellae of lipids, and subsequently got encapsulated in lipid vesicles upon rehydration⁸⁵. RNA-like oligomers up to 50 nucleotides were synthesized from adenosine 5'-monophosphate and uridine 5'-monophosphate using dehydration/rehydration cycles⁸⁶.

Lastly, a theoretical model, taking into account the meteorite showers that brought extraterrestrial materials onto the early Earth, estimated the time for the origin of RNA on the early Earth⁸⁷. The model concluded that impacting meteorites and carbonaceous interstellar dust particles could deliver soluble organic compounds like nucleobases to small ponds, and subsequent dry-wet cycling could have enabled the formation of nucleotides, their subsequent concentration, and polymerization into RNA⁸⁷.

The studies summarized above show the possible synthesis of lipid monomers, nucleotides and RNA molecules during dry-wet cycling of warm ponds either in an aqueous environment alone, or in contact with solid mineral surfaces. These findings support both the RNA world and Lipid world hypothesis. At the same time, they suggest a role for mineral-water interfaces for the emergence of life.

Overall, the warm pond hypothesis supports the view that a sufficient amount of organic molecules with appropriate chemical functionality, an aqueous environment and mineral surfaces are sufficient prerequisites to lead to the emergence of the first protocells.

2.3.2. Deep-sea hydrothermal vents

Deep sea hydrothermal vents, which are fissures on the seafloor discharging geothermally heated water, are considered as potential sites for the life's origin^{25, 79}. Until recently, only one type of high temperature hydrothermal vents was known, the black smokers with temperatures of ~250-400 °C. The hydrothermal vents contain high concentrations of dissolved CO₂ and H₂S gases, leading to a very acidic pH of ~2-3. At the locations where the fluid is released from the vent come in contact with alkaline ocean water, concentration, redox and thermal gradients are created. These gradient regions are suitable for the synthesis of organic compounds and metabolic reactions. The name *black smokers* originate from the dark colored metal sulfide minerals and CH₄, and H₂ gases released from the vents. One example of a black smoker is the Rainbow hydrothermal field in the Azores region of the Atlantic ocean^{25, 79}.

In 2001, a different kind of hydrothermal vents, referred to as *white smokers*, was discovered. White smokers are a type of sub-sea vent systems; two examples are the Lost City Hydrothermal field (LCHF) in the mid-atlantic,⁸⁸ and the Strytan hydrothermal field in the Eyjarfjörður in northern Iceland⁸⁹. The temperature of the white smokers is much lower, around 60-90 °C, and pH is ~9-11. Around the vents, the pH of the ambient sea water is 8. They have white colored calcium and magnesium carbonate precipitates, hence the name. The hydrothermal activity in these vents is driven by the chemical reactions between seawater, olivine in the ocean crust and dissolved CO₂. The reactions result in the formation of serpentine, magnetite and either brucite or magnesite, while releasing dissolved silica and H₂ or CH₄^{25, 79, 90}. The X-ray diffraction analysis of samples from chimneys in the LCHF revealed the presence of calcite (CaCO₃), aragonite (CaCO₃) and brucite (Mg(OH)₂)⁸⁸. Similar calcium- and magnesium-containing silicate minerals are found on the white smokers in Iceland⁹¹. These chimneys support dense microbial communities such as methane-producing- and consuming Archaea, sulfur and metal-oxidizing, and sulfate reducing bacteria^{79, 90}.

The relatively low temperatures in the white smokers are particularly suitable for organic synthesis, and thus the emergence of ancient thermophilic life forms on Earth. Syntheses of numerous organic compounds including amino acid oligomers, various aliphatic and aromatic hydrocarbons, carboxylic acids and pyruvate were predicted with a geochemical model computer code, which simulated the mixing warm, alkaline, serpentine-derived reducing fluids around white smoker vents with cool and oxygenated sea water^{25, 92}. Additionally, finite element simulations showed that strong thermal gradients in conjunction with fine pores of minerals in the vents could concentrate small organic molecules such as

nucleotides and nucleic acids⁹³. The findings have been confirmed experimentally; fatty acids concentrating in a microcapillary thermal diffusion column self-assemble into vesicles and encapsulate concentrated DNA oligonucleotides spontaneously⁹⁴.

2.3.3. Comparison of conditions associated with primitive cell constituents

Both the hydrothermal ponds and deep-sea hydrothermal vents have favorable properties, but also limitations, with regard to the formation of protocells⁹⁵.

Both shallow surface water and sea water can shield organic material from longtime UV exposure and damage by radiation⁸¹. In surface ponds, organic compounds are exposed to UV radiation during dry periods, which might be advantageous for the catalysis of some reactions. Light energy, however, cannot be utilized much in deep-sea vents, since it cannot penetrate through the ocean and reach these regions.

In terms of temperature, the range found in alkaline vents and surface ponds is tolerable for microbial life, as compared to the black smokers. The upper limit of temperature for life is set by biophysical and biochemical properties, one of which is the stability of hydrogen bonds. Hydrogen bonds are necessary for storage of information as DNA, information transfer to RNA and protein synthesis. It is necessary for folding and maintaining catalytic and structural functions of proteins within the cell. Hydrogen bonds cannot be maintained above 90 °C⁹⁶.

The pH is especially important for fatty acid membranes which are only stable at a very narrow range close to the pKa of the carboxylate group. pH values in black smokers are in the strongly acidic range (~2-3), while in white smokers moderately basic (~9-11). In surface ponds, various moderate pH values (3-8) have been measured at different sites⁹⁶.

The concentrations of various monovalent and divalent ions differs between deep-sea environments and surface pools⁹⁶. Water in volcanic land masses is evaporated seawater, which returns to the ground with precipitation. Ions can originate from the basaltic lava and dissolved volcanic gases, e.g. CO₂ and SO₂. The Mg²⁺ concentration in sea water and in both types of vents ranges from 0 to 54 mM, and the Ca²⁺ concentration from 10 to 37 mM. Detailed analysis revealed that fluids around chimneys have a low concentration of Mg²⁺, but more than a two-fold enrichment of Ca²⁺. K, Na and Cl concentrations in vents are similar to seawater⁸⁸. Samples from Kamchatka hot spring water had Ca²⁺ in the range of 0.1 to 2.5 mM, and Mg²⁺ in the μM range. Overall, the amount of mono- and divalent cations is much less in volcanic land masses compared to seawater⁹⁶. The surface pools are therefore

thought to be more favorable for self-assembly and polymerization processes than seawater. Comparative studies on self-assembly of dodecanoic acid to vesicles in seawater, and in hydrothermal water samples from the Yellowstone National park validated this hypothesis. Membrane formation is inhibited in seawater because the cations bind to carboxylate groups of fatty acids, and form a solid calcium and magnesium soap⁹⁷. These adverse effects on fatty acids can be overcome by addition of alcohols and monoglycerides into fatty acid membranes⁶³. Moreover, a concentration gradient produced by monovalent salts like NaCl and KCl across closed lipid membranes leads to excessive osmotic pressure, which can collapse or burst vesicles^{44, 61}.

2.4. Other theories and recent developments

In this section I describe recent developments, the findings regarding the extraterrestrial space, and their possible implications for the origins of life.

The panspermia (literally 'seeds everywhere') theory suggests that life could originate anywhere where conditions are favorable, and then move from one location to another through extraterrestrial space⁹⁸. Earlier work revealing the presence of organic materials in meteorites^{26-27, 99} makes this idea plausible. A relatively short time period is considered between the cooling of the Earth and appearance of microbial communities, and this is considered as strong support for panspermia¹⁰⁰. Since the conditions on the early Earth and other planets during the early years of the Solar System could have been similar, scientists hypothesized that equivalents to terrestrial life may have originated on other planets such as Mars, Venus, and the icy satellites Europa and Enceladus orbiting Jupiter and Saturn, respectively.

Research focusing on the possible sources of life in space is ongoing. Since it is technically currently challenging and costly to perform experiments in space, suitable equivalent environments are often mimicked with experimental analogues, or computer simulations.

In a simulated experimental environment mimicking giant gas clouds interspersed between stars, nucleobases were detected, which are essential components of DNA and RNA¹⁰¹. These findings support the panspermia theory. In this study, the conditions in interstellar clouds were reproduced in ultra-high vacuum reaction chambers, and continuously supplied with a gaseous mixture of H₂O, CO, NH₃ and CH₃OH at -263 °C. Upon exposure to UV photons, an icy film formed inside the chamber, which was analyzed after warming the chamber to room temperature. All three pyrimidine (cytosine, uracil and thymine) and three purine nucleobases (adenine, xanthine and hypoxanthine) were detected inside the

chamber as a result of the reactions. Previously, production of other organic molecules essential for life were also reported in interstellar ice analogues, e.g. amino acids¹⁰²⁻¹⁰³, aldehydes¹⁰⁴, glycerol¹³⁴, ribose and derivatives¹⁰⁵, and deoxyribose and derivatives¹⁰⁶.

Martian origins for the terrestrial life has been proposed due to strong evidence of once existing water on the planet, a high abundance of boron, and of phosphate¹⁰⁷. The primary role of boron has been to provide thermal and chemical stability in hostile environments throughout evolution¹⁰⁸. Phosphorus constitutes the backbone of RNA and DNA. The geochemical models of Mars predict that ancient Mars was warmer, had water and a thicker atmosphere, all suitable conditions for microorganisms to thrive¹⁰⁹. Although the possibility of microorganisms to survive the interplanetary transfer has been criticized, the panspermia hypothesis suggests that if life on Mars has existed, it would have a common origin with the life on Earth today¹⁰⁰.

Recently, phosphine (PH₃) was detected in the atmosphere of Venus¹¹⁰. This discovery received a lot of attention, as phosphine gas is produced by microbes on Earth, possibly indicating the presence of microbial life on Venus. It is not known at this point, however, if the findings are valid. An error has been detected in the original processing of the paper's data obtained from radio-telescope observations at the Atacama Large Millimeter/Submillimeter Array (ALMA) Observatory, which leads to a fainter phosphine signal¹¹¹. Currently a caution note has been attached by the journal regarding the ALMA data sets, while validation of the data is being attempted.

Some current attention has also been given to several moons in our solar system as possible other habitats of life. Evidence suggests that Jupiter's moon Europa contains a subsurface ocean which might be suitable for life¹¹². Gravity measurement data from the Galileo spacecraft indicates a 80-170 km thick combined ice-liquid water shell on a metallic and rocky core and mantle¹¹³. Models support the measurements, and indicate that the geothermal and tidal heating is sufficient to maintain a fraction of liquid water under a 10 km thick ice shell¹¹⁴. Enceladus, the moon of Saturn, is 40 times smaller than Europa, but is assumed to have a similar surface structure of liquid water, and a surrounding ice shell¹¹⁵. Since water likely exists on these bodies, and sufficient heat energy to keep the water liquid, Europa and Enceladus are extraterrestrial sites within our solar system which are highly interesting for origin of life research.

3. Surface energy and natural surfaces

3.1. Surface free energy and wetting phenomena

Solid surfaces are the key component of the hypothesis formulated in this thesis. The experimental evidence supports that the intrinsic energy of the solid surfaces drives the formation and development of the observed model protocells. Since solid surfaces were abundant on the early Earth in the form of rocks, glasses and minerals, and the basic principles of physics and materials science were certainly the same 3.8 billion years ago, it is plausible that the first cells were formed and developed with the help of surfaces.

We used high energy solid substrates fabricated in a nano-/micro-fabrication facility, as well as naturally occurring rocks, glasses and minerals. The interaction of lipid membranes with solid substrates depends on the surface energy which results from the combination of surface features such as material, net charge, hydrophilic/phobic nature of the surface and topography (roughness)¹¹⁶.

Surface energy at the molecular level arises from missing cohesive interactions. The atoms or molecules in the bulk of the material have balanced interactions with their neighboring atoms in all directions. In contrast, atoms at the surface lack physical interaction and bonds with molecules of their kind at the interface (**Figure 3.1**). These unsatisfied bonds cause an imbalance of interactive forces, leading to an increase in free energy on material's surface.

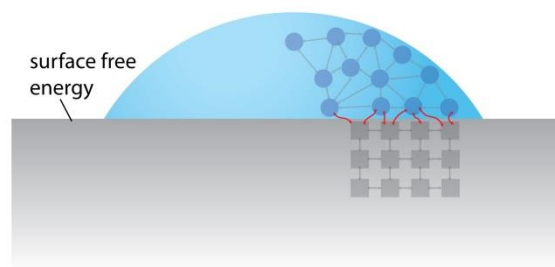


Figure 3.1. Surface molecules missing cohesive interactions.

Free energy at the interface of solid or a liquid is referred to as surface energy or surface tension. Surface energy is equal to the work that must be done to bring a molecule from bulk to surface, *i.e.*, to create new surface area¹¹⁷. For example, if a block of a solid material is broken into two pieces, and a new surface is created on each piece, the surface tension σ (unit N/m or J/m²) is then a function of work (W) per unit new surface area (A).

$$\sigma = \frac{1}{A}W \quad (3.1)$$

Surfaces are inclined to reduce their free energy by wetting, the tendency of a fluid to spread on a solid surface¹¹⁸. Wetting is favored on high energy surfaces. Wettability of a surface is determined by the force balance between the surface energies represented by Young's equation (**Figure 3.2**).

$$\gamma_{SV} = \gamma_{LS} + \gamma_{LV} \cos\theta \quad (3.2)$$

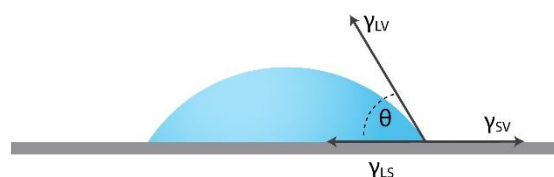


Figure 3.2. Schematic representation of the Young's equation. A fluid droplet wets a solid surface in an ambient atmosphere, creating a ternary interface.

In this equation, three interfaces are present at the edge of the droplet: a liquid-solid interface (γ_{LS}), a liquid-vapor interface (γ_{LV}) and a solid-vapor interface (γ_{SV}). θ is the contact angle at the liquid-vapor interface on the solid surface.

If the surface energy is high, the solid-vapor interfacial tension (γ_{SV}) would be high. This leads to high wettability and a low contact angle. Glass, metals and metal oxides are examples of high energy surfaces with surface tensions well above 100 mN/m, resulting in wetting with contact angles below 90°¹¹⁹. Water droplets do not spread on hydrophobic, low energy surfaces e.g. polytetrafluoroethylene (PTFE, brand name 'Teflon'); the contact angle remains above 90°. While the molecules in high energy surfaces adhere to each other with strong chemical bonds such as covalent, ionic or metallic bonds, in low energy surfaces the molecules are mostly connected to each other via weaker bonds, e.g. van der Waals or hydrogen bonds¹²⁰.

Surface charge and topography affect the wettability of a solid surface. Surface-adsorbed OH⁻ groups generally increase wettability by establishing hydrogen bonds with water molecules, leading to hydration¹²⁰⁻¹²¹. Metal and silicon oxides favor wetting by biomembranes¹¹⁶ and by other biological materials¹²². If topological features with sizes greater than 0.2 μm exist on the surface, the wetting is enhanced and the observed contact angle may change drastically¹²³. While a certain degree of roughness enhances surface wettability, in the case of extreme roughness, for example created by sharp dense pillars

covering a hydrophilic surface, the surface can turn into a super-hydrophobic surface and repel water^{117, 120-121}. Self-cleaning surfaces on which fluid droplets roll off the surface, collecting contaminants such as dust and pathogens in the process, are based on this principle¹²⁰.

Surface contamination greatly affects the surface energy and wettability, and is therefore a major concern in experimental work. Hydrocarbon-based contamination leads to a decrease in surface free energy¹²⁰. Contact of substrate surfaces with hydrocarbons needs to be carefully avoided, as well as prolonged storage in an open laboratory atmosphere. Oxygen plasma is a convenient and efficient practical means of eliminating hydrocarbon contamination, it increases surface free energy and wettability¹²⁴.

3.1.1. Surface defects and grain boundaries

The solid substrates fabricated in the nano-/micro-fabrication (cleanroom) facility have atomically flat surfaces. The surfaces of natural minerals and rocks utilized in Paper VI are not uniformly flat, even after polishing, and possess surface irregularities such as cracks, cleavage sites, fissures and grain boundaries.

The surface crystal structure of natural surfaces contributes to an altered wetting behavior. Cleavages and fractures affect the crystal structure on the exposed surface of a mineral¹²⁵. The surface atoms at the interface of cleavages can slightly deviate from their crystallographic positions leading to kinks and steps, or can be chemically altered by oxidation, hydration or hydroxylation¹²⁶. Depending on these factors, and the resulting surface density of dangling bonds, the surface free energy at these irregularities differs, compared to the continuous crystal structure. Experiments on fluorite and calcite minerals show a linear relation between surface broken bond densities and surface energy^{125, 127}. Similarly, surface potential measurements indicated that on silicate and clay surfaces with alternating structures of surface crystals, wetting and adsorption of DNA molecules and nucleotides is promoted¹²⁸.

In rock samples containing aggregates of multiple minerals, grain boundaries of two adjacent mineral domains possess high surface tension. If the composition and the lattice type of each grain are identical, but the relative orientations of their crystal lattices differ, it is classified as a homophase interface. If the grains have a different composition, it is classified as heterophase interface. In such two component systems, Young's equation is modified as follows¹²⁹⁻¹³⁰:

$$\gamma_{12} = \gamma_1 \cos \theta_1 + \gamma_2 \cos \theta_2 \quad (3.3)$$

$$\gamma_1 \sin \theta_1 = \gamma_2 \sin \theta_2 \quad (3.4)$$

In this equation, the solid-liquid interfacial energies of the two surfaces at the grain boundary are shown as γ_1 and γ_2 . θ_1 and θ_2 are the partial dihedral angles (**Figure 3.3**). When the surface tension is high at the grain boundary (γ_{12}), the contact angles are low, and the wettability at the grain boundary increases.

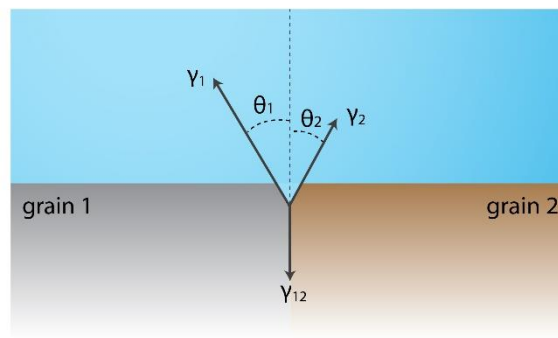


Figure 3.3. Schematic drawing depicting the wetting at the grain boundary of a mineral.

In Paper VI, on granite and eclogite, which exhibit mineral heterogeneity, model protocell formation was amplified at the grain boundaries interfacing quartz.

3.2. Natural surfaces

A mineral is a natural inorganic compound with a fixed chemical composition and a specific crystal structure. There are ~4500 known naturally occurring minerals. Primary minerals are formed from cooling and crystallization of magma. They transform by weathering to secondary minerals^{81, 126}.

In Paper VI, due to the abundance of mineral-water interfaces on the early Earth surface, minerals are proposed to play a central role in protocell formation. Examples of mineral surfaces that can protect, select, concentrate, and template organic molecules, and catalyze prebiotic reactions, have been discussed in several review articles^{1, 65, 81, 126, 131-132}.

The minerals, glasses and rock samples that we utilized in Paper VI were chosen to represent the minerals present on the prebiotic Earth. Minerals such as quartz, olivine, or feldspars, on which we experimentally observed protocell formation, are thought to have

been present in the Earth's crust in the Hadean era, which corresponds to the time when protocells have most likely emerged^{81, 132}.

Clay minerals including montmorillonite are the minerals most frequently utilized for origin of life studies. Polymerization of peptides^{69-70, 83} and RNA^{66-68, 71} have been reported on clays. The synthesis of phospholipids on clays¹⁷ as well as the formation of fatty acid vesicles^{50, 72} have also been shown in bulk in the presence of clay microparticles.

In Paper VI we have studied protocell formation on a meteorite specimen (Northwest Africa (NWA) 7533) which originates from Mars. NWA 7533 (and its pair NWA 7034) represents the planet's crust¹³³ and it is believed to originate from the southern highlands of Mars¹³⁴. The NWA 7034/7533 meteorites have a fine-grained (~1 μm) interclast crystalline matrix in which ancient crustal components are preserved¹³⁵. The zircons recorded in the meteorites are more than 4.4 billion years old, presenting nearly the entire geologic history of Mars¹³⁶. Recent investigation of the chemical and isotopic compositions of NWA 7533 indicated early oxidation of the planet's crust by impacts in the presence of liquid water as early as 4.4 billion years ago¹³⁷. Elemental analysis of 7533 revealed presence of pyroxene, feldspar and some oxides¹³⁴⁻¹³⁵. In addition to the information obtained from meteorites, the Observatoire pour la Mineralogie, l'Eau, les Glaces et l'Activité (OMEGA) instrument on board of the Mars Express spacecraft with visible/near-infrared reflectance measurements identified clay minerals such as montmorillonite and olivine ($(\text{Mg,Fe})_2\text{SiO}_4$) on the surface of Mars¹³⁸⁻¹³⁹. Other minerals e.g. plagioclase, silicates, hematite, basaltic glass, sulfates were also detected. These findings provided confirmation of the presence of liquid water on the surface of Mars in the past¹⁴⁰. Since it is evident that the water existed on Mars, it is conceivable that Mars was a habitat for water-based life. The similarity of the natural surfaces on Mars to the ones on Earth inspired us to investigate the possibility of the formation and development of protocells on the Martian meteorite material.

4. Lipid membranes and membrane mechanics

4.1. Amphiphiles

Amphiphilic molecules have a hydrophilic (polar) head group and a lipophilic (non-polar) hydrocarbon tail. In water, amphiphiles disrupt the highly dynamic hydrogen bonding between the water molecules, increase order and decrease the entropy of the system. To reduce the free energy of the system, the amphiphiles self-assemble. Self-assembly due to the 'hydrophobic effect' minimizes the interface of the amphiphile molecules to water, increases the entropy, and thus minimizes the cost of the system's free energy. Hydrophobic attraction at the hydrocarbon tail-water interface, and the hydrophilic, ionic or steric repulsion of the amphiphile head groups determine the packing geometry of amphiphilic molecules¹⁴¹.

A fatty acid consists of a carboxylate head group with single hydrocarbon chain. Fatty acids have been proposed as monomers of first compartments on the early Earth, especially those with short carbon chains (C_8 - C_{10})^{38, 142}. Phospholipids are structurally more complex than the fatty acids, and consist of a hydrophilic, phosphate containing head group and two hydrophobic tails which contain 10-18 carbons per chain (**Figure 4.1**). The synthesis of various phospholipids has been experimentally shown to occur under potentially prebiotic conditions¹⁷⁻²⁰.

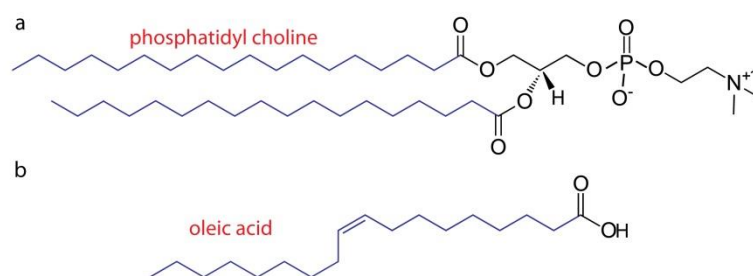


Figure 4.1. Chemical structure of (a) phosphatidylcholine and (b) oleic acid (C_{18}).

The dynamic nature of the fatty acids has been considered essential for facilitated permeability and growth of primitive cell membranes. Fatty acid monomers are not firmly anchored, so they can insert into and escape from the membrane on a time scale of nanoseconds to microseconds¹⁴³. Unlike phospholipids, fatty acids can also flip-flop between the two leaflets of a bilayer rapidly within milliseconds¹⁴⁴. In case of fast membrane growth, these features enable the uniform expansion of the inner and outer leaflet areas.

Fatty acid membranes are relatively more permeable to small polar molecules than those made from phospholipids^{43, 145}, which increases the possibility of encapsulation of compounds such as nucleotides in a prebiotic environment. Due to their single chain structure and relatively smaller hydrophobic interface, compared to the double chain in phospholipids, the critical micelle concentration of fatty acids is generally higher than phospholipids. For fatty acid monomers to self-assemble to primitive compartments, they are therefore required to be present at comparatively higher concentrations. Additionally, fatty acids can only form bilayers in a narrow pH range. Phospholipids can form compartments with stable bilayers under a wide range of pH, temperatures and salt concentrations, all of which are present in hydrothermal vents, which are proposed sites for the origin of life^{142 38, 53, 143, 146}.

Model protocells composed of materials other than lipids have been described. For example coacervates, which are gel-like aqueous entities composed of macromolecules. Coacervates are able to efficiently encapsulate macromolecules, e.g. enzymes, and accommodate enzymatic reactions. However, they lack a membrane envelope with selective permeability and exhibit low stability⁵⁴⁻⁵⁵.

4.1.1. Fatty acid vesicles

The ability of unsaturated fatty acids to form vesicles, the so called 'ufasomes', was first shown by Gebicki and Hicks¹⁴⁷, who used oleic acid in their study. In spite of its 18 carbon long chain, oleic acid has been commonly utilized in origins of life research, since its prebiotic synthesis was shown¹⁷. As mentioned above, fatty acids are sensitive to ambient environmental conditions such as pH, salinity, temperature, and the presence of divalent cations¹⁴⁸⁻¹⁴⁹. Forming bilayers from fatty acids is a challenging task. Fatty acids can form bilayers when the pH of the aqueous solution is close to the pK_a of the carboxylate group of the fatty acid. The pK_a is defined as the negative logarithm of the equilibrium constant. When the pH of the system is close to the pK_a of the fatty acids, the molecules in their protonated and ionized form are at equilibrium. The protonated and ionic carboxylate groups can then form stable bilayer structures through hydrogen bonding^{38, 53, 142-143, 150}. If the pH is significantly lower than the pK_a , fatty acid molecules are protonated, uncharged and can form oil droplets. At high pH, fatty acids assemble into micelles with a liquid-like hydrocarbon interior surrounded by the polar head groups exposed to the aqueous phase (**Figure 4.2**)¹⁵¹.

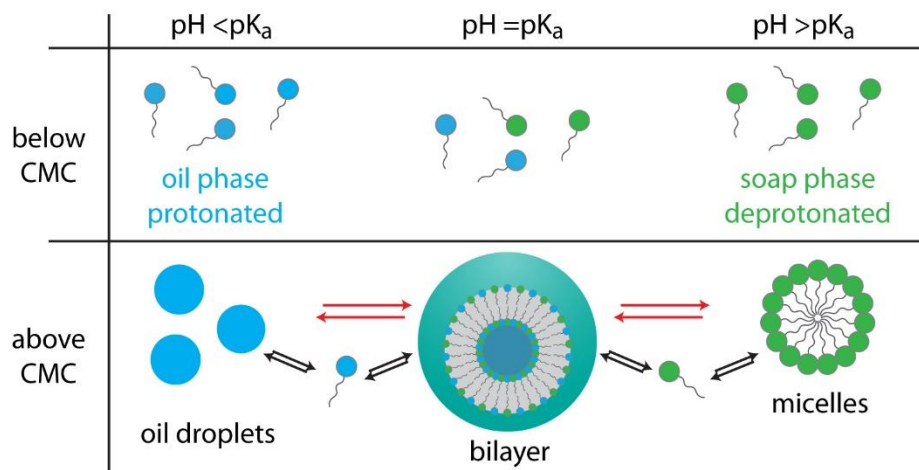


Figure 4.2. Schematic overview over fatty acid assemblies in water in different pH regions below and above the critical micelle concentration.

Mono- and divalent cations such as Na^+ , Mg^{2+} and Ca^{2+} are disruptive for fatty acid bilayers. While the difference in the concentration of monovalent cations across the bilayer can apply osmotic pressure leading to a decrease of vesicle volume or complete collapse, divalent cations bind the carboxylate head groups and precipitate the fatty acids. Due to the incompatibility of fatty acids with salt containing oceans, it has been hypothesized that fresh water ponds might have accommodated the origin of life^{63, 96}.

In several studies, improved bilayer stability has been observed when fatty acids were combined with other amphiphiles⁵³. For example, a mixture of fatty alcohols and fatty acid glycerol esters were shown to enable bilayer and vesicle formation from fatty acids in a wide pH range, and in the presence of mono and divalent ions⁶³. Decanoic acid combined with its alcohol decanol allow for stable compartments, which can encapsulate and protect the encapsulated enzyme catalase from degradation by protease present in the external solution¹⁵². Mixtures of fatty acids of different chain length, e.g. C_{10} - C_{15} , lead to the formation of stable vesicles under alkaline hydrothermal conditions with high salt content and elevated temperature ($\sim 70^\circ\text{C}$)¹⁵³. Another study reported that vesicle membranes composed of fatty acids and phospholipids were stable even at high Mg^{2+} concentrations. Mg^{2+} is important for RNA chemistry, hence the ‘RNA world’ and the origins of life⁶¹. In Paper V we also reported stable and consistent compartment formation from reservoirs of fatty acid-phospholipid mixtures in the presence of Ca^{2+} ions.

Upon addition of fatty acid micelles to an aqueous suspension containing pre-existing fatty acid or phospholipid vesicles, the micelles prefer to incorporate into the preexisting vesicles instead of forming vesicles themselves. In this way, the original vesicles act as template for

the added micelles, giving rise to the so-called ‘matrix effect’^{47, 154}. When phospholipids are used as a template, it is proposed that fatty acid monomers initially bind to the external monolayer of the phospholipid bilayer, followed by flip-flop into the internal monolayer. The free fatty acids in the surrounding environment later interact preferentially with fatty acids in the bilayer. This leads to the growth of elongated unilamellar structures, which later split into similarly sized vesicles, keeping the size distribution strongly biased towards the original vesicles⁴⁸⁻⁴⁹. An example of vesicular structures formed according to the matrix effect, are the “filamentous” vesicles, which later divide into smaller vesicles^{43, 46, 58}. Growth and division processes driven by the matrix effect have been reported in several instances with oleic acid/oleate and POPC vesicles¹⁵⁵⁻¹⁵⁷.

4.1.2. Phospholipid vesicles

The plasma membrane of modern cells consists mainly of phospholipids. Due to their cylinder-like molecular structure, phospholipids efficiently assemble to bilayers (**Figure 4.3**). The most common phospholipids present in the cell membrane are phosphatidylcholine (PC), phosphatidic acid (PA), phosphatidylglycerol (PG) and phosphatidylethanolamine (PE). Artificial biomimetic lipid membranes composed of phospholipids are commonly employed to represent selected cell structures and functions¹⁵⁸. They are particularly useful to characterize membrane-protein interactions¹⁵⁹. Small lipid vesicles (100-200 nm) are used as drug-carriers¹⁶⁰.

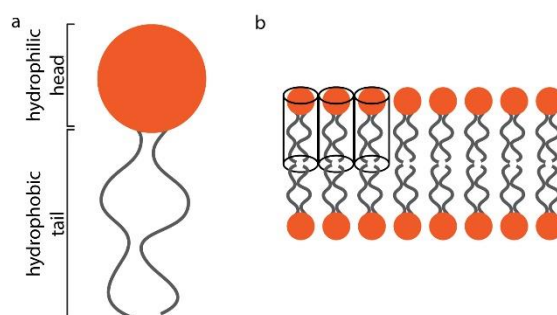


Figure 4.3. Schematic drawing of (a) a phospholipid molecule and (b) its cylindrical molecular shape in a self-assembled phospholipid bilayer.

Phospholipids are considered as suitable materials for protocell membranes. Synthesis of PE and PC were shown to occur under prebiotic conditions¹⁸⁻²⁰. PA and PG were synthesized during dry cycles in hot ponds in the presence of silicate minerals as

condensing agents¹⁷. Phospholipids such as PC can spontaneously assemble into vesicles at concentrations as low as 10^{-9} - 10^{-12} M⁵³. The low critical assembly concentration, compatibility with divalent cations, stability in varying pH, temperature and ionic strength, make phospholipids appear favorable over fatty acids molecules for protocell formation and development. Although phospholipids are relatively impermeable to charged compounds¹⁶¹, mechanical tension-driven transient pore formation in phospholipid membranes would allow the uptake and encapsulation of ambient components¹⁶².

Besides the commonly utilized spherical unilamellar compartments, phospholipids can also readily form multilamellar vesicles (MLVs)¹⁶³. Multilamellar reservoirs are detected in numerous biological cell types under normal and pathological conditions. The cellular lamellar bodies store and secrete lipids¹⁶⁴, help balance membrane tension¹⁶⁵ and are associated with biogenesis of organelles¹⁶⁶⁻¹⁶⁸.

Various techniques can be applied to form MLVs¹⁶⁹. For the work in this thesis, we employed the dehydration-rehydration method which will be described in detail in Part 5.

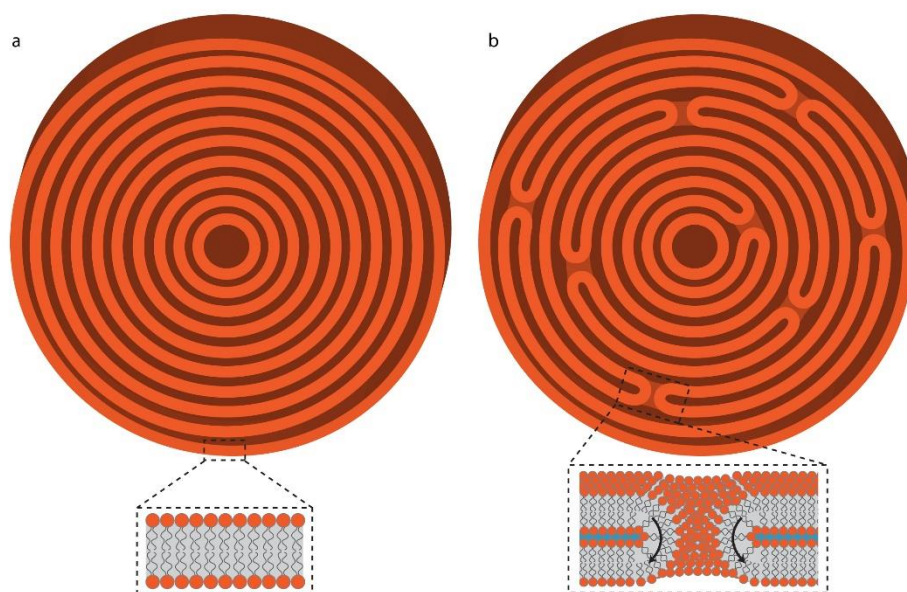


Figure 4.4. Schematic drawing of multilamellar vesicle (MLV) structures. (a) defect-free onion shell vesicle, (b) featuring “handle pore” defects.

Multilamellar vesicles are usually depicted as perfectly aligned, defect-free bilayer structures. In this scenario, there is no apparent connection between the lamellas. In reality, the multilayers contain membrane defects^{166, 170-171} (**Figure 4.4**). This is an important aspect, as the interconnected structure of MLVs allows unraveling of the stacked lipid bilayer and

enables lipid spreading on solid supports by acting as a reservoir. The transformation of a multilamellar reservoir into a flat membrane structure is the first and fundamental step for the formation of nanotube-mediated protocells described in this thesis.

4.2. Membrane mechanics

Lipid bilayer membranes have high aspect ratio; they are 5 nm thick and they can extend up to several millimeters along the membrane plane. A lipid membrane can be therefore treated as a thin, 2D elastic sheet, the elastic energy F of which is described as follows:

$$F = \int dA \left[\frac{\kappa}{2} (c_1 + c_2 - c_0)^2 + \bar{\kappa} c_1 c_2 + \sigma \right] \quad (4.1)$$

In this equation, the first and second terms are referred to as Helfrich membrane curvature energy¹⁷². The first term corresponds to the bending energy of a lipid membrane. dA is the surface area element, and κ is the bending rigidity which is an indicator of the membrane's resistance to a change in its curvature ($10\text{-}20 k_b T$)¹⁷³. c_1 and c_2 are the two principle curvatures, and c_0 is the spontaneous curvature. The spontaneous curvature occurs when lipid molecules in the different monolayer leaflets of a bilayer have structural differences and create an asymmetry. This is not an important term in our work, because the composition of inner and outer leaflet is identical. The second term is the Gaussian curvature, and $\bar{\kappa}$ is the Gaussian modulus which is negative and on the same order of magnitude as κ ¹⁷⁴. If the membrane topology does not change drastically, and rather undergoes simple transformations, the integral over the Gaussian curvature remains constant¹⁷⁴. For the work contained in this thesis, the Gaussian term is not relevant in comparison with the influence of the bending energy. The last term is the membrane tension. Membrane tension elevates due to stretching, which causes the distance between the lipid molecules to increase, and the number of lipid molecules per unit membrane area to decrease. Experimentally it has been shown that a lipid membrane can be stretched up to 5% of its initial area¹⁷³ before the membrane tension reaches $\sim 5\text{-}10$ mN/m (lysis tension) and ruptures.

4.3. Formation of vesicles

In an aqueous environment, lipids self-assemble into bilayers due to the hydrophobic effect as explained in 4.1. The newly formed bilayer is a free-standing disc, at the periphery of which lipids arrange themselves to a micelle like membrane edge in order to avoid the contact with water (**Figure 4.5**). At the membrane edge the distance between the lipid molecules is high and their hydrophobic moieties are exposed to water, which creates edge

tension. The edge energy cost proportionally increases with the circumference length of the patch¹⁷⁵. The energy cost of the membrane edge is defined by:

$$E_{edge} = 2\pi r\gamma \quad (4.2)$$

where r is the radius of the disc (**Figure 4.5**) and γ is the edge tension, which has been experimentally determined to be 5-10 pN^{162, 176}.

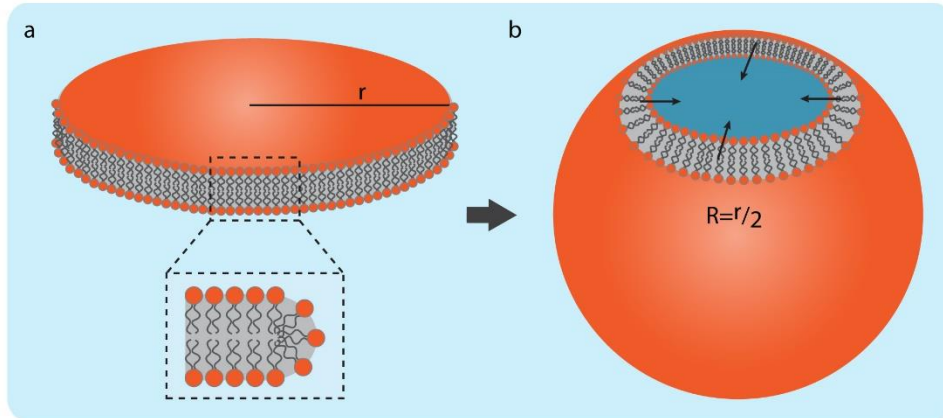


Figure 4.5. Schematic drawing depicting the transformation of (a) a flat membrane to (b) a spherical vesicle. The edge of the disc-shaped membrane is drawn to reveal the bilayer structure, a more realistic representation of the structure of the closed edge is given in the inset to (a).

While the free-standing disc is growing upon increase of the concentration of lipid molecules, the edge tension increases. To be able to avoid the energetic penalty associated with the rising edge tension, the membrane would close up to form a spherical vesicle, which is free of any membrane edges. Bending, however, also requires energy.

We can calculate the bending energy of a spherical vesicle with principal curvatures $c_1 = c_2 = \frac{1}{R}$ as the following:

$$E_{bend} = 4\pi R^2 \left[\frac{\kappa}{2} \left(\frac{1}{R} + \frac{1}{R} + 0 \right)^2 + \bar{\kappa} \frac{1}{R} \frac{1}{R} \right] \quad (4.3)$$

$$E_{bend} = 4\pi R^2 \left[\frac{2\kappa}{R^2} + \frac{\bar{\kappa}}{R^2} \right] \quad (4.4)$$

$$E_{bend} = 4\pi(2\kappa + \bar{\kappa}) \quad (4.5)$$

The bending modulus, κ , is a material dependent value. A typical value of κ for lipid membranes is 10-20 k_bT (k_bT room = 4×10^{-21} J)¹⁷³. $\bar{\kappa}$, the Gaussian modulus, is negative and on the same order of magnitude as κ ¹⁷⁴.

A spherical vesicle would form if the edge energy of the disc is greater than the bending energy required to form a vesicle:

$$\frac{E_{bend}}{E_{edge}} < 1 \quad (4.6)$$

$$\frac{4\pi(2\kappa+\bar{\kappa})}{2\pi r\gamma} < 1 \quad (4.7)$$

$$r > \frac{2(2\kappa+\bar{\kappa})}{\gamma} \quad (4.8)$$

If r is larger than $\frac{20 kbT}{10 pN}$ which is on the order of nanometers, the lipid bilayer would bend to form a small vesicle.

4.4. Supported membranes

Surface supported lipid bilayers are arguably the most commonly employed form of model membrane systems for studying membrane properties in a multitude of contexts. They are, for example, used to develop biomedical applications, biosensors¹⁷⁷, biocompatible implant devices¹⁷⁸ and to study drug binding mechanisms¹⁷⁹.

One method to form supported membranes is Langmuir Blodgett/Langmuir Schaefer deposition¹⁸⁰⁻¹⁸¹. Briefly, a solid substrate is submerged into an aqueous solution and lipid molecules at the air-water interface are forced to move onto the submerged substrate.

Another method involves the rupture of small unilamellar vesicles (SUVs) with diameters of up to 200 nm, deposited onto a surface^{116, 182}. Following adhesion, each SUV ruptures and forms a small lipid patch. Adhesion of numerous SUVs to the surface and merging of all small lipid patches over time results in a continuous bilayer film^{116, 119}.

Supported membranes can also be formed by self-spreading of multilamellar lipid reservoirs¹⁸³⁻¹⁸⁴. Once MLVs in an aqueous environment come in contact with the surface, they spontaneously spread. The spreading is driven by the Marangoni flow, which is the mass transfer between two fluids along an interface in a surface tension gradient. The lipid membrane migrates from low (reservoir) towards high tension (spreading membrane edge), and wets the surface reducing the total surface free energy of the system¹⁸⁵.

Spreading on a solid support can be in form of a mono-, single- or double bilayer (**Figure 4.6**) depending on the nature of the solid substrate e.g. high or low energy, hydrophilic or hydrophobic^{116, 186}. Monolayer spreading is observed on hydrophobic surfaces, such as fluoropolymers or the epoxy SU-8¹⁸⁷. On hydrophilic high energy substrates, e.g. glass,

single bilayers spread by sliding motion¹⁸⁸⁻¹⁸⁹, and on SiO₂, double bilayers by a tank tread¹⁸³ motion. In the latter case, the bilayer at the spreading edge rolls, where the proximal (lower with respect to the surface) bilayer is immobilized on the surface and distal (upper) bilayer slides over the proximal bilayer¹⁸⁴. The adhesion of the lipid film on the surface can be facilitated by the presence of fusogenic agents. On hydrophilic, negatively charged surfaces, multivalent ions, e.g. Ca²⁺, Mg²⁺, bridge lipid headgroups to the surface^{185, 188}. There remains a thin, lubricating layer of water between the lipids and solid substrate¹⁹⁰.

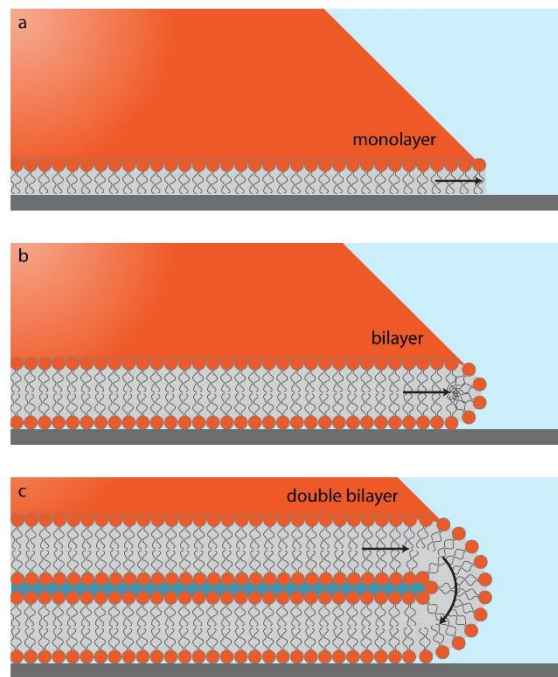


Figure 4.6. Spreading modes of lipid membranes on solid supports. Depending on the surface properties and lipid source, (a) monolayers, (b) bilayers, or (c) double bilayers are formed.

4.5. Double bilayer spreading

In my studies, I used multilamellar reservoirs which self-spread in form of a double bilayer membrane^{183, 191}.

During self-spreading, surface tension at the substrate-aqueous buffer interface (σ_A) must be higher than the tension at the surface-with lipid film interface (σ_L), leading to an overall positive value of spreading tension (σ_S) (**Figure 4.7**). The internal tension of the MLV (σ_0) opposes the σ_S . When the spreading power (S) has a positive value, spreading occurs spontaneously.

$$\sigma_S = \sigma_A - \sigma_L \quad (4.9)$$

$$S = \sigma_S - \sigma_0 = \sigma_A - \sigma_L - \sigma_0 \quad (4.10)$$

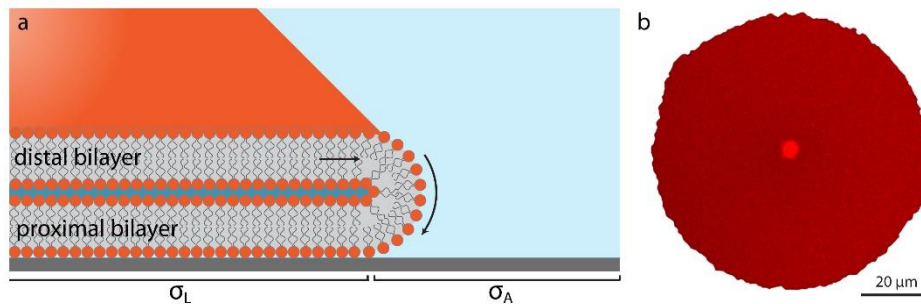


Figure 4.7. Self-spreading of double bilayer. (a) Schematic drawing of a rolling double bilayer on a high energy substrate, leading to a difference in interfacial tension between the lipid-wetted and non-wetted surface areas. (b) Confocal micrograph of a circularly spreading patch (top view). The bright spot in the middle of the patch is the MLV.

4.6. Membrane rupturing

The spreading of the double bilayer continues until the multilamellar reservoir is depleted, or exhausted due to the defects between layers. Although spreading slows down or stops completely with the consumption of the reservoir, the adhesion energy at the solid support would remain constant. This means that while the spreading edge of the patch favors wetting, the reservoir cannot provide sufficient lipid supply. The lipid membrane can stretch no more than a few percent of its surface area. The membrane tension then increases, and at some point exceeds the value of lysis tension ($5\text{-}10\text{ mN/m}$)¹⁷³. This results in the rupturing of the distal bilayer (**Figure 4.8**) where it breaks open and retracts on the proximal bilayer towards the peripheries of the lipid patch. Two forms of non-trivial ruptures (pores other than circular), exhibiting floral and fractal morphologies, were reported in 2010¹⁹¹(**Figure 4.8**).

Ruptures resembling flower patterns are mostly observed near the reservoir at the center of the circular membrane lipid patch and propagate towards the edge. Floral pores continuously grow until the double bilayer entirely transforms into a single bilayer on the solid substrate. Fractal ruptures most frequently appear along the circumference of the lipid patch and propagate inwards in an intermittent manner, in the form of avalanches. The type of rupture depends on the amount of pinning between two stacked bilayers established by the multivalent cations. High density of pinning has been shown, with computational models, to favor the fractal morphology¹⁹²⁻¹⁹³. Experimentally we do not have much control over the number and location of pinning sites. Both types of ruptures can be observed in the same experimental chamber on two different membrane patches positioned next to each other

and in some cases both rupture forms are observed on different parts of the same membrane patch, as shown in the example in (Figure 4.8).

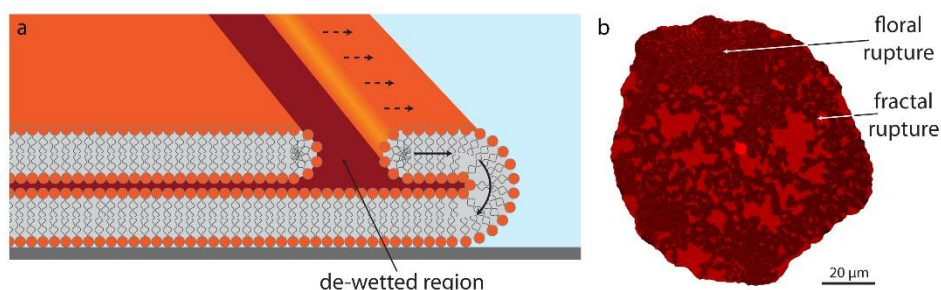


Figure 4.8. Rupturing of a double bilayer membrane. (a) The distal membrane breaks open and de-wets the proximal membrane. (b) Confocal micrograph of a ruptured double bilayer patch, showing large area (floral) and small irregular (fractal) fractures. The brighter regions are the remaining distal membrane fragments. Nanotube formations are visible in the upper floral region.

4.7. Tube formation

In Paper I, we have shown that following the floral membrane rupturing, a carpet of lipid nanotubes form on the distal bilayer. During propagation of the rupture, the regions of the distal membrane pinned to the proximal bilayer remain undisturbed, followed by the formation of thin membrane threads pulled between the rupturing membrane edge and the immobilized distal membrane regions. Due to the rapidly elongating membrane edges, the edge energy cost of the membrane increases. To avoid the energy penalty of increasing edge tension, these thin, lengthy membrane regions wrap up into nanotubular structures (Figure 4.9).

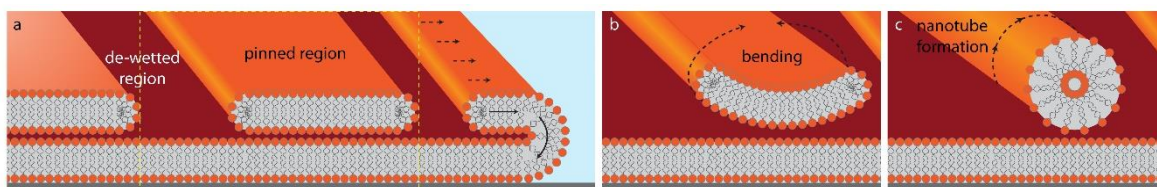


Figure 4.9. Schematic drawing of membrane nanotube formation on a ruptured double bilayer. (a) Formation of a narrow isolated membrane strip, which is pinned to the proximal bilayer, during the tension-induced rupture process. (b) Spontaneous reduction of the high edge energy by closing of the flat structure to form a tubular conduit. The nanotube is not drawn to scale.

We explain the motive for the transformation from a thin lipid bilayer region to a nanotube by calculating the free energy of the system. Edge energy cost of rectangular membrane patch is a product of its length (l) and the edge tension (γ) (5-10 pN^{162, 176}).

$$E_{edge} = l\gamma \quad (4.11)$$

Bending energy of a lipid nanotube can be derived from the Helfrich bending energy equation¹⁷². For a nanotubular structure with radius r and length l , principal curvatures are $c_1 = 0$ and $c_2 = \frac{1}{r}$.

$$E_{bend} = 2\pi r l \left[\frac{\kappa}{2} \left(0 + \frac{1}{r} \right)^2 + \bar{\kappa} \frac{1}{r} \cdot 0 \right] \quad (4.12)$$

$$E_{bend} = 2\pi r l \left[\frac{\kappa}{2r^2} \right] \quad (4.13)$$

$$E_{bend} = \frac{\pi l \kappa}{r} \quad (4.14)$$

This shows that the bending energy cost of a nanotube increases with its length. As mentioned before, bending occurs if the edge tension energy is greater than the bending energy needed for curving a flat bilayer into a nanotube.

$$\frac{E_{bend}}{E_{edge}} < 1 \quad (4.15)$$

$$\frac{\frac{\pi l \kappa}{r}}{l\gamma} < 1 \quad (4.16)$$

$$\frac{\pi \kappa}{r\gamma} < 1 \quad (4.17)$$

Equation 4.17 shows that after reaching to a length of a few nanometers, a rectangular patch pinned to the proximal bilayer would bend to a nanotube.

The total free energy of a membrane nanotube¹⁷² is:

$$F = \frac{\pi l \kappa}{r} + 2\pi r l \sigma \quad (4.18)$$

$$\frac{\partial f_{nanotube}}{\partial r} = 0 \quad (4.19)$$

Where $f_{nanotube}$ is the energy of the nanotube per unit length, which leads to:

$$f_{nanotube} = \frac{\pi \kappa}{r} + 2\pi r \sigma \quad (4.20)$$

At equilibrium, the radius of the nanotube is determined by the balance of bending modulus and membrane tension¹⁹⁴:

$$r = \sqrt{\frac{\kappa}{2\sigma}} \quad (4.21)$$

At constant membrane tension (0.01-0.05 mN/m¹⁹⁵), this corresponds to a nanotube of ~100 nm radius.

4.8. Diffusion and tension-driven transport through nanotubes

Lipid nanotubes enable the transport of molecules by molecular diffusion¹⁹⁶ or Marangoni flow¹⁹⁷. Components smaller than the diameter of a nanotube (~100 nm) can diffusively migrate inside the tubes¹⁹⁸. Inter-cellular lipid nanotube structures utilized for signaling and transport of cellular constituents, even organelles, have been observed in various biological structures¹⁹⁹⁻²⁰⁰. I have not investigated the transport phenomena through lipid nanotubes inside the networks, but here I provide some estimated time scales for diffusion of molecules inside the lipid nanotubes bridging spherical lipid compartments.

If we consider two lipid vesicles (with radii of 2.5 μm) connected via a nanotube (10 μm length and 50 nm radius), where one encapsulates small dye molecules e.g. fluorescein, the time that is required for concentration of fluorescein to equilibrate throughout the structure can be calculated as^{196, 201}:

$$t = \frac{L_t}{\pi D (r_t)^2} \cdot \frac{V_1 V_2}{V_1 + V_2} \quad (4.22)$$

The diffusion coefficient (D) of fluorescein in water at room temperature is $25 \times 10^{-10} \text{ m}^2/\text{s}$ ²⁰². The time for diffusion from one vesicle to the other via the nanotube is calculated to be $t \approx 7 \text{ min}$.

The time (t_{entry}) that molecules reach the opening of the nanotube inside a large vesicle must also be taken into account. This can be calculated from the equation below²⁰¹:

$$t_{\text{entry}} = \frac{r_v^3}{D r_t} \quad (4.23)$$

For the fluorescein molecule, $t = \sim \text{ms}$.

In conclusion, a small molecule such as fluorescein can diffuse through a 10 μm long nanotube between two giant vesicles on a time scale of the order of minutes.

In addition to molecular diffusion, the transport of material through lipid nanotubes can be enabled by membrane tension gradients. The cargo is moving along with the lipid flow towards the region of high tension, therefore not only internalized, but also externally

attached cargo can be transported. The time for tension driven flow in the same vesicle-nanotube system described above is:

$$t = \left(\frac{r_v}{r_t}\right)^3 \frac{\eta l}{\Delta\sigma} f \quad (4.24)$$

Where (f) is the fraction of total vesicle volume (V), η is the viscosity of the water (10^{-3} Pa) and $\Delta\sigma$ is the difference in tension between two locations on the membrane¹⁹⁷. Transfer of 10% of volume of the vesicle ($f=0.1$), when the tension difference is 0.01 mN/m, can occur in ~10 seconds.

4.9. Protocell nucleation, growth and division

Lipid nanotubes are highly curved bilayer structures; therefore they are energetically costly. To minimize the surface free energy, nanotubes will tend to reduce their curvature, often by transforming to a spherical vesicle, provided that excess lipid material is available. In the case of floating lipid nanotubes, this transformation occurs in a very short time frame (seconds), leading to stomatocyte-like vesicular structures with a folded double bilayer²⁰³. Direct transformation into a spherical vesicle is in this special case not possible due to the significantly differing number of lipid molecules in the inner and outer leaflet of the tubular membrane, as compared to a vesicle membrane³, and the extremely low inter-leaflet flip flop rate of phospholipids.

In surface-adhered vesicle-nanotube networks, the nanotubes are pinned to the underlying bilayer, preventing them from rapidly forming spherical vesicles. Instead, the vesicles form via enlargement of fragments of the lipid nanotubes over longer time periods, from hours up to days (**Figure 4.10**), unless an externally applied stimulus (e.g. temperature increase) facilitates this transformation⁵.

The sites of nucleation of vesicular compartments on nanotubes are mostly the intersection of two or three nanotubes: V- and Y-junctions²⁰⁴. Once nucleated, the vesicles grow continuously if there is sufficient lipid material available. The replacement of the membrane area during the spontaneous transformation of nanotube to vesicles was estimated to be $\sim 2 \times 10^{-3} \mu\text{m}^2\text{s}^{-1}$ in Paper I. At elevated temperatures (Paper III) this rate increases by three orders of magnitude to $\sim 2 \mu\text{m}^2\text{s}^{-1}$. The temperature increases lipid fluidity, as well as membrane tension due to defect formation,²⁰⁵ and accelerates the growth of vesicular compartments due to the tension driven (Marangoni) flow of lipids towards the area of increased temperature.

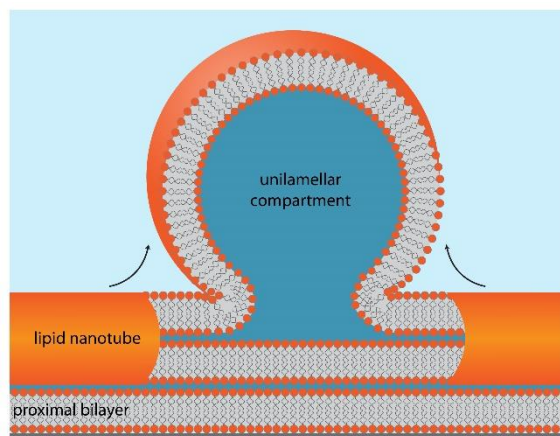


Figure 4.10. Vesicle nucleation from a lipid nanotube. Curvature-induced tension in a nanotube section is alleviated by the supply of lipid material from a connected (remote) source, e.g. a multilamellar reservoir, which leads to the formation of a vesicle.

Fusion of initially intact lipid compartments involves the subsequent steps of adhesion, lipid mixing in outer monolayers, pore opening by membrane rupture and mixing of internal contents, all of which require energy. Multiple examples have been reported involving UV-exposure²⁰⁶, electrofusion²⁰⁷, thermal cycles²⁰⁵, protein action²⁰⁸ and DNA linkers²⁰⁹.

Membrane-membrane adhesion is not equivalent to fusion. However, prior to fusion, adhesion of adjacent mutually adhered compartments can be induced by divalent cations such as Ca^{2+} ^{188, 210}. When two vesicles adhere, they deform until the adhesion stress is in equilibrium with elastic stress²¹¹⁻²¹³. The relation between the bilayer-bilayer adhesion energy and membrane tension can be expressed as^{173, 188}:

$$W = 2\sigma(1 - \cos\theta) \quad (4.25)$$

where W is the adhesion energy, σ is membrane tension and θ is the angle between two adhered vesicles at the edge of the contact line. Using equation eq. 4.25 and micrographs, the adhesion energy between the bilayers of two giant unilamellar vesicles in the presence of 1-10 mM Ca^{2+} was determined to be 0.02-0.03 mN/m¹⁸⁸. In Paper III, we induced the fusion of adjacent lipid compartments by locally heating the membrane. Elevated temperatures increase membrane fluidity and induce stress in bilayers, causing membrane expansion and exposure of parts of the hydrophobic chains to water²⁰⁵. Additionally, disorder of structural water at the membrane surface increases, and the membrane surface becomes more hydrophobic. As a consequence, membranes of two adjacent vesicles fuse^{205, 214}.

Our mathematical model and experimental findings in Paper III support that fusion of compartments positioned on the same nanotube is enhanced and energetically more

favorable compared to the fusion of compartments on separate nanotubes. In the latter, fusion still takes place, but a stable pore remains between the compartments.

Division of primitive cells requires splitting of the lipid membrane, hence energy input to overcome the edge energy of the defect formed at the separation site. In the following section I will discuss experimental observations reporting on the division of simple protocells which lack molecular machinery.

If mechanical force is applied, some vesicular structures other than spherical compartments, for example elongated vesicles in solution, can more efficiently divide into similarly sized vesicles, *i.e.* 'daughter cells', (**Figure 2.1**). The elongation of the vesicle starts with rapid insertion of lipid monomers to the membrane of a lipid vesicle. This leads to formation of filamentous structures due to the fast membrane area- and slow volume expansion. The filamentous vesicles can later, with external energy supply, divide into small daughter vesicles, *e.g.* by extrusion, or shear force applied with sonication^{43, 50, 58}. This reported system serves as evidence indicating that fluid flow through porous rocks near possible geological sites at the origin of life could enable protocell division.

One other possible mechanism leading to the division of the elongated vesicles is pearling, where a tubular membrane spontaneously transforms into vesicles connected with very thin nano-sized tethers, resembling a string of beads. Later, shear force disrupts the membrane connections between the vesicles, leading to division of protocells⁶⁰.

Yet another way by which division might have occurred is the growth of daughter vesicles as subcompartments inside a protocell followed by their release from parental compartment²¹⁵. This requires supply of additional chemical compounds to the system. When oleic acid/oleate vesicles are supplied with oleic anhydride, the hydrolyzed anhydride molecules form an inclusion vesicle inside the mother vesicle. The inclusion vesicle is then released from the mother vesicle.

Our findings in Paper I lead to the development of a new division hypothesis²¹⁶. Firstly, in the case that inside one of the neighboring vesicles in a protocell-nanotube network, a genetic polymer replicates, and some of it travels through the nanotubular highway to an adjacent vesicle, this would correspond to the distribution of the content over two different model protocells. Secondly, we have shown in Paper I that the surface adhered protocells can physically separate from the rest of the network with the help of hydrodynamic flow induced by an open-volume microfluidic device. The separated vesicles can migrate and reattach at remote locations. Therefore the division of protocells may have occurred at the same time as their surface-assisted formation. In principle, primitive protocells in vesicle-

nanotube networks would be able to chemically communicate and transport materials through the nanotubular connections.

We have also proposed a pseudo-division mechanism in Paper IV, where surface-associated subcompartments of enveloping protocells become 'daughter cells' after the envelope eventually disintegrates. The formation of subcompartments is mediated by the interaction of protocell's basal membrane with the mineral-like surfaces supports.

4.10. Membrane permeability and transient pores

Under prebiotic conditions, three possible ways of encapsulation have been suggested. The first is the simultaneous dehydration/rehydration of vesicles and solutes. When amphiphile layers are rehydrated, solutes become entrapped inside the newly formed vesicles²¹⁷⁻²¹⁸. The second is the formation of amphiphile molecules from their precursors, and their subsequent self-assembly in an environment containing the solutes²¹⁹. In this case, the self-assembly and encapsulation of solutes will occur simultaneously. The third mechanism involves aerosol-based vesicle formation. The sea surface acts in this case as a concentrator of surfactants. Evaporation results in the formation of water aerosols enveloped in an inverse lipid monolayer where hydrophilic moieties face the encapsulated content from the ocean and hydrophobic tails are exposed to the air. Later, the exposure of airborne aerosol particles to sunlight evaporates some of the water from the interior, and induces reentry to water. While reentering, the monolayer droplet acquires the second monolayer from the sea surface and forms a stable bilayer vesicle in the ocean²²⁰.

In Paper I, II, III, VI, growing protocell-nanotube networks in the presence of solutions containing small dye molecules, RNA or DNA oligomers, we demonstrated the encapsulation of these compounds by the vesicular compartments. The resulting high encapsulation efficiency indicated the presence of tension-induced transient pores in the membrane¹⁶². After exchanging the ambient solution, the contents of some of the vesicles is maintained. Some of the pores must therefore have been permanently closed after the membrane is relaxed.

In lipid vesicles, pore opening is driven by membrane tension, which instantly decreases upon pore formation, since the lipid molecules are distributed over a membrane area reduced by the pore size. Also, pore opening leads to leakage of contents, decreasing the vesicle radius and relaxing the membrane further^{162, 176}. At the same time, opening of a pore creates an edge tension (5-10 pN^{162, 176}) which is proportional to the circumference of the circular pore²²¹⁻²²². This edge tension drives the closure of the pore.

It is also possible that some of the encapsulation occurs during the wrapping of the flat bilayer regions to nanotubes. However, our calculations showed that a volume from a ~8 nm nanotube is needed to fill up a 5 μm vesicle. We do not observe such lengthy lipid nanotubes in our experiments, and suggest that the major route to encapsulation is the presence of transient membrane pores. We later showed in Paper IV with a finite element method-based model that this was a feasible mechanism.

In Paper I, III-VI, we used hydrodynamic flow to induce formation of transient pores on bilayers, and observed the spontaneous encapsulation of fluorescein and RNA or DNA molecules. Additionally, in Paper II, we showed pore formation induced by SMA polymer, and consequently the leakage of content from surface adhered vesicular compartments.

The lipid bilayer is selectively permeable to some small molecules. The composition of the bilayer is the factor that affects the permeability the most, in particular the length and degree of unsaturation of the hydrocarbon chains. Furthermore, salinity, ionic strength, pH, temperature and presence of divalent cations have an influence on the bilayer stability and permeability⁵³. Accordingly, in blended phospholipid/fatty acid membranes, the permeability is higher than in membranes composed of phospholipids only⁶¹.

5. Methods

5.1. Preparation of lipid vesicles

Multilamellar vesicles/reservoirs (MLVs) were prepared by using various lipid species including fatty acids, or total lipid extracts from plants or animals.

The commonly used dehydration-rehydration technique²²³ was employed for MLV preparation (**Figure 5.1**).

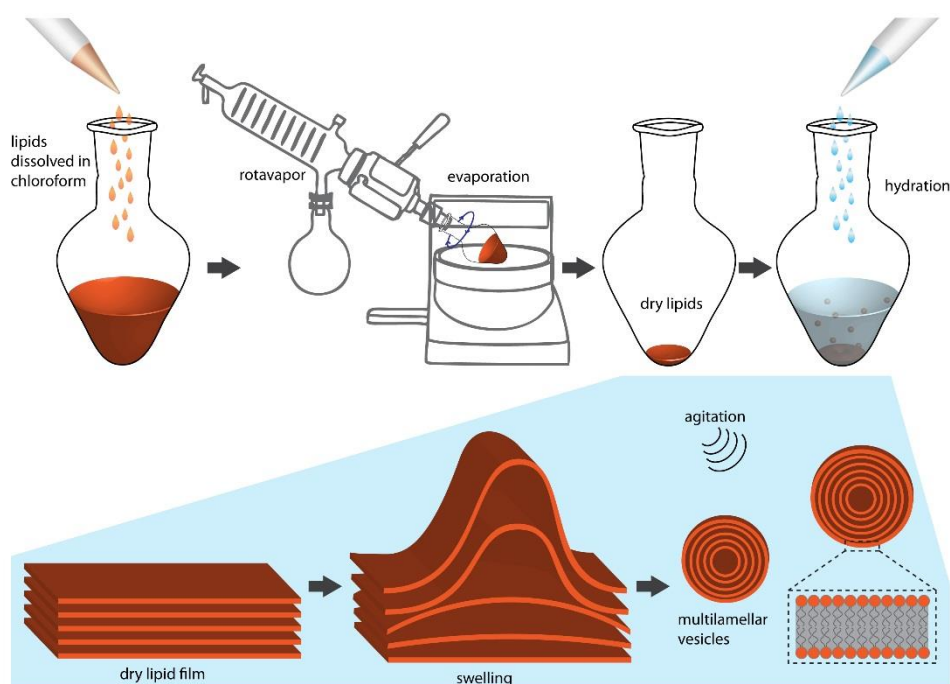


Figure 5.1. The dehydration-rehydration process.

In this method, the lipid species are first dissolved in a desired ratio in chloroform. The solvent is evaporated under vacuum (20kPa, 150 Torr) while slowly rotating to form a homogeneous dry lipid film at the flask wall. The dry lipid layers are then rehydrated overnight with a buffer containing 1% glycerol forming vesicles at various sizes and lamellae. The presence of glycerol would prevent complete dehydration of the lipid film and enable bilayer separation²²⁴. Sonication of the solution decreases the size and lamellarity of the reservoirs, which can be controlled by the exposure time. The MLV stock solution can be stored at -20 °C, and used when needed. For preparation of samples, 4 μ l from this stock suspension is placed on a glass coverslip, dehydrated using a vacuum desiccator for approximately 20 min. The dry film is rehydrated using a buffer suitable for the experiment.

In Paper V, MLVs from fatty acids and phospholipids were prepared using the dehydration-rehydration method. The amphiphile residence time of fatty acids is low comparing to phospholipids, and free fatty acid molecules are anticipated in the solution. It is possible to determine the amount of free fatty acids floating in the solution using a free fatty acid quantification kit^{43, 61}, which we utilized in Paper V.

MLVs can also be formed from pure fatty acids as we have shown in Paper V. However, handling fatty acids is challenging and the reproducibility was low. Fatty acid vesicles are highly sensitive to pH, salinity, the presence of divalent cations and temperature of the solution¹⁴⁸⁻¹⁴⁹. Fatty acids are thermodynamically stable at a narrow pH range and can form bilayers when the pH in their aqueous environment is close to the pK_a of the carboxylate group of the fatty acid. After evaporation of the organic solvent under vacuum, the formed dry film must be rehydrated considering the pK_a and the melting temperature of the fatty acid used. At low pH, molecules are protonated and uncharged, and tend to form oil droplets. When the pH of the solution used for rehydration is close to the pK_a of the fatty acid, it leads to the formation of an equimolar amount of protonated and ionized fatty acids. When the degree of protonation is close to 50%, protonated and ionized fatty acids undergo hydrogen bonding ($RCOO^- \cdot HOOCR$) to form stable bilayer vesicles^{38, 53, 142-143, 150-151}. At high pH, they are deprotonated, negatively charged, and form micelles. The critical concentration at which the fatty acids bilayers and vesicles will form (CVC), must be considered while forming fatty acid vesicles. The CVC is higher than the value for phospholipids. This concentration increases when length and degree of unsaturation decreases^{53, 225}.

Continuous sonication of the MLV suspension described above leads to the formation of a suspension of smaller vesicles, which were further processed to small unilamellar vesicles (SUVs), used in Paper II. SUVs were formed via extrusion where the sonicated lipid suspension was pushed through a polycarbonate membrane, using a syringe-based plunger system multiple times²²⁶. As a result, the MLVs break up into a monodisperse population of vesicles with an average size close to the pore size, e.g. 100-200 nm.

5.2. Surface fabrication and characterization

5.2.1. Surface fabrication

The high energy surfaces used in all papers in this thesis were fabricated and characterized in MinaLab or MC2, the state-of-art nano- and microfabrication facilities (cleanroom) at the University of Oslo and at Chalmers University of Sweden. A cleanroom environment, where

the concentration of airborne microparticles is tightly controlled, is necessary to obtain well defined, uncontaminated surfaces and structures.

Silicon dioxide (SiO_2) and aluminum (Al) films used for this thesis work were fabricated using electron-beam (e-beam) evaporation, a physical vapor deposition technique²²⁷. Glass cover slides are loaded into the instrument and evacuated to approximately 10^{-4} Torr. The Tungsten filament inside the chamber is resistively heated until it starts emitting electrons. A high voltage is applied to accelerate the electrons, and strong magnetic field to focus them onto a crucible containing the material to be deposited. The material evaporates and its vapor condenses on the glass substrate (**Figure 5.2a**). E-beam evaporation has several advantages compared to other evaporation techniques. For instance, the e-beam can heat materials to higher temperatures comparing to methods involving a resistive crucible heater. This makes e-beam evaporation useful for deposition of metals including the ones with high melting temperature. Deposition rates as high as $50 \mu\text{m/s}^{-1}$ can be achieved with e-beam evaporation. The focused e-beam only heats the source material while the crucible body is water cooled, allowing high purity deposition of the source material²²⁷. For monitoring the thickness in real-time during deposition, a quartz crystal based microbalance (QCM) is used. The thickness is determined by monitoring the change of the resonance frequency of the crystal resonator, caused by the increasing mass of the deposited film.

The aluminum oxide (Al_2O_3) films used in Paper IV were fabricated using Atomic Layer Deposition (ALD), a chemical vapor deposition technique²²⁷⁻²²⁸. In this technique the glass cover slips are initially loaded to the chamber and evacuated. The system relies on alternate pulsing of the precursor gases onto the surface of the substrate. The ALD process is shown in **Figure 5.2b** for the deposition of Al_2O_3 . Initially, the precursor $\text{Al}(\text{CH}_3)_3$ is pulsed to the chamber and chemisorbs on the surface, releasing a molecule of methane while forming a dense monolayer. Subsequent purge with an inert gas such as N_2 removes the gaseous byproduct and all unbound precursor molecules from the chamber. Next, the second precursor H_2O is introduced, which reacts with the precursor monolayer, produces a solid Al_2O_3 monolayer, and more CH_4 byproduct. A subsequent purging step with an inert gas removes the byproduct²²⁸. As by each deposition cycle the film thickness increases at a constant rate; one of the most important characteristics of ALD is the accurate and easy control of film thickness. To create an approximately 10 nm Al_2O_3 film, 100 deposition cycles are required. One drawback of ALD is the low deposition rate in the order of 100-300 nm/h²²⁷.

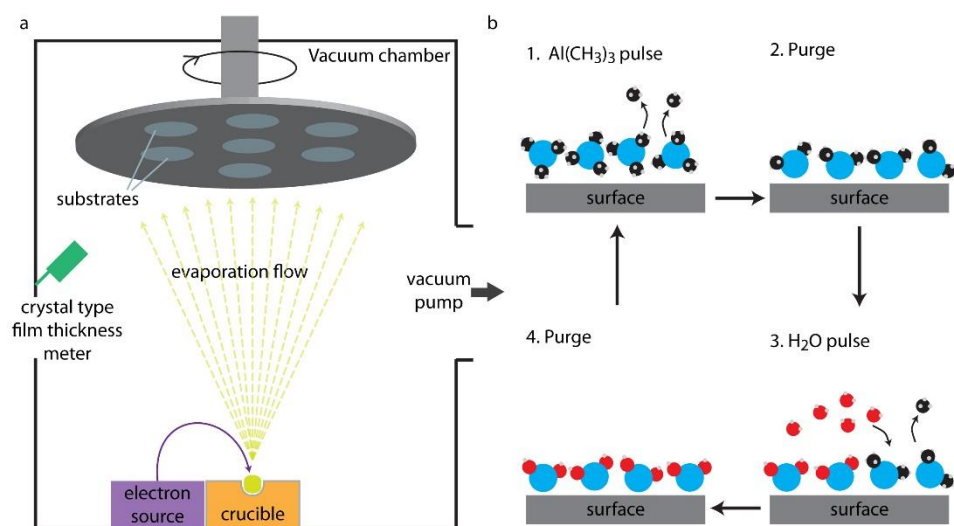


Figure 5.2. E-beam evaporation and ALD process.

The thickness of the deposited thin films was measured using an ellipsometer. It measures the change in polarization of light when light is reflected from the sample surface. The measurements provide in a contactless fashion accurate information about the thickness of the film. Ellipsometry measurements need to be interpreted with an appropriate model, which is specific to the deposited film and substrate²²⁹.

Prior to use, all surfaces were oxygen plasma treated, predominantly for removing organic contaminants. Oxygen radicals react with any hydrocarbon contamination they encounter. At the end of the reaction, formed CO_2 and H_2O are pumped out of the system²³⁰. The oxygen plasma also serves to uniformly oxidize the silicon and aluminium oxide surfaces, which improves the wettability.

5.2.2. Preparation of thin sections of natural surfaces

Thin polished sections of rocks, minerals and meteorite were used as solid supports in Paper VI. In optical mineralogy, 30 μm thin sections are used to investigate the optical properties of the minerals with polarizing light microscopy, and information can be obtained on the origin and the evolution of the rock. We used 170 μm thick sections since this matched the cover glass thickness for the confocal microscopes we employ. To prepare the petrographic sections, initially a thin section from a rock is cut with a diamond saw. It is then mounted in epoxy resin onto a bed, and polished to the desired thickness. An acetone-soluble epoxy was used in our studies, so that the thin sections can be retrieved for the experiments under the microscope.

5.3. Microscopy

5.3.1. Fluorescence and confocal laser scanning microscopy

Laser scanning confocal microscopy was used in all experimental work shown in this thesis as a tool to visualize the behavior of fluorescently labeled lipid membranes. Confocal microscopy enables enhanced observation of micro- and nano- structures)²³¹⁻²³².

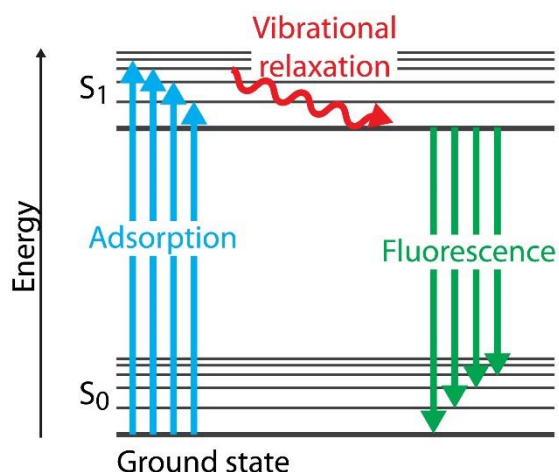


Figure 5.3. Simplified Jablonski diagram, showing the energy levels of the ground and first excited state, and the transitions relevant for absorption and deactivation by re-emission (fluorescence).

The thickness of the lipid bilayer we used in our experiments is approximately 4-5 nm and optically transparent. We used fluorescently tagged lipid molecules and visualized biomembranes with confocal fluorescence microscopy. Fluorophores can be irradiated with laser light at a specific wavelength. As a result of this excitation, the fluorophore molecules elevate an electron from the ground state (S_0) to excited state (S_1). Different vibrational stages are allowed in the excited state; the electron returns to S_0 by emitting a photon, *i.e.* fluorescing, within 10^{-7} to 10^{-9} s at a longer wavelength. These processes and energy levels are shown in the Jablonski diagram in **Figure 5.3**. Other deactivation processes are neglected in this scheme.

Absorption and fluorescence emission properties, especially the absorption and emission wavelengths are important for designing an experiment containing more than one fluorophore. The property of different fluorophores to absorb and emit light at specific wavelengths, allows visualization of different molecules or regions in a sample simultaneously. In our experiments we commonly visualized labeled lipid membranes together with other fluorescently labeled compounds *e.g.* fluorescent dyes, RNA, DNA.

Another important parameter to consider is the process of photo-bleaching. Long term or intense exposure to light under ambient conditions typically results in photo-bleaching and gradually reduces the fluorescence emission from the initially labeled sample. This can affect the fluorescence signal-based quantitative measurements, and needs to be accounted for.

There are a variety of light sources in fluorescence microscopy. In the state-of-the-art fluorescence microscopes, the illumination is provided commonly by a laser source. Lasers are desired for high and adjustable intensity and monochromaticity in comparison to continuum sources, such as the Xe arc lamp.

Laser scanning confocal microscopy (LSCM)²³¹, is particularly suitable for thin fluorescent samples such as the phospholipid membranes, because a pinhole aperture allows collecting light from a focal plane of a thickness ranging from 0.5 to 1.5 μm , and the light from out of focus areas is eliminated (**Figure 5.4**). This way the depth of field can be controlled, and by collecting images from serial optical sections, 3D micrographs can be reconstructed. One disadvantage is the relatively poor time resolution which is in the range of ms to s. The acquisition rate can be improved to by increasing the scanning speed, reducing the size of the scanned area and reducing the number of pixels.

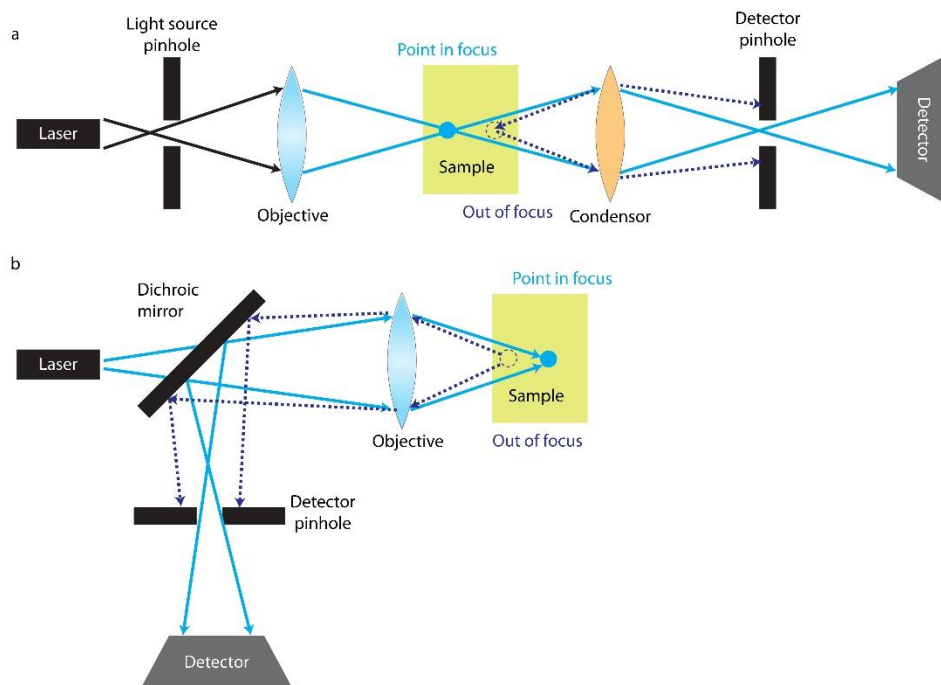


Figure 5.4. Transmission and reflection imaging modes in confocal microscopy.

There are two possible base geometries for the confocal microscope; in the upright microscope set up the objective is above the sample, and in the inverted setup, below. Inverted microscopes are more suitable for the usage of micromanipulators, injection needles, the microfluidic pipette and IR-laser systems we utilized in our studies. We have employed an inverted confocal microscope in all our studies except for the experiments involving the opaque surfaces in Paper VI. For those samples, we used an upright confocal microscope with reflected light illumination. The main difference between transmission and reflection modes is the detection of reflected light from the sample in the upright microscope versus the transmitted light in the inverted microscope. The upright microscopes contain one objective and pinhole for imaging in reflection mode, versus two in transmission mode (**Figure 5.4**). In transmission mode, light passes through the first pinhole and reaches the objective, focusing the light onto the sample. Then a second lens brings the light to the detector. The second pinhole in front of the detector blocks the out-of-focus light, and only the signal from focused z-plane is collected. The same fundamental confocal microscopy principle is applied in upright microscopes, this time using the reflected light from the sample instead of the transmitted light, directed via a dichroic mirror to the detector (**Figure 5.4**).

Objectives are the most important components of a microscope. They gather and focus light to produce a high quality image. I mostly used a 40X magnification immersion oil objective with a numerical aperture (NA) of 1.3 for imaging. The NA shows the ability of an objective lens to gather diffracted light in order to form an image with good resolution. Transparent immersion oil with a high refractive index fills the gap between the front element of the lens and the sample, thus also contributes to the NA. Larger NA objectives can resolve finer details in the sample. In this combination, the lateral resolution of our inverted confocal microscope can reach ~150 nm. In the upright confocal microscope, we used a 40X water immersion objective (NA 0.8).

Optimal cover glass thickness is also an important parameter in confocal microscopy. Most of the objectives we used are designed for a standard cover glass with a thickness of $170 \pm 5 \mu\text{m}$ and a refractive index of 1.5. Especially objectives with high NA are sensitive to cover glass thickness. In Paper VI we sectioned and polished the natural surfaces down to final thickness of $170 \pm 5 \mu\text{m}$, accordingly.

A fluorescence-based method, the fluorescence recovery after photobleaching (FRAP), was used in Paper II to measure the fluidity of solid-supported bilayers. FRAP shows the recovery of the fluorescence signal in a specific region in the sample after it is completely photo-bleached due to exposure to high intensity illumination. The recovery indicates the lateral mobility of the constituents in the sample. Determination of the rate of recovery allows

for calculating diffusion coefficients. First a defined, small area on the sample, e.g. lipid membrane, is exposed to a high-intensity laser beam until the fluorophores in this area are irreversibly photo-bleached. If the membrane is fluid, the lipid molecules will diffuse in the 2D plane of the membrane, *i.e.*, the bleached molecules will diffuse out of the recently photo-bleached region while the fluorescence lipids will enter it. This leads to the gradual increase of the fluorescence signal, hence the fluorescence recovery.

5.3.1. Variable pressure scanning electron microscopy (VP SEM)

Scanning electron microscopy is one of the essential techniques for microstructural analysis of materials providing information about topological features, morphology, compositional differences, crystal structure and orientation. In SEM, electron beams are accelerated to moderately high energy and positioned onto the sample by electromagnetic fields. The electrons interact with the atoms on the sample surface, and signals resulting from the interaction with each atom have unique physical properties and energies. Secondary electrons which are ejected from the outer shell of surface atom, or the backscattered electrons that change their trajectory while escaping the sample, are typically used to generate SEM image contrast²³³.

We employed VP SEM in Paper VI for the characterization of the natural surfaces, which differs from the traditional SEM in terms of the chamber pressure. While traditional SEM operates with pressures on the order of 10^{-6} Torr ($\sim 10^{-5}$ Pa), VP SEM is operated at pressures ranging from ~ 10 to 3000 Pa. This allows the imaging and analysis to be performed without a conductive coating of the sample²³⁴.

In addition to the high-resolution imaging of the sample, semi-quantitative elemental analysis of the sample surface can be done with an energy dispersive X-ray (EDX) spectrometry in conjunction with the SEM²³⁵. For this application, the intensity of X-ray emission from the sample surface is detected. Since all elements except H and He produce characteristic x-rays, scanning of the sample generates an elemental composition map of its surface.

5.4. The microfluidic pipette

Microfluidics is a miniaturization technology for manipulating small volumes of liquid of 10^{-9} to 10^{-18} liters in micrometer-sized channels²³⁶. Microfluidic technology provides the ability to transport and process very small amount of liquids in a controlled fashion, featuring low

material consumption and fast transport times. Microfluidic devices are characterized by turbulence-free (laminar) liquid flow described by low Reynolds numbers. Under laminar flow conditions, fluids move in a well-predictable manner, and streams can coexist for a prolonged time, while constituents are exchanged solely by diffusion.

In all papers in this thesis, we used a 'microfluidic pipette' fabricated from the optically transparent soft elastomer polydimethylsiloxane (PDMS). The pipette²³⁷ is a non-contact, open volume microfluidic device which can be directed to a specific region on the sample for superfusion. At the tip of the device, facing the volume of interest above the sample, a parallel three-channel arrangement produces an open fluid volume of defined composition. Positive pressure on the middle channel injects the fluid, whereas negative pressure at the adjacent channels aspirates the solution, creating a stably confined re-circulation zone (**Figure 5.5**). The size of the re-circulation zone is controlled by varying the outflow to inflow ratio, and objects within a ~100 μm range are effectively superfused. The flow in the recirculation zone is characterized by a large Péclet number, indicative of a high flow velocity-to-diffusion coefficient ratio, which inhibits diffusion across the boundary of the recirculation zone, such that the circulated solution does not disperse into the ambient buffer. We loaded the pipette with the different reagent solutions required, and submerged it into the buffer solutions inside the observation chamber. It was positioned close to the surface and to area of interest using 3-axis water hydraulic micromanipulators.

In Paper II, the microfluidic pipette was used to form bilayer membranes on solid glass supports in-situ. In Paper I, it was used to collect the nanotube attached GUVs inside the pipette by increasing negative pressure, hence the inflow. The aspiration channels lead to a collection wells from which the accumulated liquid was retrieved with an automatic pipette. In Papers II, III, IV, V and VI, the pipette was used for exposure of lipid compartments to genetic materials (DNA or RNA oligonucleotides), to fluorescein or to the styrene maleic anhydride polymer.

5.5. Near infrared (NIR) laser heating system

In Papers III, IV and VI, a 1470 nm IR-B semiconductor diode laser, coupled into the experiment by means of an optical fiber, was used to locally increase the temperature of the lipid membrane assembly. Infrared light is a particular wavelength range of electromagnetic radiation, also known as thermal radiation. The near infrared band is categorized as IR-A (780 nm-1.4 μm) and IR-B (1.4 μm -3000 μm). Since absorption by the water in biological samples is efficient above 1450 nm²³⁸, we used the long wavelength infrared B (IR-B) on

the biological membranes in their aqueous environment, and limited the absorption locally by exposure through an optical fiber. To induce and rapidly grow the compartments on nanotubes in Paper III, we heated selected regions on the lipid nanotube networks. The fiber tip (**Figure 5.5**) was positioned approximately 50 μm above the surface, and it was kept within 100-150 μm in x-y direction from the area of interest. To determine the local temperature, a calibrated micro-thermocouple was manipulated into the radiation cone at the fiber tip. At high laser powers, the measured temperatures were biased by the self-absorption of the micro-thermocouple, and indicated values above the boiling point of water. Accordingly, taking into account the influence of strong local heat convection providing a continuous upwards stream of medium above the lipid bilayer on the surface, we moved the thermocouple above the radiation cone excluded the data points in the 0-40 μm range in z-direction. As a result, we estimated the local temperature at higher laser powers to reach values up to 70 and 90 $^{\circ}\text{C}$.

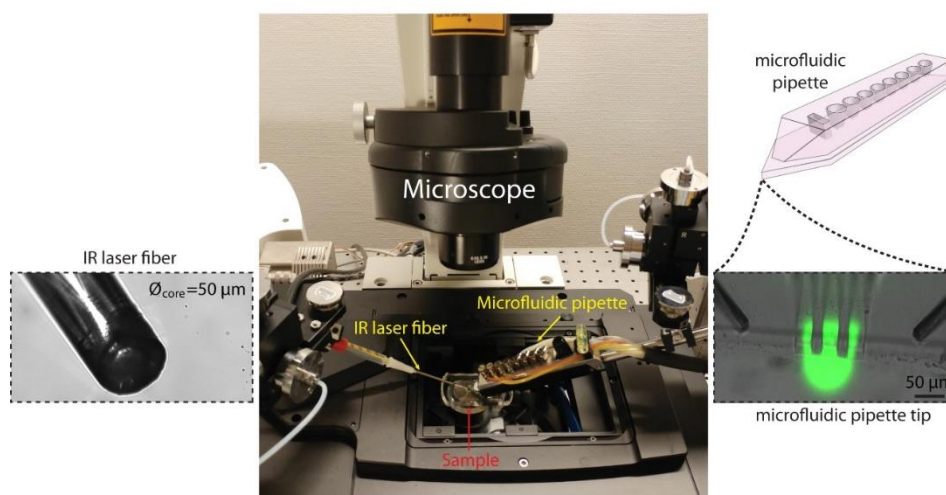


Figure 5.5. Microfluidic pipette and IR laser mounted onto our inverted confocal microscope. The left inset shows the tip of the flat-ended optical fiber, and the inset on the right shows the schematic drawing of the pipette along with a fluorescence micrograph of the hydrodynamically confined volume at its tip, used to superfuse the membrane regions of interest.

5.6. Genetic materials

In Papers III, V and VI, fluorophore conjugated RNA and/or DNA oligonucleotides of various lengths were used to visualize encapsulation and chemical reaction inside the model protocells. Vesicular compartments were either matured in a buffer containing the oligonucleotides or later selectively exposed to them via the microfluidic pipette. Our experiments do not require sterile conditions. However, when preparing and handling

oligonucleotides, sterile equipment and nuclease free water were used to prevent degradation of nucleic acids by nucleases in the environment.

In Paper VI we employed a non-enzymatic entropy driven DNA reaction²³⁹, summarized in **Figure 5.6**. One of the reactants is a double stranded DNA (dsDNA) which contains a 20 base pair duplex, and 6 nucleotides as overhanging domain “toehold”. The toehold domain of the dsDNA is short enough to bind to the other reactant, a short single stranded DNA (ssDNA) referred to as the invading strand. The binding initiates the strand displacement reaction. The DNA strand with the toehold domain dimerizes with the complementary invading strand. A fluorescently labeled but initially quenched short strand of the original duplex is released, and starts emitting. We grew the vesicular compartments in a buffer containing the quencher-fluorophore dimer. The excess dimers in solution were removed in several washing cycles and target ssDNA was exposed to the compartments using the microfluidic pipette. Fluorescence signal occurring as a result of this entropy-driven reaction was observed and monitored inside some of the vesicles.

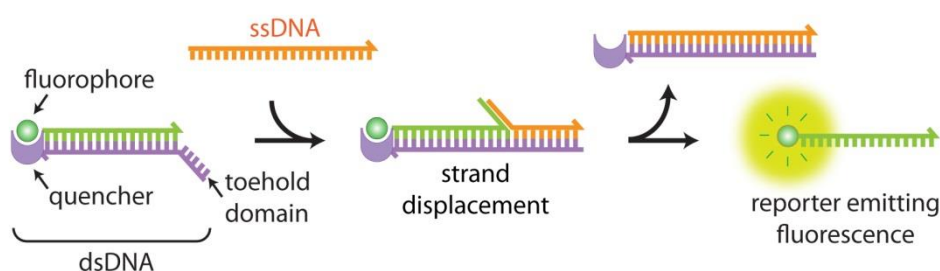


Figure 5.6. DNA strand displacement reaction monitored by the release of a quenched fluorescent marker during strand exchange.

In Paper III, we showed the uptake of fluorescently-labeled RNA oligonucleotides, and compared the encapsulation efficiencies of the relatively small fluorescein molecule, and the larger RNA. In Paper V, we showed that the model protocells made from membranes containing phospholipids and fatty acids, can encapsulate RNA rapidly and in higher efficiency.

5.7. Mathematical model and simulations

The use of mathematical models and computer simulations are needed to overcome limitations of the experimental system, for example to understand dynamic membrane behavior at the molecular- or mesoscale. One of the most commonly used methods in

numerical analysis is the finite element method (FEM). In this method, the first step is the discretization of a complex object into a small finite number of elements. Then these finite elements are connected through a virtual network, and equations defining each element are solved simultaneously. Combining the individual results leads to the characterization of the behavior of the whole structure.

In Paper I, we applied FEM simulations to determine the changes in membrane bending energy during the nucleation of model protocells. In Paper IV, FEM simulations were performed to estimate the encapsulation of fluorescein through transient pores in vesicles of varying size and pore size over time. In Paper III, simulations were performed to determine the mechanism of fusion between vesicular compartments.

6. Summary of the Main Findings in the Papers

Paper I. Nanotube-mediated Path to Protocell Formation

In Paper I, we reported on the self-transformation of phospholipid reservoirs upon contact with solid surfaces to unilamellar membrane compartments interconnected with nanotubes. We described, step-by-step, the topological changes that occurred following the contact of MLVs with the SiO₂ surface: (i) spreading as a double bilayer membrane, (ii) rupturing of the distal membrane, (iii) formation of nanotubes from parts of the distal membrane, and (iv) swelling of the nanotube fragments into vesicular compartments. Fluorescent intensity analysis of the micrographs revealed that the compartments were strictly unilamellar. The process is governed by the minimization of membrane bending energy, hence the surface-free energy. The transformation from a highly curved nanotube to a spherical giant vesicle was described by a mathematical model and finite element method simulations. We finally showed that the compartments were able to encapsulate and maintain small molecules present in the ambient aqueous environment, separated them from the network by means of a gentle hydrodynamic flow, and migrated them to remote locations. The findings in this paper serve as a foundation for the general hypothesis of this thesis.

Paper II. Styrene Maleic Acid Copolymer Induces Pores in Biomembranes

The interaction between styrene-maleic acid (SMA) copolymers and phospholipid bilayers was investigated in Paper II. Different concentrations of SMA copolymers were deposited on solid-supported bilayers of varying compositions, and the associated pore formation was followed with a laser-scanning confocal microscope. The results showed formation of visible defects/pores in the membrane upon interaction with the polymer. The observations were complemented by surface acoustic resonance sensor measurements, which quantified porosity changes in the deposited lipid film upon exposure to polymer. We also followed surface adhered giant unilamellar compartments encapsulating fluorescein, as described in Paper I, using them as indicator for polymer-induced pore formation in free standing vesicular bilayers. While 0.1% (w/v) polymer did not cause any visible poration in the membrane or effect the integrity of the compartments, 0.5% polymer induced pore formation indicated by the leakage of fluorescein from the compartments without loss of volume and shape. Further exposure to 1% polymer solution resulted in disintegration and collapse of the vesicles. Solubilization of lipid bilayers by increasing amounts of SMA polymer was also validated with turbidity measurements and transmission electron microscopy of small unilamellar vesicle suspensions exposed to the SMA polymer.

Paper III. Rapid Growth and Fusion of Protocells in Surface-adhered Membrane Networks

In Paper III, the impact of mild temperature gradients on the vesicle-nanotube networks described in Paper I was investigated. The temperature gradients created using an IR-source locally cause instant nucleation and growth of vesicular compartments, and even fusion of adjacent compartments. We showed that slight increase in temperature from 20 to ~40 °C leads to instant nucleation of small vesicles from lipid nanotube networks. At ~70 °C, rapid growth of small vesicles to giant sizes was observed. We reported the formation of model protocells rapidly within seconds, and their maturation to cell-like size over a period of only a few minutes (vs. minutes/hours in Paper I). Similarly, the newly nucleated compartments co-localized at the Y- and V-junctions where two or three nanotubes intersect. By increasing the temperature to ~90 °C, we induced fusion of adjacent compartments residing on the same or different nanotubes. Finite element simulations revealed that the fusion of the compartments on the same nanotube is energetically more favorable and leads to complete fusion. After merging of the compartments located on parallel nanotubes, a stable pore is formed and full fusion is prevented. Lastly, we showed the spontaneous encapsulation of RNA oligomers into protocells and the redistribution of the internalized RNA among compartments once fusion is induced by exposure to heat.

Paper IV. Subcompartmentalization and Pseudo-division of Model Protocells

In Paper IV, the subcompartmentalization of dome-shaped, surface adhered giant lipid compartments was shown, mediated by the changes in surface-membrane adhesion. Upon depletion of Ca^{2+} , which initially enables the adhesion between the surface and the compartment, a fraction of the membrane on the solid support is released, forming small invaginations with high membrane curvature. Due to the high tension in these curved membrane areas, lipid material from distal membrane with relatively low tension migrate to the surface region via Marangoni flow. As a result, spherical, bubble-like compartments emerge over time on the basal membrane. Increase in temperature, using the same method employed in Paper III, accelerated the formation of the subcompartments and induced their fusion. We showed the uptake of small dye molecules by the primary volume of the protocell as well as the encapsulation and segregation of such molecules by the subcompartments. Lastly, we reported on a primitive division mechanism where the original protocell disintegrates and each subcompartment becomes a daughter cell.

Paper V. Mixed fatty acid-phospholipid protocell networks

Surface-assisted protocell formation from fatty acid containing reservoirs was shown in Paper V, occurring in the same fashion as reported on phospholipid assemblies in Paper I. Upon contact of the reservoirs comprised of fatty acids and phospholipids with a SiO₂ surface, protocellular compartments form autonomously, proceeding via the same topological changes that were described in Paper I for the phospholipids. Mixtures of phospholipids and fatty acids, e.g. myristoleic acid or oleic acid, lead in some cases to colony-like growth of clustered protocells. We further showed that the protocells were able to encapsulate and maintain ambient compounds such as fluorescein and RNA oligomers. We monitored the uptake of each protocell and calculated the permeability coefficients. The results indicated slightly higher permeability to fluorescein and RNA with increased fatty acid fractions in the membrane.

Paper VI. Early Earth and Martian meteorite surfaces enable protocell colony formation

Autonomous formation and growth of protocells on 20 Earth surfaces and a Martian meteorite were reported in Paper VI. We added multilamellar lipid reservoirs to an observation chamber containing a thin section of an innate solid surface submerged in an aqueous solution and observed the changes with confocal microscopy. We observed the spreading of the reservoirs, rupturing and all the other following transformations reported in Paper I, leading to the lipid nanotube-protocell networks. The formation of dense protocell colonies was observed predominantly at the surface irregularities such as cracks, fissures and grain boundaries. SEM-EDX analysis of the surface regions showing protocell amplification in rocks revealed protocell formation consistently, but not exclusively, at the interface of quartz-containing grains in rocks. Protocells stemming from the nanotubes as well as the foam-like protocell colonies were observed on the Martian meteorite. The latter transformed into multiple smaller colonies over time. Finally, we showed that the protocells were able to encapsulate functional RNA and DNA fragments present in the ambient environment, and accommodated a non-enzymatic, entropy driven DNA strand replacement reaction.

7. Conclusions and Future Outlook

The work in this thesis suggests a pathway for protocell formation and development alternative to the 'bulk hypothesis', in which the amphiphiles self-assemble to spherical compartments freely suspending an aqueous solution. In the newly proposed pathway, the solid surfaces are a key component.

The interactions of surfaces with lipid reservoirs have been characterized in an interdisciplinary effort, combining biophysical chemistry, nanotechnology and mathematical modeling. The results show a wide spectrum of consistent behavior, such as the formation of protocell nanotube networks, subcompartmentalization, and protocellular colony formation. Only a few assumptions are required to translate these observations to the early Earth: sufficient amphiphilic material, high energy surfaces and a suitable aqueous environment needed to be present.

One of the novel aspects of this work was the characterization of lipid assembly transformations resulting in the formation of model protocells that are physically linked to each other via nanotubes. Nanotubular highways between current biological cells, which act as transporters of signaling molecules, even organelles, were discovered as recently as in 2006. Structurally similar toroidal (hollow) nanotubes could have allowed the passage of molecules and chemical communication between the first protocells, while still confining the materials inside an intact membrane barrier. Therefore, a next step is to show molecular diffusion and tension-driven transport of prebiotically relevant compounds within such networks. This can potentially help us understand how primitive compartments could have communicated and shared contents in order to replicate and advance in development.

In the future, several consecutive cycles of protocell formation and their separation from the network, can possibly be established by fusing reservoirs with protocells freshly isolated from the network. Using more diverse mixtures of different amphiphiles, as well as different surface materials will expand the understanding of suitable inorganic-organic interfaces and can provide further insights into the conditions for protocell development on the early Earth.

I also showed the spontaneous encapsulation of small water-soluble molecules as well as RNA and DNA by the surface-adhering protocell model. One of the encapsulation experiments involved a DNA strand replacement reaction occurring inside the compartments. Currently there are many studies on artificial cells that aim at genetic replication, elongation of genetic polymers and protein expression. Coupling cell free expression and prebiotic chemistry with surface-assisted protocellular compartments would be one of the future perspectives of this research.

Proto-cell colony formation and division on meteorite NWA 7533 showed that it is possible for amphiphilic reservoirs to transform to protocellular structures on extraterrestrial minerals. Our results align timely with the exciting developments of the Perseverance rover recently landing on Mars, looking for evidence of biosignatures, past microbial life and water. Until 2031, when samples from different parts of the red planet are scheduled to be brought to Earth, the Martian meteorites that we currently have, along with other existing extraterrestrial samples, will be further investigated for new aspects of surface-mediated primitive cell formation outside of our planet.

Finally, although not the focus of this thesis, surface-lipid interactions are also relevant for biomedical, industrial and technological processes, for example for the development of biosensors, biocompatible implants, and drug delivery devices. In addition to the surface-lipid interactions, protein-lipid interactions can be studied using the giant unilamellar membrane compartments consistently produced in the presented system. They allow, for example, direct observation of membrane proteins on free-standing but stable fluid membranes, which can be easily maintained and visualized under a microscope.

References

1. Westall, F.; Brack, A., The Importance of Water for Life. *Space Science Reviews* **2018**, *214* (2), 50.
2. Gánti, T. A., *The principles of life*. Oxford :, 2003.
3. Caetano-Anollés, G.; Seufferheld, M. J., The Coevolutionary Roots of Biochemistry and Cellular Organization Challenge the RNA World Paradigm. *Microbial Physiology* **2013**, *23* (1-2), 152-177.
4. Köksal, E. S.; Liese, S.; Kantarci, I.; Olsson, R.; Carlson, A.; Gözen, I., Nanotube-Mediated Path to Protocell Formation. *ACS Nano* **2019**, *13* (6), 6867-6878.
5. Köksal, E. S.; Liese, S.; Xue, L.; Ryskulov, R.; Viitala, L.; Carlson, A.; Gözen, I., Rapid Growth and Fusion of Protocells in Surface-Adhered Membrane Networks. *Small* **2020**, *16* (38), 2002529.
6. Orwick Rydmark, M.; Christensen, M. K.; Köksal, E. S.; Kantarci, I.; Kustanovich, K.; Yantchev, V.; Jesorka, A.; Gözen, I., Styrene maleic acid copolymer induces pores in biomembranes. *Soft Matter* **2019**, *15* (39), 7934-7944.
7. Spustova, K.; Köksal, E. S.; Ainla, A.; Gözen, I., Subcompartmentalization and Pseudo-Division of Model Protocells. *Small n/a* (n/a), 2005320.
8. Haldane, J. B., Rationalist Annual. *The origin of Life* **1929**, 148.
9. Oparin, A. I., *The Origin of Life*. Dover Publications: 1965.
10. Miller, S. L., A production of amino acids under possible primitive earth conditions. *Science* **1953**, *117* (3046), 528-529.
11. Kitadai, N.; Maruyama, S., Origins of building blocks of life: A review. *Geoscience Frontiers* **2018**, *9* (4), 1117-1153.
12. Chyba, C.; Sagan, C., Endogenous production, exogenous delivery and impact-shock synthesis of organic molecules: an inventory for the origins of life. *Nature* **1992**, *355* (6356), 125-132.
13. Sahai, N.; Kaddour, H.; Dalai, P., The Transition from Geochemistry to Biogeochemistry. *Elements* **2016**, *12*, 389-394.
14. Cleaves, H. J.; Chalmers, J. H.; Lazcano, A.; Miller, S. L.; Bada, J. L., A Reassessment of Prebiotic Organic Synthesis in Neutral Planetary Atmospheres. *Origins of Life and Evolution of Biospheres* **2008**, *38* (2), 105-115.
15. Rushdi, A. I.; Simoneit, B. R. T., Lipid Formation by Aqueous Fischer-Tropsch-Type Synthesis over a Temperature Range of 100 to 400 °C. *Origins of life and evolution of the biosphere* **2001**, *31* (1), 103-118.
16. McCollom, T. M.; Ritter, G.; Simoneit, B. R., Lipid synthesis under hydrothermal conditions by Fischer-Tropsch-type reactions. *Orig Life Evol Biosph* **1999**, *29* (2), 153-66.
17. Hargreaves, W. R.; Mulvihill, S. J.; Deamer, D. W., Synthesis of phospholipids and membranes in prebiotic conditions. *Nature* **1977**, *266* (5597), 78-80.
18. Rao, M.; Eichberg, J.; Oró, J., Synthesis of phosphatidylethanolamine under possible primitive earth conditions. *J Mol Evol* **1987**, *25* (1), 1-6.
19. Rao, M.; Eichberg, J.; Oró, J., Synthesis of phosphatidylcholine under possible primitive Earth conditions. *Journal of Molecular Evolution* **1982**, *18* (3), 196-202.

20. Patel, B. H.; Percivalle, C.; Ritson, D. J.; Duffy, C. D.; Sutherland, J. D., Common origins of RNA, protein and lipid precursors in a cyanosulfidic protometabolism. *Nature Chemistry* **2015**, 7 (4), 301-307.
21. Blackmond, D. G., The Origin of Biological Homochirality. *Cold Spring Harbor perspectives in biology* **2019**, 11 (3), a032540.
22. Budin, I.; Szostak, J. W., Expanding Roles for Diverse Physical Phenomena During the Origin of Life. *Annual Review of Biophysics* **2010**, 39 (1), 245-263.
23. Frank, F. C., On spontaneous asymmetric synthesis. *Biochimica et Biophysica Acta* **1953**, 11, 459-463.
24. Soai, K.; Shibata, T.; Morioka, H.; Choji, K., Asymmetric autocatalysis and amplification of enantiomeric excess of a chiral molecule. *Nature* **1995**, 378 (6559), 767-768.
25. Dalai, P.; Kaddour, H.; Sahai, N., Incubating Life: Prebiotic Sources of Organics for the Origin of Life. *Elements* **2016**, 12 (6), 401-406.
26. Sephton, M. A., Organic compounds in carbonaceous meteorites. *Nat Prod Rep* **2002**, 19 (3), 292-311.
27. Deamer, D. W.; Pashley, R. M., Amphiphilic components of the Murchison carbonaceous chondrite: surface properties and membrane formation. *Orig Life Evol Biosph* **1989**, 19 (1), 21-38.
28. Rich, A.; Kasha, M.; Pullman, B., Horizons in biochemistry. Eds. M. Kasha and B. Pullman, Academic Press, New York **1962**, 103.
29. Gilbert, W., Origin of life: The RNA world. *Nature* **1986**, 319 (6055), 618-618.
30. Johnston, W. K.; Unrau, P. J.; Lawrence, M. S.; Glasner, M. E.; Bartel, D. P., RNA-Catalyzed RNA Polymerization: Accurate and General RNA-Templated Primer Extension. *Science* **2001**, 292 (5520), 1319.
31. Szostak, J. W.; Bartel, D. P.; Luisi, P. L., Synthesizing life. *Nature* **2001**, 409 (6818), 387-390.
32. Leslie E, O., Prebiotic Chemistry and the Origin of the RNA World. *Critical Reviews in Biochemistry and Molecular Biology* **2004**, 39 (2), 99-123.
33. Becker, S.; Feldmann, J.; Wiedemann, S.; Okamura, H.; Schneider, C.; Iwan, K.; Crisp, A.; Rossa, M.; Amatov, T.; Carell, T., Unified prebiotically plausible synthesis of pyrimidine and purine RNA ribonucleotides. *Science* **2019**, 366 (6461), 76.
34. Kaiser, R. I.; Maity, S.; Jones, B. M., Synthesis of Prebiotic Glycerol in Interstellar Ices. *Angewandte Chemie International Edition* **2015**, 54 (1), 195-200.
35. Kofoed, J.; Reymond, J.-L.; Darbre, T., Prebiotic carbohydrate synthesis: zinc-proline catalyzes direct aqueous aldol reactions of α -hydroxy aldehydes and ketones. *Organic & Biomolecular Chemistry* **2005**, 3 (10), 1850-1855.
36. Powner, M. W.; Gerland, B.; Sutherland, J. D., Synthesis of activated pyrimidine ribonucleotides in prebiotically plausible conditions. *Nature* **2009**, 459 (7244), 239-242.
37. Segré, D.; Ben-Eli, D.; Deamer, D. W.; Lancet, D., The Lipid World. *Origins of life and evolution of the biosphere* **2001**, 31 (1), 119-145.
38. Walde, P., Surfactant Assemblies and Their Various Possible Roles for the Origin of Life. *Origins of life and evolution of the biosphere : the journal of the International Society for the Study of the Origin of Life* **2006**, 36, 109-50.
39. Grochmal, A.; Prout, L.; Makin-Taylor, R.; Prohens, R.; Tomas, S., Modulation of Reactivity in the Cavity of Liposomes Promotes the Formation of Peptide Bonds. *Journal of the American Chemical Society* **2015**, 137 (38), 12269-12275.

40. Luisi, P. L.; Varela, F. J., Self-replicating micelles — A chemical version of a minimal autopoietic system. *Origins of life and evolution of the biosphere* **1989**, *19* (6), 633-643.
41. Bachmann, P. A.; Walde, P.; Luisi, P. L.; Lang, J., Self-replicating reverse micelles and chemical autopoiesis. *Journal of the American Chemical Society* **1990**, *112* (22), 8200-8201.
42. Bachmann, P. A.; Luisi, P. L.; Lang, J., Autocatalytic self-replicating micelles as models for prebiotic structures. *Nature* **1992**, *357* (6373), 57-59.
43. Budin, I.; Szostak, J. W., Physical effects underlying the transition from primitive to modern cell membranes. *Proceedings of the National Academy of Sciences* **2011**, *108* (13), 5249.
44. Dalai, P.; Ustriyana, P.; Sahai, N., Aqueous magnesium as an environmental selection pressure in the evolution of phospholipid membranes on early earth. *Geochimica et Cosmochimica Acta* **2018**, *223*, 216-228.
45. Conde-Frieboes, K.; Blöchliger, E., Synthesis of lipids on the micelle/water interface using inorganic phosphate and an alkene oxide. *Bio Systems* **2001**, *61*, 109-14.
46. Chen, I. A.; Szostak, J. W., A kinetic study of the growth of fatty acid vesicles. *Biophysical journal* **2004**, *87* (2), 988-998.
47. Rasi, S.; Mavelli, F.; Luisi, P. L., Matrix Effect in Oleate Micelles-Vesicles Transformation. *Origins of life and evolution of the biosphere* **2004**, *34* (1), 215-224.
48. Rogerson, M. L.; Robinson, B. H.; Bucak, S.; Walde, P., Kinetic studies of the interaction of fatty acids with phosphatidylcholine vesicles (liposomes). *Colloids Surf B Biointerfaces* **2006**, *48* (1), 24-34.
49. Markvoort, A. J.; Pflieger, N.; Staffhorst, R.; Hilbers, P. A. J.; van Santen, R. A.; Killian, J. A.; de Kruijff, B., Self-reproduction of fatty acid vesicles: a combined experimental and simulation study. *Biophysical journal* **2010**, *99* (5), 1520-1528.
50. Hanczyc, M. M.; Fujikawa, S. M.; Szostak, J. W., Experimental Models of Primitive Cellular Compartments: Encapsulation, Growth, and Division. *Science* **2003**, *302* (5645), 618.
51. Chen, I. A.; Roberts, R. W.; Szostak, J. W., The emergence of competition between model protocells. *Science* **2004**, *305* (5689), 1474-6.
52. Saha, R.; Verbanic, S.; Chen, I. A., Lipid vesicles chaperone an encapsulated RNA aptamer. *Nature Communications* **2018**, *9* (1), 2313.
53. Monnard, P.-A.; Deamer, D. W., Membrane Self-Assembly Processes: Steps Toward the First Cellular Life. In *The Minimal Cell: The Biophysics of Cell Compartment and the Origin of Cell Functionality*, Luisi, P. L.; Stanó, P., Eds. Springer Netherlands: Dordrecht, 2011; pp 123-151.
54. Monnard, P. A.; Walde, P., Current Ideas about Prebiological Compartmentalization. *Life (Basel)* **2015**, *5* (2), 1239-63.
55. Egel, R., Origins and emergent evolution of life: the colloid microsphere hypothesis revisited. *Orig Life Evol Biosph* **2014**, *44* (2), 87-110.
56. Deamer, D., The Role of Lipid Membranes in Life's Origin. *Life* **2017**, *7* (1).
57. Lai, Y.-C.; Chen, I. A., Protocells. *Current Biology* **2020**, *30* (10), R482-R485.
58. Zhu, T. F.; Szostak, J. W., Coupled Growth and Division of Model Protocell Membranes. *Journal of the American Chemical Society* **2009**, *131* (15), 5705-5713.

59. Simard, J. R.; Pillai, B. K.; Hamilton, J. A., Fatty Acid Flip-Flop in a Model Membrane Is Faster Than Desorption into the Aqueous Phase. *Biochemistry* **2008**, *47* (35), 9081-9089.
60. Bar-Ziv, R.; Moses, E., Instability and "Pearling" States Produced in Tubular Membranes by Competition of Curvature and Tension. *Physical Review Letters* **1994**, *73* (10), 1392-1395.
61. Jin, L.; Kamat, N. P.; Jena, S.; Szostak, J. W., Fatty Acid/Phospholipid Blended Membranes: A Potential Intermediate State in Protocellular Evolution. *Small* **2018**, *14* (15), 1704077.
62. Kanavarioti, A.; Bernasconi, C. F.; Doodokyan, D. L.; Alberas, D. J., Magnesium ion catalyzed phosphorus-nitrogen bond hydrolysis in imidazolide-activated nucleotides. Relevance to template-directed synthesis of polynucleotides. *Journal of the American Chemical Society* **1989**, *111* (18), 7247-7257.
63. Monnard, P.-A.; Apel, C. L.; Kanavarioti, A.; Deamer, D. W., Influence of Ionic Inorganic Solutes on Self-Assembly and Polymerization Processes Related to Early Forms of Life: Implications for a Prebiotic Aqueous Medium. *Astrobiology* **2002**, *2* (2), 139-152.
64. Dalai, P.; Sahai, N., Mineral–Lipid Interactions in the Origins of Life. *Trends in Biochemical Sciences* **2019**, *44* (4), 331-341.
65. Bernal, J. D., The Physical Basis of Life. *Proceedings of the Physical Society. Section B* **1949**, *62* (10), 597-618.
66. Ferris, J. P.; Ertem, G., Oligomerization of ribonucleotides on montmorillonite: reaction of the 5'-phosphorimidazolide of adenosine. *Science* **1992**, *257* (5075), 1387-9.
67. Ferris, J. P., Montmorillonite Catalysis of 30–50 Mer Oligonucleotides: Laboratory Demonstration of Potential Steps in the Origin of the RNA World. *Origins of life and evolution of the biosphere* **2002**, *32* (4), 311-332.
68. Huang, W.; Ferris, J. P., Synthesis of 35–40 mers of RNA oligomers from unblocked monomers. A simple approach to the RNA world. *Chemical Communications* **2003**, (12), 1458-1459.
69. Rode, B. M., Peptides and the origin of life¹. *Peptides* **1999**, *20* (6), 773-786.
70. Lambert, J.-F., Adsorption and Polymerization of Amino Acids on Mineral Surfaces: A Review. *Origins of Life and Evolution of Biospheres* **2008**, *38* (3), 211-242.
71. Erastova, V.; Degiacomi, M. T.; G. Fraser, D.; Greenwell, H. C., Mineral surface chemistry control for origin of prebiotic peptides. *Nature Communications* **2017**, *8* (1), 2033.
72. Hanczyc, M.; Mansy, S.; Szostak, J., Mineral Surface Directed Membrane Assembly. *Origins of life and evolution of the biosphere : the journal of the International Society for the Study of the Origin of Life* **2007**, *37*, 67-82.
73. Sahai, N.; Kaddour, H.; Dalai, P.; Wang, Z.; Bass, G.; Gao, M., Mineral Surface Chemistry and Nanoparticle-aggregation Control Membrane Self-Assembly. *Scientific Reports* **2017**, *7* (1), 43418.
74. Oleson, T. A.; Sahai, N., Interaction energies between oxide surfaces and multiple phosphatidylcholine bilayers from extended-DLVO theory. *J Colloid Interface Sci* **2010**, *352* (2), 316-26.
75. Oleson, T. A.; Sahai, N.; Pedersen, J. A., Electrostatic effects on deposition of multiple phospholipid bilayers at oxide surfaces. *Journal of Colloid and Interface Science* **2010**, *352* (2), 327-336.

76. Mojzsis, S.; Harrison, T.; Pidgeon, R., Oxygen-isotope evidence from ancient zircons for liquid water at the Earth's surface 4,300 Myr ago. *Nature* **2001**, *409*, 178-81.
77. Hassenkam, T.; Andersson, M. P.; Dalby, K. N.; Mackenzie, D. M. A.; Rosing, M. T., Elements of Eoarchean life trapped in mineral inclusions. *Nature* **2017**, *548* (7665), 78-81.
78. Djokic, T.; Van Kranendonk, M. J.; Campbell, K. A.; Walter, M. R.; Ward, C. R., Earliest signs of life on land preserved in ca. 3.5 Ga hot spring deposits. *Nature Communications* **2017**, *8* (1), 15263.
79. Martin, W.; Baross, J.; Kelley, D.; Russell, M. J., Hydrothermal vents and the origin of life. *Nature Reviews Microbiology* **2008**, *6* (11), 805-814.
80. Damer, B.; Deamer, D., Coupled Phases and Combinatorial Selection in Fluctuating Hydrothermal Pools: A Scenario to Guide Experimental Approaches to the Origin of Cellular Life. *Life* **2015**, *5* (1).
81. James Cleaves II, H.; Michalkova Scott, A.; Hill, F. C.; Leszczynski, J.; Sahai, N.; Hazen, R., Mineral-organic interfacial processes: potential roles in the origins of life. *Chemical Society Reviews* **2012**, *41* (16), 5502-5525.
82. Kompanichenko, V. N.; Poturay, V. A.; Karpov, G. A., Organic compounds in thermal water: The Mutnovskii area and the Uzon caldera. *Journal of Volcanology and Seismology* **2016**, *10* (5), 305-319.
83. Lahav, N.; White, D.; Chang, S., Peptide formation in the prebiotic era: thermal condensation of glycine in fluctuating clay environments. *Science* **1978**, *201* (4350), 67-9.
84. Topozini, L.; Dies, H.; Deamer, D. W.; Rheinstädter, M. C., Adenosine Monophosphate Forms Ordered Arrays in Multilamellar Lipid Matrices: Insights into Assembly of Nucleic Acid for Primitive Life. *PLOS ONE* **2013**, *8* (5), e62810.
85. Rajamani, S.; Vlassov, A.; Benner, S.; Coombs, A.; Olasagasti, F.; Deamer, D., Lipid-assisted Synthesis of RNA-like Polymers from Mononucleotides. *Origins of Life and Evolution of Biospheres* **2008**, *38* (1), 57-74.
86. DeGuzman, V.; Vercoutare, W.; Shenasa, H.; Deamer, D., Generation of oligonucleotides under hydrothermal conditions by non-enzymatic polymerization. *J Mol Evol* **2014**, *78* (5), 251-62.
87. Pearce, B. K. D.; Pudritz, R. E.; Semenov, D. A.; Henning, T. K., Origin of the RNA world: The fate of nucleobases in warm little ponds. *Proceedings of the National Academy of Sciences* **2017**, *114* (43), 11327.
88. Kelley, D. S.; Karson, J. A.; Blackman, D. K.; Früh-Green, G. L.; Butterfield, D. A.; Lilley, M. D.; Olson, E. J.; Schrenk, M. O.; Roe, K. K.; Lebon, G. T.; Rivizzigno, P.; the, A. T. S. P., An off-axis hydrothermal vent field near the Mid-Atlantic Ridge at 30° N. *Nature* **2001**, *412* (6843), 145-149.
89. Marteinson, V. T.; Kristjánsson, J. K.; Kristmannsdóttir, H.; Dahlkvist, M.; Sæmundsson, K.; Hannington, M.; Pétursdóttir, S. K.; Geptner, A.; Stoffers, P., Discovery and Description of Giant Submarine Smectite Cones on the Seafloor in Eyjafjörður, Northern Iceland, and a Novel Thermal Microbial Habitat. *Applied and Environmental Microbiology* **2001**, *67* (2), 827.
90. Kelley, D. S.; Karson, J. A.; Früh-Green, G. L.; Yoerger, D. R.; Shank, T. M.; Butterfield, D. A.; Hayes, J. M.; Schrenk, M. O.; Olson, E. J.; Proskurowski, G.; Jakuba, M.; Bradley, A.; Larson, B.; Ludwig, K.; Glickson, D.; Buckman, K.; Bradley, A. S.; Brazelton, W. J.; Roe, K.; Elend, M. J.; Delacour, A.; Bernasconi, S. M.; Lilley, M. D.;

- Baross, J. A.; Summons, R. E.; Sylva, S. P., A Serpentinite-Hosted Ecosystem: The Lost City Hydrothermal Field. *Science* **2005**, 307 (5714), 1428.
91. Stanulla, R.; Stanulla, C.; Bogason, E.; Pohl, T.; Merkel, B., Structural, geochemical, and mineralogical investigation of active hydrothermal fluid discharges at Strýtan hydrothermal chimney, Akureyri Bay, Eyjafjörður region, Iceland. *Geothermal Energy* **2017**, 5 (1), 8.
 92. Shock, E. L.; Schulte, M. D., Organic synthesis during fluid mixing in hydrothermal systems. *Journal of Geophysical Research: Planets* **1998**, 103 (E12), 28513-28527.
 93. Baaske, P.; Weinert, F. M.; Duhr, S.; Lemke, K. H.; Russell, M. J.; Braun, D., Extreme accumulation of nucleotides in simulated hydrothermal pore systems. *Proceedings of the National Academy of Sciences* **2007**, 104 (22), 9346.
 94. Budin, I.; Bruckner, R. J.; Szostak, J. W., Formation of protocell-like vesicles in a thermal diffusion column. *J Am Chem Soc* **2009**, 131 (28), 9628-9.
 95. Deamer, D. W.; Georgiou, C. D., Hydrothermal Conditions and the Origin of Cellular Life. *Astrobiology* **2015**, 15 (12), 1091-1095.
 96. Deamer, D.; Damer, B.; Kompanichenko, V., Hydrothermal Chemistry and the Origin of Cellular Life. *Astrobiology* **2019**, 19 (12), 1523-1537.
 97. Milshteyn, D.; Damer, B.; Havig, J.; Deamer, D., Amphiphilic Compounds Assemble into Membranous Vesicles in Hydrothermal Hot Spring Water but Not in Seawater. *Life* **2018**, 8 (2).
 98. Kamminga, H., Life from space — A history of panspermia. *Vistas in Astronomy* **1982**, 26, 67-86.
 99. Martins, Z., Organic molecules in meteorites. *IAU Focus Meeting* **2016**, 29B, 411.
 100. Nicholson, W. L., Ancient micronauts: interplanetary transport of microbes by cosmic impacts. *Trends in Microbiology* **2009**, 17 (6), 243-250.
 101. Oba, Y.; Takano, Y.; Naraoka, H.; Watanabe, N.; Kouchi, A., Nucleobase synthesis in interstellar ices. *Nature Communications* **2019**, 10 (1), 4413.
 102. Muñoz Caro, G. M.; Meierhenrich, U. J.; Schutte, W. A.; Barbier, B.; Arcones Segovia, A.; Rosenbauer, H.; Thiemann, W. H. P.; Brack, A.; Greenberg, J. M., Amino acids from ultraviolet irradiation of interstellar ice analogues. *Nature* **2002**, 416 (6879), 403-406.
 103. Bernstein, M. P.; Dworkin, J. P.; Sandford, S. A.; Cooper, G. W.; Allamandola, L. J., Racemic amino acids from the ultraviolet photolysis of interstellar ice analogues. *Nature* **2002**, 416 (6879), 401-403.
 104. de Marcellus, P.; Meinert, C.; Myrgorodska, I.; Nahon, L.; Buhse, T.; d'Hendecourt, L. L. S.; Meierhenrich, U. J., Aldehydes and sugars from evolved precometary ice analogs: Importance of ices in astrochemical and prebiotic evolution. *Proceedings of the National Academy of Sciences* **2015**, 112 (4), 965.
 105. Meinert, C.; Myrgorodska, I.; de Marcellus, P.; Buhse, T.; Nahon, L.; Hoffmann, S. V.; d'Hendecourt, L. L. S.; Meierhenrich, U. J., Ribose and related sugars from ultraviolet irradiation of interstellar ice analogs. *Science* **2016**, 352 (6282), 208.
 106. Nuevo, M.; Cooper, G.; Sandford, S. A., Deoxyribose and deoxysugar derivatives from photoprocessed astrophysical ice analogues and comparison to meteorites. *Nature Communications* **2018**, 9 (1), 5276.
 107. Kirschvink, J.; Weiss, B., Mars, Panspermia, and the Origin of life: Where did it all begin? *Palaeontol. Electron.* **2002**, 4.

108. Scorei, R., Is Boron a Prebiotic Element? A Mini-review of the Essentiality of Boron for the Appearance of Life on Earth. *Origins of Life and Evolution of Biospheres* **2012**, *42* (1), 3-17.
109. Ehlmann, B. L.; Mustard, J. F.; Murchie, S. L.; Poulet, F.; Bishop, J. L.; Brown, A. J.; Calvin, W. M.; Clark, R. N.; Marais, D. J. D.; Milliken, R. E.; Roach, L. H.; Roush, T. L.; Swayze, G. A.; Wray, J. J., Orbital Identification of Carbonate-Bearing Rocks on Mars. *Science* **2008**, *322* (5909), 1828.
110. Greaves, J. S.; Richards, A. M. S.; Bains, W.; Rimmer, P. B.; Sagawa, H.; Clements, D. L.; Seager, S.; Petkowski, J. J.; Sousa-Silva, C.; Ranjan, S.; Drabek-Maunder, E.; Fraser, H. J.; Cartwright, A.; Mueller-Wodarg, I.; Zhan, Z.; Friberg, P.; Coulson, I.; Lee, E. I.; Hoge, J., Phosphine gas in the cloud decks of Venus. *Nature Astronomy* **2020**.
111. Jane S. Greaves, A. M. S. R., William Bains, Paul B. Rimmer, David L. Clements, Sara Seager, Janusz J. Petkowski, Clara Sousa-Silva, Sukrit Ranjan, Helen J. Fraser, Re-analysis of Phosphine in Venus' Clouds. *arXiv* **2020**.
112. Chyba, C. F.; Phillips, C. B., Possible ecosystems and the search for life on Europa. *Proceedings of the National Academy of Sciences* **2001**, *98* (3), 801.
113. Anderson, J. D.; Schubert, G.; Jacobson, R. A.; Lau, E. L.; Moore, W. B.; Sjogren, W. L., Europa's Differentiated Internal Structure: Inferences from Four Galileo Encounters. *Science* **1998**, *281* (5385), 2019.
114. Ojakangas, G. W.; Stevenson, D. J., Thermal state of an ice shell on Europa. *Icarus* **1989**, *81* (2), 220-241.
115. McKay, C. P.; Porco, C. C.; Altheide, T.; Davis, W. L.; Kral, T. A., The Possible Origin and Persistence of Life on Enceladus and Detection of Biomarkers in the Plume. *Astrobiology* **2008**, *8* (5), 909-919.
116. Jõemetsa, S.; Spustova, K.; Kustanovich, K.; Ainla, A.; Schindler, S.; Eigler, S.; Lobovkina, T.; Lara-Avila, S.; Jesorka, A.; Gözen, I., Molecular Lipid Films on Microengineering Materials. *Langmuir* **2019**, *35* (32), 10286-10298.
117. Israelachvili, J. N., 17 - Adhesion and Wetting Phenomena. In *Intermolecular and Surface Forces (Third Edition)*, Israelachvili, J. N., Ed. Academic Press: San Diego, 2011; pp 415-467.
118. Vogler, E. A., Water and the acute biological response to surfaces. *Journal of Biomaterials Science, Polymer Edition* **1999**, *10* (10), 1015-1045.
119. Czolkos, I.; Jesorka, A.; Orwar, O., Molecular phospholipid films on solid supports. *Soft Matter* **2011**, *7* (10), 4562-4576.
120. Nychka, J. A.; Gentleman, M. M., Implications of wettability in biological materials science. *JOM* **2010**, *62* (7), 39-48.
121. Giovambattista, N.; Debenedetti, P. G.; Rosky, P. J., Enhanced surface hydrophobicity by coupling of surface polarity and topography. *Proceedings of the National Academy of Sciences* **2009**, *106* (36), 15181.
122. Spriano, S.; Sarath Chandra, V.; Cochis, A.; Uberti, F.; Rimondini, L.; Bertone, E.; Vitale, A.; Scolaro, C.; Ferrari, M.; Cirisano, F.; Gautier di Confiengo, G.; Ferraris, S., How do wettability, zeta potential and hydroxylation degree affect the biological response of biomaterials? *Materials Science and Engineering: C* **2017**, *74*, 542-555.
123. Bollen, C. M. L.; Papaioanno, W.; Van Eldere, J.; Schepers, E.; Quirynen, M.; Van Steenberghe, D., The influence of abutment surface roughness on plaque accumulation and peri-implant mucositis. *Clinical Oral Implants Research* **1996**, *7* (3), 201-211.

124. Gentleman, M. M.; Ruud, J. A., Role of Hydroxyls in Oxide Wettability. *Langmuir* **2010**, 26 (3), 1408-1411.
125. Gao, Z.-y.; Sun, W.; Hu, Y.-h.; Liu, X.-w., Anisotropic surface broken bond properties and wettability of calcite and fluorite crystals. *Transactions of Nonferrous Metals Society of China* **2012**, 22 (5), 1203-1208.
126. Hazen, R. M.; Sverjensky, D. A., Mineral surfaces, geochemical complexities, and the origins of life. *Cold Spring Harbor perspectives in biology* **2010**, 2 (5), a002162-a002162.
127. Gao, Z.; Fan, R.; Ralston, J.; Sun, W.; Hu, Y., Surface broken bonds: An efficient way to assess the surface behaviour of fluorite. *Minerals Engineering* **2019**, 130, 15-23.
128. Valdrè, G.; Moro, D.; Ulian, G., Mineral surface–organic matter interactions: basics and applications. *IOP Conference Series: Materials Science and Engineering* **2012**, 32, 012027.
129. Kaplan, W. D.; Chatain, D.; Wynblatt, P.; Carter, W. C., A review of wetting versus adsorption, complexions, and related phenomena: the rosetta stone of wetting. *Journal of Materials Science* **2013**, 48 (17), 5681-5717.
130. Wynblatt, P. In *Introduction to Interfaces and Diffusion*, Materials Issues for Generation IV Systems, Dordrecht, 2008//; Ghetta, V.; Gorse, D.; Mazière, D.; Pontikis, V., Eds. Springer Netherlands: Dordrecht, 2008; pp 393-424.
131. Gillams, R. J.; Jia, T. Z., Mineral Surface-Templated Self-Assembling Systems: Case Studies from Nanoscience and Surface Science towards Origins of Life Research. *Life* **2018**, 8 (2).
132. Brack, A., Chapter 10.4 - Clay Minerals and the Origin of Life. In *Developments in Clay Science*, Bergaya, F.; Lagaly, G., Eds. Elsevier: 2013; Vol. 5, pp 507-521.
133. Agee, C. B.; Wilson, N. V.; McCubbin, F. M.; Ziegler, K.; Polyak, V. J.; Sharp, Z. D.; Asmerom, Y.; Nunn, M. H.; Shaheen, R.; Thiemens, M. H.; Steele, A.; Fogel, M. L.; Bowden, R.; Glamoclija, M.; Zhang, Z.; Elardo, S. M., Unique Meteorite from Early Amazonian Mars: Water-Rich Basaltic Breccia Northwest Africa 7034. *Science* **2013**, 339 (6121), 780.
134. Humayun, M.; Nemchin, A.; Zanda, B.; Hewins, R. H.; Grange, M.; Kennedy, A.; Lorand, J. P.; Göpel, C.; Fieni, C.; Pont, S.; Deldicque, D., Origin and age of the earliest Martian crust from meteorite NWA 7533. *Nature* **2013**, 503 (7477), 513-516.
135. Santos, A. R.; Agee, C. B.; McCubbin, F. M.; Shearer, C. K.; Burger, P. V.; Tartèse, R.; Anand, M., Petrology of igneous clasts in Northwest Africa 7034: Implications for the petrologic diversity of the martian crust. *Geochimica et Cosmochimica Acta* **2015**, 157, 56-85.
136. Costa, M. M.; Jensen, N. K.; Bouvier, L. C.; Connelly, J. N.; Mikouchi, T.; Horstwood, M. S. A.; Suuronen, J.-P.; Moynier, F.; Deng, Z.; Agranier, A.; Martin, L. A. J.; Johnson, T. E.; Nemchin, A. A.; Bizzarro, M., The internal structure and geodynamics of Mars inferred from a 4.2-Gyr zircon record. *Proceedings of the National Academy of Sciences* **2020**, 117 (49), 30973.
137. Deng, Z.; Moynier, F.; Villeneuve, J.; Jensen, N. K.; Liu, D.; Cartigny, P.; Mikouchi, T.; Siebert, J.; Agranier, A.; Chaussidon, M.; Bizzarro, M., Early oxidation of the martian crust triggered by impacts. *Science Advances* **2020**, 6 (44), eabc4941.
138. Bibring, J.-P.; Langevin, Y.; Gendrin, A.; Gondet, B.; Poulet, F.; Berthé, M.; Soufflot, A.; Arvidson, R.; Mangold, N.; Mustard, J.; Drossart, P., Mars Surface Diversity as Revealed by the OMEGA/Mars Express Observations. *Science* **2005**, 307 (5715), 1576.

139. Mustard, J. F.; Poulet, F.; Gendrin, A.; Bibring, J. P.; Langevin, Y.; Gondet, B.; Mangold, N.; Bellucci, G.; Altieri, F., Olivine and Pyroxene Diversity in the Crust of Mars. *Science* **2005**, *307* (5715), 1594.
140. Bandfield, J. L., Global mineral distributions on Mars. *Journal of Geophysical Research: Planets* **2002**, *107* (E6), 9-1-9-20.
141. Israelachvili, J. N., 20 - Soft and Biological Structures. In *Intermolecular and Surface Forces (Third Edition)*, Israelachvili, J. N., Ed. Academic Press: San Diego, 2011; pp 535-576.
142. Schrum, J. P.; Zhu, T. F.; Szostak, J. W., The origins of cellular life. *Cold Spring Harbor perspectives in biology* **2010**, *2* (9), a002212-a002212.
143. Chen, I. A.; Walde, P., From Self-Assembled Vesicles to Protocells. *Cold Spring Harbor Perspectives in Biology* **2010**, *2* (7).
144. Kamp, F.; Zakim, D.; Zhang, F.; Noy, N.; Hamilton, J. A., Fatty Acid Flip-Flop in Phospholipid Bilayers Is Extremely Fast. *Biochemistry* **1995**, *34* (37), 11928-11937.
145. Sacerdote, M. G.; Szostak, J. W., Semipermeable lipid bilayers exhibit diastereoselectivity favoring ribose. *Proceedings of the National Academy of Sciences* **2005**, *102* (17), 6004.
146. Morigaki, K.; Walde, P., Fatty acid vesicles. *Current Opinion in Colloid & Interface Science* **2007**, *12* (2), 75-80.
147. Gebicki, J. M.; Hicks, M., Ufasomes are Stable Particles surrounded by Unsaturated Fatty Acid Membranes. *Nature* **1973**, *243* (5404), 232-234.
148. Hargreaves, W. R.; Deamer, D. W., Liposomes from ionic, single-chain amphiphiles. *Biochemistry* **1978**, *17* (18), 3759-3768.
149. Haines, T. H., Anionic lipid headgroups as a proton-conducting pathway along the surface of membranes: a hypothesis. *Proceedings of the National Academy of Sciences* **1983**, *80* (1), 160.
150. Namani, T.; Walde, P., From Decanoate Micelles to Decanoic Acid/Dodecylbenzenesulfonate Vesicles. *Langmuir* **2005**, *21* (14), 6210-6219.
151. Cistola, D. P.; Hamilton, J. A.; Jackson, D.; Small, D. M., Ionization and phase behavior of fatty acids in water: application of the Gibbs phase rule. *Biochemistry* **1988**, *27* (6), 1881-8.
152. Apel, C. L.; Deamer, D. W.; Mautner, M. N., Self-assembled vesicles of monocarboxylic acids and alcohols: conditions for stability and for the encapsulation of biopolymers. *Biochimica et Biophysica Acta (BBA) - Biomembranes* **2002**, *1559* (1), 1-9.
153. Jordan, S. F.; Ramm, H.; Zheludev, I. N.; Hartley, A. M.; Maréchal, A.; Lane, N., Promotion of protocell self-assembly from mixed amphiphiles at the origin of life. *Nature Ecology & Evolution* **2019**, *3* (12), 1705-1714.
154. Lonchin, S.; Luisi, P. L.; Walde, P.; Robinson, B. H., A Matrix Effect in Mixed Phospholipid/Fatty Acid Vesicle Formation. *The Journal of Physical Chemistry B* **1999**, *103* (49), 10910-10916.
155. Berclaz, N.; Blöchliger, E.; Müller, M.; Luisi, P. L., Matrix Effect of Vesicle Formation As Investigated by Cryotransmission Electron Microscopy. *The Journal of Physical Chemistry B* **2001**, *105* (5), 1065-1071.
156. Berclaz, N.; Müller, M.; Walde, P.; Luisi, P. L., Growth and Transformation of Vesicles Studied by Ferritin Labeling and Cryotransmission Electron Microscopy. *The Journal of Physical Chemistry B* **2001**, *105* (5), 1056-1064.

157. Peterlin, P.; Arrigler, V.; Kogej, K.; Svetina, S.; Walde, P., Growth and shape transformations of giant phospholipid vesicles upon interaction with an aqueous oleic acid suspension. *Chemistry and Physics of Lipids* **2009**, *159* (2), 67-76.
158. Salehi-Reyhani, A.; Ces, O.; Elani, Y., Artificial cell mimics as simplified models for the study of cell biology. *Experimental Biology and Medicine* **2017**, *242* (13), 1309-1317.
159. Sarkis, J.; Vié, V., Biomimetic Models to Investigate Membrane Biophysics Affecting Lipid-Protein Interaction. *Frontiers in bioengineering and biotechnology* **2020**, *8*, 270.
160. Torchilin, V. P., Recent advances with liposomes as pharmaceutical carriers. *Nature Reviews Drug Discovery* **2005**, *4* (2), 145-160.
161. Monnard, P. A.; Deamer, D. W., Nutrient uptake by protocells: a liposome model system. *Orig Life Evol Biosph* **2001**, *31* (1-2), 147-55.
162. Karatekin, E.; Sandre, O.; Guitouni, H.; Borghi, N.; Puech, P.-H.; Brochard-Wyart, F., Cascades of Transient Pores in Giant Vesicles: Line Tension and Transport. *Biophysical Journal* **2003**, *84* (3), 1734-1749.
163. Bangham, A. D.; Horne, R. W., Negative staining of phospholipids and their structural modification by surface-active agents as observed in the electron microscope. *Journal of Molecular Biology* **1964**, *8* (5), 660-IN10.
164. Schmitz, G.; Müller, G., Structure and function of lamellar bodies, lipid-protein complexes involved in storage and secretion of cellular lipids. *Journal of Lipid Research* **1991**, *32* (10), 1539-1570.
165. Haagsman, H. P.; Van Golde, L. M. G., Synthesis and Assembly of Lung Surfactant. *Annual Review of Physiology* **1991**, *53* (1), 441-464.
166. Stratton, C., The ultrastructure of multilamellar bodies and surfactant in the human lung. *Cell and Tissue Research* **2004**, *193*, 219-229.
167. Hariri, M.; Millane, G.; Guimond, M. P.; Guay, G.; Dennis, J. W.; Nabi, I. R., Biogenesis of multilamellar bodies via autophagy. *Molecular biology of the cell* **2000**, *11* (1), 255-268.
168. Weaver, T. E.; Na, C.-L.; Stahlman, M., Biogenesis of lamellar bodies, lysosome-related organelles involved in storage and secretion of pulmonary surfactant. *Seminars in Cell & Developmental Biology* **2002**, *13* (4), 263-270.
169. Patil, Y. P.; Jadhav, S., Novel methods for liposome preparation. *Chemistry and Physics of Lipids* **2014**, *177*, 8-18.
170. Camp, R. R.; Byun, J.; Jacob, R., Electron Microscopy Analysis of Multilamellar Vesicles Prepared from Synthetic Lipids: A Model System for Studying Membrane Structure in the Molecular Cell Biology Classroom and Laboratory. *Microscopy Today* **2004**, *12* (5), 40-45.
171. Gozen, I.; Dommersnes, P.; Orwar, O.; Jesorka, A., Evidence for membrane flow through pores in stacked phospholipid membranes. *Soft Matter* **2012**, *8* (23), 6220-6225.
172. Helfrich, W., Elastic properties of lipid bilayers: theory and possible experiments. *Z Naturforsch C* **1973**, *28* (11), 693-703.
173. Rawicz, W.; Olbrich, K. C.; McIntosh, T.; Needham, D.; Evans, E., Effect of chain length and unsaturation on elasticity of lipid bilayers. *Biophysical journal* **2000**, *79* (1), 328-339.
174. Hu, M.; Briguglio, J. J.; Deserno, M., Determining the Gaussian curvature modulus of lipid membranes in simulations. *Biophysical journal* **2012**, *102* (6), 1403-1410.

175. Antonietti, M.; Förster, S., Vesicles and Liposomes: A Self-Assembly Principle Beyond Lipids. *Advanced Materials* **2003**, *15* (16), 1323-1333.
176. Zhelev, D. V.; Needham, D., Tension-stabilized pores in giant vesicles: determination of pore size and pore line tension. *Biochimica et Biophysica Acta (BBA) - Biomembranes* **1993**, *1147* (1), 89-104.
177. Castellana, E. T.; Cremer, P. S., Solid supported lipid bilayers: From biophysical studies to sensor design. *Surface Science Reports* **2006**, *61* (10), 429-444.
178. Kasemo, B., Biological surface science. *Surface Science* **2002**, *500* (1), 656-677.
179. Li, H.; Zhao, T.; Sun, Z., Analytical techniques and methods for study of drug-lipid membrane interactions. *Reviews in Analytical Chemistry* **2018**, *37* (1).
180. Moraille, P.; Badia, A., Nanoscale Stripe Patterns in Phospholipid Bilayers Formed by the Langmuir–Blodgett Technique. *Langmuir* **2003**, *19* (19), 8041-8049.
181. Charitat, T.; Bellet-Amalric, E.; Fragneto, G.; Graner, F., Adsorbed and free lipid bilayers at the solid-liquid interface. *The European Physical Journal B - Condensed Matter and Complex Systems* **1999**, *8* (4), 583-593.
182. Reimhult, E.; Kasemo, B.; Höök, F. Rupture pathway of phosphatidylcholine liposomes on silicon dioxide *International journal of molecular sciences* [Online], 2009, p. 1683-1696. PubMed.
183. Raedler, J.; Strey, H.; Sackmann, E., Phenomenology and Kinetics of Lipid Bilayer Spreading on Hydrophilic Surfaces. *Langmuir* **1995**, *11* (11), 4539-4548.
184. Gözen, I.; högskola, C. t.; bioteknik, C. t. h. l. f. k.-o., *The Self-spreading Double Bilayer: Advances in Lipid Membrane Nanotechnology*. Chalmers University of Technology: 2013.
185. Lobovkina, T.; Gözen, I.; Erkan, Y.; Olofsson, J.; Weber, S. G.; Orwar, O., Protrusive growth and periodic contractile motion in surface-adhered vesicles induced by Ca²⁺-gradients. *Soft Matter* **2010**, *6* (2), 268-272.
186. Johnson, J. M.; Ha, T.; Chu, S.; Boxer, S. G., Early steps of supported bilayer formation probed by single vesicle fluorescence assays. *Biophys J* **2002**, *83* (6), 3371-9.
187. Czolkos, I.; Erkan, Y.; Dommersnes, P.; Jesorka, A.; Orwar, O., Controlled Formation and Mixing of Two-Dimensional Fluids. *Nano Letters* **2007**, *7* (7), 1980-1984.
188. Akashi, K.-i.; Miyata, H.; Itoh, H.; Kinoshita, K., Formation of Giant Liposomes Promoted by Divalent Cations: Critical Role of Electrostatic Repulsion. *Biophysical Journal* **1998**, *74* (6), 2973-2982.
189. Nissen, J.; Gritsch, S.; Wiegand, G.; Rädler, J. O., Wetting of phospholipid membranes on hydrophilic surfaces - Concepts towards self-healing membranes. *The European Physical Journal B - Condensed Matter and Complex Systems* **1999**, *10* (2), 335-344.
190. Tamm, L. K.; McConnell, H. M., Supported phospholipid bilayers. *Biophysical Journal* **1985**, *47* (1), 105-113.
191. Gözen, I.; Dommersnes, P.; Czolkos, I.; Jesorka, A.; Lobovkina, T.; Orwar, O., Fractal avalanche ruptures in biological membranes. *Nat Mater* **2010**, *9* (11), 908-12.
192. Gupta, A.; Gözen, I.; Taylor, M., A cellular automaton for modeling non-trivial biomembrane ruptures. *Soft Matter* **2019**, *15* (20), 4178-4186.
193. Taylor, M.; Gözen, I.; Patel, S.; Jesorka, A.; Bertoldi, K., Peridynamic Modeling of Ruptures in Biomembranes. *PLOS ONE* **2016**, *11* (11), e0165947.

194. Rossier, O.; Cuvelier, D.; Borghi, N.; Puech, P. H.; Derényi, I.; Buguin, A.; Nassoy, P.; Brochard-Wyart, F., Giant Vesicles under Flows: Extrusion and Retraction of Tubes. *Langmuir* **2003**, *19* (3), 575-584.
195. Kozlov, M. M.; Chernomordik, L. V., Membrane tension and membrane fusion. *Current opinion in structural biology* **2015**, *33*, 61-67.
196. Lizana, L.; Konkoli, Z., Diffusive transport in networks built of containers and tubes. *Physical Review E* **2005**, *72* (2), 026305.
197. Dommersnes, P. G.; Orwar, O.; Brochard-Wyart, F.; Joanny, J. F., Marangoni transport in lipid nanotubes. *Europhysics Letters (EPL)* **2005**, *70* (2), 271-277.
198. Sott, K.; Lobovkina, T.; Lizana, L.; Tokarz, M.; Bauer, B.; Konkoli, Z.; Orwar, O., Controlling Enzymatic Reactions by Geometry in a Biomimetic Nanoscale Network. *Nano Letters* **2006**, *6* (2), 209-214.
199. Rustom, A.; Saffrich, R.; Markovic, I.; Walther, P.; Gerdes, H.-H., Nanotubular Highways for Intercellular Organelle Transport. *Science* **2004**, *303* (5660), 1007.
200. Gözen, I.; Dommersnes, P., Biological lipid nanotubes and their potential role in evolution. *The European Physical Journal Special Topics* **2020**, *229* (17), 2843-2862.
201. Dagdug, L.; Berezhkovskii, A. M.; Shvartsman, S. Y.; Weiss, G. H., Equilibration in two chambers connected by a capillary. *The Journal of Chemical Physics* **2003**, *119* (23), 12473-12478.
202. Melcrová, A.; Pokorna, S.; Pullanchery, S.; Kohagen, M.; Jurkiewicz, P.; Hof, M.; Jungwirth, P.; Cremer, P. S.; Cwiklik, L., The complex nature of calcium cation interactions with phospholipid bilayers. *Scientific Reports* **2016**, *6* (1), 38035.
203. Stepanyants, N.; Zhang, H.; Lobovkina, T.; Dommersnes, P.; Jeffries, G. D. M.; Jesorka, A.; Orwar, O., Spontaneous shape transformation of free-floating lipid membrane nanotubes. *Soft Matter* **2013**, *9* (21), 5155-5159.
204. Bilal, T.; Gözen, I., Formation and dynamics of endoplasmic reticulum-like lipid nanotube networks. *Biomaterials Science* **2017**, *5* (7), 1256-1264.
205. Chaudhury, M. K.; Ohki, S., Correlation between membrane expansion and temperature-induced membrane fusion. *Biochimica et Biophysica Acta (BBA) - Biomembranes* **1981**, *642* (2), 365-374.
206. Suzuki, Y.; Nagai, K. H.; Zinchenko, A.; Hamada, T., Photoinduced Fusion of Lipid Bilayer Membranes. *Langmuir* **2017**, *33* (10), 2671-2676.
207. Büschl, R.; Ringsdorf, H.; Zimmermann, U., Electric field-induced fusion of large liposomes from natural and polymerizable lipids. *FEBS Letters* **1982**, *150* (1), 38-42.
208. Maezawa, S.; Yoshimura, T.; Hong, K.; Duzgunes, N.; Papahadjopoulos, D., Mechanism of protein-induced membrane fusion: fusion of phospholipid vesicles by clathrin associated with its membrane binding and conformational change. *Biochemistry* **1989**, *28* (3), 1422-1428.
209. Chan, Y.-H. M.; van Lengerich, B.; Boxer, S. G., Effects of linker sequences on vesicle fusion mediated by lipid-anchored DNA oligonucleotides. *Proceedings of the National Academy of Sciences* **2009**, *106* (4), 979.
210. Wilschut, J.; Papahadjopoulos, D., Ca²⁺-induced fusion of phospholipid vesicles monitored by mixing of aqueous contents. *Nature* **1979**, *281* (5733), 690-692.
211. Evans, E.; Needham, D., Physical properties of surfactant bilayer membranes: thermal transitions, elasticity, rigidity, cohesion and colloidal interactions. *The Journal of Physical Chemistry* **1987**, *91* (16), 4219-4228.

212. Leckband, D.; Israelachvili, J., Intermolecular Forces in Biology. *Quarterly reviews of biophysics* **2001**, *34*, 105-267.
213. Israelachvili, J. N., 21 - Interactions of Biological Membranes and Structures. In *Intermolecular and Surface Forces (Third Edition)*, Israelachvili, J. N., Ed. Academic Press: San Diego, 2011; pp 577-616.
214. Arnold, K., Chapter 19 - Cation-Induced Vesicle Fusion Modulated by Polymers and Proteins. In *Handbook of Biological Physics*, Lipowsky, R.; Sackmann, E., Eds. North-Holland: 1995; Vol. 1, pp 903-957.
215. Wick, R.; Walde, P.; Luisi, P. L., Light microscopic investigations of the autocatalytic self-reproduction of giant vesicles. *Journal of the American Chemical Society* **1995**, *117* (4), 1435-1436.
216. Gözen, İ., A Hypothesis for protocell division on the early Earth. *ACS Nano* **2019**, *13* (10), 10869-10871.
217. Deamer, D. W.; Barchfeld, G. L., Encapsulation of macromolecules by lipid vesicles under simulated prebiotic conditions. *Journal of Molecular Evolution* **1982**, *18* (3), 203-206.
218. Monnard, P.-A.; Oberholzer, T.; Luisi, P., Entrapment of nucleic acids in liposomes. *Biochimica et Biophysica Acta (BBA) - Biomembranes* **1997**, *1329* (1), 39-50.
219. Walde, P.; Wick, R.; Fresta, M.; Mangone, A.; Luisi, P. L., Autopoietic Self-Reproduction of Fatty Acid Vesicles. *Journal of the American Chemical Society* **1994**, *116* (26), 11649-11654.
220. Dobson, C. M.; Ellison, G. B.; Tuck, A. F.; Vaida, V., Atmospheric aerosols as prebiotic chemical reactors. *Proceedings of the National Academy of Sciences* **2000**, *97* (22), 11864.
221. Sandre, O.; Moreaux, L.; Brochard-Wyart, F., Dynamics of transient pores in stretched vesicles. *Proceedings of the National Academy of Sciences* **1999**, *96* (19), 10591.
222. Brochard-Wyart, F.; de Gennes, P. G.; Sandre, O., Transient pores in stretched vesicles: role of leak-out. *Physica A: Statistical Mechanics and its Applications* **2000**, *278* (1), 32-51.
223. Karlsson, M.; Nolkranz, K.; Davidson, M. J.; Strömberg, A.; Ryttsén, F.; Åkerman, B.; Orwar, O., Electroinjection of Colloid Particles and Biopolymers into Single Unilamellar Liposomes and Cells for Bioanalytical Applications. *Analytical Chemistry* **2000**, *72* (23), 5857-5862.
224. Jesorka, A.; Stepanyants, N.; Zhang, H.; Ortmen, B.; Hakonen, B.; Orwar, O., Generation of phospholipid vesicle-nanotube networks and transport of molecules therein. *Nature Protocols* **2011**, *6* (6), 791-805.
225. Walde, P.; Trishool, N.; Kenichi, M.; Helmut, H., Formation and Properties of Fatty Acid Vesicles (Liposomes). 2006; Vol. 1, pp 1-19.
226. Hope, M. J.; Bally, M. B.; Webb, G.; Cullis, P. R., Production of large unilamellar vesicles by a rapid extrusion procedure. Characterization of size distribution, trapped volume and ability to maintain a membrane potential. *Biochimica et Biophysica Acta (BBA) - Biomembranes* **1985**, *812* (1), 55-65.
227. Martín-Palma, R. J.; Lakhtakia, A., Chapter 15 - Vapor-Deposition Techniques. In *Engineered Biomimicry*, Lakhtakia, A.; Martín-Palma, R. J., Eds. Elsevier: Boston, 2013; pp 383-398.

228. Leskelä, M.; Niinistö, J.; Ritala, M., 4.05 - Atomic Layer Deposition. In *Comprehensive Materials Processing*, Hashmi, S.; Batalha, G. F.; Van Tyne, C. J.; Yilbas, B., Eds. Elsevier: Oxford, 2014; pp 101-123.
229. Podraza, N. J.; Jellison, G. E., Ellipsometry☆. In *Encyclopedia of Spectroscopy and Spectrometry (Third Edition)*, Lindon, J. C.; Tranter, G. E.; Koppenaal, D. W., Eds. Academic Press: Oxford, 2017; pp 482-489.
230. Dukes, C.; Baragiola, R., Compact plasma source for removal of hydrocarbons for surface analysis. *Surface and Interface Analysis* **2009**, *42*, 40-44.
231. Lavrentovich, O. D., Confocal Fluorescence Microscopy. In *Characterization of Materials*, Kaufmann, E. N., Ed. 2012; pp 1-15.
232. Nadeau, J. L.; Davidson, M. W., Optical Microscopy. In *Characterization of Materials*, Kaufmann, E. N., Ed. 2012; pp 1-22.
233. Leonard, D. N.; Chandler, G. W.; Seraphin, S., Scanning Electron Microscopy. In *Characterization of Materials*, Kaufmann, E. N., Ed. 2012; pp 1-16.
234. Thiel, B., Variable Pressure Scanning Electron Microscopy. In *Springer Handbook of Microscopy*, Hawkes, P. W.; Spence, J. C. H., Eds. Springer International Publishing: Cham, 2019; pp 319-344.
235. Newbury, D. E., Energy Dispersive Spectrometry. In *Characterization of Materials*, pp 1-26.
236. Whitesides, G. M., The origins and the future of microfluidics. *Nature* **2006**, *442* (7101), 368-373.
237. Ainla, A.; Jeffries, G. D. M.; Brune, R.; Orwar, O.; Jesorka, A., A multifunctional pipette. *Lab on a Chip* **2012**, *12* (7), 1255-1261.
238. Wilson, R. H.; Nadeau, K. P.; Jaworski, F. B.; Tromberg, B. J.; Durkin, A. J., Review of short-wave infrared spectroscopy and imaging methods for biological tissue characterization. *Journal of biomedical optics* **2015**, *20* (3), 030901.
239. Zhang, D. Y.; Turberfield, A. J.; Yurke, B.; Winfree, E., Engineering Entropy-Driven Reactions and Networks Catalyzed by DNA. *Science* **2007**, *318* (5853), 1121-1125.

Appendix

Paper I

Paper II



Styrene maleic acid copolymer induces pores in biomembranes

Marcella Orwick Rydmark,^a Mikkel Killingmoe Christensen,^b Elif Senem Köksal,^b Ilayda Kantarci,^b Kiryl Kustanovich,^c Ventsislav Yantchev,^c Aldo Jesorka^{id}^c and Irep Gözen^{id}*^{bcd}

Cite this: *Soft Matter*, 2019, 15, 7934

Received 11th July 2019,
Accepted 3rd September 2019

DOI: 10.1039/c9sm01407a

rsc.li/soft-matter-journal

We investigated the interactions between styrene–maleic acid (SMA) copolymers and phospholipid bilayers, using confocal microscopy and surface acoustic wave resonance (SAR) sensing. For the first time we experimentally observed and followed pore formation by SMA copolymers in intact supported bilayers and unilamellar vesicles, showing that fluorescein, a water-soluble organic compound with a mean diameter of 6.9 Å, can traverse the membrane. Our findings are in agreement with recent theoretical predictions, which suggested that SMA copolymers may insert along the plane of the bilayer to form stable toroidal pores.

Tonge *et al.* showed in 2001 that styrene maleic acid (SMA) copolymers consisting of hydrophobic styrene and hydrophilic maleic acid monomer units have the ability to solubilize lipids without the necessity for detergents, and in 2006 patented formulations that efficiently transformed lipid bilayers into stable nano-sized bilayer disks at neutral pH.^{1,2} Subsequently, SMA copolymers were utilized for detergent-free extraction of proteins directly from native cell bilayers into stable bilayer disks, commonly referred to as ‘native nanodiscs’.^{3,4} Since then, interest in SMA copolymers has increased, and they have been successfully employed in a variety of functional, biophysical, and structural studies with membrane proteins in their native, or native-like lipidic environment.^{5–8} The elucidation of the nature of the interaction of the SMA copolymer with the bilayers benefits membrane protein isolation and investigation. The SMA copolymer-assisted, detergent-free isolation of membrane proteins preserves native interactions of membrane proteins with lipid species and other proteins, and provides insights into protein structure and function. In this capacity, SMA copolymers are particularly versatile compounds, which have already made a significant contribution to membrane protein research.

To date, most studies examining the physicochemical aspects of lipid–SMA copolymer interactions have focused on the fully formed bilayer discs, where information related to the ordering of lipid acyl chains, the orientation of the styrene

group with respect to the bilayer normal, and the approximate width of polymer that encircles the lipid bilayer was obtained.^{9,10} Several works have also reported on how lipid physicochemical properties (lipid acyl chain length, dynamics, and headgroup type) affect disk formation.¹¹ Still, the formation mechanism of the discs is not known, though possible sequences of steps have been predicted under consideration of initial SMA copolymer–lipid headgroup interactions, intercalation into, and saturation of the membrane, as well as solubilization and formation of discs.¹² Very recently, molecular dynamics simulations predicted that SMA copolymers may induce water-filled pores in membranes prior to their solubilization into lipid particles.¹³ These pores are nanometer-sized and should allow passage of small water-soluble molecules.

We devised a series of experiments to verify the predictions of the theoretical study, and investigated lipid–SMA copolymer interactions on solid-supported planar lipid bilayer patches, and surface-adhered giant unilamellar liposomes. To be able to characterize the interactions at the mesoscale, we applied SMA–copolymer to the supported bilayers and the vesicles in a controlled manner, using an open-space microfluidic device, and observed the resulting transformations under a confocal microscope. We further characterized the interaction of SMA with the supported bilayers by means of a surface acoustic wave resonance (SAR) sensor device, which responds to mass deposition/film formation and accompanied viscosity changes on a surface. These observations pointed to alterations in supported membrane morphology including swelling and pore formation upon exposure to the polymer. In experiments involving surface-adhered giant vesicles with fluorescein encapsulated in the interior volume we directly observed loss of internal contents upon exposure to SMA copolymer solution, while the volume and shape

^a Department of Biosciences, University of Oslo, 0316 Oslo, Norway

^b Centre for Molecular Medicine Norway, Faculty of Medicine, University of Oslo, 0318 Oslo, Norway. E-mail: irep@uio.no

^c Department of Chemistry and Chemical Engineering, Chalmers University of Technology, 412 96 Göteborg, Sweden

^d Faculty of Mathematics and Natural Sciences, University of Oslo, 0315 Oslo, Norway



of the spherical vesicle were maintained, indicating that poration precedes membrane solubilization.

Materials and methods

SUV formation and polymer preparation

All lipids were purchased from Avanti Polar Lipids (Alabama, USA), and in all cases, preparations were formed freshly to avoid vesicle fusion and aggregation. Table 1 summarizes the different lipid species used in the experiments with the corresponding polymer concentrations tested on each species. Briefly, lipids dissolved in chloroform (10 mg ml^{-1}) were dispensed into a round-bottomed flask, and chloroform was removed under reduced pressure ($\sim 20 \text{ kPa}$) using a rotary evaporator to produce a dry lipid film. The film was rehydrated in buffer (PBS buffer pH 7.4 containing 5 mM Tris base, 30 mM K_3PO_4 , 30 mM KH_2PO_4 , 3 mM $\text{MgSO}_4 \cdot 7\text{H}_2\text{O}$, 0.5 mM Na_2EDTA) resulting in a 1 mg ml^{-1} suspension (dehydration/rehydration method).^{14,15} $50 \mu\text{l}$ of the desired vesicle stock solutions were diluted (1:10) with TRIS buffer (10 mM Tris base, 125 mM NaCl, 1 mM Na_2EDTA , pH 7.4), and sonicated for 10 min in an ultrasonic cleaner USC-TH (35 kHz, $+30 \text{ }^\circ\text{C}$, VWR) and extruded through a $0.1 \mu\text{m}$ pore size filter 11 times using the Avanti mini extruder. The pre-hydrolyzed form of styrene-maleic anhydride, (Lipodisq[®] Styrene:Maleic Anhydride Copolymer 3:1, pre-hydrolyzed) with the styrene and maleic acid monomers present in a 3:1 ratio¹⁶ was purchased from Sigma and prepared in the same buffers containing the lipid suspensions to achieve the desired final concentration. Other specific details of the polymer are as follows: M_w (weight average): $\sim 9500 \text{ Da}$; M_n (number average): $\sim 3050 \text{ Da}$; the polydispersity index is accordingly ~ 3.11 .

Lipid film formation and polymer exposure

A schematic of the experimental set-up for forming supported bilayer patches is shown in Fig. 1. A laser scanning confocal microscope (Leica TCS SP8, Leica Microsystems GmbH, Wetzlar, Germany) was used. The supported lipid bilayers were formed *in situ* by transforming SUVs on a glass substrate (WillCo Wells B.V. Amsterdam, NL), using an open-space microfluidic multi-channel pipette¹⁷ (Fluicell AB, Sweden). For deposition of the lipids, the microfluidic pipette was positioned using a 3-axis water hydraulic micromanipulator (Narishige, Japan) $10\text{--}20 \mu\text{m}$ above the surface and the recirculation of SUVs (0.1 mg ml^{-1}) was initiated (Fig. 1a). This leads to the adhesion of SUVs onto the solid surface, rupturing and eventual merging of the individual

ruptured lipid patches into a circular homogeneous planar bilayer¹⁷ (Fig. 1a). Approximately 2 minutes after forming the lipid patch, this time SMA copolymer was applied to the newly formed bilayer *via* the pipette which in some instances lead to pore formation (Fig. 1b). All experiments were performed at constant room temperature of $18 \text{ }^\circ\text{C}$.

Fluorescence recovery after photobleaching (FRAP)

FRAP experiments were performed on lipid films using the FRAP module in the Leica confocal software, using a 40×1.25 oil objective and the white light laser at 488 nm , with 100% intensity. A circular region of interest (ROI) of ($d = 10 \mu\text{m}$) on each lipid patch was defined. The ROIs were sequentially exposed to steps of pre-bleaching (12 s) and bleaching (40 s). The recovery was monitored for 257 s post-bleaching. All experiments were performed at constant room temperature of $18 \text{ }^\circ\text{C}$.

Surface acoustic resonance measurements

A microfluidics-integrated surface acoustic wave (SAW) sensor in surface acoustic resonance (SAR) configuration, as described in Kustanovich *et al.*^{18,19} was used to follow membrane and polymer surface deposition. Fabrication, performance data and measurement environment are specified in the same work.¹⁹ Briefly, the microelectromechanical (MEMS) device utilizes surface acoustic wave resonance (SAR), which is conceptually similar to the quartz crystal microbalance (QCM) with respect to resonance frequency downshifts of the resonator upon mass deposition on its surface. The SAW resonator/transducer acts as a combined transmitter and read-out element. The mass load-sensing elements of the SAR sensor are the reflective gratings of the device, and changes in wave characteristics (phase velocity and reflectivity) largely determine the SAW resonance frequency shifts. This allows the simultaneous study of two complementary sensing parameters: the shift of resonance frequency and the shift of the conductance magnitude at resonance, revealing details about structural changes in the sensing layer. The viscoelastic properties of the layer strongly depend on the layer morphology. More specifically, mass deposition results in resonant frequency downshifts, while interactions that alter the viscoelastic properties of the sensing layer can be characterized by changes in the magnitude of the conductance peak, and *vice versa*. The SAR sensor used here operates at a frequency of $\sim 186 \text{ MHz}$, with noise levels below 0.5 ppm for resonance frequencies, and below 6 ppm for the conductance peak. These numbers determine the limit of frequency detection ($3\sigma < 1.5 \text{ ppm}$) and the limit of conductance magnitude detection ($3\sigma < 18 \text{ ppm}$). All experiments were performed using a temperature-regulated stage set to $21 \text{ }^\circ\text{C}$.

The sensor surface is composed of SiO_2 , which supports the transformation of a lipid suspension into a supported POPC bilayer film similarly to the glass (borosilicate) surfaces used in the confocal microscopy experiments. Although the polymer interaction strengths and kinetics may differ between the two surfaces, the mobility of the lipids largely determines the behavior of the membrane on a solid support. Lipids on glass and SiO_2 form bilayers of similar mobility.

Table 1 Lipid species and associated polymer concentrations tested on them for the confocal microscopy experiments

Lipid type ^a	Polymer concentration tested
POPC 1-palmitoyl-2-oleoyl-glycero-3-phosphocholine	0.1, 0.3, 0.5, 1.0
Soybean polar lipids	0.1, 0.3, 0.5, 0.7, and 1
DMPC 1,2-dimyristoyl-sn-glycero-3-phosphocholine	0.1, 0.3, 0.5, 0.7, and 1

^a All lipids were doped with 1% rhodamine-PE.



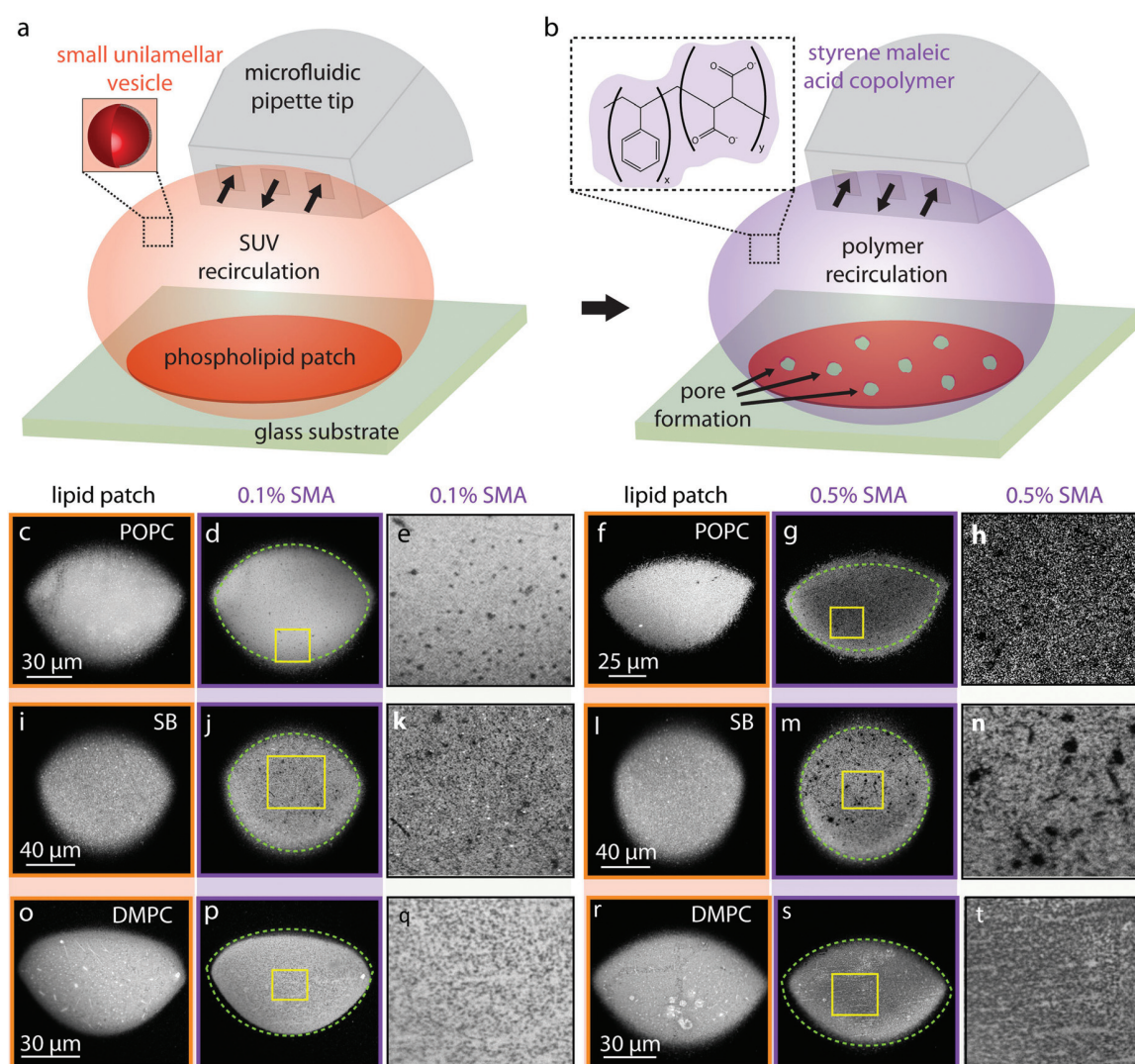


Fig. 1 Formation of molecular lipid films and their exposure to SMA copolymer. (a and b) Schematic drawing summarizing the experimental set-up. (a) Lipid particles were recirculated above a glass substrate using a microfluidic pipette which results in formation of a circular lipid bilayer patch. (b) Upon formation of the lipid film, the SMA copolymer solution was applied which in some instances lead to pore formation. The styrene to maleic acid monomer ratio $x : y$ is 3 : 1. (c–t) Confocal microscopy images of circular lipid bilayer patches from top view. (c and f; i and l; o and s) POPC, soybean, DMPC bilayers, respectively; formed on the surface before polymer exposure. (d, j and p) Lipid patches after exposure to 0.1% SMA copolymer. (e, k and q) magnified versions of yellow frames in (d, j and p). (g, m and s) Lipid patches after exposure to 0.5% SMA copolymer. (h, n and t) magnified versions of yellow frames in (g, m and s). The green dashed-lines representing the contour of the lipid films before polymer exposure have been superimposed over their polymer-exposed versions.

Fluorescein encapsulating giant unilamellar vesicle (GUV) formation on solid supported bilayer

Fluorescein-encapsulating GUVs on a solid support were formed as it was described by Köksal *et al.*²⁰ MLVs containing 50% soybean polar lipid extract, 49% *E. coli* polar lipid extract and 1% rhodamine-PE were prepared with the dehydration and rehydration method described above. Lipid reservoirs were placed on 84 nm SiO₂ deposited glass substrates, fabricated with E-beam and thermal PVD using EvoVac (Ångstrom Engineering), in HEPES buffer containing 10 mM HEPES, 100 mM NaCl and 4 mM CaCl₂, 100 μM fluorescein disodium salt, Sigma Aldrich),

pH 7.8. After the lipid reservoirs self-spread as a double bilayer and rupture,²¹ GUVs emerge spontaneously from the surface-adhered nanotubular networks.²⁰ During growth of the vesicles within several hours, fluorescein is encapsulated, which was confirmed by confocal microscopy. Thereafter, the excess dye is removed from the ambient buffer by exchanging it with fluorescein-free HEPES buffer. The open-volume microfluidic device/pipette described above positioned by a 3-axis water hydraulic micromanipulator was used to expose the surface adhered GUVs on a limited area to SMA copolymer solutions of 0.1%, 0.5% and 1% w/v in 10 mM HEPES, 100 mM NaCl pH 7.8. A 20× (NA: 0.75) air objective of the confocal laser scanning



microscope was used for acquisition of fluorescence images. The utilized excitation/emission wavelengths for fluorophore imaging were 560/583 nm for rhodamine, and 488/515 nm for fluorescein. Median filtering was applied to fluorescence micrographs by means of the NIH Image-J Software.

Transmission electron microscopy (TEM) experiments

Samples were prepared for transmission electron microscopy as described in Asadi *et al.*²² Briefly, 0.5 mg ml⁻¹ SUVs made from soybean polar lipids, DMPC or POPC, in the presence and absence of SMA copolymer, were adsorbed on 200 mesh formvar coated copper grids for five minutes followed by washing on 6 drops with milliQ H₂O. Grids were then incubated for five minutes on ice on drops with methylcellulose-uranylacetate mixture (800 μ l 2% methylcellulose and 200 μ l 4% uranyl acetate), looped out and dried. Images were recorded at 120 kV on a JEOL 1400plus Transmission Electron Microscope.

Results and discussion

Effect of SMA copolymer on molecular lipid films

We investigated the effects of the SMA copolymer by directly dispensing it onto fluorescently labeled molecular lipid films formed on solid supports by direct writing with an open-space microfluidic device, and observing the changes in membrane structure and morphology with a confocal microscope (Fig. 1). This experiment provided visual evidence that the membrane is locally compromised through the formation of defects, the size of which is related to the concentration of the polymer solution used.

Briefly, fluorescently labeled small unilamellar vesicles (SUVs) were circulated above a glass substrate using an open space microfluidic device (microfluidic pipette²³), which results in adhesion of the SUVs to the surface of the exposed substrate area, followed by rupturing of the SUVs and formation of a planar lipid bilayer patch^{17,24,25} (Fig. 1a).

Three different lipid species were tested: 1-palmitoyl-2-oleoyl-*glycero*-3-phosphocholine (POPC) (Fig. 1c–h), soybean lipids (Fig. 1i–n), and 1,2-dimyristoyl-*sn-glycero*-3-phosphocholine (DMPC) (Fig. 1o–u). These lipids were chosen based upon their known ability to form fluid, planar bilayers on glass substrates (POPC),¹⁷ their importance in biological, biophysical and structural studies (soybean lipids),^{21,26,27} and their extensive use in SMA-related physicochemical studies, most notably DMPC.^{9,10,12} Note that POPC and DMPC lipids are zwitterionic. At room

temperature, POPC is above its gel phase transition temperature²⁸ and fluid, DMPC is below it and in its gel phase.²⁹ Soybean polar lipid extract is a mixture of various lipids present in soybean lipids *e.g.* phosphatidylcholine (PC), phosphatidylethanolamine (PE), phosphatidylinositol (PI) and phosphatidic acid (PA). Soybean phospholipids reveal no transitions in the range between 3 to 80 °C.³⁰ Membranes composed of soybean lipids possess an overall negative charge, due to the 25 wt% contents of the negatively charged lipids PA and PI.

The average fluorescence intensities of each lipid patch presented in Fig. 1, before and after the application of SMA copolymers are presented in Table 2. For each lipid patch before and after polymer exposure, the mean intensity in a circular region of interest positioned at the center of the membrane has been determined. The 2D lipid membrane is incompressible; the fluorescence intensity of the membrane is therefore proportional to the lipid molecules/lipid material affected.

The fluidity of the lipid patches, an indicator for the establishment of a continuous biomimetic lipid membrane, was initially determined by means of fluorescence recovery after photobleaching (FRAP) measurements (Fig. 2). The FRAP results for the membranes created from POPC lipid vesicles show quick recovery and confirm fluidity, whereas the lipid patches composed of soybean and DMPC lipids do not fully recover.

Fig. 1b shows the second part of the experiment schematically, where by switching from lipid particle to SMA copolymer exposure, pores are introduced into the surface-supported membrane. We observed small pores on POPC bilayers after the addition of the 0.1% polymer (Fig. 1d and e). After exposure to 0.5% polymer solution (Fig. 1g and h), the average fluorescence intensity of the membrane drops significantly (65%, Table 2) accompanied by an area expansion of the lipid patch (dashed line in Fig. 1g). The lipid patch in Fig. 1f grows in size (Fig. 1g), suggesting the SMA copolymer strongly acts upon the membrane, and displaces lipids from the initial patch on the solid support.

Fig. 1i and l shows lipid patches created from soybean polar lipid particles. Soybean polar lipids are a complex lipid mixture composed primarily of PC, PE, PI and PA, possessing an overall net negative charge. While it is possible to deposit the lipid particles onto the glass substrate, the circular patches have a grainy appearance (Fig. 1i and l), indicating that formation of a homogeneous lipid bilayer does not fully occur. FRAP confirms this, as no recovery of the photo-bleached regions is observed (Fig. 2). This means that the SUVs remain semi-fused on the

Table 2 Average fluorescence intensities of each lipid patch (*cf.* Fig. 1) before and after the application of SMA copolymers

	Average patch intensity before polymer exposure	Average patch intensity after 0.1% SMA exposure	Average patch intensity before polymer exposure	Average patch intensity after 0.5% SMA exposure
POPC	122 ^a (<i>A</i> _{ROI} : 2895)	114 (<i>A</i> _{ROI} : 2757)	107 (<i>A</i> _{ROI} : 2221)	38 (<i>A</i> _{ROI} : 2333)
SB	100 (<i>A</i> _{ROI} : 3410)	90 (<i>A</i> _{ROI} : 3644)	108 (<i>A</i> _{ROI} : 3680)	76 (<i>A</i> _{ROI} : 3842)
DMPC	140 (<i>A</i> _{ROI} : 1738)	130 (<i>A</i> _{ROI} : 1615)	158 (<i>A</i> _{ROI} : 1709)	101 (<i>A</i> _{ROI} : 1682)

^a Each cell shows the mean intensity of the selected region of interest (ROI, top), and the affected area (bottom). The intensity is denoted in levels of an 8bit image (0–255 levels) in the associated selected ROI. The second row contains the area of each circular ROI in μm^2 .



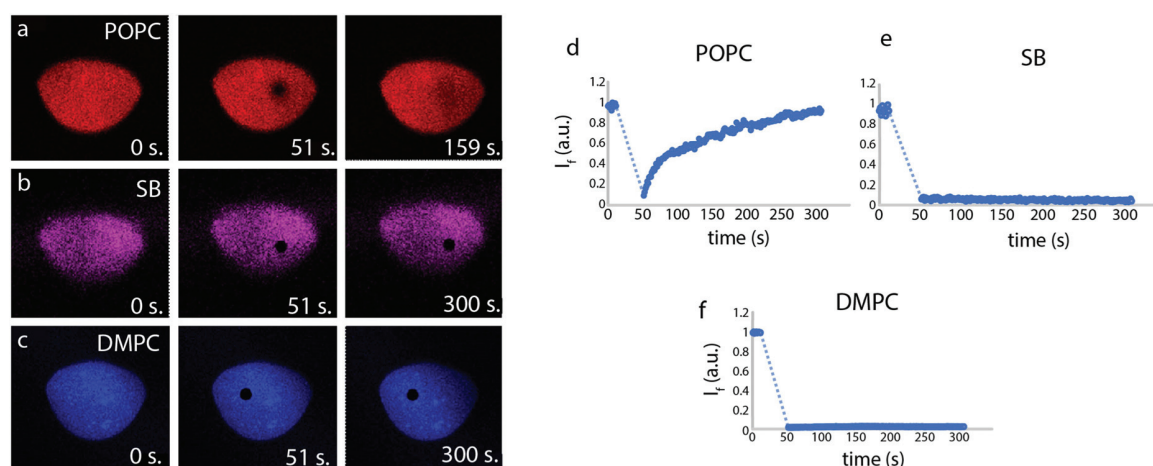


Fig. 2 (a–c) Snapshots from the fluorescence recovery after photobleaching (FRAP) experiments performed on solid supported membranes composed of POPC, soybean, and DMPC lipids. (d–f) Plots showing FRAP data of the membranes shown in (a–c): POPC, SB and DMPC lipids, respectively. POPC membranes recover their overall fluorescence over time, whereas SB and DMPC remain completely photo-bleached.

glass substrate, but not all of them rupture and form a planar bilayer in the time frame of the experiment. After exposure to the 0.1% (Fig. 1j and k) and 0.5% SMA copolymer (Fig. 1m and n), large uncovered surface areas between 0.5–3.9 μm in size become visible in the lipid films resulting in a 30% decrease in mean fluorescence intensity of the initial lipid patch (Table 2). Since the lipid patch is not continuous and consists of small vesicles adhering to the surface, the SMA copolymer must be reversing the adhesion of these vesicles to the substrate. This fraction of the lipid patch dissolves, leading to larger uncovered regions on the surface (Fig. 1k and n). Since the patch is not fluid as a whole, there are no distinct edge effects as observed with POPC, and the patch size does not increase over time.

In a third series (Fig. 1o–t), we performed the same procedure with DMPC lipid vesicles. The formed patches resulted in bilayers that are also not continuous, as the photo-bleached regions do not recover (Fig. 2). With 0.1% SMA copolymer solution (Fig. 1p and q), the formation of small defects is observed. The poration, *i.e.*, removal of lipid material from the patch, becomes more apparent with 0.5% SMA copolymer solution. The DMPC lipid film shown in Fig. 1o and r visibly decreases in size upon polymer exposure (Fig. 1p and s). Simultaneously, the mean fluorescence intensity of the patch is decreased by 36% (Table 2).

Next, a microfluidics-integrated surface acoustic wave resonance (SAR) sensor, effectively a microscale equivalent of a quartz crystal microscale (QCM)^{18,19} was used to analyze surface deposition and surface-based transformations of POPC lipids and SMA copolymer (Fig. 3). The SAR sensor measures changes in surface acoustic wave resonance frequency (mass deposition) and conductance (resistance to transfer of acoustic energy) that can be related to lipid film formation and depletion, as well as changes in viscoelastic properties of the deposited material, respectively.

Buffer loading resulted in an initial frequency decrease with respect to the unloaded dry device (Fig. 3a). Lipid deposition causes further frequency reduction, due to mass increase from

bilayer formation (Fig. 3a). Three different concentrations of SMA copolymer were successively applied next: 0.01%, 0.1% and 1% (Fig. 3a). Compared to the sensor, our microscopy results are less detailed, *e.g.*, the size of the pores forming after 0.1% polymer exposure are quite small, and not directly visible due to the diffraction limit; 0.5% lead to significantly larger pores, and 1% complete disassociation of the membrane. In contrast, the sensor can detect mass changes as small as at 0.01%. In order to obtain a wider view on the concentration range of effective interaction, a concentration below 0.1% was chosen for one of the sensor measurements. The magnitude of frequency downshifts after each SMA copolymer exposure indicates that the polymer deposits with each application, and that the amount of immobilized SMA copolymer on the membrane depends on the SMA copolymer concentration in the supplied solution. This can mean the surface is slowly saturated, or that the polymer builds up on an already saturated surface.

The bare, lipid-free sensor surface was next exposed to the same SMA copolymer concentration series (Fig. 3b). Here, a similar concentration dependent build-up of polymer was observed between 0.01 and 0.1% SMA copolymer concentration, while at 1% w/v SMA copolymer, the frequency down-shift on the bare surface exceeds that on the lipid-coated surface shown in Fig. 3a. This suggests that the lipid bilayer blocks SMA copolymer association with the SiO_2 surface, or that the mass lost as a result of membrane solubilization exceeds the mass gained from polymer deposition in the surface areas exposed in the pore regions. The crossover point between the two graphs in Fig. 3e points to a concentration between 0.4 and 0.5% w/v, in which this coverage limitation sets in. To distinguish whether this is the point at which surface saturation occurs or whether it is related to a transformation of surface properties, analysis of the simultaneously recorded conductance data (Fig. 3c and d) must also be taken into account.

Upon lipid deposition, the conductance of the sensor increases, *i.e.*, surface acoustic wave (SAW) energy confinement within the



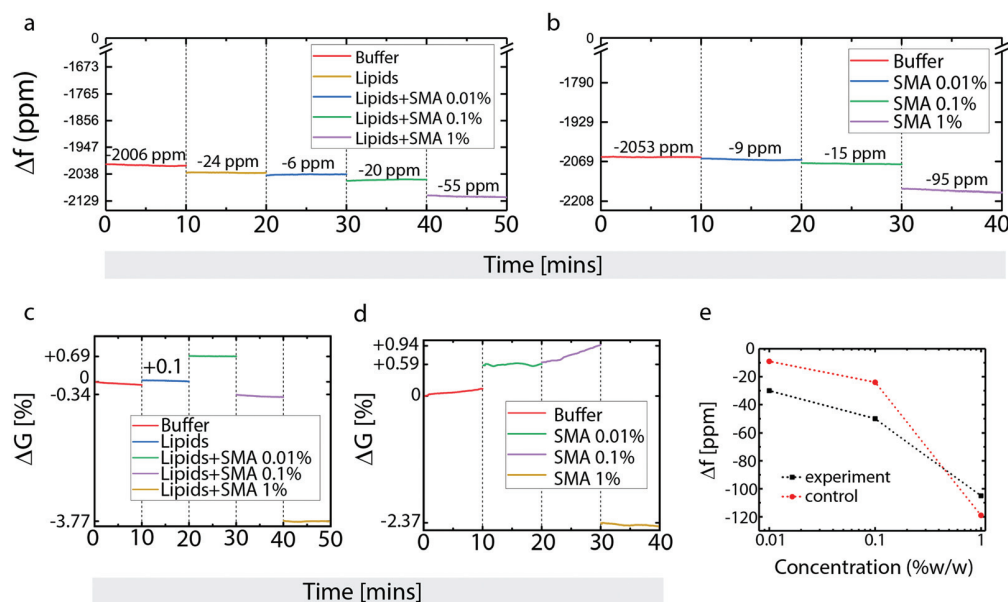


Fig. 3 SAR sensor data for POPC lipid and SMA copolymer deposition onto a SiO_2 support. (a and b) Time-resolved frequency response (Δf , in parts per million) of the SAR sensor upon sequential loading with lipids and SMA copolymer (a), and SMA copolymer only (b). The colors encode the signals for the individual deposits. (c and d) Time-resolved conductance (ΔG , in percentage) response of the SAR sensor upon sequential loading with lipids and SMA copolymer (c), and SMA copolymer only as control (d). The signals are normalized to the conductance of the lipid coated and bare sensor, respectively, before the exposure to SMA copolymer solution. (e) Calibration curve for the lipid membrane/SMA copolymer interaction (black line) and the reference on the unmodified sensor surface (red line).

device is enhanced (Fig. 3c). This indicates a change in viscoelastic properties that reduces the losses of SAW energy through the surface into the liquid. This typically occurs upon mass addition under increasing coverage of the surface, or structural changes such as increased rigidity, or healing of surface defects. Deposition of 0.01% SMA copolymer results in a further increase of the conductance, suggesting that the SMA copolymer initially increases membrane rigidity and/or reduces surface defects (Fig. 3c).

Upon deposition of 0.1% w/v SMA copolymer solution, the conductance sharply drops, suggesting structural changes in the lipid bilayer, which is in agreement of the findings on supported lipid films, where lipid solubilization and disruption occurs at this concentration. (Fig. 3c). Addition of 1% w/v SMA copolymer solution results in the conductance dropping even further (Fig. 3c).

Experiments on the bare sensor surfaces show different behavior in one key aspect (Fig. 3d). Between 0.01% and 0.1% w/v SMA copolymer concentrations, the conductance values are unstable and increase steadily over time (Fig. 3d), which is not observed in the presence of a lipid film (Fig. 3d). This indicates that the SMA copolymer becomes more rigid, possibly due to a structural/conformational re-arrangement, or association/entanglement of polymer chains. At 1% w/v the conductance drops to a degree comparable to what was observed on the lipid membrane (Fig. 3d). The similarity of these two readings suggests that the polymer–surface interactions are similar in both cases, with the polymer–surface interaction dominating even in the presence of the (already strongly disrupted) lipid membrane. The increased mass, coupled to conductance

reduction, suggests that the polymer film causes viscous loading to the acoustic waves, possibly through swelling and formation of a hydrogel layer. The polymer/water network coupled to the SiO_2 coating is sensed as a mass increase within the limits of the SAW penetration depth, while actually the SAW losses through the less rigid hydrogel matrix increase, and are recorded as a conductance decrease.

The sensor measurements confirm the findings from the patch deposition/SMA exposure experiments shown in Fig. 1. In the experiment on POPC film shown in Fig. 1f and g, lipid material is removed from the film, but an area expansion of the lipid bilayer occurs at the same time. This indicates that SMA copolymer is displacing, but not removing lipid material adhered to the surface, which leads to expansion of the patch border outwards. It appears that polymer is adhering to the surface in the patch areas that have been freed from lipid material, *i.e.*, polymer successfully competes with lipids for surface area coverage. Sensor and confocal data are in full agreement. The rough calibration curve depicted in Fig. 3e shows a mass increase on both the lipid film and the bare surface. The relative mass increase on the bare surface exceeds that on the lipid-coated surface substantially at higher polymer concentrations, indicating that the polymer interaction with the surface in this concentration range is dominant in the presence of a surface support. The study on supported membranes also shows that polymer interaction with the membrane are “one-sided”, meaning that open space on the opposite side of the membrane is not necessary for the opening of membrane pores, indirectly supporting the theoretical



findings that the polymer largely lines the rim of the generated pores.

Effect of SMA copolymer on free-standing GUV membranes

To confirm that pore formation occurs in free-standing lipid bilayers, and is not primarily driven by the increased gain of free surface energy associated with the displacement of lipids from surface regions by polymer, adhered GUVs composed of soybean polar lipid and *E. coli* polar lipids (50/50% w/w) encapsulating a fluorescein solution were produced and exposed to SMA copolymer (Fig. 4). In contrast to the solid-supported lipid film experiments, here only a limited fraction of the surface area is adhered to the solid substrate (Fig. 4a). Note that this area is, unlike in a supported membrane, obscured by the vesicle body and thus not accessible to the liquid environment. This allows for observing the lipid membranes in a quasi-suspended manner,

where the position of the GUVs is maintained on the support, and polymer effects can be observed in real-time over extended time spans. The GUVs used in the experiments contain fluorescein (mean diameter 6.9 Å) in their internal volume. The encapsulation of fluorescein occurs during the formation of the vesicles in fluorescein-enriched external solution, which is exchanged for dye-free buffer after maturation of the vesicles. Due to the difference in fluorescence emission between the rhodamine-labeled GUVs and encapsulated fluorescein, it is possible to observe both the lipid vesicles and the internalized fluorescein simultaneously. We applied the SMA copolymer to the vesicles *via* the microfluidic pipette (Fig. 4b) used in the previous experiments on supported membranes. This mode of application in a hydrodynamically confined volume ensures that the polymer is present in the volume around selected vesicles only during exposure, and consistently at the specified concentration.

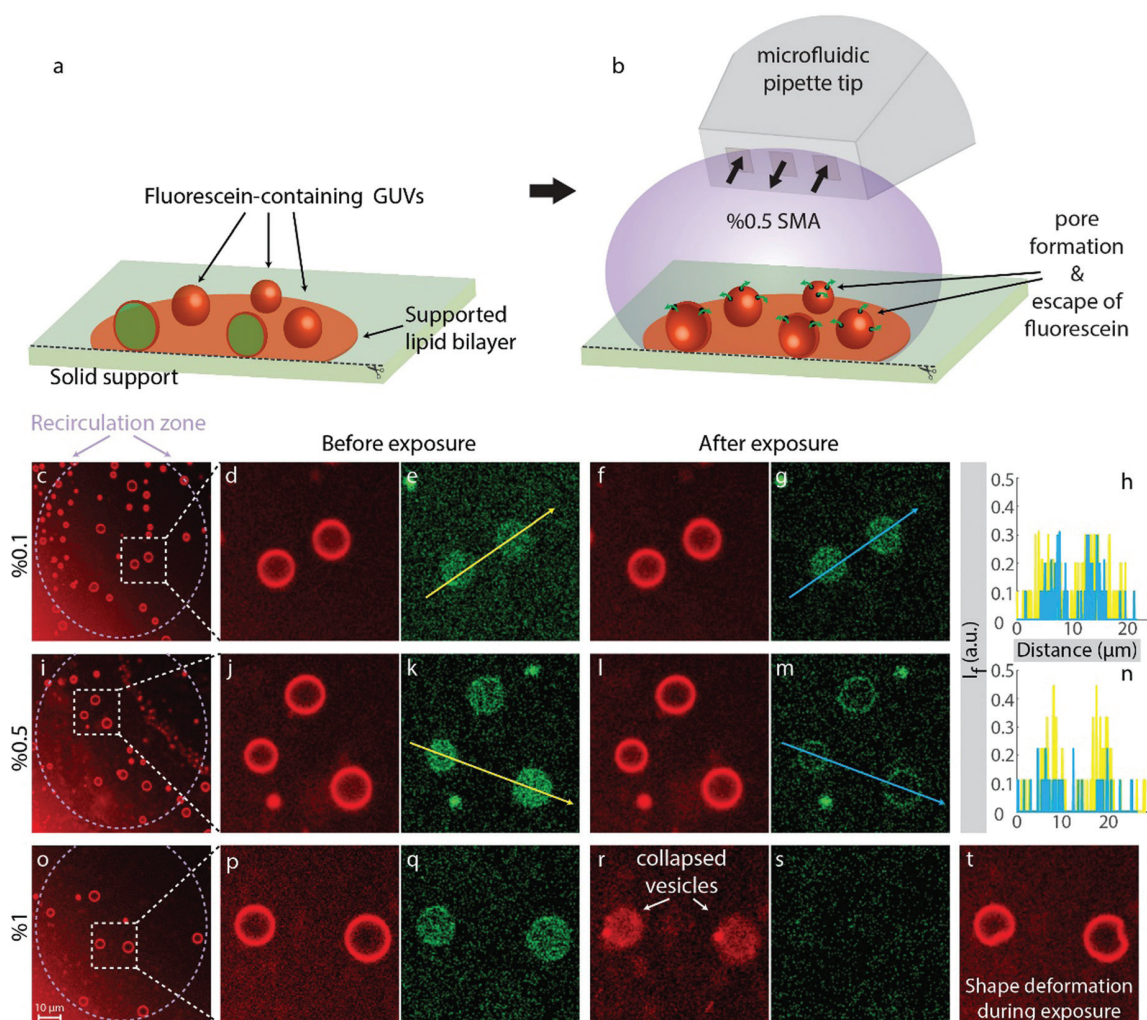


Fig. 4 Poration of fluorescein-encapsulating surface-adhered GUVs with SMA copolymer. (a and b) Experimental setup. GUVs are formed on the solid support, and a microfluidic pipette tip is used to add the SMA copolymer. (c–t) Confocal micrographs of the experiment summarized in (a and b). (c, d, i, j, o and p) Three different regions on the lipid patch where the SMA copolymer was applied at varying concentrations: (c–h) 0.1%, (i–n) 0.5% and (o–t) 1% w/v. The plots in (h and n) show the fluorescent intensity of encapsulated fluorescein (arbitrary unit) before (yellow) and after (blue) SMA exposure. (t) shows the drastic shape deformations observed during 1% polymer exposure depicted in (o–s).



We chose three regions on the solid support populated with GUVs and applied three different concentrations of the SMA copolymer to the GUVs in each region: 0.1% (Fig. 4c–h), 0.5% (Fig. 4i–n) and 1% (Fig. 4o–t). At 0.1% SMA copolymer concentration, no significant changes were observed with respect to fluorescence signal collected from the internalized fluorescein (Fig. 4d–g). The vesicles appeared intact, and the dye remained encapsulated (Fig. 4f and g). The fluorescence intensities along the arrows depicted in Fig. 4e and j, corresponding to the intensities before (yellow color) and after (blue color) exposure to the 0.1% polymer solution, are shown in Fig. 4h, indicating no effective alterations of the membrane. Increasing the concentration to 0.5% did not lead to the disruption of the GUVs, but caused rapid release of internalized fluorescein (Fig. 4j–m). The emission intensities along the arrows depicted in Fig. 4k and m, corresponding to the intensities before (yellow color) and after (blue color) the 0.5% polymer exposure, are shown in Fig. 4n, indicating the presence of water-filled pores, large enough to allow for the passage of fluorescein molecules ($\geq 7 \text{ \AA}$). 1% w/v SMA copolymer fully solubilized the GUVs (Fig. 4o–t). Note that the vesicular membranes in Fig. 4m fluoresce in the fluorescein channel. This is due to the slight overlap between the absorption spectra of fluorescein and rhodamine B. The weak absorption of membrane-associated Rho B at 488 nm also causes a minute amount of fluorescence, leading to the weak cross-over signal, *i.e.*, a green ring. During exposure to 1% SMA copolymer we observed drastic shape deformations (Fig. 4t). The peculiar shape of the vesicles, visible in this figure, points towards a single giant pore forming in the membrane during exposure, which will eventually lead to osmotic breakdown of the vesicle, and collapse. Note that the vesicles in this system are in a low tension regime, due to the connection to a large lipid nanotube network on the surface (fluid lipid reservoir). That entails that unstabilized small pores would rapidly contract and close, according to the line tension in the pore edge.³¹ The collapse of the vesicles indicates that the polymer-lipid interaction has a stabilizing effect on the pore edge; it compensates the line tension and thus keeps the pore open. It can be assumed that the polymer removes lipid material continuously from the edge of the pore, increasing its size, until the vesicle finally folds onto the surface (Fig. 4r and s). Alternatively, smaller pores could be formed in large numbers and continuously merge, reducing the overall pore edge tension. During this process, lipid material could be simultaneously separated from the vesicle membrane (Fig. 6). The observation is in principle in agreement with the prediction of Xue *et al.*,¹³ and also supported by the finding that adhered DMPC membrane patches dissolve noticeably from the edges (Fig. 1o, p and r, s). We suggest that the polymer adheres to the membrane, increases its rigidity (which is strongly supported by the increase in sensor conductance at low SMA concentrations), then penetrates the membrane to form defects, where it lines the pore perimeter and dissolves lipid material from the edge, causing pore enlargement to an extent dependent on polymer concentration. The formation of a single large pore is consistent with earlier reports on flat giant unilamellar vesicles

in an experimental system which employs Ca^{2+} to stabilize the pore by pinning.³²

Supported membranes vs. spherical membranes (vesicles)

0.1% SMA copolymer creates visible membrane defects in supported membranes, but no noticeable pore formation was observed on the same concentration when applied to spherical containers. 0.5% SMA copolymer porates the vesicle membrane efficiently, as is evident from the loss of internalized contents. Planar supported membranes show a major loss of lipid material upon exposure.

According to the SAR sensor measurements, SMA copolymer associates with the membrane, but equally strongly to the bare, lipid-free surface. Between 0.01 and 0.1% SMA copolymer, the conductance measurements, which report on membrane rigidity and general transparency to acoustic energy, indicate a strong change in membrane properties that is associated with a mass increase at the surface. In conjunction with confocal microscopy on supported fluid membranes, the sensor findings suggest that there is a mass increase even though lipid is removed, resulting from interaction of the polymer with the surface. Lipid is removed from the surface (decrease in fluorescence intensity), and simultaneously displaced (increase of patch outer diameter). Our findings on supported membranes clearly indicate that the polymer-induced pore formation does not require the availability of both hydrophilic faces of the membrane, but benefits from the presence of a rigid bottom layer. The presence of the surface appears to have a supporting influence on the impact of the polymer on the membrane. This finding might also be relevant to the cytoskeleton supporting the cell membranes under the influence of the polymer. Studies of SMA interaction on cells with weakened cytoskeleton, *e.g.* by zeiosis-inducing reagents, could reveal more information on such connection.

Effect of 3 : 1 SMA copolymer on small unilamellar vesicle (SUV) suspensions

To further characterize polymer-induced morphological changes, negative-stain electron microscopy was performed on a small unilamellar vesicles (SUVs) suspension (Fig. 5). Since the final lipid : polymer ratios in the confocal microscopy experiments are unknown, but the exact concentration of lipid and polymer need to be established in order to only partially solubilize the vesicle membrane, we first recorded turbidity curves (Fig. 5a–c). Turbidity assays are a routine way to determine detergent-solubilization curves for liposomes, and have also previously been used monitor the solubilization of lipids by SMA copolymers.³³ In all samples a slight increase in turbidity occurs, which is less obvious for POPC and DMPC (Fig. 5a and c) than for soybean lipids (Fig. 5b), followed by a decrease to baseline levels. In detergent-solubilization curves of liposomes, small changes in turbidity, similar to those seen here, are linked to disrupted bilayer vesicles, rather than more complex worm-like structures that scatter more light.³⁴ The small absorbance increases that are observed along the overall decrease (marked with asterisks) are likely to be due to some unspecified structural intermediates that may form along the solubilization pathway.



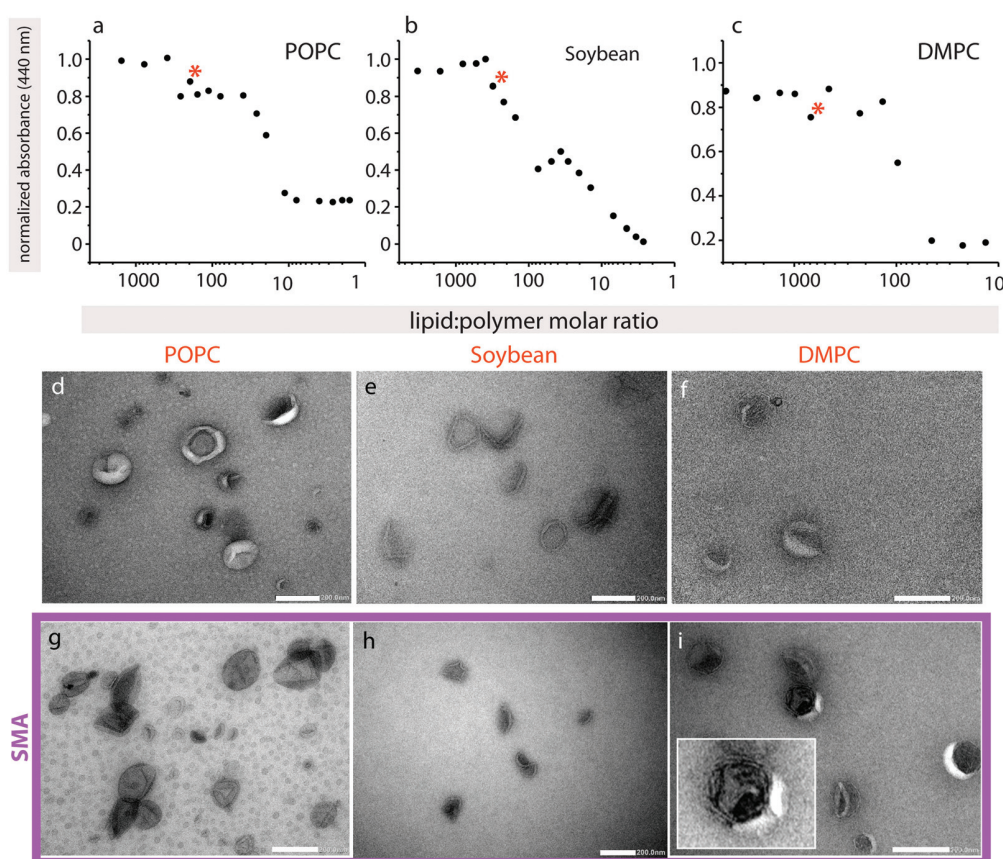


Fig. 5 Lipid solubilization. (a–c) Turbidity curves in the presence of SMA copolymer for POPC, Soybean and DMPC lipids. The polymer : lipid ratio that was chosen for EM images is marked with a red asterisk in each plot. (d–i) TEM images showing the vesicles produced from different lipids in the absence (d–f) and presence (g–i) of 3 : 1 SMA copolymer. Differences in background color are largely attributed to uneven staining, where background in POPC in the presence of SMA copolymer appears to have less stain present than for POPC only. The inset in panel (i) is a magnified image of a multilamellar vesicle. Scale bars: 200 nm.

For TEM, we chose lipid : polymer ratios where we expect partial polymer-induced vesicle disruption of the lipid vesicles, but not their full solubilization. Soybean SUVs in the absence of SMA copolymer appear well-formed (Fig. 5e), with a visible bilayer, and are approximately 70–120 nm in diameter. SMA copolymer addition results in a collapsed structure, where the vesicles display an inward concavity (Fig. 5h). They appear generally still intact, and the bilayer is present. These observations are in agreement with the turbidity assay that also indicates a simple disruption of the bilayer rather than the formation of a more complex lipid–polymer phase. These observations suggest that SMA-induced disruption of the bilayer leads to escape of the liquid within the samples upon dehydration and application of the vacuum, leading to their collapse. This is in excellent agreement with fluorescein encapsulation assays on quasi-suspended GUVs, where at intermediate polymer concentrations the fluorescein is also able to escape the intact vesicle. POPC liposomes without polymer are approximately 70–150 nm in diameter, and are more donut-shaped in appearance (Fig. 5d). The liposomes appear to burst in the presence of polymer (Fig. 5g), and the average SUV size appears somewhat smaller (40–110 nm). DMPC SUVs

in the absence of polymer were heterogeneous in size, and many were already collapsed, possibly due to the inclusion of sonication in preparing them, making the observation of SUV morphological changes upon SMA copolymer addition more difficult (Fig. 5f). However, we did observe a significant increase in vesicle multilamellarity (see Fig. 5i inset) that was not observed in the other lipid types (Fig. 5i).

One possible assumption for the pathway to the formation of pores in membranes under the influence of SMA copolymer can be formulated. This involves polymer chains lining the edge of the pores formed (as suggested by Xue *et al.*), compensating for the edge line tension. It is possible that as the number of pores increase, they may merge to form isolated lipid islands that would break out to form SMA-supported lipid bilayer discs (Fig. 6). SAR sensor data on the supported membranes indeed show that a mass loss occurs at higher polymer concentrations in excess of the mass gain explainable by adhesion of polymer in open pore areas. External data from biomembranes which form lipid discs including membrane proteins,^{5–8} support the island formation pathway, while the confocal microscopy data also provide strong support for the edge-dissolution pathway.



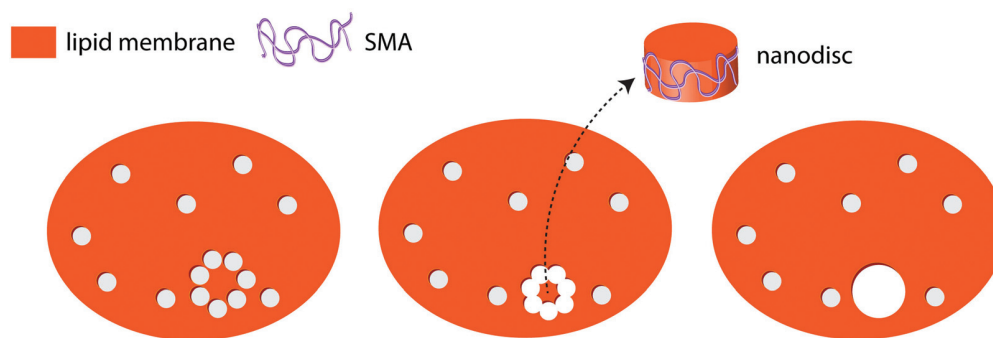


Fig. 6 A possible mechanism for SMA–nanodisc formation from lipid bilayers (top view). Small pores induced by the SMA copolymer (left panel) eventually merge forming a lipid island (middle panel). The lipid island moves out of the lipid bilayer as a SMA–lipid disc complex (middle and right panel).

Conclusion

We found experimental evidence that SMA copolymer forms pores in lipid bilayers, both on solid-supported membranes and in free-standing bilayers of unilamellar vesicles. The work supports the theoretical prediction of SMA copolymer-induced pores, published by Xue *et al.* in 2018.¹³ We do not have, however, sufficient data to claim with certainty that the mechanism proposed by the authors is the exact one found in the experimental system. The results altogether confirm that SMA copolymers cause water-filled pores in lipid bilayers, well complementing the recent theoretical predictions.

Conflicts of interest

The authors declare the following competing financial interest(s): AJ is co-inventor of the microfluidic multichannel pipette, and minority share holder of Fluicell AB, the company that markets the microfluidic pipette. No payments or financial gain were a reason for, or a direct consequence of, the research contained within the manuscript.

Acknowledgements

The authors thank Norbert Roos and Antje Hofgaard (Electron Microscopy Laboratory, Dept. of Biosciences, University of Oslo) for technical assistance. This work was made possible through financial support obtained from the Research Council of Norway (Forskingsrådet) Project Grant 274433, UiO: Life Sciences Convergence Environment, the Swedish Research Council (Vetenskapsrådet) Project Grant 2015-04561 as well as the startup funding provided by the Centre for Molecular Medicine Norway & Faculty of Mathematics and Natural Sciences at the University of Oslo. A.J. acknowledges H2020 ITN “Chemical Reaction Networks – CReaNET” – Ref. 812868 and the Swedish Foundation for Strategic Research (SSF) (GMT14-0077). M.O.R. gratefully acknowledges funding from the Research Council of Norway Project Grant 240909.

References

- 1 S. R. Tonge and B. J. Tighe, *Adv. Drug Delivery Rev.*, 2001, **53**, 109–122.
- 2 S. R. Tonge, *Compositions comprising a lipid and copolymer of styrene and maleic acid*, UK Pat., WO/2006/129127, 2006.
- 3 T. J. Knowles, R. Finka, C. Smith, Y. P. Lin, T. Dafforn and M. Overduin, *J. Am. Chem. Soc.*, 2009, **131**, 7484–7485.
- 4 M. Orwick-Rydmark, J. E. Lovett, A. Graziadei, L. Lindholm, M. R. Hicks and A. Watts, *Nano Lett.*, 2012, **12**, 4687–4692.
- 5 Z. Stroud, S. C. L. Hall and T. R. Dafforn, *Methods*, 2018, **147**, 106–117.
- 6 J. M. Dörr, S. Scheidelaar, M. C. Koorengel, J. J. Dominguez, M. Schäfer, C. A. van Walree and J. A. Killian, *Eur. Biophys. J.*, 2016, **45**, 3–21.
- 7 S. C. Lee, T. J. Knowles, V. L. G. Postis, M. Jamshad, R. A. Parslow, Y. P. Lin, A. Goldman, P. Sridhar, M. Overduin, S. P. Muench and T. R. Dafforn, *Nat. Protoc.*, 2016, **11**, 1149–1162.
- 8 C. Sun, S. Benlekbir, P. Venkatakrisnan, Y. Wang, S. Hong, J. Hosler, E. Tajkhorshid, J. L. Rubinstein and R. B. Gennis, *Nature*, 2018, **557**, 123–126.
- 9 M. Jamshad, V. Grimard, I. Idini, T. J. Knowles, M. R. Dowle, N. Schofield, P. Sridhar, Y. Lin, R. Finka, M. Wheatley, O. R. T. Thomas, R. E. Palmer, M. Overduin, C. Govaerts, J. M. Ruyschaert, K. J. Edler and T. R. Dafforn, *Nano Res.*, 2015, **8**, 774–789.
- 10 M. C. Orwick, P. J. Judge, J. Procek, L. Lindholm, A. Graziadei, A. Engel, G. Gröbner and A. Watts, *Angew. Chem., Int. Ed.*, 2012, **51**, 4653–4657.
- 11 J. J. Dominguez Pardo, C. A. van Walree, M. R. Egmond, M. C. Koorengel and J. A. Killian, *Chem. Phys. Lipids*, 2019, **220**, 1–5.
- 12 S. Scheidelaar, M. C. Koorengel, C. A. van Walree, J. J. Dominguez, J. M. Dörr and J. A. Killian, *Biophys. J.*, 2016, **111**, 1974–1986.
- 13 M. Xue, L. Cheng, I. Faustino, W. Guo and S. J. Marrink, *Biophys. J.*, 2018, **115**, 494–502.
- 14 E. S. Köksal, P. F. Belletati, G. Reint, R. Olsson, K. D. Leitl, I. Kantarci and I. Gözen, *J. Visualized Exp.*, 2019, **2019**, e58923.
- 15 M. Karlsson, K. Nolkranz, M. J. Davidson, A. Stromberg, F. Ryttsen, B. Akerman and O. Orwar, *Anal. Chem.*, 2000, **72**, 5857–5862.
- 16 A. D. Goddard, P. M. Dijkman, R. J. Adamson, R. I. Dos Reis and A. Watts, *Methods Enzymol.*, 2015, **556**, 405–424.
- 17 A. Ainla, I. Gözen, B. Hakonen and A. Jesorka, *Sci. Rep.*, 2013, **3**, 2743.



- 18 K. Kustanovich, V. Yantchev, V. Kirejev, G. D. M. Jeffries, T. Lobovkina and A. Jesorka, *J. Micromech. Microeng.*, 2017, **27**, 114002.
- 19 K. Kustanovich, V. Yantchev, A. Olivefors, B. Ali Doosti, T. Lobovkina and A. Jesorka, *J. Micromech. Microeng.*, 2019, **29**, 024001.
- 20 E. S. Koksall, S. Liese, I. Kantarci, R. Olsson, A. Carlson and I. Gozen, *ACS Nano*, 2019, **13**, 6867–6878.
- 21 I. Gözen, P. Dommersnes, I. Czolkos, A. Jesorka, T. Lobovkina and O. Orwar, *Nat. Mater.*, 2010, **9**, 908–912.
- 22 J. Asadi, S. Ferguson, H. Raja, C. Hacker, P. Marius, R. Ward, C. Pliotas, J. Naismith and J. Lucocq, *Micron*, 2017, **99**, 40–48.
- 23 A. Ainla, G. D. M. Jeffries, R. Brune, O. Orwar and A. Jesorka, *Lab Chip*, 2012, **12**, 1255–1261.
- 24 E. Reimhult, F. Höök and B. Kasemo, *Langmuir*, 2003, **19**, 1681–1691.
- 25 P. S. Cremer and S. G. Boxer, *J. Phys. Chem. B*, 1999, **103**, 2554–2559.
- 26 X. Zhuang, A. Ou and J. B. Klauda, *J. Chem. Phys.*, 2017, **146**, 215103.
- 27 R. G. Efremov, C. Gatsogiannis and S. Raunser, *Methods Enzymol.*, 2017, **594**, 1–30.
- 28 S. Leekumjorn and A. K. Sum, *J. Phys. Chem. B*, 2007, **111**, 6026–6033.
- 29 W. Chen, F. Duša, J. Witos, S. K. Ruokonen and S. K. Wiedmer, *Sci. Rep.*, 2018, **8**, 14815.
- 30 S. D. O'Neill and A. C. Leopold, *Plant Physiol.*, 1982, **70**, 1405–1409.
- 31 E. Karatekin, O. Sandre, H. Guitouni, N. Borghi, P. H. Puech and F. Brochard-Wyart, *Biophys. J.*, 2003, **84**, 1734–1749.
- 32 I. Gözen, B. Ortmen, I. Pöldsalu, P. Dommersnes, O. Orwar and A. Jesorka, *Soft Matter*, 2013, **9**, 2787–2792.
- 33 C. Vargas, R. C. Arenas, E. Frotscher and S. Keller, *Nanoscale*, 2015, **7**, 20685–20696.
- 34 M. C. A. Stuart and E. J. Boekema, *Biochim. Biophys. Acta, Biomembr.*, 2007, **1768**, 2681–2689.

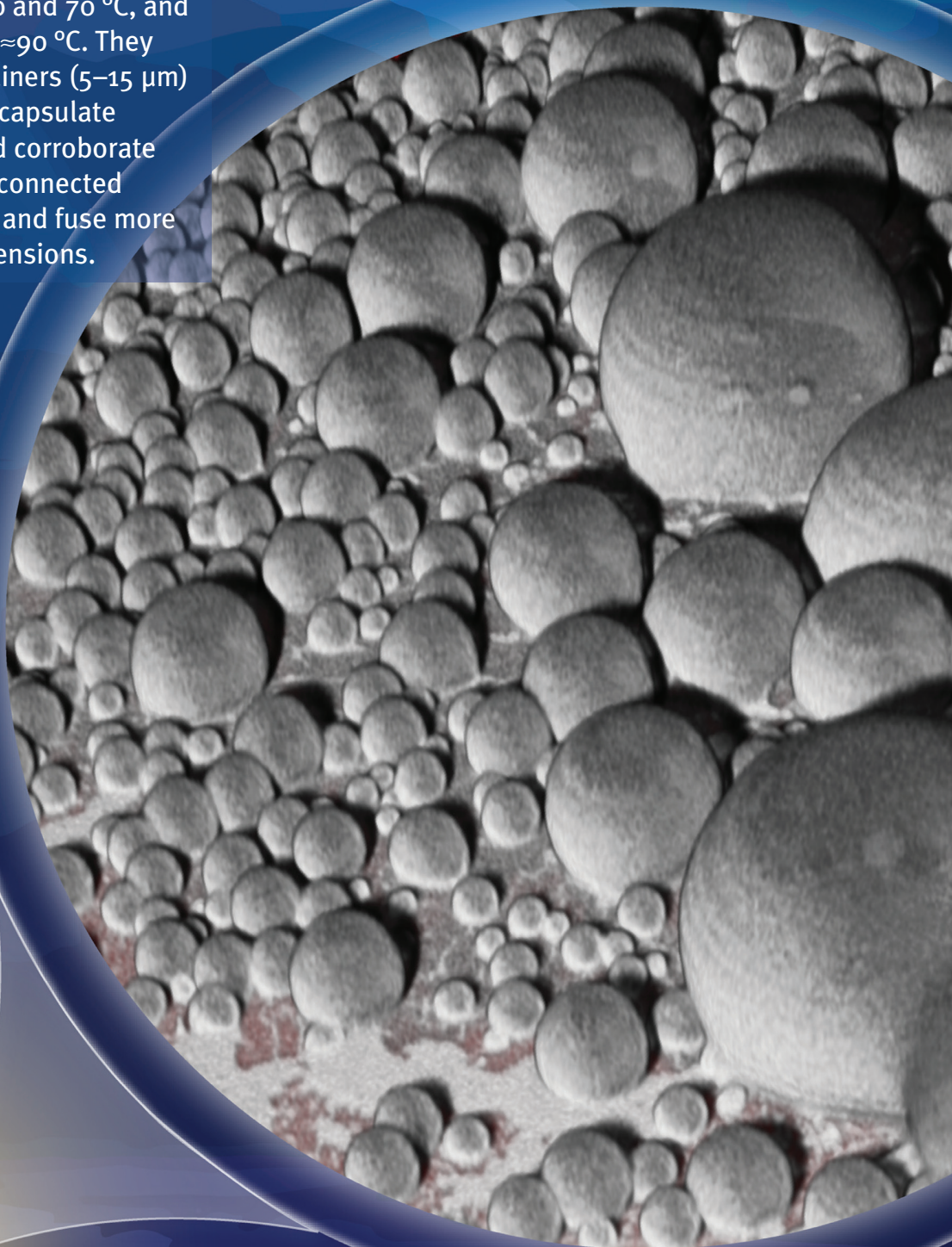


Paper III

NANO · MICRO small

Protocells

In article number 2002529, İrep Gözen and co-workers present experimental evidence that nucleation and growth of protocell-like membrane compartments from surface-adhered lipid nanotube networks are significantly enhanced at temperatures between 40 and 70 °C, and fusion can be initiated at ≈ 90 °C. They show that the microcontainers (5–15 μm) formed in this manner encapsulate and redistribute RNA, and corroborate that lipid nanotube–interconnected neighboring vesicles join and fuse more rapidly than in bulk suspensions.



Rapid Growth and Fusion of Protocells in Surface-Adhered Membrane Networks

Elif S. Köksal, Susanne Liese, Lin Xue, Ruslan Ryskulov, Lauri Viitala, Andreas Carlson, and Irep Gözen*

Elevated temperatures might have promoted the nucleation, growth, and replication of protocells on the early Earth. Recent reports have shown evidence that moderately high temperatures not only permit protocell assembly at the origin of life, but can have actively supported it. Here, the fast nucleation and growth of vesicular compartments from autonomously formed lipid networks on solid surfaces, induced by a moderate increase in temperature, are shown. Branches of the networks, initially consisting of self-assembled interconnected nanotubes, rapidly swell into microcompartments which can spontaneously encapsulate RNA fragments. The increase in temperature further causes fusion of adjacent network-connected compartments, resulting in the redistribution of the RNA. The experimental observations and the mathematical model indicate that the presence of nanotubular interconnections between protocells facilitates the fusion process.

In a recent report, we showed the autonomous formation and growth of surface adhered protocell populations as a result of a sequence of topological transformations on a solid substrate.^[3] Briefly, upon contact with a mineral-like solid substrate, a lipid reservoir spreads as a double bilayer membrane. The distal membrane (upper bilayer with respect to the surface) ruptures and forms a carpet of lipid nanotubes. Over the course of a few hours, fragments of these nanotubes swell into giant, strictly unilamellar vesicular compartments. This relatively slow process is entirely self-driven and only requires a lipid reservoir as source, a solid surface, and surrounding aqueous media. The resulting structure consists of thousands

1. Introduction

The important role of solid surface support for the autonomous formation of primitive protocells has been suggested earlier in the context of the origin of life.^[1,2] Hanczyc et al. showed that vesicle formation from fatty acids was significantly enhanced in the presence of solid particle surfaces consisting of natural minerals or synthetic materials.^[1,2] Particularly the silicate-based minerals accelerated the vesicle generation.

of lipid compartments, which are physically connected to each other via a network of nanotubes. This formation process and the ability of these compartments to encapsulate ambient molecules, and to separate and migrate to remote locations, lead to the formulation of a new protocell hypothesis.^[4] This addresses open questions about how primitive protocells might have formed and replicated on the early Earth, what exact physico-chemical mechanisms governed the growth and division of the membranes, and how cargo, e.g., RNA or other contents, was encapsulated and distributed. Prevailing hypotheses involving the self-assembly of amphiphiles in bulk aqueous medium explain the formation of protocells, but not the necessary subsequent steps, e.g., growth, replication, division, in a satisfactory manner.

In the former study, which was conducted at constant room temperature, the protocell nucleation and growth are slow processes occurring over the course of hours to days.^[3] Under natural conditions, fluctuations in temperature are expected, the impact of which on the reported system has not been considered. Since the growth process is slow, the compartments often do not reach sizes large enough to establish physical contact in a reasonable time frame, and remain too far apart for fusion. Fusion has been considered a feasible means of protocell growth, a step required for self-proliferation.^[5] In addition, the mechanical or osmotic stress on bilayer compartments can over time lead to the collapse of vesicular structures.^[6]


In our current study we show that a temperature increase significantly accelerates the formation of membrane compartments and further initiates their fusion, which supports the recent findings of Jordan et al.^[7] The accelerated nucleation and growth lead to maturation of compartments, which eventually

E. S. Köksal, L. Xue, Dr. I. Gözen
Centre for Molecular Medicine Norway
Faculty of Medicine
University of Oslo
Oslo 0318, Norway
E-mail: irep@uio.no

Dr. S. Liese, Dr. A. Carlson
Department of Mathematics
Faculty of Mathematics and Natural Sciences
University of Oslo
Oslo 0315, Norway

R. Ryskulov, Dr. L. Viitala, Dr. I. Gözen
Department of Chemistry and Chemical Engineering
Chalmers University of Technology
Göteborg SE-412 96, Sweden

Dr. I. Gözen
Department of Chemistry
Faculty of Mathematics and Natural Sciences
University of Oslo
Oslo 0315, Norway

 The ORCID identification number(s) for the author(s) of this article can be found under <https://doi.org/10.1002/smll.202002529>.

DOI: 10.1002/smll.202002529

establish physical contact. The adjacent vesicular membranes fuse, resulting in redistribution of cargo, e.g., oligoribonucleotides. Nucleation and transformations strictly occur on the lipid nanotube networks and creates consistently and exclusively unilamellar membranous compartments. In addition to the experiments, we provide a finite element model which emphasizes that the presence of nanotubular connections between protocells facilitates the fusion. The findings can explain how protocells on the early Earth might have undergone rapid growth and replication, and provide new insight into our recently developed nanotube–protocell network hypothesis.^[4]

2. Results

2.1. Enhanced Protocell Formation and Growth

We deposited a multilamellar reservoir on a SiO₂ surface. Note that the choice of substrate material has a profound influence on the nature of the surfactant film formed on the surface. On silicon dioxide the formation of a lipid double bilayer occurs consistently by spreading.^[8] The reservoir spontaneously spreads on the surface in form of a circular double bilayer membrane.^[9] The distal of the two stacked bilayers (upper bilayer with respect to the surface), ruptures due to continuous tensile stress,^[9] resulting in formation of a network of nanotubes on the proximal bilayer.^[3] Fragments of the nanotubes swell over time, and form unilamellar vesicular compartments. The autonomous transformation of lipid reservoirs into networks of surface-adhered protocells interconnected by lipid nanotubes, has been described by Köksal et al.^[3]

This precursor structure is a lipid nanotube network residing on a bilayer patch (Figure 1a). Each liquid-filled nanotube has a cylindrical cross-section and consists of a single bilayer (inset to Figure 1a).^[3] Next, we engage an IR-B ($\lambda = 1470$ nm) laser to achieve a mild temperature increase in the vicinity of the membrane (Figure 1b).^[10] The IR radiation is applied through an optical fiber positioned by means of a mechanical micro-manipulator on an inverted microscope (Section S1, Supporting Information). The position of the IR-laser fiber tip with respect to the lipid nanotube-covered membrane region is indicated by the yellow dashed lines in Figure 1c. Due to the flat fiber tip, the laser radiation is not focused, but affects a cone-shaped water volume that extends to the solid surface. Details of the experimental setup are shown in Figure S1 of the Supporting Information. The formation of giant unilamellar vesicles from disordered membrane layers induced by localized heating (>25 °C) has been reported before.^[11,12] In our experiments, the thermal gradient leads to the instant formation and growth of vesicular compartments exclusively from the lipid nanotubes (Figure 1b). The formed compartments are strictly unilamellar^[3] which is in contrast to the vesicles reported by Billerit et al.^[11,12] where a lamellarity distribution typical for swelling of stacked bilayers was observed. The majority of techniques for artificial vesicle generation feature this distribution.^[13,14] Figure 1c–e (Movie S1, Supporting Information) show the laser scanning confocal microscopy time series of the process schematically described in Figure 1a,b. Over the course of a few minutes of IR exposure, the unilamellar compartments form from the lipid

nanotubes and rapidly grow (Figure 1d,e). The fiber is positioned above the sample at a tilted angle, therefore the beam projects onto an ellipse-shaped area, clearly visible from the distribution of the protocells in Figure 1d,e. The image series in Figure 1f–k (Movie S1, Supporting Information) demonstrate that the formed compartments are colocalized with the nanotubes. During growth the compartments maintain their positions. In Figure 1l,m the transformation from tube to spherical compartment, is schematically shown. Due to the temperature increase, the membrane viscosity is reduced and tension increases, leading to rapid inflow of lipids from low tension areas. Combined with a reduction of the high membrane curvature, this results in minimization of the surface free energy of the system,^[3] which is the driving force for the transformation.

Figure 2a (Movie S1, Supporting Information) is a snapshot from a confocal time series of a heated membrane region, showing protocell growth. We created 31 elliptical rings (a quarter of each shown as a yellow dashed line) on the membrane and calculated the protocell densities, i.e., the number of protocells per area between two consecutive rings ($\Delta A r_x$). An exception is the smallest ellipse at the center which is considered as a whole. Figure 2b is a plot of the protocell density in each ring versus the minor ellipse radius (r_x) in Figure 2a. The graph indicates that the protocell density increases with the temperature, which, due to the acceptance-cone of the fiber is gradually decreasing with distance from the center. The image series in Figure 2c–f shows a membrane section decorated with lipid nanotubes, progressing to vesicular compartments. The confocal scans were recorded close to the proximal membrane (panel e), and across the equator of the vesicular compartments (panel d). Panel (f) is a 3D reconstruction of the nanotube-adhered protocells in panels (d and e). For comparison, five selected compartments in the different panels of Figure 2e,f are marked with numbers.

We used a microthermocouple to determine the temperature of the affected region in the experiments. The details of the measurement have been presented in Section S2 of the Supporting Information. The estimated temperatures are 40–90 °C. ≈ 40 °C leads to rapid nucleation, and ≈ 70 °C to rapid growth. ≈ 90 °C results in fusion of the compartments, which will be described in detail below.

For the membrane section depicted in Figure 2c–f (Movie S3, Supporting Information), the total count of the protocells versus time is shown in Figure 2g, and the average protocell diameter versus time in Figure 2h. The compartments nucleate instantly with activation of the IR-laser. Their number remains constant (Figure 2g), while their diameter is increasing (Figure 2h). The size distribution of the protocells at five different time points throughout the experiment is shown in Figure 2i. Small protocells ($d < 1$ μm) dominating at the early stages (orange histogram), later evolve into larger protocells ($d > 3$ μm , blue and purple histograms). The development of the membrane area and the internal volume of the protocells during the experiment (Figure 2c–f) is shown in Figure 2j. The total membrane area was ≈ 1250 μm^2 at the end of the experiment. This corresponds to a nanotube of 4 mm length ($\varnothing = 100$ nm). We do not observe such a high tubular density in Figure 2c. The membrane material forming the protocells therefore likely originates from a remote membrane reservoir and migrates through the nanotubes.^[15,16] A comparison between panel (c) and (e) reveals that

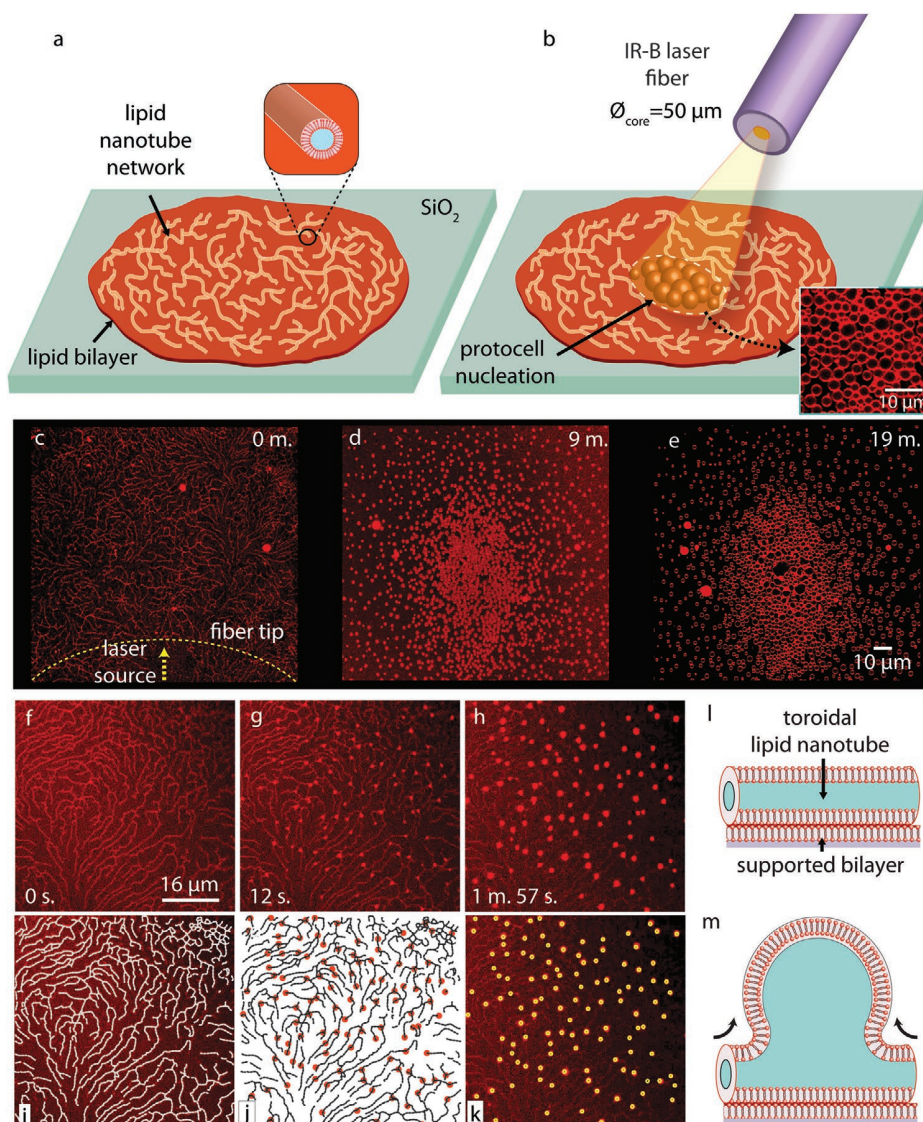


Figure 1. Heat-induced protocell formation from surface-adhered lipid nanotubes. a,b) Schematic drawing summarizing the experiment. (a) Network of hollow lipid nanotubes (inset) is residing on a SiO₂-adhered bilayer. (b) Rapid formation of protocells from the nanotubes as a result of mild heating. Inset on the lower right corner shows the confocal image of protocells formed as a result of this process. All experiments have been performed in biological buffers. c–e) Laser scanning confocal microscopy time series of the process schematically described in (a) and (b). f–k) Confocal images showing that the formed compartments and the nanotubes have colocalized. During growth, the compartments maintain their positions. (l) The outline of the nanotubes in panel (f). (j) The positions of the nucleation sites in (g), indicated with the red circles, are superimposed on the network outlined in (i). (k) The positions of the nucleation sites in (g and j) are superimposed on the image in (h). l–m) Schematic drawing depicting the transformation from a nanotube to a vesicular compartment.

the majority of the nanotubes remain intact. This means that they are not the major source of protocells formed in the process. Provision of the membrane material through the proximal bilayer is in principle also possible, but we have earlier presented the argument that this is rather unlikely.^[3]

2.2. Protocell Fusion

We observe that the temperature increase further induces fusion of adjacent compartments. **Figure 3a,b** shows a mem-

brane region in which rapid merging was observed. In **Figure 3a** the protocells are shown before fusion, and in **Figure 3b** after fusion. The areas in which fusion of two or more compartments occurs, are encircled in white dashed lines and numbered (panel a). The merged compartments are represented in **Figure 3b** by the same numbers. **Figure 3c** shows the number (orange graph) and average diameter (blue graph) of the protocells shown in **Figure 3a,b** over time (cf., Section S3 for details of the image analyses). The total number of compartments decreases, and the average diameter increases accordingly (panel c). The images in **Figure 3** (Movies S4 and S5, Supporting Information) show

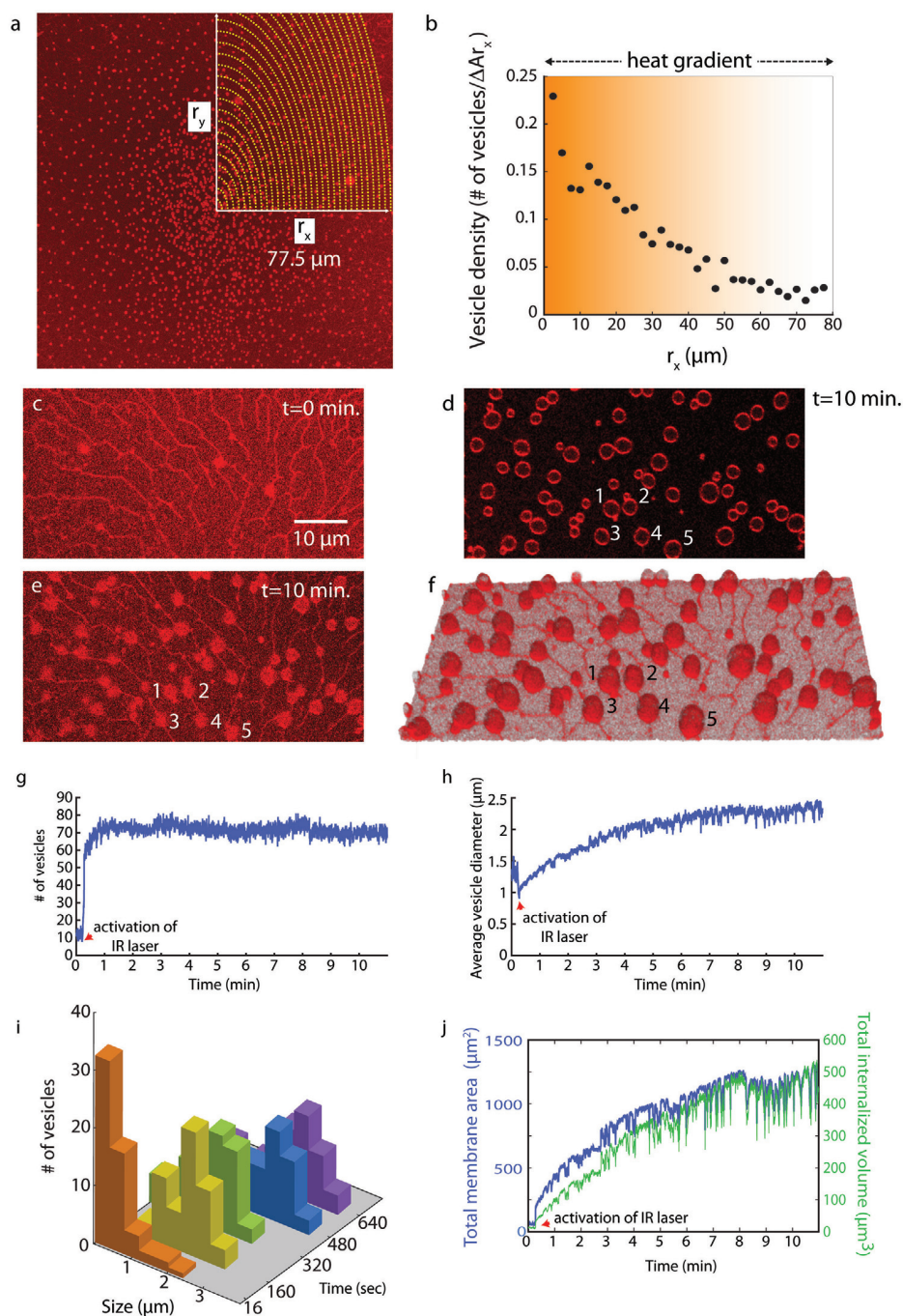


Figure 2. Characterization of protocell formation and growth induced by a mild heat gradient. a) laser scanning confocal image of a large membrane region with nucleating protocells. The area exposed to the IR laser is split to 31 hypothetical elliptical rings, the minor radius of which is expressed as r_y and the major radius, r_x . A quarter of the outline of each ring is shown in yellow dashed lines. r_x of the outmost ring is $77.5 \mu\text{m}$. b) Plot showing the protocell density over distance r_x . The protocell density is calculated as the number of protocells in each individual elliptical ring. c–f) Confocal images of a nanotube network leading to nucleation and growth of protocells exposed to heat gradients for 10 min. c) Nanotube network before local heat exposure (d) cross-section of protocell sample from the equator after heat exposure (top view). (e) Cross-section of sample close to the surface after heat exposure (top view). (f) 3D reconstruction of the formed protocells. Plot showing g) the number and h) the average diameter of the protocells formed in (c–f) over 10 min. i) The histograms depicting the size distribution of protocells over time. Each color represents the size distribution at a given time point. j) Plots showing total membrane area and total membrane volume of the protocells in (c–f) during their formation and growth.

different surface regions of the same confocal microscopy recording. The black arrows in panel (c), labeled with panel names, indicate the time points at which the corresponding images were recorded.

We explored whether fusion events only occur among the compartments residing on the same nanotube, or if the fusion between compartments on different nanotubes is possible. We therefore investigated membrane regions of known network topology. Figure 3d–g,h–k shows the fusion of two different sets of compartments, each set residing on the same nanotube (black dashed lines). Three compartments marked with green asterisks in Figure 3d merge into a single protocell within a few seconds (panels e–g). In Figure 3h–k, five protocells (yellow asterisks) merge. In both cases, the fusing protocells reside on the same nanotube. If protocells located on different nanotubes grow and eventually establish physical contact, we also observe fusion events. Figure 3l–p (red asterisks) and Figure 3q–u (blue asterisks) depict two examples. The original positions of the nanotubes in each recording are indicated by black dashed lines (Figure 3l,q).

2.3. Mechanism of Fusion

Increase in temperature results in an increase in fluidity of the membrane, leading to the rapid fusion of the initially distinct, adjacent membranes.^[17,18] Upon fusion, the membranes relax to a form that minimizes the membrane energy. The transformation from two small containers to a single large one reduces the curvature, while the membrane area is maintained. In our experiments, fusion of nanotube-connected lipid compartments can occur in two different ways: it either begins near their equator, i.e., where their lateral extension is the largest and the compartments touch first (Figure 4a), or they fuse at the base, mediated by the connecting membrane nanotube (Figure 4b). In order to determine which of these two scenarios is energetically the most favorable, we performed a set of numerical finite element simulations (cf., Section S4, Supporting Information, for details).^[19,20] Since the thickness of the lipid bilayer (≈ 5 nm) is much smaller than the typical size of the membrane tube (>100 nm) and the attached compartment (>1 μm), we treated the membrane as a thin elastic surface. For the simulation, we considered two adjacent vesicular compartments of the same size, where the compartments share a surface-adhered membrane tube. The edges of the numerical domains were defined by open nanotubes which were restricted to form a cylinder of radius r_t . The tube length was set to $15 r_t$ and the total membrane area to $450 r_t^2$. In dimensional units this corresponds to two spherical compartments, each with a diameter of ≈ 0.4 μm , connected through a tube with a diameter of ≈ 100 nm.

We keep the membrane area in the simulations constant such that the membrane shape and energy are solely determined by the minimization of the bending energy. In the initial configuration, the two compartments either form a fusion pore (neck) near their equator (Figure 4a), or they fuse by consuming the nanotube (Figure 4b). In both cases the bending energy of two well separated compartments, i.e., narrow neck with small Δl_n , is similar to the energy of two independent spherical compartments. In the latter case, we consider the

portion of the tube that connects the two compartments, the neck region. In each simulation the circumference of the neck is kept constant, while the position of the neck is free and hence determined by the energy minimization. Figure 4c shows the development of the bending energies for fusion initiated at the equator (squares) and at the tube (circles), as we systematically increase the neck circumference Δl_n . We obtain the bending energy, according to the Helfrich theory^[21] by integrating the square of the mean curvature H over the membrane surface area A : $E = \int dA \frac{\kappa}{2} H^2$, where κ is the bending rigidity. The energy is normalized by the bending energy of a spherical vesicle, $E_{\text{sph}} = 8\pi\kappa$. If the vesicle fusion starts at the tube, we observe an increase in neck circumference Δl_n . Note that in this case the initial circumference $2\pi r_t$ is subtracted. As the neck expands, the vesicles fuse and the surface free energy decreases. For vesicle fusion at the base, the energy approaches that of a single spherical vesicle. By contrast, for vesicles fusing at the equator, the energy reaches a plateau that is about 75% larger than the energy of a spherical vesicle. If the vesicles start to fuse at their equator, a circular pore forms between the fusion site and the membrane tube. Our simulations show that the pore stabilizes with a diameter (IV in Figure 4a) similar to the diameter of the membrane tube (Figure 4d). The fusion process should predominantly start at the tube, since this scenario is energetically more favorable and allows for complete fusion of the two vesicles (cf., Section S4, Supporting Information, for model, and Section S5, Supporting Information, for corresponding experimental observations).

2.4. Encapsulation and Redistribution of RNA upon Fusion

In order to investigate the merging of the contents of fusing compartments, we employed an open-space microfluidic pipette^[22] and loaded several compartments with fluorescently labeled RNA oligomers (Figure 5a). Open-space microfluidic delivery is an effective means to create a local chemical environment. Subsequently applied mild heating led to the fusion of the RNA-loaded protocells with adjacent, initially unloaded compartments, and the RNA oligomers were redistributed (Figure 5b). Figure 5c (Movie S7, Supporting Information) shows the loading process: a population of surface-adhered protocells in the recirculation zone of the microfluidic device, dispensing a solution containing fluorescent RNA fragments (top view). The border of the recirculation zone is marked with white dashed lines (Figure 5c). Initially, the protocells appear as black dots within the recirculation zone, since they only contain buffer (Figure 5c). Over time, some of the protocells encapsulate the RNA fragments (Figure 5d). Encapsulation of water-soluble fluorescein inside the surface-adhered protocells was shown earlier in a similar experiment at ambient temperature,^[3] and explained by the involvement of transient pores of sufficient size and stability. We observe that the encapsulation efficiency of RNA oligomers is significantly smaller than of fluorescein (cf., Section S6, Supporting Information, for comparative experiments). We attribute this to both the size and the charge differences between the molecules. Figure 5e–m is a sequence depicting how the RNA fragments are redistributed

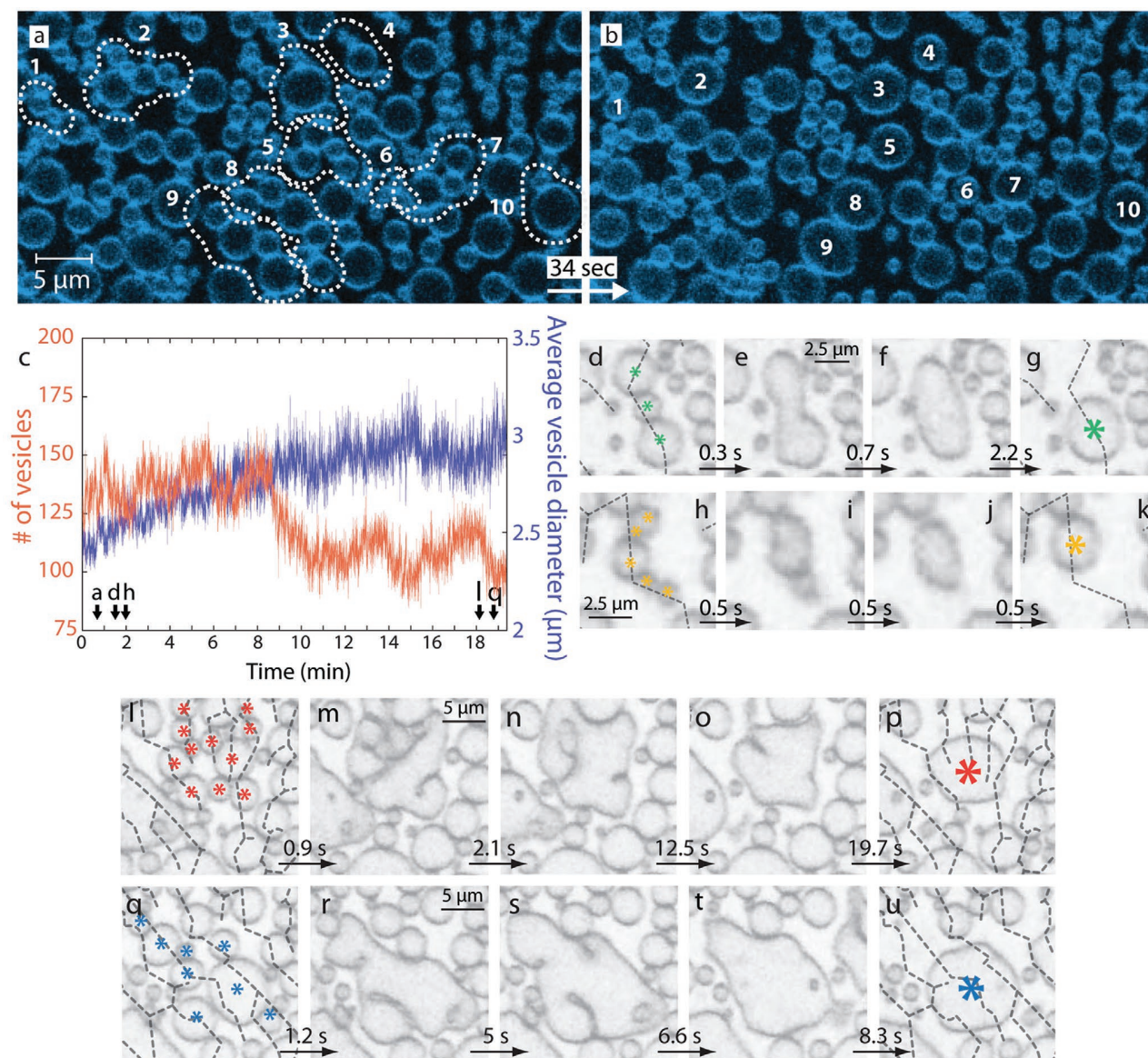


Figure 3. Heat induced protocell fusion. a,b) Confocal images showing the fusion of several protocells formed out of a lipid nanotube network upon exposure to the IR laser. The blue color assigned to the labeled lipid membranes is resulting from the false coloring of the gray scale images of the fluorescence signals, and is assigned arbitrarily. (a) The group of protocells which later merge after exposure to heat gradient, are encircled with dashed lines. Each encircled region is numbered. (b) The merged protocells. Each protocell has been formed or grown as a result of the fusion of the multiple, originally separated protocells shown in (a). The group of protocells and their fused version are numbered identically in (a) and (b). c) Plots showing the number of protocells (orange graph) and average protocell diameter (blue graph) over the complete course of the experiment partly shown in (a and b). d–k) Protocell fusion on same nanotube. (d–g) and (h–k) Two different fusion events in which the protocells on the same nanotube rapidly merge. l–u) Fusion of protocells which are originally located on separate nanotubes. (l–p) and (q–u) Two different events during which vesicular compartments, originally located on different nanotubes, later fuse.

during fusion. Figure 5c–g shows both the membrane and the RNA fluorescence emission channels, Figure 5h–j the membrane, and Figure 5k–m the RNA. Figure 5n–p shows the fluorescence intensity along the lines indicated with white dashed arrows in Figure 5k–m, respectively. The initially separate signals in Figure 5n merge into a signal of lower intensity (Figure 5o,p). The decrease may be due to two reasons. Upon activation of the IR laser the fluorescence intensity is

reduced.^[23] It is also possible that some of the internal contents is lost by leakage. The closure of the pores and retaining of the bulk of the encapsulated material is consistent with our earlier experiments of ≈ 3 orders of magnitude longer duration (seconds vs hours). Figure 5r–t (Movie S7, Supporting Information) shows snapshots of the fusion process of three compartments. In Figure 5s depicts the diffusion of fluorescent fragments during shape optimization of merging containers.

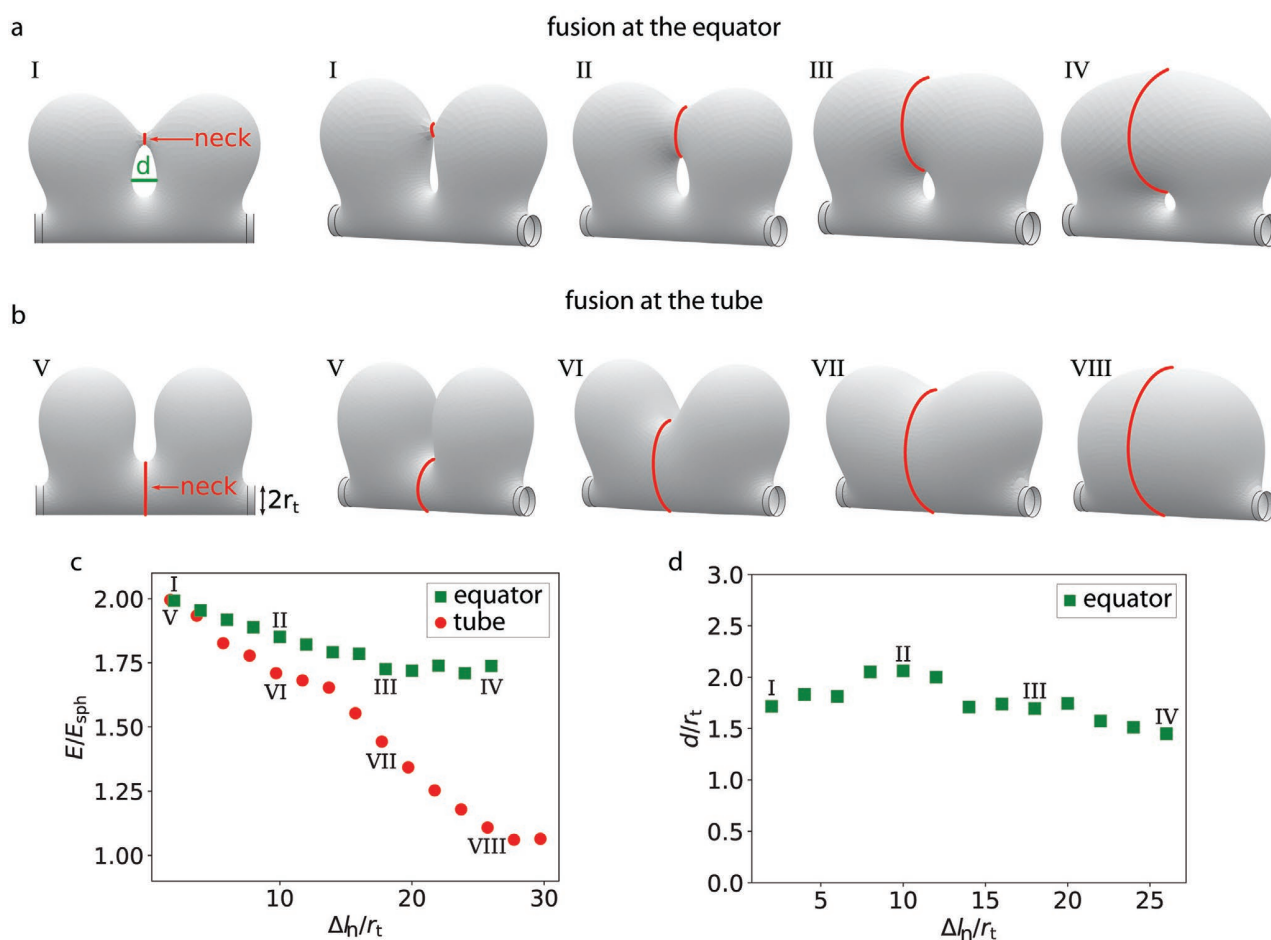


Figure 4. Mathematical model for fusion. Two compartments of equal size are connected to a membrane tube with diameter $2r_t$. Simulation snapshots are shown as the compartments fuse either a) at the compartments' equator region or b) at the connecting tube. The outer left snapshots on (a) and (b) show a side view parallel to the membrane tube, while the other snapshots are tilted to better illustrate the expansion of the fusion neck. c) The bending energy E , rescaled by the bending energy of the spherical compartment E_{sph} , decreases as the length of the contact line Δl_c increases. d) If the compartments fuse initially at their equator, a cavity forms between the fusion site and the membrane tube, with a stable diameter d that is similar to the diameter of the membrane tube.

3. Discussion

3.1. Protocell Nucleation Sites

Figure 2g reveals that, once the protocells nucleate, their total number remains constant during growth. This indicates that the sites of the nucleation are predetermined and nucleation is enhanced by the increased temperature. In Figure 1j the locations of the nucleation appear to coincide with Y- and V-junctions^[24] on the nanotubes. Such membrane topologies are caused by pinning, i.e., simultaneous binding of Ca^{2+} to multiple lipid head-groups, which is facilitating the cohesion between two stacked bilayers^[9,25,26] or between a bilayer and a solid interface.^[9,27,28] In a previous study, the transformation of a Y-junction to a small vesicle, due to chemical chelator-induced depinning of Ca^{2+} , has been already shown.^[24] In the current study, the Ca^{2+} depinning and reversal of membrane adhesion is not caused by chelators, but is due to the temperature increase.^[10] The compartments are also observed exclusively at junction points (Figure 1j).

3.2. Mechanism of Rapid Growth and Fusion

The main driving force for the transformation of the nanotubes to protocellular compartments is the minimization of membrane curvature. The natural growth process in the previously reported system was slow ($\approx h$).^[3] The membrane replacement rate for the spontaneous inflation of a tube to a $5 \mu m$ vesicle, was estimated to be $\approx 2 \times 10^{-3} \mu m^2 s^{-1}$.^[3] By contrast, in the current study the transformation occurs within minutes. We estimate the replacement rate to be $2 \mu m^2 s^{-1}$, about three orders of magnitude higher than observed at room temperature. We attribute the facilitated protocell growth to the enhanced ability of lipid material to flow to the area of nucleation, due to the temperature increase in that area. The locally elevated temperature causes an increase in the membrane fluidity and in the membrane tension in the affected area. The tension increase causes Marangoni flow of lipids in the surrounding membrane region with relatively low membrane tension, toward the heated membrane region with high tension.

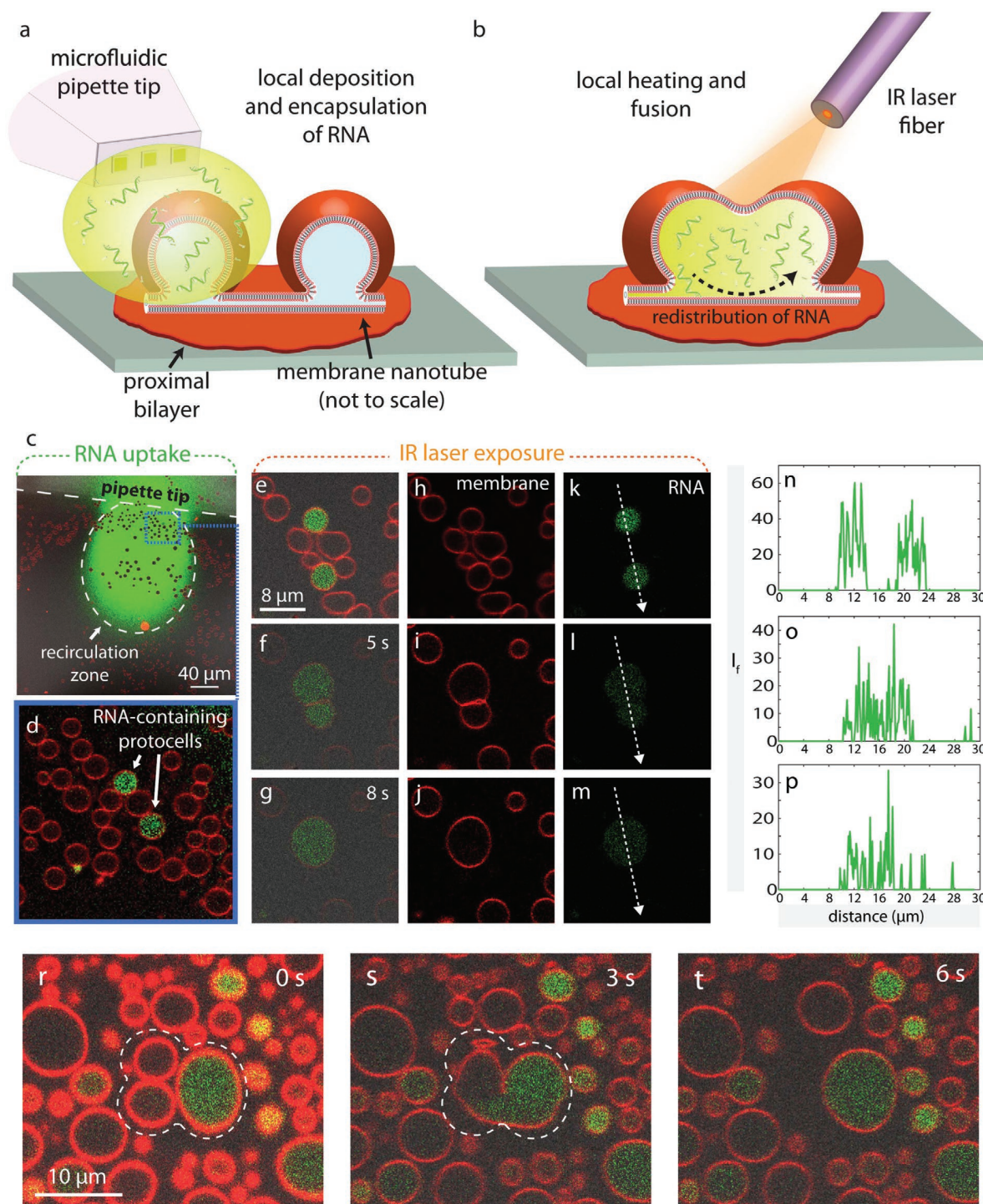


Figure 5. RNA encapsulation and redistribution. a,b) Schematic drawing showing the experimental setup. (a) An open-space microfluidic device is used for the superfusion of RNA-oligonucleotides with a designated membrane area populated with protocells. (b) IR laser is activated to induce fusion, leading to the redistribution of pre-encapsulated RNA into the fused protocell. c,d) RNA uptake. (c) Confocal image of a membrane area with the microfluidic pipette recirculating RNA above it (top view). The protocells in the recirculation zone appear as black dots. (d) Magnified view of the blue frame in (c) after termination of recirculation. Two protocells contain RNA. e–m) Laser scanning confocal microscopy images showing the fusion of RNA encapsulating protocells and redistribution of contents upon fusion. (e–g) Membrane, RNA fluorescence, and bright field channels are overlaid. (h–j) Membrane fluorescence channel only. (k–m) RNA fluorescence channel only. n–p) Plots showing the fluorescence intensity over the white dashed arrows in (k), (l), and (m), respectively. r–t) Laser scanning confocal microscopy images showing the fusion of RNA-encapsulating protocells and redistribution of contents upon fusion. Membrane, RNA fluorescence, and bright field channels are overlaid.

The result is the rapid growth of previously nucleated vesicular buds to cell-sized unilamellar compartments, some of which eventually establish physical contact with each other.

Fusion of lipid compartments that are in close proximity does not occur spontaneously, but requires external stimuli. There have been several studies focusing on the fusion of giant amphiphile vesicles as model systems of proto- or contemporary cells. The reported fusion mechanisms vary. Some examples are the fusion driven by attraction of oppositely charged vesicles,^[29] fusion induced by multivalent ions between vesicles of special amphiphilic compositions, e.g., Eu³⁺^[30] or La³⁺,^[31] ultraviolet light radiation-induced fusion,^[32] electrofusion,^[33] fusion involving amphiphilic catalysts,^[34] also in combination with thermal cycles and pH changes,^[35] and the fusion mediated by the hybridization of complementary SNARE proteins^[36] or DNA linkers,^[37] embedded in initially distinct vesicle membranes.

The vesicular membranes we utilize in this study do not contain embedded species which would facilitate fusion. The membranes and their individual monolayer leaflets possess the same composition, thus they are free of spontaneous curvature and have the same electrostatic potential. All experiments are performed at constant pH, under identical conditions. The main stimulus for fusion is the controlled increase in temperature. The temperature increase is known to lower the microviscosity of the membrane and facilitate the formation of defects, especially in the presence of multivalent ions.^[38,39] Ca²⁺ binding perturbs the membrane by pulling the headgroups inward,^[25,38] causing formation of defects. With localized heating this process is facilitated,^[39] resulting in fusion.^[40]

3.3. Impact of Nanotubes in Growth and Fusion

Figures 3 and 4 show that the nanotubes, which physically connect distant protocells, facilitate fusion. During growth, the nanotubes can provide an additional advantage for compound delivery. They provide a transport pathway for a continuous influx of molecules through the network, by which larger molecules can potentially also be transported. The transport of molecules or particles through nanotubes occurs by diffusion,^[41,42] or is tension-driven (Marangoni flow).^[15,16] The transport phenomena within the nanotube networks have not been investigated here, but the earlier established evidence of nanotube-enhanced transport between lipid vesicles combined with the involvement of nanotubes in the fusion process, as elucidated in this study, points to a beneficial contribution of an existing tubular network for growth, transport, and fusion of protocells.

3.4. Impact of Temperature in the Context of Origin of Life

In this study we show that a successive increase in temperature from 20 °C to ≈40, 70, and 90 °C on a nanotube network facilitates the nucleation, growth, and fusion of surface adhered protocells. The role of temperature has been a central discussion point in the origin of life debate.^[43] The competing hypotheses regarding the environment for the emergence of the RNA

world, concentrate either around deep ocean hydrothermal vents, or around warm ponds.^[43] A major criticism for the emergence of life in hydrothermal environment^[44] has been the hot temperatures, large pH gradients, high salinity, and high concentrations of divalent cations, which may adversely affect the amphiphile compartment formation. The hot environments typically referred to in such discussion involve black smoker type hydrothermal vents where temperature can commonly exceed 300 °C. In 2000, a new type of hydrothermal vent: the Lost City hydrothermal field (LCHF) with a chemical composition similar to lavas that erupted into the primordial oceans on early Earth, was discovered.^[45] The temperature range of the LCHF is 40–90 °C, surprisingly similar to the experimental conditions used in this work that promote compartment formation, growth and fusion. This temperature range also represents the conditions in warm ponds: 50–80 °C.^[43] Recent evidence shows that the mixtures of single chain amphiphiles form vesicles most readily at temperatures of ≈70 °C in aqueous solutions containing mono- and divalent cations in broad pH range.^[7] In the light of these observations, it appears that warm temperatures of ponds or LCHFs can allow and even favor protocell compartmentalization. Our investigation focusing on the subsequent steps, i.e., the rapid growth and fusion, is in alignment with these recent findings.

Apart from temperature, another point disfavoring the hydrothermal vent hypothesis over the warm pond hypothesis, has been the lack of dry-wet cycles, which is known to significantly facilitate polymerization, e.g., from nucleotides to RNA.^[43] In our experiments, the lipid reservoirs, i.e., multilamellar vesicles (MLVs), from which the double bilayer films spread and proceed to protocell formation, are the product of a dry-wet cycle. The lipid layers form in a dry environment and upon hydration they spontaneously form MLVs. It is conceivable that this is a repeatable process. Accordingly, protocell formation, growth, and fusion events we report here can in principle occur during dry-wet cycles. Potentially, a new cycle of protocell formation–growth–division can be started by attachment and fusion of fresh lipid reservoirs, i.e., multilamellar vesicles, to protocells that have been generated, grown, separated, and resettled on the substrate. It should be possible to experimentally investigate if simulated dry–wet, day–night, heating–cooling cycles support the formation of new protocell generations.

4. Conclusion

We show that the nucleation, growth, and fusion of protocells are significantly accelerated and enhanced at temperatures ranging from 40 to 90 °C. Some of the protocells generated in this manner have been demonstrated to encapsulate RNA, and to redistribute it upon fusion with other compartments. In the context of protocell development on the early Earth, these results suggest that both Lost City-type hydrothermal vents, and warm ponds could have been a suitable environment for protocell formation, growth, and fusion events. Additionally, a supporting surface in conjunction with the physical interconnections provided by the spontaneously formed nanotubular networks pose an advantage over lipid assemblies in bulk solution. Neighboring vesicles can join and fuse more rapidly

than in bulk suspensions, where protocells would only randomly encounter each other for limited periods of time. To what extent it is possible for emerging protocells to chemically communicate prior to, and during, fusion processes through interconnecting tubes remains to be elucidated. If this can be verified, new hypotheses for primordial chemical transformations within primitive membrane structures in the early Earth environment can be experimentally investigated.

5. Experimental Section

Surface Fabrication and Characterization: An ≈ 84 nm SiO_2 film was deposited onto Menzel Gläser (rectangular) or Wilco Well (circular) glass substrates by either E-beam, or thermal Physical Vapor Deposition, using an EvoVac (Ångström Engineering) or L560K (Leybold) evaporator. The thickness of the films was verified by ellipsometry (SD 2000 Philips). No precleaning was performed before deposition. The substrates were stored at room temperature prior to use.

Formation of Lipid Nanotube Network and Protocells: The lipid nanotube network on a solid supported bilayer was formed as described earlier.^[3] Briefly, a stock suspension of multilamellar lipid reservoirs containing 50% soybean polar lipid extract, 49% *Escherichia coli* polar lipid extract, and 1% Rhodamine-PE or Cy5-PE was prepared by the dehydration/rehydration method.^[46] An aliquot from this suspension (4 μL) was dehydrated in a desiccator for 20 min. The dry film was rehydrated with HEPES buffer (≈ 1 mL) containing HEPES (10×10^{-3} M) and NaCl (100×10^{-3} M), pH 7.8, for 10 min to form multilamellar reservoirs. The reservoirs were then transferred into an open-top observation chamber on a SiO_2 substrate. The chamber contained HEPES buffer (≈ 1 mL) with HEPES (10×10^{-3} M), NaCl (100×10^{-3} M), and CaCl_2 (4×10^{-3} M), pH = 7.8. On the SiO_2 substrate the reservoirs self-spread as a double bilayer. The distal bilayer ruptures,^[9] and a nanotubular network forms on the proximal bilayer.^[3] Protocells on nanotubes were either formed spontaneously overnight (RNA redistribution experiments) or within seconds or minutes using local IR-B radiation (nucleation, growth, and fusion).

Heating System: The lipid nanotube network was heated locally using IR-B laser radiation through a flat optical fiber tip. A 1470 nm semiconductor diode laser (Seminex) in combination with a 50 μm core diameter, 0.22 NA multimode optical fiber (Ocean Optics), was used. The fiber was prepared by removing the outer sheath cladding, followed by carefully cutting and polishing using a fiber cleaning kit (Ocean Optics). The fiber was positioned using a 3-axis water hydraulic micromanipulator (Narishige, Japan) and the tip was located at 50 μm from the surface, resulting in a volume of ≈ 1 nL being efficiently heated. Three different laser intensities were employed. The laser current was adjusted to 0.72 A (protocell nucleation), 0.97 A (growth), and 1.21 A (fusion). The temperature was determined directly by a microthermocouple in situ (cf., Section S2, Supporting Information, for details).

Encapsulation with Microfluidic Pipette: An open-volume microfluidic device/pipette (Fluicell AB, Sweden),^[22] positioned using a second 3-axis water hydraulic micromanipulator (Narishige, Japan), was used to expose the matured surface-adhered protocells to Ca^{2+} -HEPES buffer containing fluorescein sodium salt (100×10^{-6} M) (Sigma-Aldrich) and FAM-conjugated RNA oligonucleotides (40×10^{-6} M) (Dharmacon, USA), at pH 7.8.

Microscopy Imaging: A confocal laser scanning microscopy system (Leica SP8, Germany), with an HCX PL APO CS 40x (NA 1.3) oil objective was used for acquisition of the confocal images. The utilized excitation/emission wavelengths for the imaging of the fluorophores, were as follows: λ_{ex} : 560 nm, λ_{em} : 583 nm for membrane fluorophore Rhodamine-PE, λ_{ex} : 655 nm, λ_{em} : 670 nm for Cy5, λ_{ex} : 488 nm, λ_{em} : 515 nm for fluorescein (SI), λ_{ex} : 494 nm, λ_{em} : 525 nm for FAM.

Image Processing/Analysis: 3D fluorescence images were reconstructed using the Leica Application Suite X Software (Leica Microsystems,

Germany). Image enhancements to fluorescence images were performed with the NIH Image-J Software and Adobe Photoshop CS4 (Adobe Systems, USA). The colors assigned to the labeled lipid membranes (red and blue) and to labeled RNA (green) are resulting from the false coloring of the gray scale images of the fluorescence signals, and are assigned arbitrarily. Schematic drawings and image overlays were created with Adobe Illustrator CS4 (Adobe Systems, USA). Protocell counts, density, size distribution, total membrane area, and volume analyses were also performed in Image-J and plotted in Matlab R2018a. The analysis of protocell number and size over time during fusion was performed with Matlab. Fluorescence intensity profiles were drawn in Matlab after applying median filtering.

Supporting Information

Supporting Information is available from the Wiley Online Library or from the author.

Acknowledgements

The authors thank A. Jesorka from Chalmers University of Technology, Sweden, for technical advice on temperature measurements. This work was made possible through financial support obtained from the Research Council of Norway (Forskingsrådet), Project Grant No. 274433, UiO: Life Sciences Convergence Environment, the Swedish Research Council (Vetenskapsrådet), Project Grant No. 2015-04561, as well as the startup funding provided by the Centre for Molecular Medicine Norway (RCN 187615), and the Faculty of Mathematics and Natural Sciences at the University of Oslo. S.L. and A.C. gratefully acknowledge funding from the Research Council of Norway, Project Grant No. 263056, and R.R. the H2020 ITN “Chemical Reaction Networks – CReaNET” – Ref. 812868.

Conflict of Interest

The authors declare no conflict of interest.

Author Contributions

E.S.K. and I.G. designed the research, E.S.K., S.L., L.X., R.R., A.C., and I.G. performed the research, E.S.K., L.X., R.R., and L.V. analyzed the experimental data, and all authors contributed to the drafting of the paper. I.G. suggested the investigation of the behavior of lipid compartments in thermal gradients and supervised the project.

Keywords

lipid nanotubes, origin of life, protocells, temperature-induced fusion

Received: April 21, 2020

Revised: June 26, 2020

Published online: August 9, 2020

[1] M. M. Hanczyc, S. S. Mansy, J. W. Szostak, *Origins Life Evol. Biospheres* **2007**, *37*, 67.

[2] M. M. Hanczyc, S. M. Fujikawa, J. W. Szostak, *Science* **2003**, *302*, 618.

[3] E. S. Koksals, S. Liese, I. Kantarci, R. Olsson, A. Carlson, I. Gozen, *ACS Nano* **2019**, *13*, 6867.

- [4] İ. Gözen, *ACS Nano* **2019**, *13*, 10869.
- [5] B. Xu, J. Xu, T. Yomo, *Biochem. Soc. Trans.* **2019**, *47*, 1909.
- [6] O. Sandre, L. Moreaux, F. Brochard-Wyart, *Proc. Natl. Acad. Sci. USA* **1999**, *96*, 10591.
- [7] S. F. Jordan, H. Ramm, I. N. Zheludev, A. M. Hartley, A. Marechal, N. Lane, *Nat. Ecol. Evol.* **2019**, *3*, 1705.
- [8] S. Jõemetsa, K. Spustova, K. Kustanovich, A. Ainla, S. Schindler, S. Eigler, T. Lobovkina, S. Lara-Avila, A. Jesorka, I. Gözen, *Langmuir* **2019**, *35*, 10286.
- [9] I. Gozen, P. Dommersnes, I. Czolkos, A. Jesorka, T. Lobovkina, O. Orwar, *Nat. Mater.* **2010**, *9*, 908.
- [10] I. Gözen, M. Shaali, A. Ainla, B. Örtmen, I. Pöldsalu, K. Kustanovich, G. D. M. Jeffries, Z. Konkoli, P. Dommersnes, A. Jesorka, *Lab Chip* **2013**, *13*, 3822.
- [11] C. Billerit, I. Węgrzyn, G. D. M. Jeffries, P. Dommersnes, O. Orwar, A. Jesorka, *Soft Matter* **2011**, *7*, 9751.
- [12] C. Billerit, G. D. M. Jeffries, O. Orwar, A. Jesorka, *Soft Matter* **2012**, *8*, 10823.
- [13] C. I. McPhee, G. Zorinants, W. Langbein, P. Borri, *Biophys. J.* **2013**, *105*, 1414.
- [14] K. I. Akashi, H. Miyata, H. Itoh, K. Kinoshita Jr., *Biophys. J.* **1996**, *71*, 3242.
- [15] R. Karlsson, M. Karlsson, A. Karlsson, A. S. Cans, J. Bergenholtz, B. Åkerman, A. G. Ewing, M. Voinova, O. Orwar, *Langmuir* **2002**, *18*, 4186.
- [16] P. G. Dommersnes, O. Orwar, F. Brochard-Wyart, J. F. Joanny, *Europhys. Lett. (EPL)* **2005**, *70*, 271.
- [17] G. Bolognesi, M. S. Friddin, A. Salehi-Reyhani, N. E. Barlow, N. J. Brooks, O. Ces, Y. Elani, *Nat. Commun.* **2018**, *9*, <https://doi.org/10.1038/s41467-018-04282-w>.
- [18] J. Prives, M. Shinitzky, *Nature* **1977**, *268*, 761.
- [19] K. A. Brakke, *Exp. Math.* **1992**, *1*, 141.
- [20] K. A. Brakke, Surface Evolver Manual Version 2.70, **2013**.
- [21] W. Helfrich, *Z. Naturforsch. C* **1973**, *28*, 693.
- [22] A. Ainla, G. D. M. Jeffries, R. Brune, O. Orwar, A. Jesorka, *Lab Chip* **2012**, *12*, 1255.
- [23] I. Węgrzyn, A. Ainla, G. D. M. Jeffries, A. Jesorka, *Sensors* **2013**, *13*, 4289.
- [24] T. Bilal, I. Gözen, *Biomater. Sci.* **2017**, *5*, 1256.
- [25] A. Melcrová, S. Pokorna, S. Pullanchery, M. Kohagen, P. Jurkiewicz, M. Hof, P. Jungwirth, P. S. Cremer, L. Cwiklik, *Sci. Rep.* **2016**, *6*, <https://doi.org/10.1038/srep38035>.
- [26] K. I. Akashi, H. Miyata, H. Itoh, K. Kinoshita Jr., *Biophys. J.* **1998**, *74*, 2973.
- [27] T. Lobovkina, I. Gözen, Y. Erkan, J. Olofsson, S. G. Weber, O. Orwar, *Soft Matter* **2010**, *6*, 268.
- [28] A. Kunze, F. Zhao, A. K. Marel, S. Svedhem, B. Kasemo, *Soft Matter* **2011**, *7*, 8582.
- [29] D. P. Pantazatos, R. C. MacDonald, *J. Membr. Biol.* **1999**, *170*, 27.
- [30] C. K. Haluska, K. A. Riske, V. Marchi-Artzner, J. M. Lehn, R. Lipowsky, R. Dimova, *Proc. Natl. Acad. Sci. USA* **2006**, *103*, 15841.
- [31] T. Tanaka, M. Yamazaki, *Langmuir* **2004**, *20*, 5160.
- [32] Y. Suzuki, K. H. Nagai, A. Zinchenko, T. Hamada, *Langmuir* **2017**, *33*, 2671.
- [33] N. G. Stoicheva, S. W. Hui, *Biochim. Biophys. Acta, Biomembr.* **1994**, *1195*, 31.
- [34] K. Adamala, J. W. Szostak, *Nat. Chem.* **2013**, *5*, 495.
- [35] K. Kurihara, Y. Okura, M. Matsuo, T. Toyota, K. Suzuki, T. Sugawara, *Nat. Commun.* **2015**, *6*, <https://doi.org/10.1038/ncomms9352>.
- [36] J. J. Diao, Y. Ishitsuka, H. Lee, C. Joo, Z. L. Su, S. Syed, Y. K. Shin, T. Y. Yoon, T. Ha, *Nat. Protoc.* **2012**, *7*, 921.
- [37] Y. H. M. Chan, B. van Lengerich, S. G. Boxer, *Proc. Natl. Acad. Sci. USA* **2009**, *106*, 979.
- [38] M. A. Wilson, A. Pohorille, *J. Am. Chem. Soc.* **1996**, *118*, 6580.
- [39] P. Urban, S. R. Kirchner, C. Mühlbauer, T. Lohmüller, J. Feldmann, *Sci. Rep.* **2016**, *6*, <https://doi.org/10.1038/srep22686>.
- [40] T. D. Ingolia, D. E. Koshland, *J. Biol. Chem.* **1978**, *253*, 3821.
- [41] L. Lizana, Z. Konkoli, *Phys. Rev. E* **2005**, *72*, <https://doi.org/10.1103/PhysRevE.72.026305>.
- [42] L. Lizana, Z. Konkoli, O. Orwar, *J. Phys. Chem. B* **2007**, *111*, 6214.
- [43] B. K. D. Pearce, R. E. Pudritz, D. A. Semenov, T. K. Henning, *Proc. Natl. Acad. Sci. USA* **2017**, *114*, 11327.
- [44] D. Milshteyn, B. Damer, J. Havig, D. Deamer, *Life* **2018**, *8*, 11.
- [45] W. Martin, J. Baross, D. Kelley, M. J. Russell, *Nat. Rev. Microbiol.* **2008**, *6*, 805.
- [46] M. Karlsson, K. Nolkranz, M. J. Davidson, A. Stromberg, F. Ryttsen, B. Åkerman, O. Orwar, *Anal. Chem.* **2000**, *72*, 5857.



Supporting Information

for *Small*, DOI: 10.1002/smll.202002529

Rapid Growth and Fusion of Protocells in Surface-Adhered
Membrane Networks

*Elif S. Köksal, Susanne Liese, Lin Xue, Ruslan Ryskulov, Lauri Viitala, Andreas Carlson, and Irep Gözen**

Supplementary Information for:

Rapid Growth and Fusion of Protocells in Surface-adhered Membrane Networks

Elif S. Köksal, Susanne Liese, Lin Xue, Ruslan Ryskulov, Lauri Viitala, Andreas Carlson, Irep Gözen*

*To whom correspondence should be addressed. Email: irep@uio.no

This PDF file includes:

Supplementary text

S1. Experimental setup

S2. Characterization of IR-laser heating

S3. Image analyses

S4. Details of computational model

S5. Stable pore formation in fused compartments

S6. Encapsulation of fluorescein vs. RNA by the protocells

Figures S1 to S7

Captions for movies S1 to S7

References for SI

Other supplementary materials for this manuscript include the following:

Movies S1 to S7

Matlab Script: Detection of vesicular compartments from micrographs

S1. Experimental setup

The optical fiber for co-application of IR-B radiation and the microfluidic pipette for the superfusion of RNA-oligonucleotides were positioned above the substrate surface, using 3-axis water hydraulic micromanipulators (**Figure S1**). The tip of the fiber and the pipette are placed on opposite sides in order to target the same membrane area on the

substrate. The inset in the upper left corner of **Figure S1** shows the flat polished tip of the optical fiber with a core diameter of 50 μm .

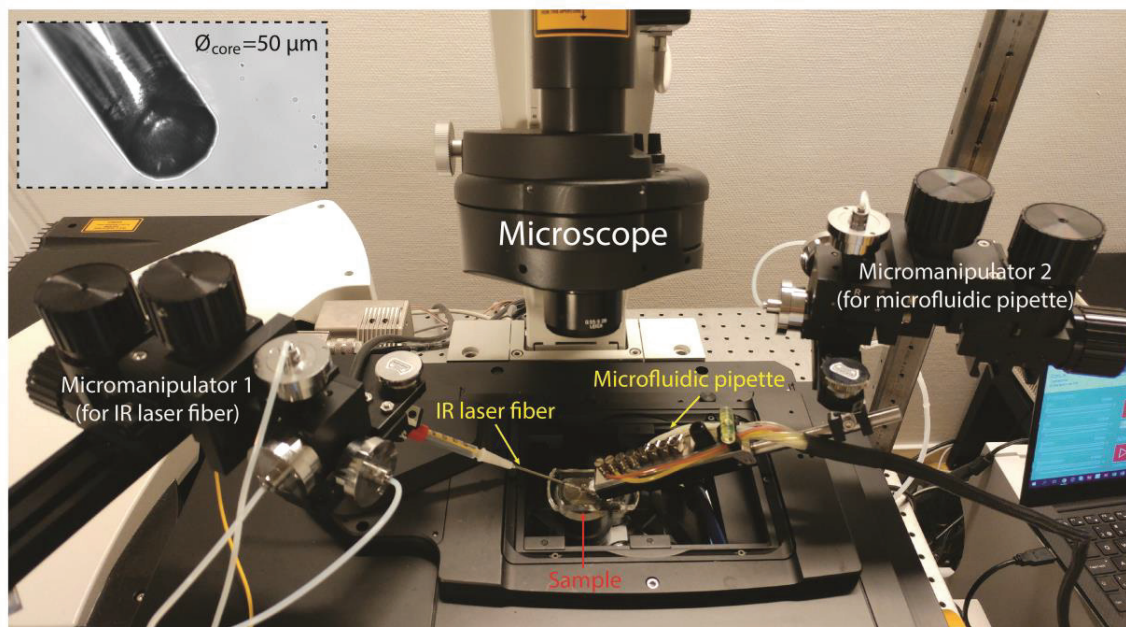


Figure S1 | Photograph of the experimental setup. Inset: flat tip of the IR laser fiber.

S2. Characterization of IR-laser heating

The local temperature changes caused by the IR laser heating were estimated from the absolute temperature measurements with a CHCO-005 E-type microtemp thermocouple (junction diameter: 25 μm , Omega Engineering, UK). Optical fiber and thermocouple were positioned above the sample using motorized micromanipulators (Scientifica, UK) (**Figure S2a**). For the measurements, the thermocouple was placed above the surface in the center of the heated region. Temperatures were recorded while the thermocouple was lifted up in z-direction in 10 μm steps. Measurements were performed for three different laser intensities, as employed in the compartment formation, growth and merging experiments. Plots of the obtained data are presented in **Figure S2b**.

Due to the unavoidable direct absorption of IR irradiation by the thermocouple itself, the measured temperatures are somewhat higher than the actual temperatures in the medium. This is particularly grave in the range between 0-40 μm in z-direction (open circles in **Figure S2b**), where the measured temperatures increase to unphysical values above the boiling point of water. Since boiling is not observed, we can conclude that the actual temperatures are below 100 $^{\circ}\text{C}$. These data points were excluded, and only the data points shown with filled circles are fitted by means of a linear regression in order to estimate the temperature on the surface ($z=0$). According to this approximation, the lipid sample is heated up to temperatures of 39, 89 and 122 $^{\circ}\text{C}$ (as measured, see section

below for discussion of these values) when the laser diode current is 0.73, 0.97 and 1.22 A, respectively. The directly measurable laser current is stated rather than the laser power, which can be extracted from the U/I/P chart in the manufacturer data sheet (www.seminex.com) of the 4PN-104 1470 nm (NA 0.22 fiber coupled) laser diode. The continuous wave power output at 1 A corresponds to approximately 100 mW.

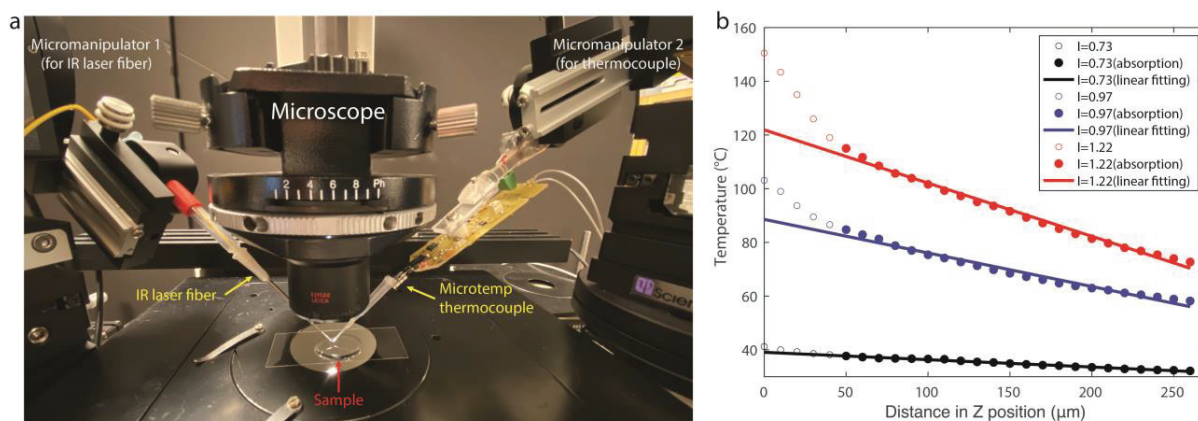


Figure S2 | Characterization of the local temperature profile caused by IR-laser heating. (a) Photograph of the experimental setup for the temperature measurement using thermocouple. (b) Plot of measured temperatures at three different laser intensities employed in the experiments.

We can distinguish between three different temperature ranges for each of the three different laser settings. There may be an additional component in the temperature/distance relationship for the two higher laser power settings for the height range between 200 and 250 μm distance from the surface, which corresponds to the situation where the thermocouple is outside the irradiated volume (cone of acceptance), which we have not considered in the analysis. At the lowest power setting, the direct absorption by the thermocouple metal is greatly reduced, due to the almost complete absorption of the light by the water volume in between fiber end and thermocouple. The measured values are for this setting accordingly very close to the actual temperatures near the membrane. Temperatures obtained from the measurements for the two higher power settings are biased by the self-absorption of the thermocouple, and need to be also corrected for the influence of strong local heat convection, which continuously supplies a stream of cold medium to the lipid assemblies on the surface. We estimate that the temperatures on the surface are likely not exceeding 70 and 90 °C for the two higher power settings. More accurate direct temperature determinations would be possible using ion conductivity measurements in a glass capillary,[1] or a different means of temperature control (bulk heating) can be considered.

S3. Image analyses

We performed image analysis using Matlab2018a to detect the compartments in the recorded micrographs to be able to count their number and to calculate their diameter, over time. Briefly, a suitable threshold to convert the gray scale micrographs to binary images, was adjusted every 250 frames of the time series to correct the intensity fluctuations, photo-bleaching and similar effects. Next, *imfindcircles* function was used to detect the circles using circular Hough transform. **Figure S3** shows a sample output image from the analysis shown in **Figure 3c**. A Matlab script has been provided as a separate supplementary file.

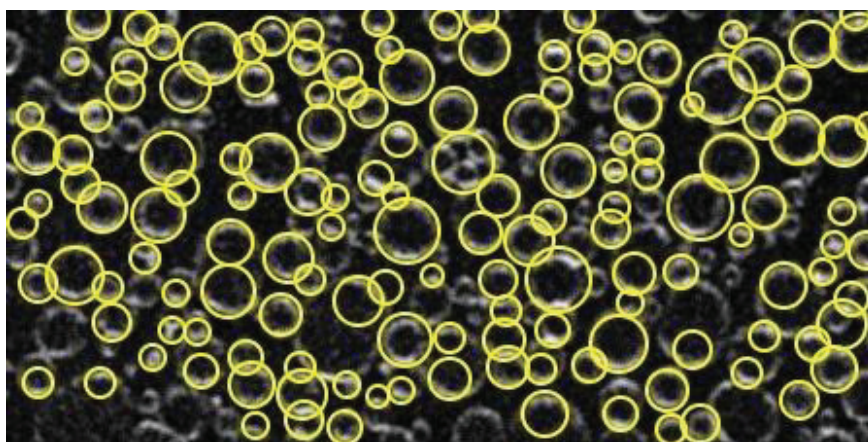


Figure S3 | Sample output image of *imfindcircles* function of Matlab, showing the identified circular compartments.

S4. Details of computational model

We perform two sets of simulations: (1) fusion initiating at the equator of the compartments and (2) fusion initiating along the connecting tube. For both simulations the initial configurations are similar (schematically depicted in **Figure S4**). In the first case, the vertices highlighted in red are connected along the contact (neck) line (red solid line in **Figure S4**), and the circumference of the contact line is constrained. In the second case, two vertices with the same initial coordinates are placed along the red dashed line in **Figure S4**, which allows us to define two faces that separate the two neighboring vesicles. In the set of simulations regarding case 1, the energy minimization leads to a separation of the vertices within the first steps, thus preventing an intersection of the two vesicles. In the second set of simulations the midline along the tube (red dashed line in **Figure S4**) is constrained. In all simulations, the outer points (shown in green in **Figure S4**) and the faces between them are constrained to a cylinder of radius 1, where we define all lengths in units of the cylinder radius. The lowest vertices and the lines connecting these vertices are constrained to a height $z=0$,

while all other vertices, lines and faces are constrained to $z > 0$. The total area is constrained to 450.

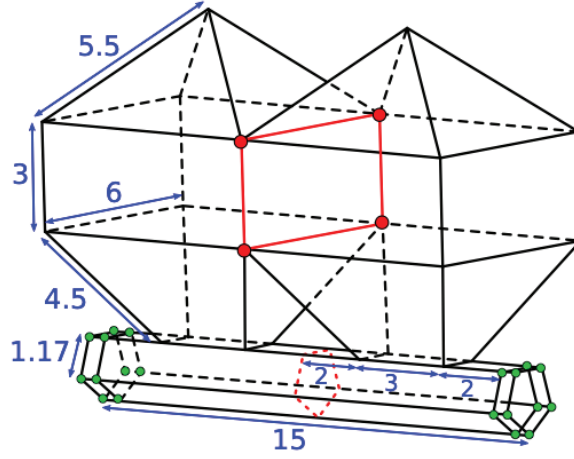


Figure S4 | Initial configuration of the simulation. All lengths are given in units of the tube radius.

We determined the bending energy by integrating the mean curvature over the entire surface, using the built-in *star_perp_sq_mean_curvature* method. The *Surface Evolver* software[2] uses finite element methods on a two-dimensional mesh in space to minimize the bending energy, which is defined as the integral of the squared mean curvature over the surface. The bending energy E_v of each vertex reads:

$$E_v = A_v \frac{3}{4} \left(\frac{\nabla A_v N_v}{N_v N_v} \right)^2, \quad (1)$$

with A_v the area of the facets adjacent to the vertex and N_v the volume gradient, which is defined as:

$$N_v = \frac{1}{6} (\mathbf{v}_1 \times \mathbf{v}_2 + \mathbf{v}_2 \times \mathbf{v}_3 + \dots + \mathbf{v}_n \times \mathbf{v}_1), \quad (2)$$

with $\mathbf{v}_1, \dots, \mathbf{v}_n$ the neighboring vertices. A detailed description of the numerical methods can be found in the *Surface Evolver* manual.[3]

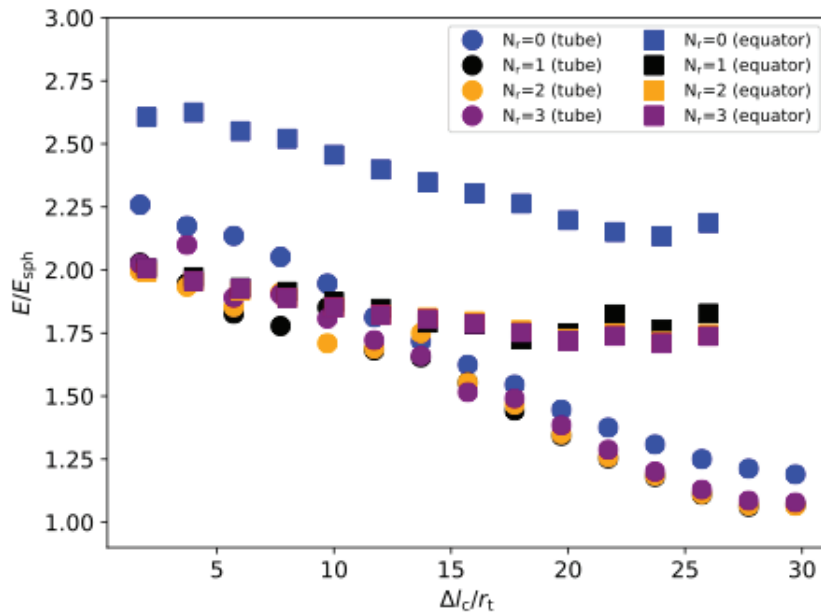


Figure S5 | The bending energy, rescaled by the energy of a spherical vesicle is shown in dependence of the length of the contact line. The number of mesh refinements N_r , corresponding to simulation step 1, 2, 3 and 4 are shown in different colors.

The equilibrated membrane shape is obtained through a series of four energy minimization steps, which read in the *Surface Evolver* letter code:

Fusion at the tube:

- step 1: {g 20; u}3;{{V;g 20}30; u ;g 20}2
- step 2: r;w 0.1;U;{V;g 50}10; U;g 20
- step 3: r;w 0.05;U;{V;g 50}10; U;g 20
- step 4: r;w 0.02;U;V;g 50;u;{V;g 50}9; U;g 20

Fusion at the equator:

- step 1: g 50; u; g 100;U; g 100;U
- step 2: r;w 0.1;{{u;g 50}4;{V;g 50}}2;g 20
- step 3: r;w 0.05;{{u;g 50}4;{V;g 50}}2;g 20
- step 4: r;w 0.02;{{u;g 50}4;{V;g 50}}2;g 20

Step 2, 3 and 4 start with a mesh refinement ('r'). In **Figure S5** we see that only the first mesh refinement leads to a significant improvement of the energy minimization. In **Figure 4** in the main text the minimal energy found within the four simulation steps is shown.

S5. Stable pore formation in fused compartments

The mathematical model for fusion shows the formation of a stable pore when fusion initiates at the equator of two adjacent compartments. We also observe stable pores in fused compartments in our experiments (**Figure S6**, also **Figure 3** of the main manuscript). Such pores are not observed before fusion, or if the fusion occurs between the compartments initially residing on the same nanotube (**Figure 3d-k** for fused compartments initially were on the same nanotube vs. **Figure 3l-u** for compartments initially were on different nanotubes).

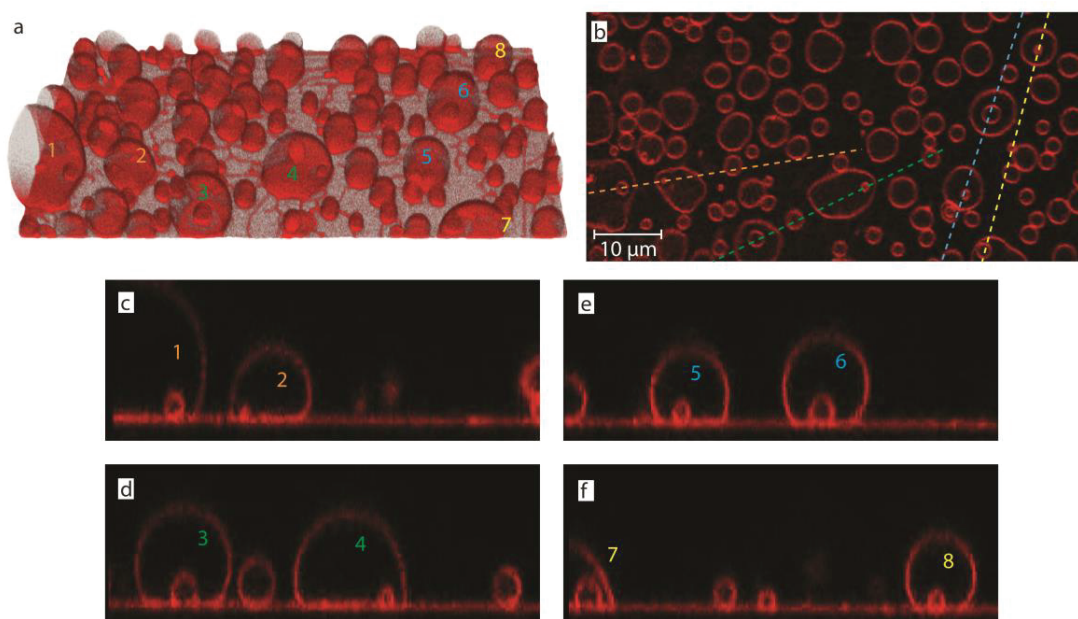


Figure S6 | Stable pores in fused compartments. (a) 3D confocal micrograph of the formed protocells (b) cross section of protocell sample close to the surface (x-y plane) (c-f) cross sections of protocell sample (x-z plane). Protocells numbered 1-8 in (a) have small cavities formed after fusion of adjacent protocells. Cross sectional profile of the numbered protocells, along the color-coded dashed lines in (b), are shown in (c-f).

S6. Encapsulation of fluorescein vs. RNA inside the protocells

As described in the manuscript, we delivered the RNA to the compartments locally using an open-space microfluidic device which resulted in the encapsulation of RNA inside some of the compartments. FAM conjugated 10 base long polyA RNA oligonucleotides were prepared in nuclease-free water. For experiments, the RNA concentration was adjusted to 40 μM with HEPES buffer. The encapsulation efficiency of free fluorescein sodium salt is compared to FAM-RNA oligonucleotides. The

fluorescein encapsulation shows higher efficiency (**Figure S7**). Only a few protocells encapsulate and maintain RNA fragments. This might be due to the higher molecular weight and structure of RNA compared to the fluorescein dye.

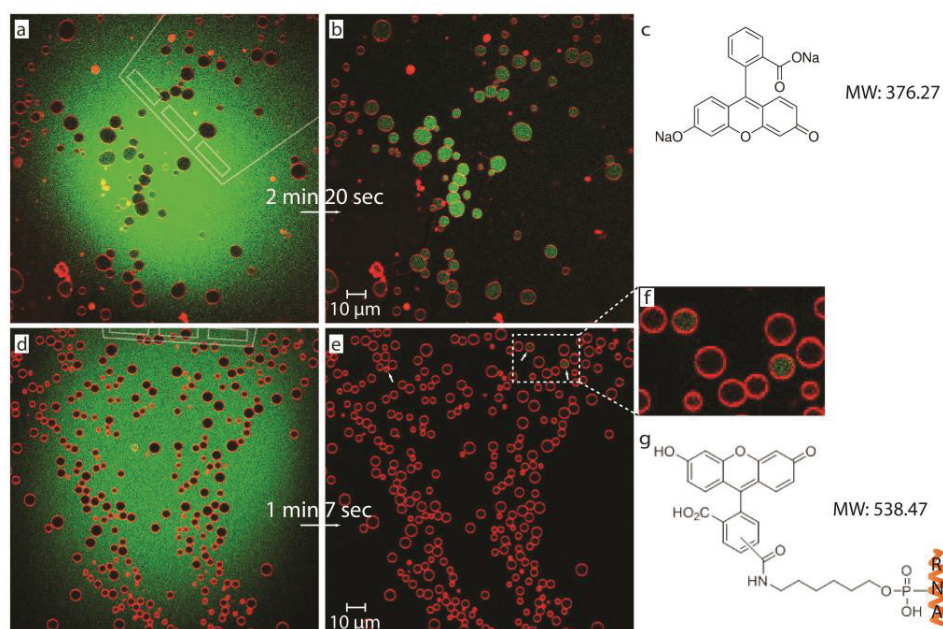


Figure S7 | Encapsulation of fluorescein dye vs. FAM conjugated RNA oligonucleotides. A microfluidic pipette is used for the superfusion of free fluorescein and FAM-conjugated RNA oligonucleotides to a membrane area populated with protocells. **(a)** Confocal micrograph of a membrane area with the microfluidic pipette re-circulating free fluorescein above it (top view). **(b)** After exposure is stopped, the initially fluorescein-free compartments are observed with fluorescein cargo. **(c)** fluorescein sodium salt molecule (MW: 376.27 g/mol). **(d)** Confocal micrograph of a membrane area with the microfluidic pipette re-circulating FAM-conjugated RNA fragments above it (top view). **(e)** After exposure, only a few protocells, shown in **(e)** (white arrows), and in **(f)**, encapsulate and maintain RNA fragments in the ambient aqueous solution. **(g)** Fluorophore-conjugated RNA molecule (MW: 538.47 g/mol).

S7. Supplementary Movies

Movie S1-3 | Rapid nucleation and growth of protocells. Movies S1-S3 show the rapid nucleation and growth of vesicular compartments from the underlying lipid nanotube network upon increase in temperature.

The region shown in Movie S1 ‘Experiment 2’ corresponds to **Figure 1c-e** and **Figure 2a**. The region shown in Movie S1 ‘Experiment 1’ corresponds to **Figure 1f-h**. ‘Experiment 1-2’ in Movie S1 is accelerated 94x and 71x, respectively.

‘Experiment 3-5’ in Movie S2 are accelerated 101x, 114x and 136x, respectively.

The region shown in Movie S3 corresponds to **Figure 2c-f**, and the movie is accelerated 5x.

Movie S4-6 | Fusion of protocells. Movie S4-S6 show the fusion of protocells on lipid nanotube networks upon exposure to higher intensity IR laser radiation.

Movie S4 and S5 correspond to **Figure 3**. In Movie S5, the outline of lipid nanotube network is overlaid to facilitate the observation of location of fusion events with respect to the nanotubes, i.e. same or different tubes. Movies are sped up 5x. Between each part (Part I-III) the recording is stopped and re-started.

Movie S6 is accelerated 85x.

Movie S7 | Encapsulation of RNA oligonucleotides and following fusion of protocells. Movie S7 shows the superfusion of FAM-conjugated RNA oligonucleotides by means of a microfluidic pipette (Part I) followed by fusion events induced by activation of the IR laser (Part II).

Movie S7 Experiment 1 and Experiment 2 correspond to **Figure 5c-m** and **Figure 5r-t**, respectively. Movies are accelerated 5x.

References

1. Zeeb, V.; Suzuki, M.; Ishiwata, S., *Journal of Neuroscience Methods* **2004**, *139* (1), 69-77. DOI 10.1016/j.jneumeth.2004.04.010.
2. Brakke, K. A., *Experimental Mathematics* **1992**, *1* (2), 141-165. DOI 10.1080/10586458.1992.10504253.
3. Brakke, K. A. *Surface Evolver Manual Version 2.70*; **2013**.

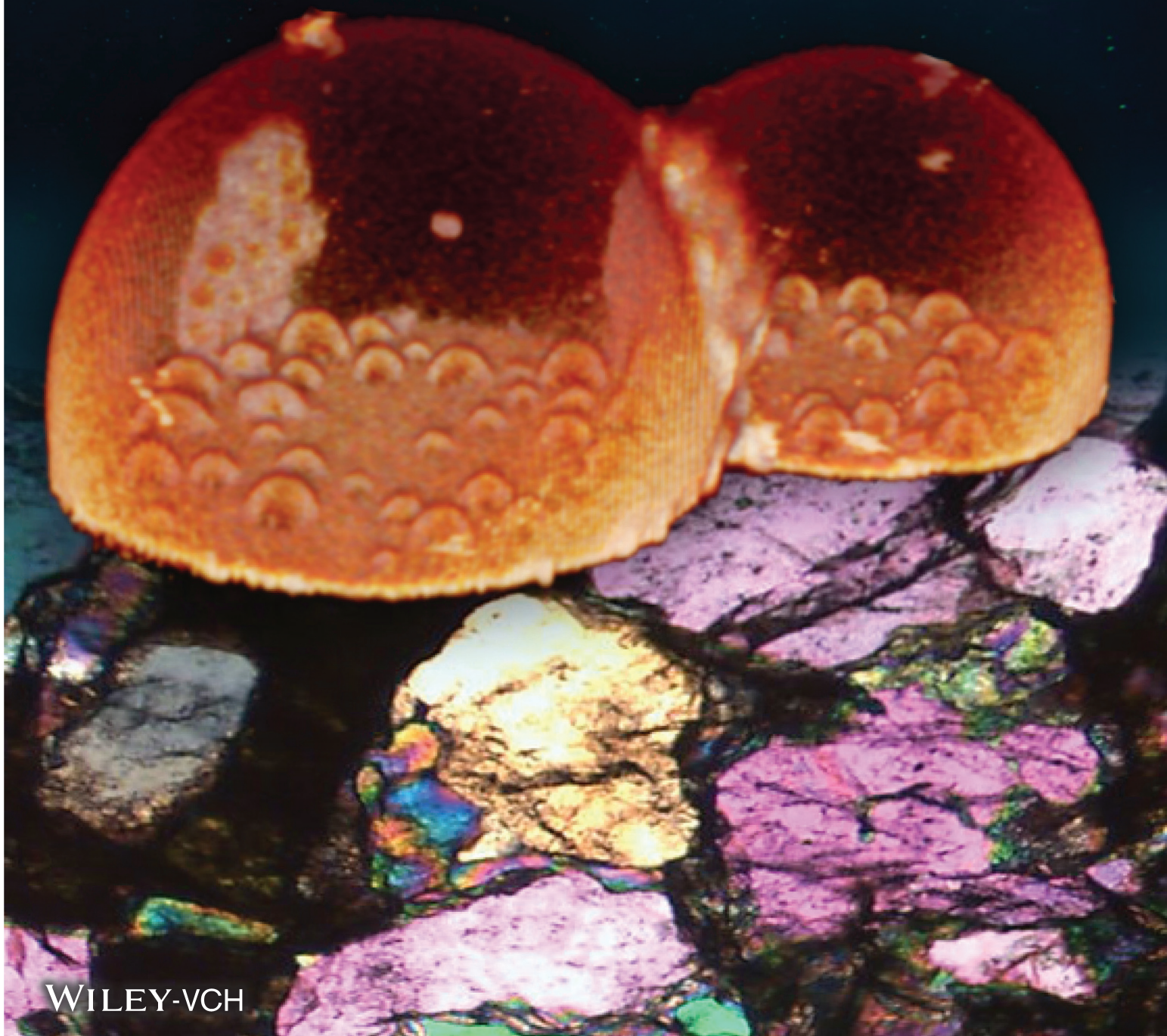
Paper IV

Vol. 17 • No. 2 • January 14 • 2021

www.small-journal.com



NANO • MICRO small



WILEY-VCH

Subcompartmentalization and Pseudo-Division of Model Protocells

Karolina Spustova, Elif Senem Köksal, Alar Ainla, and Irep Gözen*

Membrane enclosed intracellular compartments have been exclusively associated with the eukaryotes, represented by the highly compartmentalized last eukaryotic common ancestor. Recent evidence showing the presence of membranous compartments with specific functions in archaea and bacteria makes it conceivable that the last universal common ancestor and its hypothetical precursor, the protocell, may have exhibited compartmentalization. To the authors' knowledge, there are no experimental studies yet that have tested this hypothesis. They report on an autonomous subcompartmentalization mechanism for protocells which results in the transformation of initial sub-compartments to daughter protocells. The process is solely determined by the fundamental materials properties and interfacial events, and does not require biological machinery or chemical energy supply. In the light of the authors' findings, it is proposed that similar events may have taken place under early Earth conditions, leading to the development of compartmentalized cells and potentially, primitive division.

exist in other domains of life, such as in archaea and bacteria.^[1,2] Archaea, for example, have acidocalcisomes, the membrane enclosed electron-dense granular organelles rich in calcium and phosphate, which is crucial for osmoregulation and Ca²⁺ homeostasis.^[3] In cyanobacteria, membrane-bound thylakoids^[4] have been identified as compartments in which the light-dependent reactions of photosynthesis take place.

Despite the differences between eukaryotic and prokaryotic compartments in terms of structural and functional complexity, the presence of membranous compartments in procaryota^[1] establishes a possibility of compartments having existed in protocells, and being evolutionarily conserved. There is essentially no experimental material, however, on how compartments could have consistently

emerged from membranes in a prebiotic environment lacking membrane-shaping and -stabilizing proteins.

Membrane-less laboratory models of cytoplasmic suborganization have been developed inside synthetic cells, that is, giant unilamellar vesicles.^[5] These models require moderately elaborate chemical systems. A few examples of the utilized materials and mechanisms to induce compartment formation involve thermo-responsive hydrogels,^[6] pH driven protein (human serum albumin) localization^[7] or a poly(ethylene glycol)-dextran aqueous two-phase system.^[8] One study which report on the membrane-based multi-vesiculation inside amphiphilic compartments, has employed protein–ligand couples to induce this behavior, that is, biotin–avidin conjugates.^[9] Membrane-enveloped subcompartment formation in biological systems is therefore considered to be ultimately dependent on the genetic make-up of the cells.^[10]

In this study, we have investigated a protocell subcompartmentalization model on solid surfaces. The reported mechanism relies on the self-assembly and shape transformation abilities of biosurfactant bilayer membranes, and is largely governed by changes in the membrane-surface adhesion. Model protocells in form of giant unilamellar compartments are initially adhered to a solid substrate via Ca²⁺ anchors, but the adhesion is subsequently reversed upon depletion of Ca²⁺. Small membrane regions released from the surface transform into small unilamellar subcompartments inside the model protocell. They remain partially adhered to the surface and continue growing, consuming the membrane material of the primary container. The subcompartments can take up solutes

1. Introduction


The origin of the eukaryotic cell is closely associated with the development of subcompartments, which create specific micro-environments to spatially or temporally regulate biochemical reactions, simultaneously. Until recently, cellular compartmentalization was associated solely with eukaryotic systems. Recent evidence shows that membrane-enclosed compartments also

K. Spustova, E. S. Köksal, Dr. I. Gözen
Centre for Molecular Medicine Norway
Faculty of Medicine
University of Oslo
Oslo 0318, Norway
E-mail: irep@uio.no

Dr. A. Ainla
International Iberian Nanotechnology Laboratory
Braga 4715-330, Portugal

Dr. I. Gözen
Department of Chemistry
Faculty of Mathematics and Natural Sciences
University of Oslo
Oslo 0315, Norway

Dr. I. Gözen
Department of Chemistry and Chemical Engineering
Chalmers University of Technology
Göteborg SE-412 96, Sweden

 The ORCID identification number(s) for the author(s) of this article can be found under <https://doi.org/10.1002/sml.202005320>.

DOI: 10.1002/sml.202005320

from the external environment and exchange them with the primary volume. Our experiments and finite element simulations point to a parallel uptake mechanism of solutes via transient pores in the protocell membrane. The enveloping membrane can eventually rupture to release the subcompartments as independent daughter vesicles.

Previous studies indicate that surfaces might have played a role in catalysis and synthesis of compounds relevant to prebiotic chemistry, for example, enhanced polymerization of aminoacids on mineral surfaces,^[11] or the synthesis of prebiotic peptides^[12] and RNA.^[13] Our work shows that the surface-assisted subcompartmentalization of protocells is a feasible recurring process and, due to the minimal requirements, could have potentially occurred under early Earth conditions. The newly established pathway to daughter vesicles, although relatively unsophisticated, indicates that the role of materials properties-driven transformation processes of surfactant membranes in

the development of primitive protocells, as well as the enabling function of surfaces, might have been underestimated.

2. Results

2.1. Spontaneous Compartmentalization

Figure 1a is a 3D reconstruction of the subcompartments that have spontaneously formed inside a substrate-adherent model protocell. The dome-shaped lipid container of approximately 50 μm in diameter is adhered on an Al_2O_3 surface where its distal membrane envelopes tens of subcompartments of an average size of 5 μm formed on the surface. Figure 1b shows an xy cross-sectional view recorded 4 μm above the surface. Figure 1c–f contains confocal micrographs of the compartmentalization process each step of which is explained in schematics in Figure 1g–j.

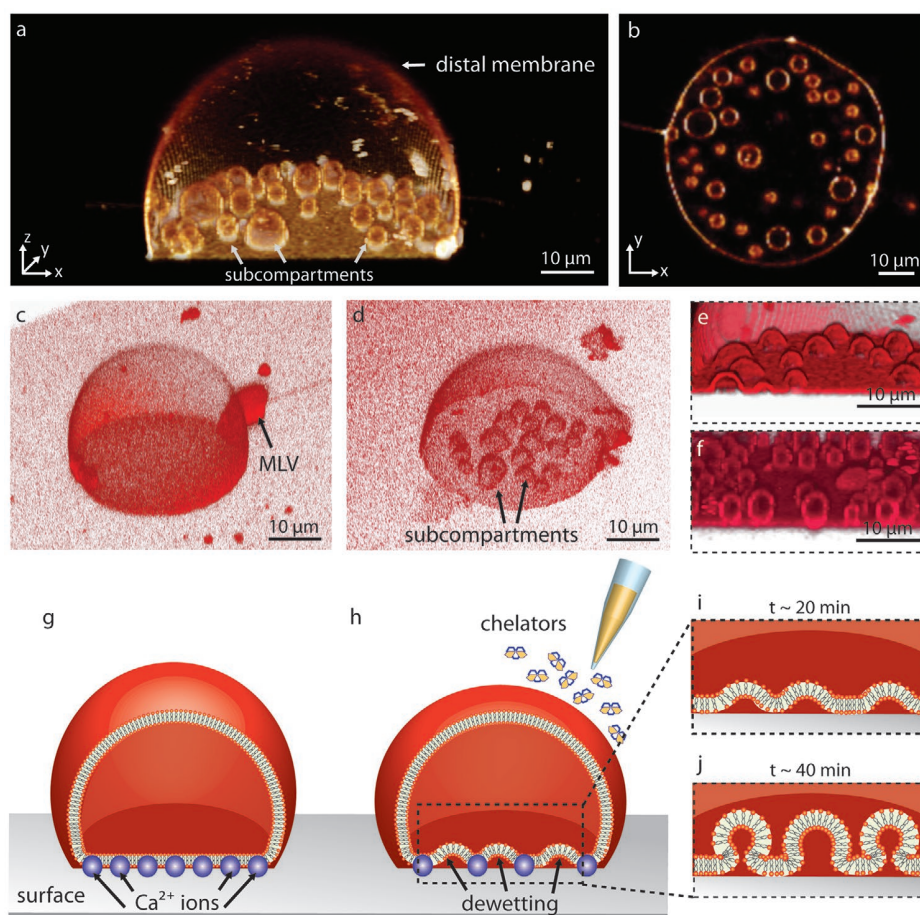


Figure 1. Subcompartmentalization in surface-adhered model protocells. a) Confocal micrograph, reconstructed in 3D, showing a model protocell enveloping several subcompartments. b) model protocell in (a) in xy cross-sectional view. Confocal micrograph of c) a model protocell adhered on a solid surface in presence of Ca^{2+} , d) a model protocell with subcompartments after chelator exposure, e) emerging subcompartments ≈ 20 min after chelator exposure, f) mature subcompartments ≈ 40 min after chelator exposure. Schematic representation of the subcompartmentalization process: g) A single model protocell consisting of a single lipid membrane, adheres onto the surface in presence of Ca^{2+} . h) Chelators are brought into the vicinity of the compartment, leading to removal of Ca^{2+} followed by subcompartmentalization. The initially surface-adhered bilayer of the model protocell transforms into i) semi-spherical, and later to j) spherical subcompartments. Micrographs in (c)–(f) are from different experiments. Membrane composition of model protocells shown in (a)–(f) is PC-DOPE. The surfaces used in (a) and (b) and (e) and (f) is Al_2O_3 , and in (c) and (d) is Al. All other experimental conditions for (a–f) were identical. Background fluorescence in (c) and (d) is due to reflection from the Al surface.

The model protocells were generated by the dehydration–rehydration method;^[14] and transferred onto the solid substrates in presence of Ca^{2+} as adhesion promoter^[15,16] (Figure 1c,g). Subsequently, by means of an automatic pipette, the ambient buffer was exchanged with a Ca^{2+} chelator-containing buffer, leading to the gradual removal of Ca^{2+} from the membrane–surface interface (Figure 1d,h). The basal membrane, that is, the adhered portion of the giant lipid container to the surface, de-wets the surface, bulges at various locations (Figure 1e,i) and transform within ≈ 40 min into spherical subcompartments (Figure 1f,j). The model protocells in Figure 1c,d are isolated. The elevated background intensity should not be mistaken for a lipid film. The substrate is composed of Al which reflects light during the imaging. A lipid reservoir, that is, multilamellar vesicle (MLV), is attached to the model protocell in Figure 1c.

2.2. Temperature-Enhanced Subcompartmentalization

Temperature has a strong influence on membrane viscosity and membrane–surface adhesion.^[17] When the temperature was

locally increased from 20 °C (room temperature) to 40 °C, the basal membrane started to de-wet the surface, forming subcompartments twice as rapidly. Figure 2a–f shows an experiment, during which the subcompartments inside a surface-adhered model protocell form at increased temperature (Movie S1, Supporting Information). The subcompartments fuse upon contact and grow in size (Movie S1, Supporting Information). For example, the three compartments which are initially distinct (yellow symbols in panel d), merge at $t = 33$ min to form a single subcompartment (yellow symbols in panel f). A similar experiment is depicted in Figure 2g–l (Movie S1, Supporting Information). Both experiments shown in Figure 2 have been performed on Al_2O_3 . The green plot in Figure 2m shows the circumference of the basal membrane depicted in Figure 2a–f, over time. The periphery of the surface-adhered portion of the lipid membrane is not retracting, as the circumference remains constant (Figure 2m, green line). The blue plot in Figure 2m represents the total membrane area utilized by the formation of subcompartments over time. The geometry of the emerging subcompartments has been assumed to be half-spheres in

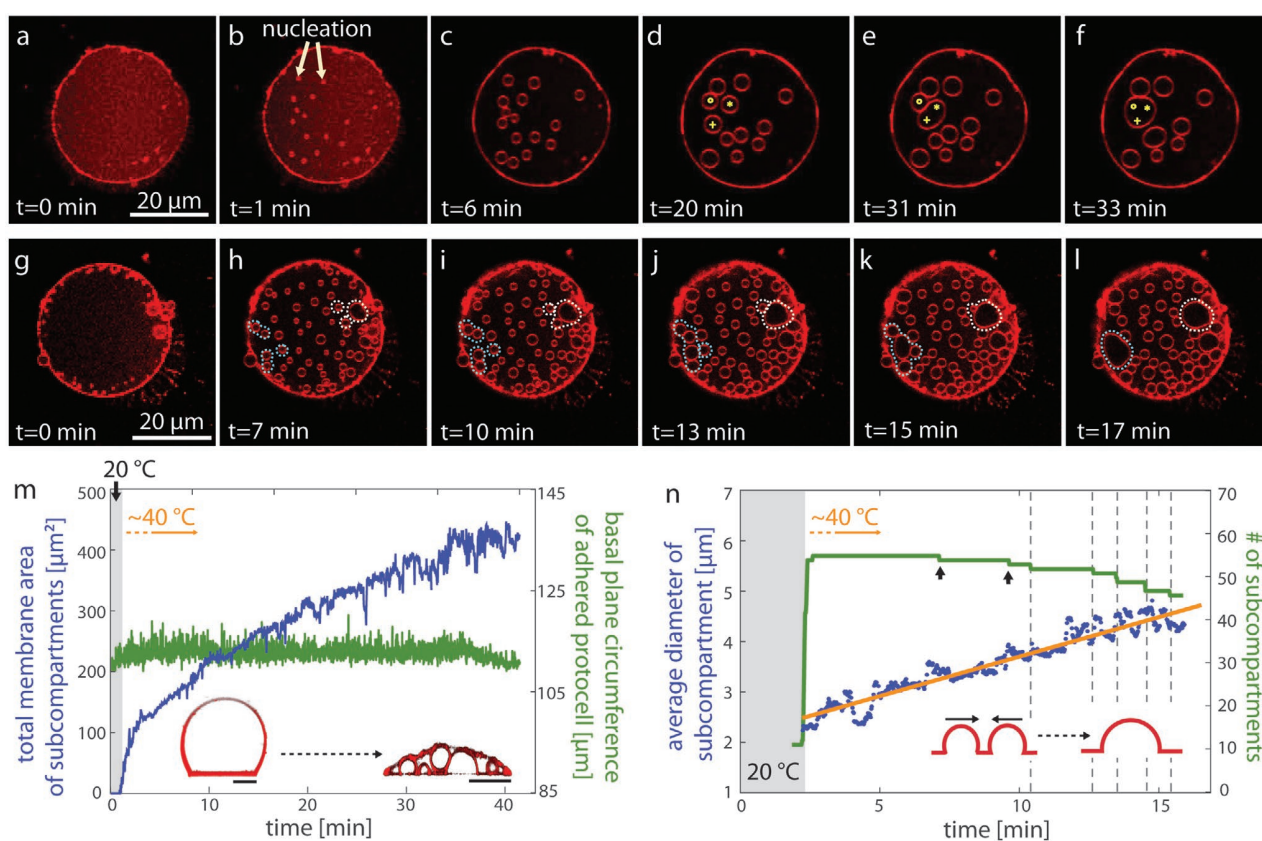


Figure 2. Enhanced subcompartmentalization at increased temperature. a–l) Confocal fluorescence micrographs showing two different experiments ((a)–(f), (g)–(l)) of temperature-enhanced subcompartmentalization (xy cross-sectional view). m) Plots showing the increase in subcompartment membrane area (blue), and the circumference of the protocell (green), versus time, for the experiment shown in (a)–(f). The inset shows the xz cross-sectional view of two protocells from different experiments before and after temperature increase. Scale bars (inset): 10 μm . n) The average diameter and number of subcompartments during the experiment shown in (g)–(l). The number of subcompartments (green plot) increases instantly with temperature increase, and decreases during fusion or, rarely, due to the sudden collapse of the subcompartments (black arrows). The inset in (n) is the schematic drawing of fusion of the subcompartments. The time point of each fusion event is marked with a dashed vertical line. The average diameter (orange line fitted to data points in blue, $d = 0.0032 \times t + 2.5$) gradually increases during subcompartment growth. The membrane of the model protocells shown in this figure is composed of PC-DOPE, and the surface is Al_2O_3 .

order to estimate the minimally required membrane area. The insets in Figure 2m shows cross sections of model protocells from two different experiments in the xz plane (side view), one at the beginning of an experiment (left) and the other after the subcompartmentalization has occurred (right). The distal membrane of the giant lipid container has decreased in area, indicating that this fraction of the membrane is partially consumed during formation. The plots in Figure 2n show the number (green) and the average diameter (blue points, orange line) of the new compartments in Figure 2g–l. With the emergence and growth of many small subcompartments, the diameter gradually increases over time. Some eventually fuse (inset), intermittently causing sudden drops in the total number (dashed vertical lines in Figure 2n). Subcompartments occasionally collapse (black arrows in Figure 2n and Movie S1, Supporting Information), presumably due to the consumption of their membrane by the competing growth of other containers in their vicinity.

2.3. Encapsulation and Isolation of Contents

The purpose of subcompartments in a biological cell is the segregation of chemical compounds and processes within individual boundaries inside the main volume of the cell (primary volume). In order to investigate the ability of the subcompartments to encapsulate molecules from the ambient environment and to maintain them, we delivered a water-soluble fluorescent compound to the exterior of each protocell (*cf.* Section S2 and S3, Supporting Information, for the details of the setup) and monitored the transmembrane transfer. Figure 3a shows a 3D micrograph (x - y - z) of a protocell on Al_2O_3 with several subcompartments, one of which maintains the encapsulated fluorescein solution. In order to achieve encapsulation in a selected model protocell, the fluorescein buffer (25 μM) was delivered with an open-space microfluidic device^[18] (Figure 3b). The presence of the compound can be switched on and off on demand, and the fluorescence signal during the cycles of exposure and removal can be monitored in real time inside the protocell and the subcompartments. We observe that during fluorescein exposure, the subcompartments rapidly encapsulate the compound, and immediately release it upon removal from the surrounding. This indicates that the compartments are not fully closed and have access to the surrounding solution through the space between the surface and the model protocell (Figure 3c). After a certain time point, some subcompartments hold the content and can maintain it during a long period of time, indicating that the size of the opening of the subcompartment is reduced, or completely sealed (Figure 3d). Upon temperature increase, the compartments appear to maintain the content longer.

Figure 3e–g depicts the time series of an encapsulation experiment at room temperature (*cf.* Movie S2, Supporting Information), with the corresponding fluorescein intensity plots of selected regions during multiple exposure cycles (Figure 3h). The fluorescence intensity of three different regions was monitored: the solution outside the protocell (region circled in white dashed lines in Figure 3f), the primary volume of the protocell (Figure 3f, yellow dashed circle) and the intensity of all of the subcompartments, which later was averaged. The plots

show an instant encapsulation of fluorescein within the subcompartments with the initiation of the exposure, and immediate release of the contents once the exposure is terminated (Figure 3h). The model protocell, on the other hand, encapsulates the fluorescence molecule gradually and maintains it.

At elevated temperatures (Figure 3i–p and Movie S2, Supporting Information), the leakage of fluorescein from the subcompartments decreases (Figure 3l), compared to the leakage in the experiment depicted in Figure 3e–g, which indicates a reduction of the size of their opening (Figures 3k,l and 3o,p). The concentration of the fluorescein inside the contracted subcompartment can eventually be slightly higher than in the internal medium of the primary volume (Figure 3l,p).

2.4. Pore-Mediated Uptake

We then examined the role of transient pores in the uptake of material from the ambient solution. As showed in Figure 3, the fluorescein molecules are encapsulated by the primary volume. To analyze the mechanism of the uptake, we exposed individual surface-adhered protocells without internal compartments to a fluorescein buffer, using an open volume microfluidic device (Figure 4 and Section S2–S3, Supporting Information). Figure 4a shows the fluorescence intensity inside 5 different protocells of similar size versus time upon exposure to fluorescein. Uptake rates varying from less than 20% of the stock solution (Figure 4a, plot in pink color) to almost 90% (plot in blue color) were observed. These uptake rates imply that it is not via simple diffusion through the membrane. We attribute this behavior to the presence of transient membrane pores, which has been previously observed and characterized in similar systems.^[19] We then compared the experimental values depicted in Figure 4a to the results of finite element model (FEM) simulations shown in Figure 4b–d. The FEM here assumes a single container of size 5 μm with membrane thickness of 1 nm. The model vesicle is exposed to the fluorescein present in the external solution. Figure 4c shows the magnified view of the pore marked with a white frame in Figure 4b.

In the model, the passage of molecules is assumed to occur through a single membrane pore (Figure 4c), $\varnothing = 5$ nm, while the diffusion through the membrane otherwise is prevented. The uptake rates of fluorescein are calculated as the fluorescein diffuses from the external solution into the model protocell through the membrane pore. The diffusion coefficient of fluorescein in water at room temperature, $D = 4.25 \times 10^{-10} \text{ m}^2 \text{ s}^{-1}$,^[20] is taken into consideration. Each plot in Figure 4d represents a different time point upon exposure changing from 0.1. to 600 s. The concentration of the fluorescein in the external medium is considered to be 100%. The plots in Figure 4d show final concentrations inside the cell at different time-points, with a steep concentration gradient inside the pore zone (green region). The pore zone is almost symmetrical in both external and internal side of the membrane interface, and reaches a distance of approximately twice the pore radius. The size of the pore zone varies with the changing pore radius (inset to Figure 4d). Further away from the pore, the concentration of the solutes can be considered homogeneous on either side (Figure 4d, red and blue area). The model protocell

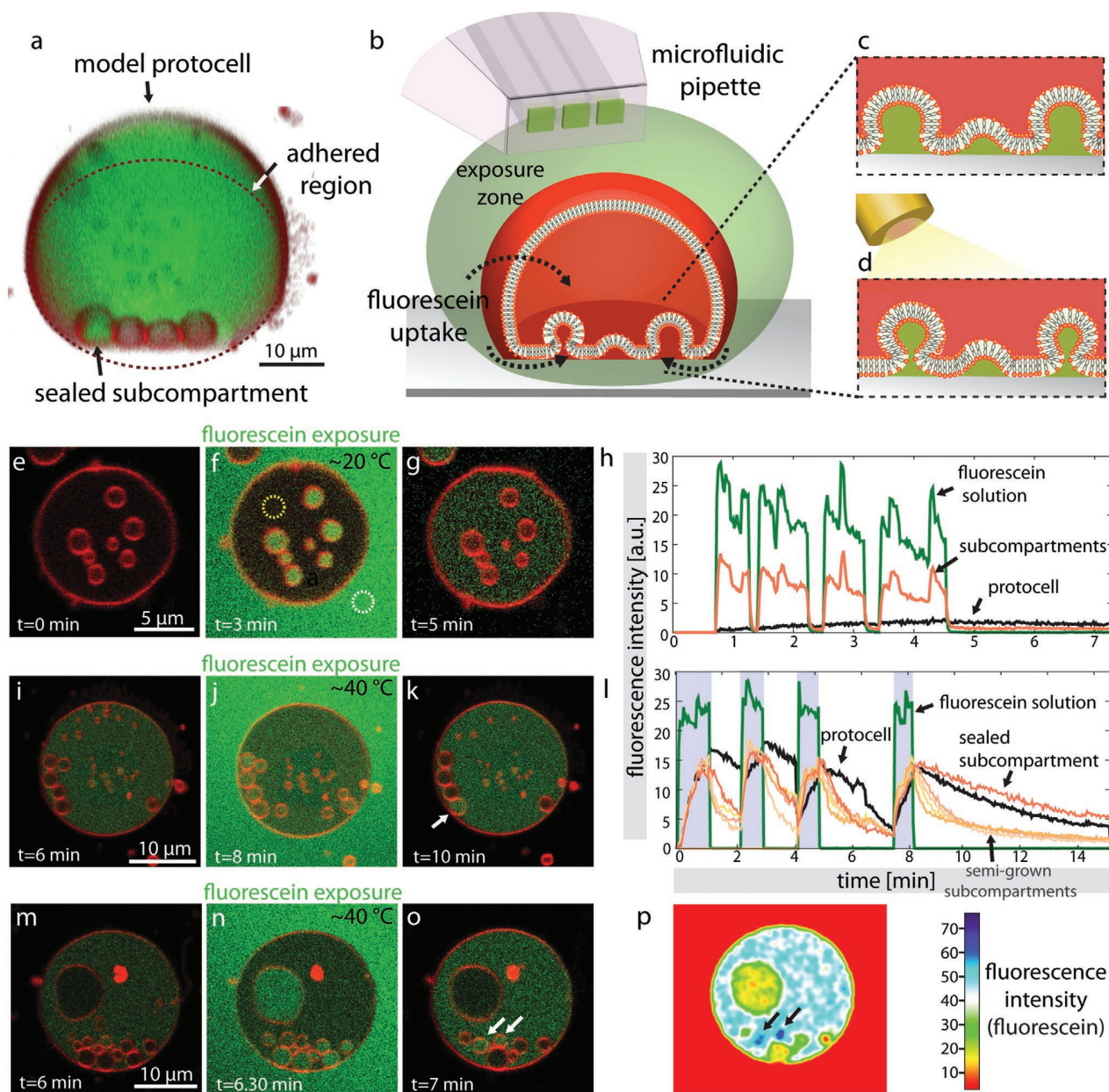
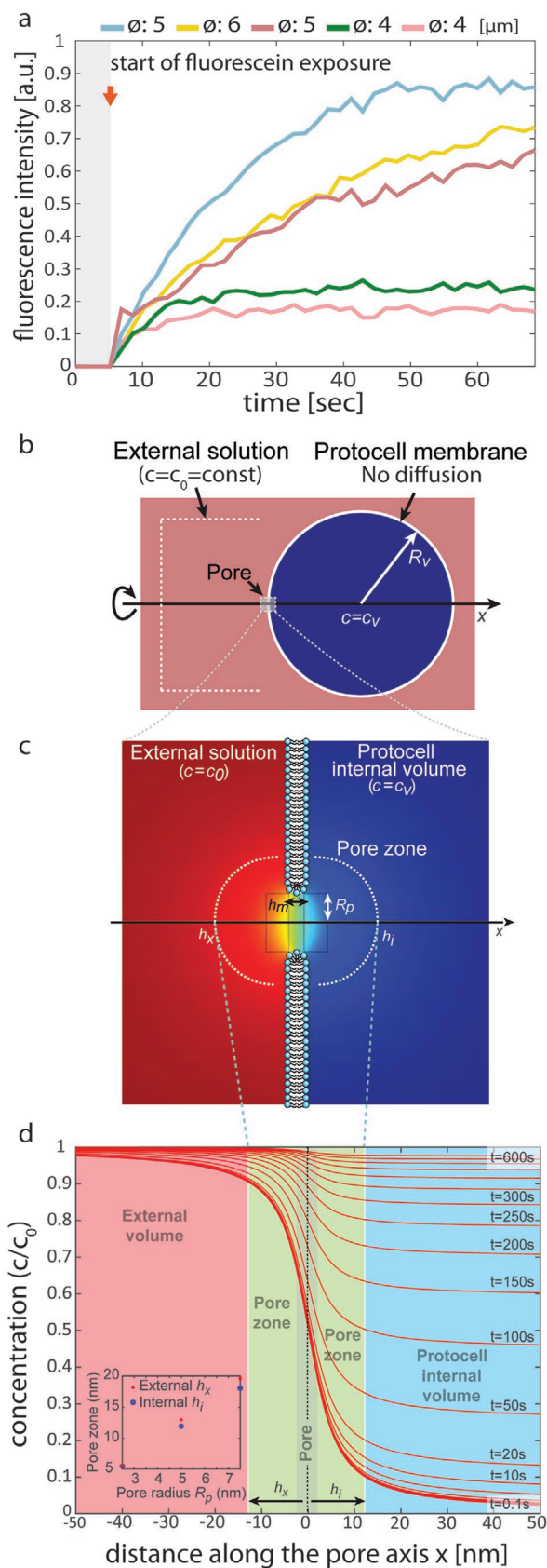


Figure 3. Encapsulation and compartmentalization of fluorescein in model protocells. a) Confocal micrograph of a model protocell, reconstructed in 3D, after pulsing with fluorescein. One of the four subcompartments maintains fluorescein content. Schematic representation of the fluorescein exposure experiment: b) The microfluidic superfusion pipette creates a fluorescein exposure zone around the model protocell. c) Semi-grown subcompartments encapsulate fluorescein during the exposure through the space at the membrane-surface interface. d) Temperature increase, together with fluorescein exposure, results in sealed subcompartments encapsulating the fluorescein. e–g,i–k,m–o) Confocal micrographs (*xy* cross section) showing the fluorescence intensity inside the subcompartments and the primary volume during fluorescein pulsing (cf. Movie S2, Supporting Information). h,l) Plots showing the fluorescence intensity of different regions versus time during the experiments shown in (e)–(g) and (i)–(k), respectively. The temperature increase during (i)–(k) is synchronized with fluorescein pulsing (gray zones in (l)). The plots in green color represent the average intensity of the stock fluorescein buffer (circle indicated by white dashed line in (f)). The plot in orange color in (h) is the arithmetic mean intensity of the subcompartments versus time. The plot in black color in (h) is the intensity of the primary volume of the protocell (circle indicated by yellow dashed line in (f)). In (l) the average intensity of each compartment have been depicted individually (orange-spectrum graphs). The color plot in (p) shows the intensity of fluorescein in (o). Black arrows show the position of the two sealed subcompartments corresponding to the entities indicated with white arrows in (o). The sealed compartments display higher fluorescence intensity compared to the other subcompartments and to the primary protocell volume. The membranes in this figure are composed of PE-PG-CA, and the surface is Al_2O_3 .



can have multiple pores further apart with no overlapping pore zones where the transport from each pore contributes linearly. The calculations for different container and pore sizes can be found in Section S4, Supporting Information.

2.5. Pseudo-Division

In some occasions we observe extensive contraction and rupturing of the distal membrane (Movie S3, Supporting Information) which results in disintegration of the original protocell, leaving behind only the intact subcompartments, that is, daughter cells (Figure 5). Figure 5a shows an xz cross section of two subcompartments with the distal membrane in direct contact. Figure 5b,c shows the xz cross section and the perspective view of daughter cells remaining after the original enveloping membrane is disintegrated. The light circular region in Figure 5c consists of a single bilayer, which is also visible in Figure 5b. A double lipid membrane surrounds this region (dark red region in Figure 5c), indicating lipid spreading around an originally isolated intact cell. Figure 5d–f shows the schematic representation of the process in Figure 5a–c. We observe daughter protocells as long as 12 hours after the addition of cheletors (Figure S5, Supporting Information). Note that the earlier observations of exchange of material between the primary volume and the ambient buffer on one hand, and the possibility of exchange between the primary volume and the subcompartments on the other hand (Figure 5d), will be discussed in the context of primitive protocell division in the following section.

3. Discussion

3.1. Compartmentalization Mechanism

Figure 1 shows that the spontaneous compartmentalization occurs when the strength of the adhesion of the protocell to the solid substrate decreases. Adhesion is mediated by the Ca^{2+} ions at the interface of the protocell membrane with the solid surface (depicted by purple spheres in Figure 1g,h). Ca^{2+} ions are known to have a fusogenic effect by binding to the lipid head groups,^[21] mediating membrane-surface,^[15,16,22] or membrane-membrane pinning.^[23] The adhesion of membranes to a solid substrate does not necessarily require Ca^{2+} in the solution,^[24–26] although its presence on the surface promotes adhesion. There

Figure 4. Uptake through transient pores. a) Fluorescein intensity inside the surface-adhered, non-compartmentalized model protocells, over time. b–d) Finite element model (FEM) of fluorescein uptake by a model protocell from the external solution through a nano-sized membrane pore. b) A single circular pore (toroidal gap) with a radius of $R_p = 5$ nm is located in the membrane of a giant compartment with radius of $R_v = 5$ μ m. c) Concentration across the membrane in the vicinity of the pore depicted in (b). The liquid volume near and inside the pore is determined to be the “pore zone” (yellow-green area). d) Concentration profile of fluorescein at the pore zone and inside the protocell at selected time points changing from 100 ms to 600 s. The inset in (d) shows the relation between the concentration gradient (extent of the pore zone) and the pore radii of 2.5, 3, 5, and 7.5 nm. The membrane of the vesicles used in (a) are composed of PC-DOPE; the surface is Al_2O_3 .

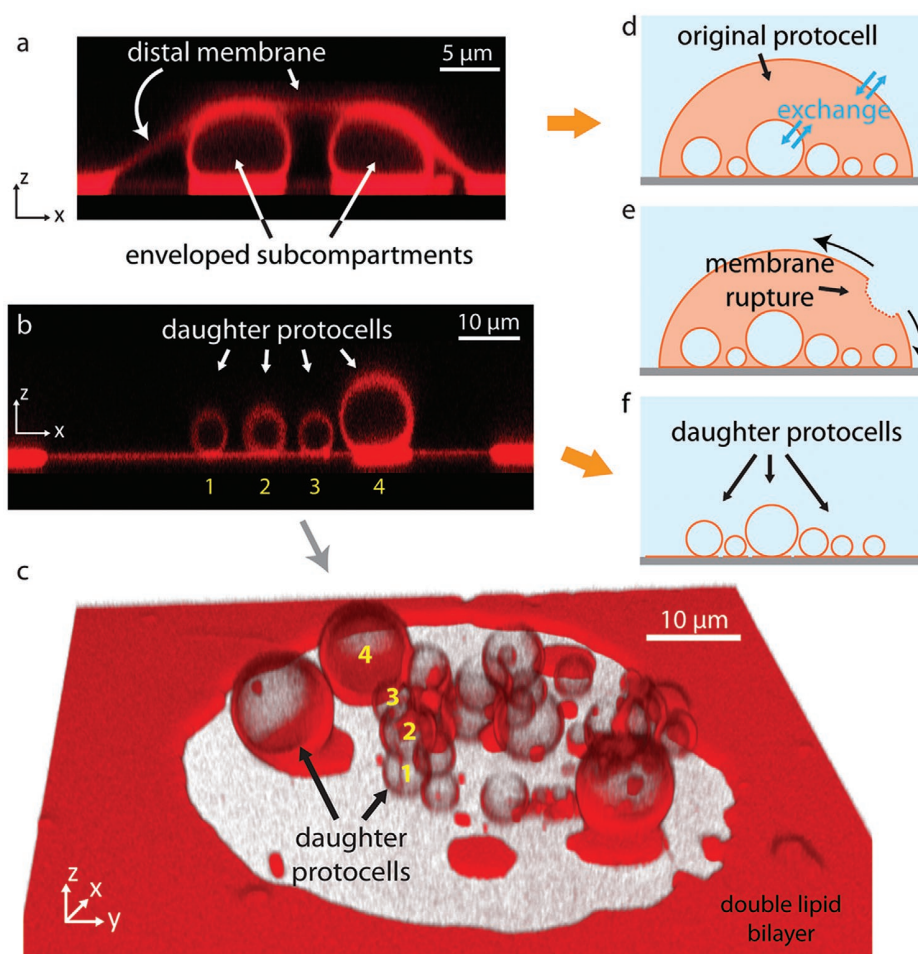


Figure 5. Pseudo-division. a) Confocal micrograph of a subcompartment (xz cross section) with the distal membrane in direct contact. b,c) Confocal micrographs of daughter cells remaining after the original enveloping membrane is disintegrated. b) xz cross section and c) the perspective view (xyz) c) Light circular region consists of a single bilayer, which is also visible in (b). d–f) Schematic representation of the process in (a)–(c). d) Material between the primary volume and the ambient buffer, and between the primary volume and the subcompartments can be exchanged. The membranes of the vesicles shown in this figure are composed of PC-DOPE; the surface is Al (with a native oxide layer).

are several Ca^{2+} -rich early Earth minerals, which might have acted as a source.^[27–29] The vesicles adhere to the substrate in a dome-like shape.^[30] Addition of chelators leads to gradual depletion of Ca^{2+} from the aqueous medium including the space between the surface and the membrane, leading to the removal of pinning points. This causes partial de-wetting at the membrane-surface interface.^[31] BAPTA which is one of the two chelators we utilized, has been shown to act as a shuttle buffer, driving Ca^{2+} out of the membrane and decreasing the Ca^{2+} concentration specifically at the membrane interface.^[32] Intercalation of EDTA, another chelator we use at mM concentrations, into the lipid head groups has been proposed to cause membrane bending and formation of invaginations.^[33] We do not think that direct interactions of BAPTA or EDTA with the membrane is the main cause of the compartmentalization, as in that case the compartments would not only form at the surface but also along the liquid interface to the protocell membrane. Formation of the compartments specifically on the solid substrate is a strong indication that the mechanism is surface

adhesion dependent. EDTA and BAPTA are strong metal chelators which were certainly not present on the early Earth. However, clay minerals were abundant in the prebiotic environment which could have played the role of the chelators in our experiments. Clay minerals are known to efficiently adsorb mono- or divalent ions including Ca^{2+} .^[34] These phyllosilicates, resemble in surface quality (flatness, homogeneity, surface potential) the synthetic surfaces used in our study.^[26] J. Szostak and co-workers showed enhanced vesicle formation upon adsorption of sheets of amphiphiles on various types of solid particle surfaces, among them clays.^[35,36]

The creases can also form spontaneously in membranes with low tension.^[22,37,38] Once the invaginations form, the transformation of these highly curved membrane regions into larger spherical compartments occurs through a self-driven process, during which the membrane curvature is reduced.^[39] A similar study, where the pinning/de-pinning occurs by means of streptavidin-biotin coupling, reports on this phenomenon.^[9] A high membrane curvature in the area of nucleation causes an

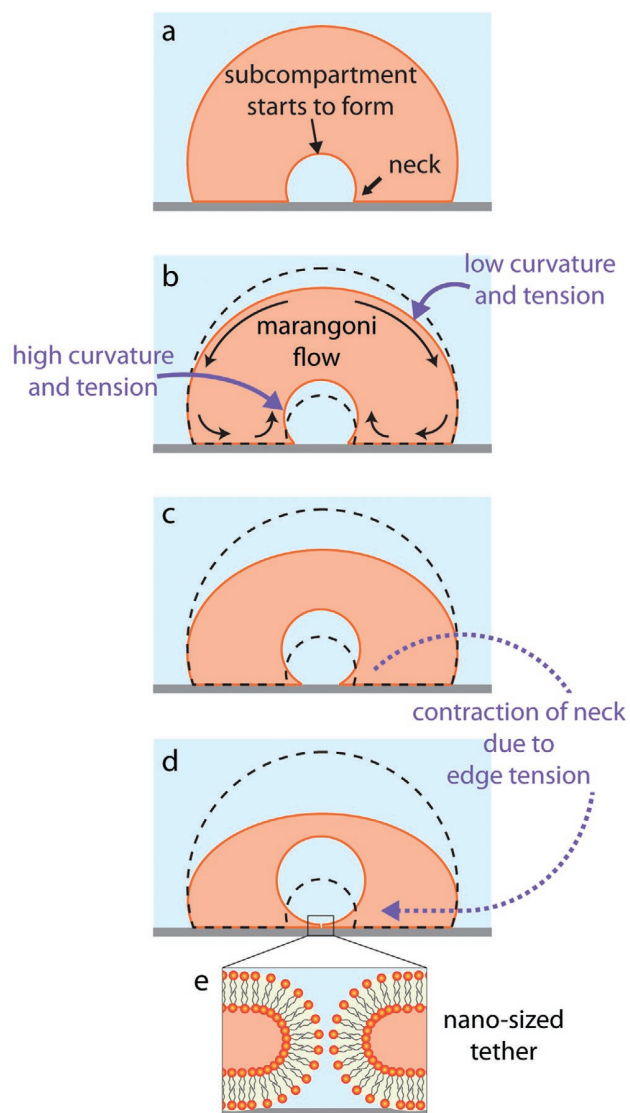


Figure 6. Subcompartmentalization mechanism. a–d) Growth of a subcompartment enveloped in a surface-adhered protocell. During growth the distal membrane is consumed. e) As pinning is removed from the contact line between the newly formed subcompartment and the surface, the contact line will contract due to edge tension transforming to a nano-sized pore or tether. The subcompartment stays connected to the basal membrane through a nano-sized pore or nanotube.

increase in the membrane tension, which leads to Marangoni flow of lipids from the region of relatively low membrane tension, that is, the distal membrane of the protocell, towards the region of higher tension. The distal membrane of the protocell is consumed as depicted in **Figure 6** (also in **Figure 1**, inset in **Figure 2m**). Additionally, an attached MLV (**Figure 1c**) can serve as a lipid source.

After a subcompartment has matured (**Figure 6b–d**), it stays connected to the basal membrane through a nano-sized pore-like connection (**Figure 6e**) as the force requirement for disconnecting the vesicle is very large: in the order of $\approx \text{mN}$ ^[16,40] versus $\approx \text{pN}$ ^[14] for pulling a membrane tether that can remain

connected through the neck. As pinning is removed from the contact line between the newly formed subcompartment and the surface, the contact line will contract due to edge tension transforming to a nano-sized pore or tether (**Figure 6e**). The area under the newly formed compartment re-wets even without the adhesion promoter Ca^{2+} lowering the surface free energy of the substrate.

We have not investigated the effect of pH and other factors, such as membrane composition or surface roughness, on compartmentalization. However, it is plausible that such factors would have a measurable impact on membrane deformations, for example due to acido-basic properties of lipids. It has been shown that pH gradients induce surface tension asymmetry, cause shape deformations and induce the formation of membrane invaginations reminiscent of mitochondrial cristae.^[41]

3.2. Temperature-Enhanced Formation

The role of temperature has been intensely discussed in the origins of life context, in particular whether high temperatures could have been beneficial or detrimental to protocell formation.^[42,43] The hydrothermal vent hypothesis which has been criticized for allowing excessively high temperatures, salinity and pH gradients is, after the discovery of “Lost City”-type hydrothermal fields (LCHFs), being reconsidered.^[43] LCHFs accommodate temperatures between 40 and 90 °C, which could have promoted the formation of prebiotic membrane compartments.^[44]

In our study, temperature increase weakens membrane-surface adhesion and causes immediate surface de-wetting,^[17] facilitating the subcompartment formation. Furthermore, it causes the membrane fluidity to increase, and enhances fusion.^[45,46] This results in accelerated growth of the subcompartments (**Movie S1**, Supporting Information). While the time scale in the case of subcompartmentalization induced by Ca^{2+} depletion ranges from several tens of minutes to an hour (**Figure 1**), it only takes a few minutes to form the compartments when the temperature is increased to 40 °C (**Figure 2a–l**). A nucleated compartment can rapidly mature and be internalized by the protocell (**Figure 2m**, inset) where some of them coalesce upon physical contact. A recent study has reported on the merging of lipid vesicles if they are in close proximity in a locally heated zone.^[47] Note that in order to elevate the temperature locally under avoidance of strong convection, we used an optical fiber and IR-B radiation (1470 nm, *cf.* Section S2 and S3, Supporting Information, for the details of the setup).

3.3. Encapsulation and Compartmentalization of External Compounds

Confining the reactants inside a membrane enclosed space and thereby bringing them into the close proximity can enhance reaction rates^[48] which is a benefit of compartmentalization in modern cells. We used anionic fluorescein as a model molecule to identify the mechanism of compartmentalization and encapsulation events. We have observed the internalization of fluorescein molecules inside the semi-grown subcompartments,

delivered locally by superfusion with a microfluidic pipette, by laser scanning confocal microscopy (Figure 3). A negatively charged dye was used to avoid electrostatic charge-based adsorption of the dye to the negatively-charged membrane.^[49] When the protocell is repeatedly pulsed with fluorescein, the fluorescence intensity inside the compartments instantly follows the external aqueous environment (Figure 3e–h and Movie S2, Supporting Information). The compartments take up fluorescein which immediately leaks out when the superfusion is terminated. This indicates that the subcompartments encapsulate the compound through the open interface to the surface, which exposes the compartments' interior to the external aqueous space. Encapsulation of the liquid at a membrane-surface interface by the invaginations has been previously reported. In that system, a protein–ligand coupling has been employed to promote the formation of the invaginations.^[9] If the subcompartment encapsulating the compound is suddenly sealed or its opening significantly reduced in size, the instant leakage of fluorescein is prevented and the fluorescence intensity decreases slowly (Figure 3l). While the leakage from the subcompartments is rapid in the initial superfusion cycles throughout the experiment, after $t \approx 8$ min the leakage from one particular subcompartment slows down (dark orange plot). Most importantly, the leakage from the subcompartments induced by heating is considerably slower, compared to the Ca^{2+} depletion-induced case (Figure 3l vs Figure 3h). Higher temperatures increase membrane fluidity, causing faster compartment growth. The compartments mature faster, likely resulting in contraction of the opening at the surface interface (Figures 3c,d and 6) to a nanosize pore or a nanotube (Figure 6e) and, accordingly, prolonged containment of internalized content (Figure 3i–l). This is in agreement with the finite element model. A single nanopore allows the equilibration of material in 600 s. (Figure 4, cf. FEM discussion below). This is confirmed by earlier studies on fluorescein diffusion through nanosized conduits.^[50]

3.4. Evidence for Pore-Mediated Encapsulation in the Primary Volume

The primary volume of the model protocell encapsulates fluorescein during multiple cycles of fluorescein exposure (Figure 3). We performed identical superfusion experiments on model protocells without subcompartments, that is, without the involvement of chelators. For different model protocells of comparable size under identical exposure conditions, the amount of encapsulated fluorescein at a given time varies from less than 20% to almost 90% of the concentration in the external medium (Figure 4a). This indicates that the means of transport through the membrane is not diffusion, which would result in each experiment in similar concentrations of the encapsulated compound at a given time. Our results are consistent with the presence of transient nano-sized pores in the membrane through which the fluorescein is diffusively internalized. It is well established that osmotic swelling of lipid vesicles causes an increase in membrane tension which leads to the formation of transient pores in the membrane.^[19,22] The adhesion of protocells to the substrate can cause a similar tension increase.^[16,22] The finite element method (FEM) simulations in Figure 4b–d

shows that transport through a single or a few nano-sized pores in the lipid membrane of a container of 5 μm size can lead to similar fluorescein concentrations inside the protocells shown in Figure 4a. According to the FEM simulations, during 100 s of uptake through a single pore, the concentration of the encapsulated fluorescein inside the protocell reaches 50% of the concentration of fluorescein in the external medium (Figure 4d). In one of the experiments (red plot in Figure 4a), the internal volume reaches 50% of the concentration of the stock fluorescein solution in 20–30 s. This corresponds to 3–5 membrane pores. It is reasonable that since 3–5 pores of nm size belong to a protocell of micron size, the pores would not overlap, and the pores would not jeopardize the integrity of the vesicle.

3.5. Implications for the Origins of Life

Origin of life studies often focus on a compartment as a whole—the (model) protocell. The possibility of consistent formation of organelle-like structures inside a protocell has not been considered plausible due to the lack of proteins and membrane-shaping machinery, which would transform the original membrane material to modular subcompartments and further stabilize them.^[10] Solid surfaces, which were abundant on the early Earth in the form of minerals, could to some extent have mimicked the role of sophisticated machinery. Surfaces intrinsically possess energy, which can promote membrane-surface interactions in several different ways.^[26] Previous studies have reported on the enhancing effects of surface associated bio- and organic chemistry relevant to the *RNA world*,^[13] including the synthesis of prebiotic peptides,^[12] nitrogen reduction, lipid self-organization, condensation-polymerization reactions, selection and concentration of amino acids and sugars as well as chiral selection.^[51] The reported surface-dependent phenomenon might pose an advantage over multi-vesiculation observed at the compartment membranes in bulk solution.^[52] Mineral surfaces have recently been shown to also induce protocell formation.^[35,36,39] Our findings reveal the capabilities of high energy surfaces, which are able to induce subcompartmentalization of adherent model protocells. We selected components which have direct representations in the prebiotic environment on the early Earth.

3.6. Flat Solid Oxide Substrates as Mineral Models

The solid model substrates Al_2O_3 and Al (with a native oxide layer) as well as SiO_2 , represent constituents of rock forming minerals on the early Earth.^[53] Al_2O_3 occurs naturally as Corundum, a mineral which has been studied and shown to amplify lipid bilayer formation.^[53] Sputtered SiO_2 corresponds to Quartz, which was associated with amino acid adsorption and peptide synthesis.^[13,54]

3.7. Protocell Models

We used giant unilamellar vesicles as protocell models. They consist of phospholipid molecules which are part of the origins

of life discussion. Several types of phospholipids have been synthesized in the laboratory under prebiotic conditions.^[55–58] Their precursor molecules were found in fluid inclusions in minerals relevant to the early Earth.^[54] A detailed list of the lipid membrane compositions and the surfaces leading to phenomena we describe in this study is provided in Section S1, Supporting Information.

The findings revealing more complex abilities of model protocells may also be important for the development of artificial cells^[59] and tissue-like materials,^[60,61] potentially in the context of drug delivery formulations and technology to produce such. Multi-compartmentalized liposome or polymerosome formulations have indeed been in the focus of biomedical investigations for improved drug and gene delivery as well as biosensing.^[62–64]

3.8. Pseudo-Division

Figure 3l reveals similar intensity levels of encapsulated fluorescence in the primary volume of the model protocell, and in one of its subcompartments. It is conceivable that the encapsulated contents are transported between the subcompartment and the primary volume through transient nano-sized membrane pores. We assume that the pores are present in the protocell membrane, which we have experimentally verified. Since the membrane surrounding the primary volume and the subcompartments are connected, and pores/defects are mobile in a fluid membrane, it is reasonable to assume that the pores can also be present in the subcompartment membrane. This would allow the transport of material across the membrane from the primary volume to the sub compartment. In some occasions the distal membrane of the model protocell ruptures, leaving multiple subcompartments, that is, the daughter cells, exposed directly to the bulk solution (Figure 5). A larger number of daughter cells can form, compared to the number of subcompartments, during the rapid collapse of the protocell (Figure S6 and Movie S3, Supporting Information). This can be anticipated, since the enveloping membrane opens up and rapidly relocates, providing excess membrane material. The relocation of the rupturing membrane evidently causes the collapse of some of the subcompartments or relocates them. This can be perceived as pseudo-division as this is not a direct splitting of the initial compartment, but a two step process starting with the transfer of internalized material to the daughter cells, followed by the disappearance of the mother protocell. We suggest that the surface mediated subcompartmentalization can therefore be viewed as starting point (pre-division) for protocell replication and division.

4. Conclusion

The question of how early in evolution cells could have had membranous subcompartments came recently into focus after their existence in archaea and bacteria has been shown. In this study we report that membrane-enveloped subcompartments consistently form in model protocells adhered on mineral-like solid substrates. The formation requires a minimum set of essential components: an amphiphile compartment, a solid

surface and an aqueous environment. External compounds can be encapsulated and transported between the primary volume of the protocell and the subcompartments. We show that when a protocell disintegrates, the subcompartments remain intact, and adhered to the substrate, suggesting the possibility of a primitive form of division. Following the earlier findings on enhancing effects of surfaces in prebiotic chemistry, this advocates that protocells with membranous subunits simultaneously running multiple reactions could have existed at the origin of life. If the process can be repeated in cycles over several protocell-subcompartment generations remains an interesting question to be elucidated.

5. Experimental Section

Preparation of Lipid Vesicles: To prepare the lipid suspensions, the dehydration and rehydration method^[14,65] was used. Various types of lipids were utilized, namely L- α -phosphatidylcholine (Soy), 18: dioleoylphosphoethanolamine, L- α -phosphoethanolamine (*Escherichia coli*), L- α -phosphatidylglycerol (*E.coli*), Cardiolipin (*E.coli*) and *E.coli* polar lipid extract. Briefly, lipids (99 wt %) and lipid-conjugated fluorophores (1 wt %) (for a detailed list of lipid compositions cf. Table S1, Supporting Information) were dissolved in chloroform leading to a final concentration of 10 mg mL⁻¹. 300 μ L of this mixture was then transferred to a 10 ml round bottom flask and the solvent was removed in a rotary evaporator at reduced pressure (20 kPa) for 6 hours to form a dry lipid film. The film was rehydrated with 3 ml of PBS buffer (5 mM Trizma Base, 30 mM K₃PO₄, 3 mM MgSO₄·7H₂O, 0.5 mM Na₂EDTA, pH 7.4 adjusted with 1 M H₃PO₄) and stored at +4 °C overnight to allow the lipid cake to swell. The sample was then sonicated for 25 s at room temperature, leading to the formation of giant compartments with varying lamellarity. For sample preparation, 4 μ L of the resulting lipid suspension was desiccated for 20 min and the dry residue rehydrated with 0.5 ml of 10 mM HEPES buffer containing 100 mM NaCl (pH 7.8, adjusted with 5 M NaOH) for 5 min. The lipid suspension was subsequently transferred onto a solid surface submerged in 10 mM HEPES buffer with the formulation mentioned above, but with the addition of 4 mM CaCl₂.

Surface Preparation: SiO₂, Al and Al₂O₃ surfaces were fabricated in the Norwegian Micro- and Nano-Fabrication Facility at the University of Oslo (MiNaLab). All thin films were deposited on glass cover slips (Menzel Gläss #1, 100–150 μ m thickness; WillCo Wells B.V., Amsterdam, NL). No pre-cleaning was performed on glass substrates before deposition. SiO₂ and Al were deposited onto the glass substrates by E-beam and thermal PVD evaporation using an EvoVac instrument (Ångstrom Engineering, Canada), to a final thicknesses of 10 nm of Al, and 84 nm of SiO₂. Al₂O₃ was deposited onto glass substrates by atomic layer deposition (Beneq, Finland), to a final thickness of 10 nm. Surfaces were used immediately after their fabrication.

Addition of Chelators and Fluorescein Molecules: For initiation of the subcompartmentalization, ambient buffer in the sample was gently exchanged with 10 mM HEPES buffer containing 100 mM NaCl, 10 mM EDTA and 7 mM BAPTA (pH 7.8, adjusted with 5 mM NaOH), using an automatic pipette 20 min after the initial deposition of the vesicles onto the substrates. All consecutive steps of the experiments were performed at same pH.

The experiments involving fluorescein exposure were performed by using a microfluidic pipette (Fluicell AB, Sweden). The surface-adhered vesicles were superfused with HEPES buffer with 100 mM NaCl, containing 25 μ M of Fluorescein Sodium Salt (pH 7.8, adjusted with 5 mM NaOH). The HEPES buffer used in the experiments shown in Figure 4a contains Ca²⁺, but is chelator-free. The vesicles used for Figure 4a are composed of identical lipid species, and are of similar size (4–6 μ m in diameter).

Local Heating: An optical fiber coupled to an IR-B laser (cf. Section S3, Supporting Information) was assembled to locally

increase the temperature in the sample.^[47,66] A semiconductor diode laser (HHF-1470-6-95, $\lambda = 1470$ nm, SemineX), driven with an 8 A power source (4308 Laser Source, Arroyo Instruments) was used in combination with an 0.22 NA multimode optical fiber with 50 μm core diameter (Ocean Optics). The fiber was located around approx. 30–50 μm from the vesicle. The laser current utilized for experiments were in the range 0.7 A, resulting in a local temperature increase to 40 °C.^[47]

Microscopy Imaging: All microscopy images were acquired with a laser scanning confocal microscopy system (Leica SP8, Germany) using a HCX PL APO CS 40x oil, NA 1.3 objective. The excitation/emission wavelengths varied with the employed fluorophores: Rhodamine ex: 560 nm em^{-1} : 583 nm (Figure S1, Supporting Information); Texas Red DHPE ex: 595 nm em^{-1} : 615 nm (Figure 1, Figure 2, Figure 4, Figure 5); ATTO 655-DHPE ex: 655 nm em^{-1} : 680 nm (Figure 3); Fluorescein ex: 488 nm, em: 515 nm (Figure 3, Figure 4).

Image Analyses: 3D fluorescence micrographs were reconstructed in Leica Application Suite X Software (Leica Microsystems, Germany). Image enhancement of fluorescence micrographs for the figures were performed with the Adobe Photoshop CS4 (Adobe Systems, USA). The fluorescence intensity analyses shown in Figures 2m,n, 3h, 3l, 3p, and 4a, were performed by using NIH ImageJ Software. For the micrograph series represented in Figure 2m,n (Movie S1, Supporting Information), median filtering was applied with ImageJ. For each vesicle in Figure 4a, the average intensity was measured within the whole vesicle interior at each time point normalized to the intensity of the exposed ambient stock solution with constant concentration. All graphs were plotted in Matlab R2018a, which was also used to generate the linear fit in Figure 2n. Schematic drawings were created with Adobe Illustrator CS4 (Adobe Systems, USA).

Finite-Element Simulations: Finite element modeling (FEM) was performed with the COMSOL Multiphysics software, using transport of dilute species physics (chds). The authors' model assumes a membrane thickness of $h_m = 1$ nm, and fluorescein diffusion coefficient of $D = 4.25 \times 10^{-10}$ m² s⁻¹.^[20] The geometry was built using cylindrical symmetry around axis x . The vesicle has a spherical shape with radius R_v , which was set to 2.5, 5, or 7.5 μm . It was assumed there was no material transport through the membrane (no flux boundary) except through one cylindrical pore (length h_p and radius R_p) positioned on the x -axis and connecting the vesicle with the external volume. The vesicle had initial internal concentration $c = 0$, while external volume had $c = c_0 = 1$. The outer boundary of the external volume was set to the constant concentration 1, mimicking a very large bath compared to the vesicle. For the simulation, the vesicle dimension was varied, while the pore dimension was set to $R_p = 5$ nm, or changed to a pore radius between 2.5 and 7.5 nm while the vesicle radius was kept $R_v = 5$ μm (cf. Section S4, Supporting Information). The simulation was transient from 0 to 600 s in 100 ms steps.

Supporting Information

Supporting Information is available from the Wiley Online Library or from the author.

Acknowledgements

This work was made possible through financial support obtained from the Research Council of Norway (Forskningsrådet), Project Grant 274433, UiO: Life Sciences Convergence Environment, the Swedish Research Council (Vetenskapsrådet), Project Grant 2015-04561, as well as the startup funding provided by the Centre for Molecular Medicine Norway (RCN 187615), and the Faculty of Mathematics and Natural Sciences at the University of Oslo. The authors thank Prof. A. Jesorka from the Biophysical Technology Laboratory at Chalmers University of Technology, Sweden, for support with the microheating setup, and for stimulating discussions.

Conflict of Interest

A.A. is a co-inventor of the multifunctional pipette, and minority share holder of Fluicell AB, the company that markets the multifunctional pipette. No payments or financial gain were a reason for, or a direct consequence of, the research contained within the manuscript.

Author Contributions

I.G. and A.A. designed the study and E.K. made the initial setup. K.S. carried out the microscopy experiments and analyzed the experimental data. A.A. developed the FEM model. I.G. suggested the investigation of the surface-induced subcompartmentalization phenomena, contributed to data evaluation, and supervised the project. All authors contributed to the writing of the manuscript.

Keywords

compartments, origin of life, protocells, solid surfaces, wetting

Received: August 28, 2020

Revised: October 15, 2020

Published online: November 23, 2020

- [1] Y. Diekmann, J. B. Pereira-Leal, *Biochem. J.* **2013**, *449*, 319.
- [2] E. Cornejo, N. Abreu, A. Komeili, *Curr. Opin. Cell Biol.* **2014**, *26*, 132.
- [3] M. J. Seufferheld, K. Kim, J. Whitfield, A. Valerio, G. Caetano-Anollés, *Biol. Direct* **2011**, *6*, 50
- [4] R. Nevo, D. Charuvi, E. Shimoni, R. Schwarz, A. Kaplan, I. Ohad, Z. Reich, *EMBO J.* **2007**, *26*, 1467.
- [5] *The Minimal Cell: The Biophysics of Cell Compartment and the Origin of Cell Functionality* (Eds: P. L. Luisi, P. Stano), Springer, New York **2011**.
- [6] M. Markström, A. Gunnarsson, O. Orwar, A. Jesorka, *Soft Matter* **2007**, *3*, 587.
- [7] L. M. Dominak, E. L. Gundermann, C. D. Keating, *Langmuir* **2010**, *26*, 5697.
- [8] M. S. Long, C. D. Jones, M. R. Helfrich, L. K. Mangeney-Slavin, C. D. Keating, *Proc. Natl. Acad. Sci. U. S. A.* **2005**, *102*, 5920.
- [9] S. Moreno-Flores, *Biochim. Biophys. Acta, Biomembr.* **2016**, *1858*, 793.
- [10] P. A. Monnard, P. Walde, *Life* **2015**, *5*, 1239.
- [11] J. F. Lambert, *Origins Life Evol. Biospheres* **2008**, *38*, 211.
- [12] V. Erastova, M. T. Degiacomi, D. G. Fraser, H. C. Greenwell, *Nat. Commun.* **2017**, *8*, 2033.
- [13] R. M. Hazen, D. A. Sverjensky, *Cold Spring Harbor Perspect. Biol.* **2010**, *2*, a002162.
- [14] M. Karlsson, K. Sott, M. Davidson, A.-S. Cans, P. Linderholm, D. Chiu, O. Orwar, *Proc. Natl. Acad. Sci. U. S. A.* **2002**, *99*, 11573.
- [15] T. Lobovkina, I. Gözen, Y. Erkan, J. Olofsson, S. G. Weber, O. Orwar, *Soft Matter* **2010**, *6*, 268.
- [16] I. Gözen, P. Dommersnes, I. Czolkos, A. Jesorka, T. Lobovkina, O. Orwar, *Nat. Mater.* **2010**, *9*, 908.
- [17] I. Gözen, M. Shaali, A. Ainla, B. Örtmen, I. Pöldsalu, K. Kustanovich, G. D. M. Jeffries, Z. Konkoli, P. Dommersnes, A. Jesorka, *Lab Chip* **2013**, *13*, 3822.
- [18] A. Ainla, G. D. M. Jeffries, R. Brune, O. Orwar, A. Jesorka, *Lab Chip* **2012**, *12*, 1255.
- [19] E. Karatekin, O. Sandre, F. Brochard-Wyart, **2003**, *52*, 486–493.
- [20] C. Culbertson, *Talanta* **2002**, *56*, 365.
- [21] A. Melcrová, S. Pokorna, S. Pullanchery, M. Kohagen, P. Jurkiewicz, M. Hof, P. Jungwirth, P. S. Cremer, L. Cwiklik, *Sci. Rep.* **2016**, *6*, 38035.

- [22] O. Sandre, L. Moreaux, F. Brochard-Wyart, *Proc. Natl. Acad. Sci.* **1999**, *96*, 10591.
- [23] K. I. Akashi, H. Miyata, H. Itoh, K. Kinoshita, *Biophys. J.* **1998**, *74*, 2973.1.
- [24] A.-L. Bernard, M.-A. Guedeau-Boudeville, L. Jullien, J.-M. Di Meglio, *Langmuir* **2000**, *16*, 6809.
- [25] C. A. Keller, B. Kasemo, *Biophys. J.* **1998**, *75*, 1397.
- [26] S. Jöemetsa, K. Spustova, K. Kustanovich, A. Ainla, S. Schindler, S. Eigler, T. Lobovkina, S. Lara-Avila, A. Jesorka, I. Gözen, *Langmuir* **2019**, *35*, 10286.
- [27] J. D. Toner, D. C. Catling, *Proc. Natl. Acad. Sci. U. S. A.* **2020**, *117*, 883.
- [28] J. Kazmierczak, S. Kempe, B. Kremer, *Curr. Org. Chem.* **2013**, *17*, 1738.
- [29] B. Burcar, A. Castañeda, J. Lago, M. Daniel, M. A. Pasek, N. V. Hud, T. M. Orlando, C. Menor-Salván, *Angew. Chem., Int. Ed.* **2019**, *58*, 16981.
- [30] U. Seifert, R. Lipowsky, *Phys. Rev. A* **1990**, *42*, 4768.
- [31] T. Bilal, I. Gözen, *Biomater. Sci.* **2017**, *5*, 1256.
- [32] M. Rousset, T. Cens, N. Vanmau, P. Charnet, *FEBS Lett.* **2004**, *576*, 41.
- [33] V. Prachayasittikul, C. Isarankura-Na-Ayudhya, T. Tantimongcolwat, C. Nantasenamat, H. J. Galla, *Acta Biochim. Biophys. Sin.* **2007**, *39*, 901.
- [34] H. Hashizume, in *Clay Minerals in Nature*, Intech Open, London **2012**.
- [35] M. M. Hanczyc, S. S. Mansy, J. W. Szostak, *Origins Life Evol. Biospheres* **2007**, *37*, 67.
- [36] M. M. Hanczyc, S. M. Fujikawa, J. W. Szostak, *Science* **2003**, *302*, 618.
- [37] C. Monzel, D. Schmidt, U. Seifert, A. S. Smith, R. Merkel, K. Sengupta, *Soft Matter* **2016**, *12*, 4755.
- [38] K. Ogłęcka, P. Rangamani, B. Liedberg, R. S. Kraut, A. N. Parikh, *eLife* **2014**, *3*, e03695.
- [39] E. S. Köksal, S. Liese, I. Kantarci, R. Olsson, A. Carlson, I. Gözen, *ACS Nano* **2019**, *13*, 6867.
- [40] K. Olbrich, W. Rawicz, D. Needham, E. Evans, *Biophys. J.* **2000**, *79*, 321.
- [41] M. I. Angelova, A. F. Bitbol, M. Seigneuret, G. Staneva, A. Kodama, Y. Sakuma, T. Kawakatsu, M. Imai, N. Puff, *Biochim. Biophys. Acta, Biomembr.* **2018**, *1860*, 2042.
- [42] B. K. D. Pearce, R. E. Pudritz, D. A. Semenov, T. K. Henning, *Proc. Natl. Acad. Sci. U. S. A.* **2017**, *114*, 11327.
- [43] W. Martin, J. Baross, D. Kelley, M. J. Russell, *Nat. Rev. Microbiol.* **2008**, *6*, 805.
- [44] S. F. Jordan, H. Ramm, I. N. Zheludev, A. M. Hartley, A. Maréchal, N. Lane, *Nat. Ecol. Evol.* **2019**, *3*, 1705.
- [45] G. Bolognesi, M. S. Friddin, A. Salehi-Reyhani, N. E. Barlow, N. J. Brooks, O. Ces, Y. Elani, *Nat. Commun.* **2018**, *9*, 1882.
- [46] J. Prives, M. Shinitzky, *Nature* **1977**, *268*, 761.
- [47] E. S. Köksal, S. Liese, L. Xue, R. Ryskulov, L. Viitala, A. Carlson, I. Gözen, *Small* **2020**, *16*, 2002529.
- [48] A. Kuchler, M. Yoshimoto, S. Luginbühl, F. Mavelli, P. Walde, *Nat. Nanotechnol.* **2016**, *11*, 409.
- [49] Y. Liu, E. C. Y. Yan, K. B. Eisenthal, *Biophys. J.* **2001**, *80*, 1004.
- [50] K. Sott, T. Lobovkina, L. Lizana, M. Tokarz, B. Bauer, Z. Konkoli, O. Orwar, *Nano Lett.* **2006**, *6*, 209.
- [51] M. Preiner, S. Asche, Becker, S. Betts, H. C. Boniface, A. Camprubi, E. Chandru, K. Erastova, V. Garg, S. G. Khawaja, N. Kostyrka, G. Machné, R. Moggioli, G. Muchowska, K. B. Neukirchen, S. Peter, B. Pichlhöfer, E. Radványi, Á. D. Rossetto, Salditt, A. Schmelling, N. M. Sousa, F. L. Tria, F. D. K. Vörös, D. Xavier, J. C., *Life* **2020**, *10*, 20.
- [52] A. L. Bernard, M. A. Guedeau-Boudeville, L. Jullien, J. M. Di Meglio, *Biochim. Biophys. Acta, Biomembr.* **2002**, *1567*, 1.
- [53] P. Dalai, N. Sahai, *Trends Biochem. Sci.* **2019**, *44*, 331.
- [54] U. Schreiber, C. Mayer, O. J. Schmitz, P. Rosendahl, A. Bronja, M. Greule, F. Keppler, I. Mulder, T. Sattler, H. F. Schöler, *PLoS One* **2017**, *12*, e0177570.
- [55] W. R. Hargreaves, S. J. Mulvihill, D. W. Deamer, *Nature* **1977**, *266*, 78.
- [56] M. Rao, J. Eichberg, J. Oró, *J. Mol. Evol.* **1982**, *18*, 196.
- [57] M. Rao, J. Eichberg, J. Oró, *J. Mol. Evol.* **1987**, *25*, 1.
- [58] D. E. Epps, E. Sherwood, J. Eichberg, J. Oró, *J. Mol. Evol.* **1978**, *11*, 279.
- [59] C. Xu, S. Hu, X. Chen, *Mater. Today* **2016**, *19*, 516.
- [60] H. Bayley, I. Cazimoglu, C. E. G. Hoskin, *Emerging Top. Life Sci.* **2019**, *3*, 615.
- [61] Q. Li, S. Li, X. Zhang, W. Xu, X. Han, *Nat. Commun.* **2020**, *11*, 232.
- [62] Y. Ai, R. Xie, J. Xiong, Q. Liang, *Small* **2020**, *16*, 1903940.
- [63] J. W. Hindley, R. V. Law, O. Ces, *SN Appl. Sci.* **2020**, *2*, 593.
- [64] Y. Elani, R. V. Law, O. Ces, *Nat. Commun.* **2014**, *5*, 5305.
- [65] E. S. Köksal, P. F. Belletati, G. Reint, R. Olsson, K. D. Leitl, I. Kantarci, I. Gözen, *JoVE* **2019**, *143*, e58923.
- [66] C. Billerit, I. Wegrzyn, G. D. M. Jeffries, P. Dommersnes, O. Orwar, A. Jesorka, *Soft Matter* **2011**, *7*, 9751.



Supporting Information

for *Small*, DOI: 10.1002/smll.202005320

Subcompartmentalization and Pseudo-Division of Model
Protocells

*Karolina Spustova, Elif Senem Köksal, Alar Ainla, and Irep
Gözen**

Supplementary Information for:

Subcompartmentalization and pseudo-division of model protocells

Karolina Spustova¹, Elif Senem Köksal¹, Alar Ainla², Irep Gözen^{1,3,4*}

¹ Centre for Molecular Medicine Norway, Faculty of Medicine, University of Oslo, 0318 Oslo, Norway

² International Iberian Nanotechnology Laboratory, 4715-330 Braga, Portugal

³ Department of Chemistry, Faculty of Mathematics and Natural Sciences, University of Oslo, 0315 Oslo, Norway

⁴ Department of Chemistry and Chemical Engineering, Chalmers University of Technology, SE-412 96 Göteborg, Sweden

*To whom correspondence should be addressed. Email: irep@uio.no

Table of contents

- S1 Lipid compositions and surfaces
- S2 Experimental setup
- S3 Heating system
- S4 Finite element simulations
- S5 Stability of daughter protocells
- S6 Product efficiency of pseudo-division

S1. Lipid compositions and surfaces

Surface	Lipid species	wt% percentage	Fluorophore (1%)	Associated figure
Al ₂ O ₃	PC:DOPE	69:30	Texas Red-DHPE ATTO 655-DHPE	Fig. 1a-b, e-f Fig. 2a-l Fig. 4a
	PE:PG:CA	67:23:9	16:0 Liss Rhod PE	Fig. 3a, e-p
Al	PC:DOPE	69:30	Texas Red-DHPE	Fig. 1c-d Fig. 5a-c Fig. S5a-f
	E.coli Ext. Pol.	99	16:0 Liss Rhod PE	Fig. S5g-j
	PE:PG:CA	67:23:9	16:0 Liss Rhod PE	Fig. S1a
SiO ₂	PE:PG:CA	67:23:9	16:0 Liss Rhod PE ATTO 655-DHPE	Fig. S1b

Table S1. Lipids, lipid-conjugated fluorophores and solid surface combinations

Abbreviations used in the table are as following:

PC : L- α -phosphatidylcholine (Soy)
 DOPE : 18:1 Dioleoylphosphoethanolamine
 PE : L- α -phosphoethanolamine (E.coli)
 PG : L- α -phosphatidylglycerol (E.coli)
 CA : Cardiolipin (E.coli)
 E.coli Ext. Pol. : E.coli polar lipid extract

All lipid products and 16:0 Liss Rhodamine PE were purchased from Avanti Polar Lipids, USA. Texas Red-DHPE was purchased from Sigma-Aldrich, USA. ATTO 655-DHPE was purchased from ATTO-TEC, Gmbh Germany.

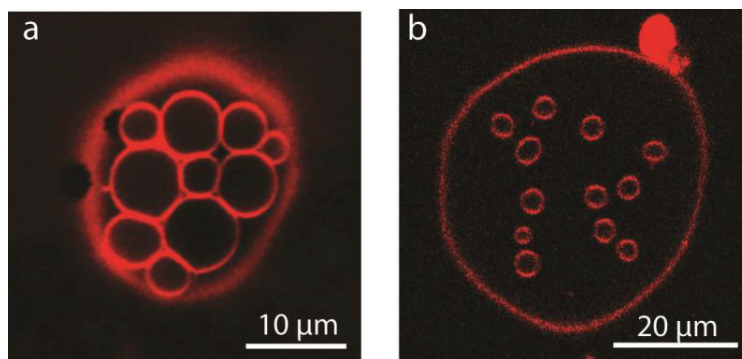


Figure S1. Subcompartmentalized model protocells made from PE-PG-CA lipids on (a) an Al surface with a native oxide layer, (b) SiO₂ surface.

S2. Experimental setup

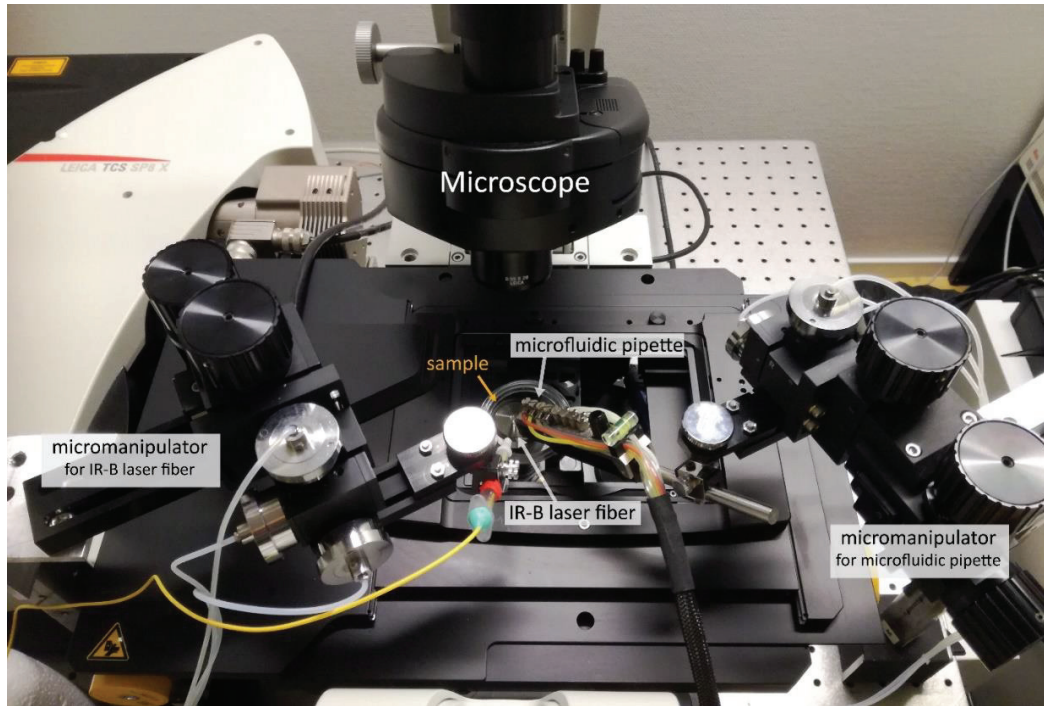


Figure S2. For the simultaneous heating and pulsing of fluorescein, an optical fiber coupled to an IR-B laser and a microfluidic pipette were positioned above the model protocells in the sample chamber, using 3-axis water hydraulic micromanipulators. The tip of the fiber and the tip of the pipette were placed in close proximity to target the same model protocell.

S3. Localized heating

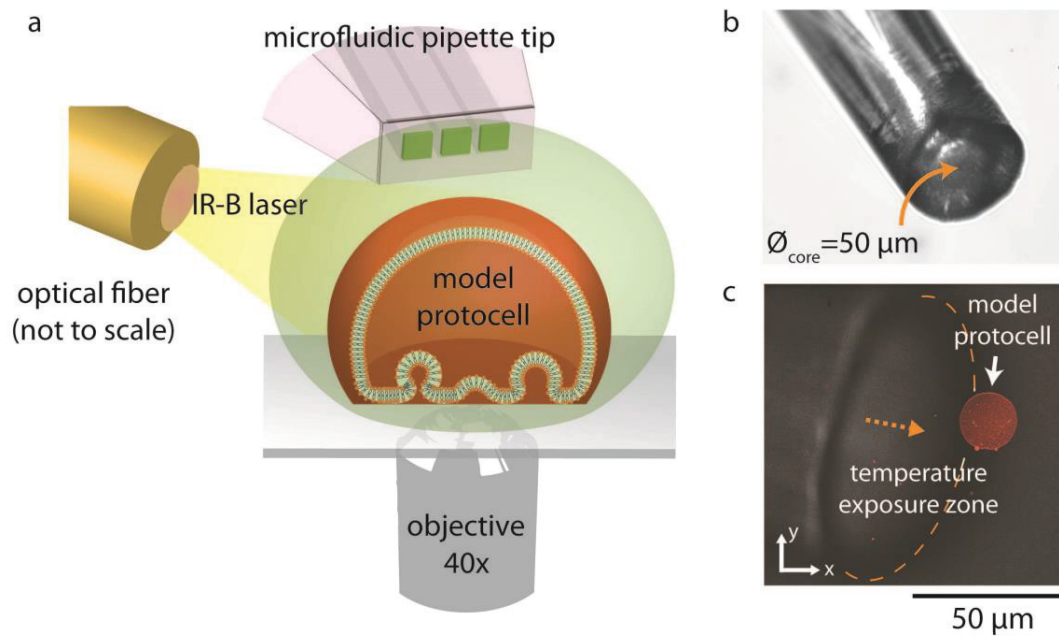


Figure S3. Localized heating. **(a)** The optical fiber is positioned above the surface near the model protocell of interest. Upon activation of the laser, the temperature in the vicinity of the protocell is increased to 40 °C. The heating can be applied with **(Fig. 3)** and without **(Fig. 2)** simultaneous fluorescein pulsing. Both the optical fiber tip and the microfluidic pipette tip are submerged into the sample buffer (not shown). **(b)** Micro-photograph of the optical fiber tip employed in the experiments. **(c)** Close up of the optical fiber tip while heating a model protocell.

S4. FEM simulations

Fig. S4 shows the concentration change in vesicles of varying size and with varying pore sizes over time, according to the FEM simulations described in the main article (**Fig. S4a**). Data sets are fitted with the function $1-e^{-kt}$, where the k is a loading rate. This is analogous to charging a capacitor through a resistor (RC circuit), where the vesicle internal volume will take the place of capacitor, and the pore will be the resistance for the loading. As expected, the loading rate increases with pore radius (**Fig. S4b**) and it is inversely proportional to the vesicle volume (**Fig. S4c**).

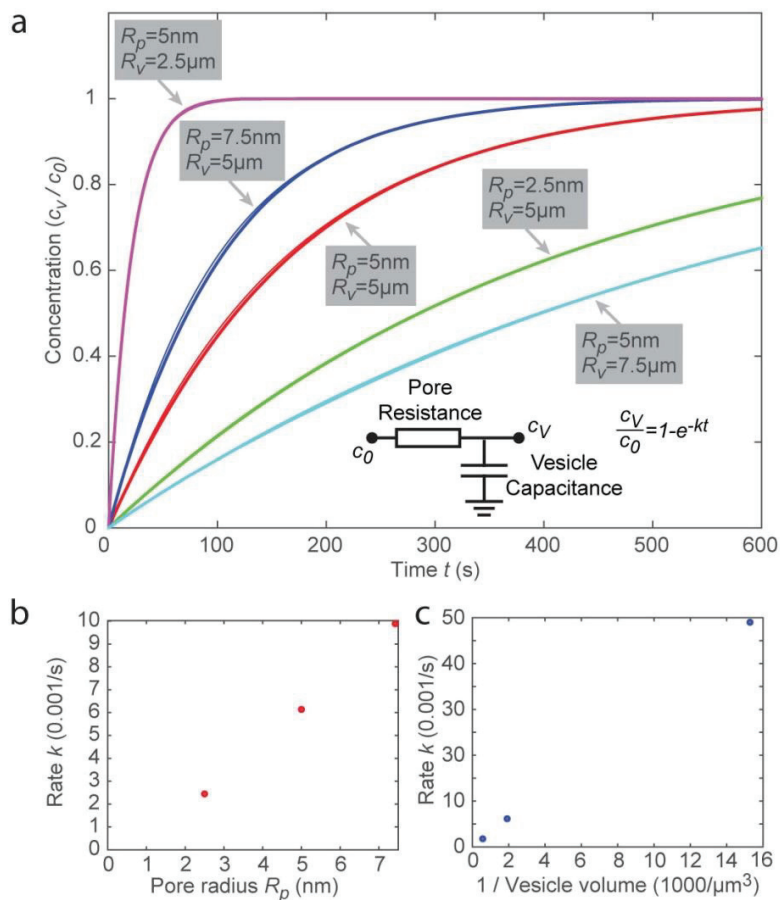


Figure S4. (a) FEM simulations showing encapsulation of fluorescein in vesicles of varying size and pore size, over time. (b) loading rate vs. pore radius, (c) loading rate vs. vesicle volume.

S5. Stability of daughter protocells

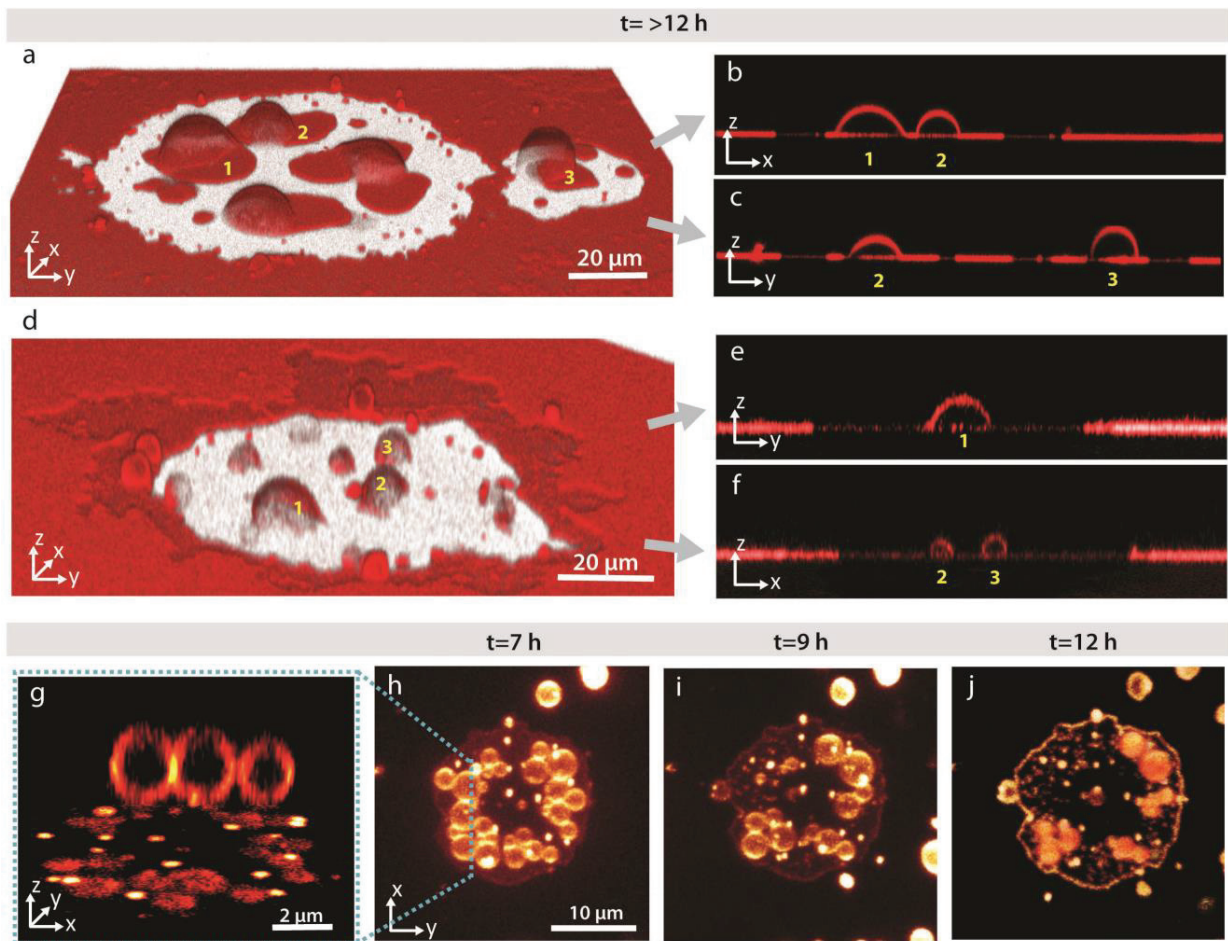


Figure S5. (a-j) Confocal micrograph of daughter protocells remaining after pseudo-division. **(a, d)** 3D reconstructed, perspective view (x-y-z) **(b-c, e-f)** cross-sections, side views (x-z/y-z). Micrographs were taken 12 hours after the addition of chelators to the ambient solution. Confocal micrographs of daughter protocells from profile view **(g)** and top view **(h-j)**. The micrographs have been acquired 7 h **(h)**, 9 h **(i)** and 12 h **(j)** after chelator addition. The membranes of the vesicles shown in this figure are composed of (a-f) PC-DOPE or (g-j) E.coli Ext. Pol.; all of the surfaces are Al (with a native oxide layer).

S6. Product efficiency of pseudo-division

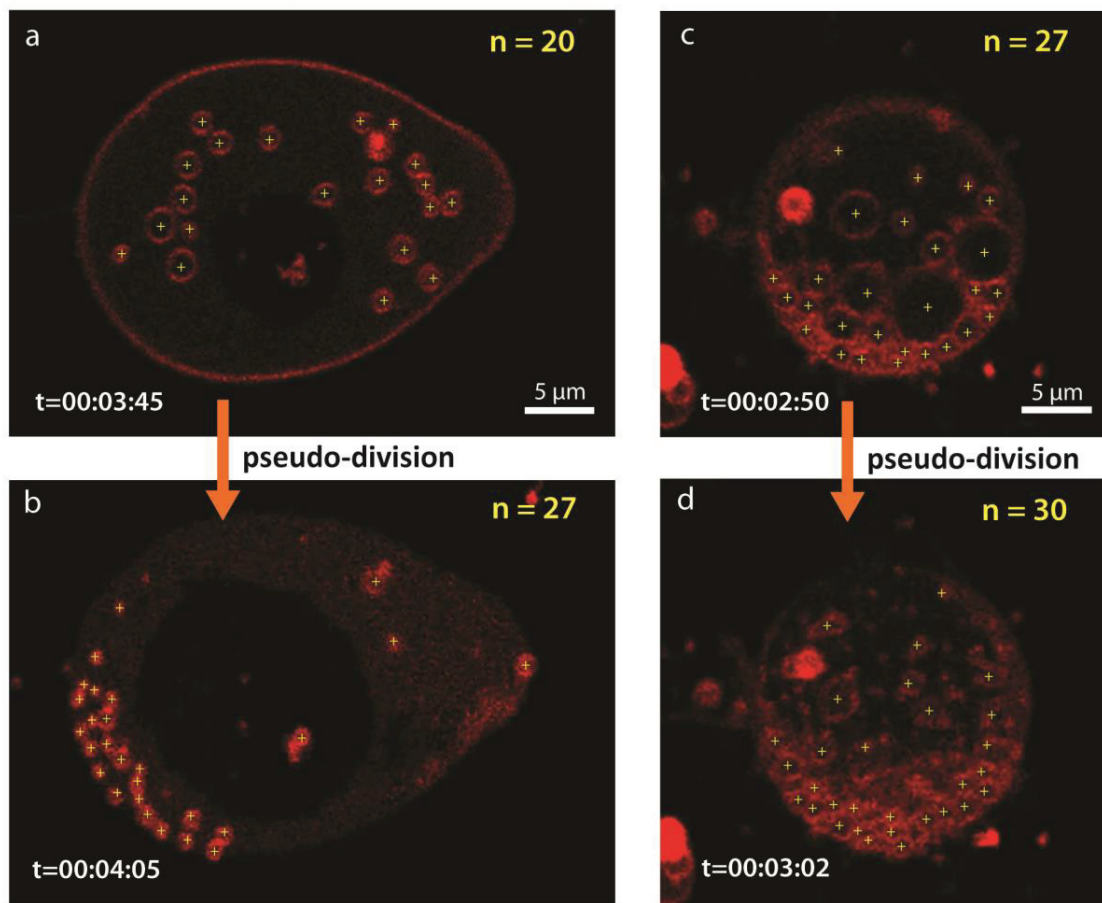


Figure S6. (a-d) Confocal micrographs showing two different experiments (a-b, c-d) where pseudo-division occurred. The number of subcompartments increase after the rupturing of the enveloping (distal) membrane (**Mov. S3**).

Supplementary Videos

Movie S1. Subcompartmentalization at increased temperature. Laser scanning confocal microscopy time series showing the temperature-induced formation, growth and fusion of the subcompartments.

Movie S2. Encapsulation and compartmentalization of fluorescein. Laser scanning confocal microscopy time series showing the encapsulation and release of the fluorescein by the subcompartments and the primary volume of the protocell. Part I: room temperature, Part II: increased temperature (40 °C).

Movie S3. Pseudo-division. Laser scanning confocal microscopy time series showing process of the pseudo-division upon disintegration of the distal membrane of the compartmentalized protocell.

Paper V

Paper VI

